

UNIVERSITY OF ALBERTA

GEOMECHANICAL BEHAVIOR OF GRAND RAPIDS FORMATION OIL SANDS

BY
CHUN ZHANG

A THESIS
SUBMITTED TO THE FACULTY OF GRADUATE STUDIES AND RESEARCH IN
PARTIAL FULFILMENT OF THE REQUIREMENT FOR THE DEGREE OF MASTER
OF SCIENCE IN GEOTECHNICAL ENGINEERING

DEPARTMENT OF CIVIL ENGINEERING

EDMONTON, ALBERTA
SPRING, 1994

Abstract

Previous limited geomechanical testing has shown that the geomechanical behavior of Cold Lake Clearwater Formation oil sands is significantly different from that of Athabasca McMurray Formation oil sands. To investigate this behavior, a testing program has been conducted to study the geomechanical properties of the Cold Lake Lower Grand Rapids Formation oil sands which have similar mineralogy and geologic history as the Clearwater Formation.

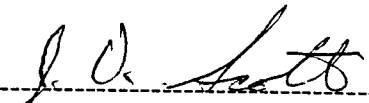
In this study, the stress-strain behavior of both sands and oil sands were reviewed and the geology and mineralogy of the Cold Lake oil sands were summarized. A detailed description of the test apparatus and test procedures used in this research project were presented. In the triaxial shear laboratory testing for the geomechanical properties, a series of stress paths were followed. Some of the stress paths simulated those encountered in field bitumen recovery processes. In the testing program, attention was especially paid to the geomechanical behavior of the oil sands in the low effective stress range which occurs during in situ bitumen recovery processes. The triaxial shear test effective confining stress level varied from 0.1 MPa to 9.5 MPa.

The isotropic bulk compressibility of the oil sands has been expressed as a power function of effective confining stress. It varies dramatically with a small change in the effective confining stress in the low effective stress range below a boundary stress of about 2.0 MPa. Grain crushing has a significant impact on the stress-strain-volume change behavior of the oil sands. An effective confining stress of 3.0 MPa was found to be the "break down" stress beyond which grain crushing is a dominant mechanism in shear. The stress-strain behavior of the oil sands following different stress paths is observed and evaluated. The failure criteria of the oil sands can not be represented by a single failure envelope. It is stress path dependent. The magnitude of grain crushing which is associated with stress paths appears to control the failure mechanism in shear. Fines content tends to increase the shear strength of the oil sands.

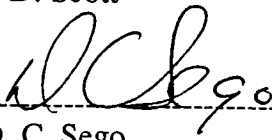
UNIVERSITY OF ALBERTA

FACULTY OF GRADUATE STUDIES AND RESEARCH

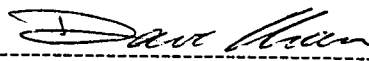
The undersigned certify that they have read, and recommend to the Faculty of Graduate Studies and Research, for acceptance, a thesis entitled **Geomechanical Behavior of Grand Rapids Formation Oil Sands** submitted by Chun Zhang in partial fulfilment of the requirements for the degree of Master of Science in Geotechnical Engineering.



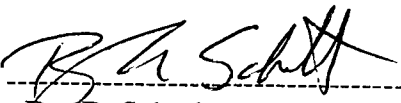
Dr. J. D. Scott



Dr. D. C. Sego



Dr. D. Chan



Dr. D. Schmitt

April 15, 1994

ACKNOWLEDGEMENTS

Funding for this research was provided by the Alberta Oil Sands Technology and Research Authority through the AOSTRA University Research Program, Agreement 980.

The research was supervised by J. D. Scott in the Department of Civil Engineering. His advice, guidance and assistance is greatly appreciated.

Mobil Oil Canada Ltd is acknowledged for providing oil sands cores and core laboratory reports for this testing program.

The author would like to thank Gerry Cyre, Steve Gamble, Christine Hereygers and other staff members for their technical assistance in the laboratory tests.

Table Of Contents

Chapter	Page
Chapter 1 Introduction	1
1.1 Objective of the Research	1
1.2 Organization of the Thesis	3
Chapter 2 Stress-Strain Behavior of Sands and Oil Sands	4
2.1 Shear Strength and Dilatancy of Sands	4
2.2 Grain Crushing	9
2.3 Stress-Strain Behavior of Oil Sands	12
2.4 Soil Models	17
2.4.1 Hyperbolic Model	17
2.4.2 Bulk Modulus and Shear Modulus	22
2.4.3 Three Moduli Hypoelastic Model	24
2.4.4 Oil Sands Models	27
2.5 Summary	28
Chapter 3 Geology of the Cold Lake Oil Sands	33
3.1 General Geology	33
3.2 Oil Sands Tested	36
3.3 Mineralogy of Cold Lake Oil Sands	38
3.4 Summary	40
Chapter 4 Test Apparatus and Procedures	46
4.1 Test Apparatus	46
4.1.1 Pressure System	46
4.1.2 Triaxial Cell	47

4.1.3 Volume Change Measuring Device	47
4.1.4 Axial Loading	48
4.1.5 Data Logging	49
4.1.6 Configuration Of Testing System	49
4.2 Specimen Preparation	50
4.2.1 Trimming Specimens	50
4.2.2 Sample Disturbance	52
4.3 Test Procedures	54
4.4 Test Program	55
Chapter 5 Isotropic Bulk Compressibility of the Lower Grand Rapids Formation Oil Sands	71
5.1 General Description	71
5.2 Test Results and Analyses	72
5.3 Estimation of In Situ Bulk Compressibility	80
5.4 Conclusions	81
Chapter 6 Stress-Strain Behavior Of the Lower Grand Rapids Formation Oil Sands	97
6.1 Drained Triaxial Compression	97
6.2 Undrained Triaxial Compression	107
6.3 Drained Compression With J_1 Constant	115
6.4 Pore Pressure Injection	124
6.5 Grain Crushing	131
6.6 Application of Hyperbolic Model To Test Results	136
6.7 Comments on Modelling the Test Results	140
Chapter 7 Conclusions	183
7.1 Summary and Conclusions	183
7.2 Further Studies	190

References	193
Appendices	199
A. Sample Calculations	199
A.1 Determination of Specimen Dimensions	
After Isotropic Consolidation	199
A.2 Calculation of Physical Parameters	200
A.3 Calculation of the Parameters in a CIU Test	202
A.4 Determination of Effective Confining Stress	
in a J_1 Constant Test	204
A.5 Pore Pressure Injection Test Procedure	204
A.6 Correction to a Stress-Strain Curve	206
B. Calibrations	209
C. Plots of Isotropic Cyclic Consolidation Results	
and Grain Size Analyses	211

List of Tables	Page
Table 3.3.1 Mineral compositions of Cold Lake oil sands	42
Table 5.1.1 Specimen data	84
Table 5.2.1 Compressibility parameter a and b	85
Table 5.2.2 Summary of compressibility measurements ($10^{-3}/\text{MPa}$) for different effective confining stresses	86
Table 5.2.3 Average C_b ($10^{-3}/\text{MPa}$) for the different oil sands cores	87
Table 5.3.1 Estimated in situ bulk compressibility	87
Table 6.1.1 Summary of consolidated drained triaxial compression results	142
Table 6.1.2 Comparison of the drained triaxial compression test results	143
Table 6.2.1 Summary of consolidated undrained triaxial compression test results	144
Table 6.2.2 Steady States in CIU Tests	145
Table 6.3.1 Summary of triaxial compression tests with J_1 constant	146
Table 6.3.2 Comparison of volumetric strain in test CD3 and CP4	147
Table 6.3.3 Comparison of volumetric strain in test CD5 and CP8	147
Table 6.4.1 Summary of pore pressure injection test results	148
Table 6.4.2 Anticipated stress condition in CAI tests	149
Table 6.5.1 Grain size analyses	150
Table 6.6.1 Hyperbolic model in CID tests	151
Table 6.6.2 Hyperbolic model in CIU tests	151
Table 6.6.3 Hyperbolic model in CIP tests	152

List of Figures	Page
Figure 2.3.1 Failure envelopes of Athabasca oil sands (after Agar, 1984)	30
Figure 2.3.2 Isotropic cyclic consolidation test on Athabasca McMurray Formation oil sand (after Kosar, 1989)	31
Figure 2.4.1 Hyperbolic stress-strain relationship	32
Figure 2.4.2 Transformed stress-strain relationship	32
Figure 3.1.1 Oil sand deposits in Alberta	43
Figure 3.1.2 Stratigraphic correlation of the Lower Cretaceous Mannville Group	44
Figure 3.3.1 Mineral composition of Cold Lake oil sands	45
Figure 4.1.1 Pressure control system	59
Figure 4.1.2 Diagram of triaxial cell	60
Figure 4.1.3 Bellow volume change measuring device	61
Figure 4.1.4 Strain controlled vertical loading system	62
Figure 4.1.5 Stress controlled vertical loading frame -- belloframe	63
Figure 4.1.6 Diagram of testing system	64
Figure 4.1.7 Innovation of the triaxial cell	65
Figure 4.2.1 Trimming specimen using tube core	66
Figure 4.2.2a Coring specimen on milling machine	67
Figure 4.2.2b Freeze slabbed cores in the cylinder	67
Figure 4.2.3 The relationship between index of disturbance and bitumen content	68
Figure 4.3.1 Test specimen set up	69
Figure 4.4.1 Stress paths followed in testing program	70
Figure 5.2.1 Test CU6: Isotropic cyclic consolidation	88
Figure 5.2.2 Test CU6: Isotropic compressibility unload #1 and #2	89
Figure 5.2.3 Test CU6: Isotropic compressibility reload #1 and #2	89

Figure 5.2.4	Test CU6: Isotropic compressibility unloading	90
Figure 5.2.5	Test CU6: Isotropic compressibility reloading	90
Figure 5.2.6	Test CU6: Isotropic compressibility unloading #1 and #2 (Semilog scale)	91
Figure 5.2.7	Test CU6: Isotropic compressibility reloading #1 and #2 (Semilog scale)	91
Figure 5.3.1	The relationship between unloading compressibility and index of sample disturbance (stress range 1.0 to 8.0 MPa)	92
Figure 5.3.2	The relationship between unloading compressibility and index of sample disturbance (stress range 0.1 to 0.5 MPa)	93
Figure 5.3.3	The relationship between reloading compressibility and index of sample disturbance (stress range 1.0 to 8.0 MPa)	94
Figure 5.3.4	The relationship between reloading compressibility and index of sample disturbance (stress range 0.1 to 0.5 MPa)	95
Figure 5.3.5	Estimated in situ isotropic bulk compressibility	96
Figure 6.1.1	Stress-strain and volume change in CID tests	153
Figure 6.1.2	The initial tangent modulus in drained triaxial compression	154
Figure 6.1.3	Axial strain in CID tests	155
Figure 6.1.4	Volumetric strain in CID tests	155
Figure 6.1.5	Axial strain at failure in drained triaxial compression	156
Figure 6.1.6	CID test failure envelope	157
Figure 6.1.7	Shear strength of oil sands in drained triaxial compression	158
Figure 6.1.8	The secant internal friction angle in CID tests	159
Figure 6.2.1	Stress-strain relationship and pore pressure change in CIU tests	160
Figure 6.2.2	Stress-strain relationship and change in pore pressure parameter A in CIU tests	161

Figure 6.2.3	Pore pressure change at failure in CIU tests	162
Figure 6.2.4	Pore pressure parameter A at failure in CIU tests	162
Figure 6.2.5	Relationship between A_f and OCR in CIU tests	163
Figure 6.2.6	Axial strain at failure in CIU tests	163
Figure 6.2.7	$s' - t$ stress path in CIU tests	164
Figure 6.2.8	Comparison of stress path in CID and CIU tests	165
Figure 6.3.1	Stress-strain relationship and volume change in CIP tests	166
Figure 6.3.2	Stress-strain relationship and volume change in test CD3 and CP4	167
Figure 6.3.3	$p' - q$ stress path in CIP tests	168
Figure 6.3.4	$s' - t$ stress path in CIP tests	169
Figure 6.3.5	Stress-strain relationship and volume change in test CP1 and CP3	170
Figure 6.4.1	$s' - t$ stress path in Pore pressure injection tests	171
Figure 6.4.2	The relationship between stress ratio and effective confining stress in CIA tests	172
Figure 6.4.3	The relationship between deviatoric stress and axial strain at failure in CIA tests	172
Figure 6.4.4a	The relationship between stress ratio and axial strain in pore pressure injection (small axial strain)	173
Figure 6.4.4b	The relationship between stress ratio and axial strain in pore pressure injection (large axial strain)	173
Figure 6.4.5	The relationship between initial stress ratio and compression stress ratio	174
Figure 6.4.6	The relationship between stress ratio and volumetric strain in pore pressure injection	174

Figure 6.4.7	The relationship between volumetric strain and axial strain in pore pressure injection	175
Figure 6.4.8	The relationship between secant friction angle and effective confining stress in CID and CAI tests	175
Figure 6.5.1	Comparison of grain size distribution in test CD1 and CP6	176
Figure 6.5.2	Comparison of grain size distribution in test CU1 and CU8	177
Figure 6.5.3	Comparison of grain size distribution in test CP3 and CP8	178
Figure 6.5.4	Comparison of grain size distribution in test CU5 and CU8	179
Figure 6.6.1	Stress-strain relationship in CID tests and hyperbolic curve fitting	180
Figure 6.6.2	Stress-strain relationship in CIU tests and hyperbolic curve fitting	181
Figure 6.6.3	Stress-strain relationship in CIP tests and hyperbolic curve fitting	182

Chapter 1

Introduction

1.1 Objective of the Research

The geotechnical constitutive behavior of oil sands has been studied in the laboratory by several researchers in recent years. Dusseault (1977) made a detailed study on the geotechnical characteristics of Athabasca oil sands which included not only the geotechnical behavior, such as shear strength and compressibility, but also the oil sands structure which for the first time was identified as a locked sand. This identification of the sand structure explained the unique behavior of oil sands compared to other sand deposits. Agar (1984) conducted a series of laboratory tests to study the behavior of oil sands at elevated temperatures and pressures. The testing program included one-dimensional thermal expansion and compression, triaxial thermal expansion and stress strain properties, and permeability change. Plewes (1984) conducted a series of consolidated-undrained triaxial shear tests with pore pressure measurement at rapid strain rates as well as triaxial tension tests. Kosar (1989) studied the constitutive behavior of oil sands and related strata through representative laboratory testing in which three pairs of coupling were involved: thermal-mechanical, hydro-mechanical and hydro-thermal. Wong et al (1993) has studied the stress-strain response of Cold Lake Clearwater Formation oil sands.

Based on these laboratory programs, several constitutive models for oil sands have been developed. Wan, Chan and Kosar (1989) proposed a non-associated generalized plasticity model for Athabasca oil sands that incorporates hardening,

softening, plastic volume expansion and contraction. Vaziri (1989) developed another oil sands model based on three mathematical concepts, hyperbolic non-linear elastic behavior, critical state elasto-plastic behavior and Mohr-Coulomb criterion at failure.

All of the above research work has been concerned with Athabasca oil sands except for a limited number of laboratory tests which has been performed on Cold Lake oil sands. This limited testing, however, has indicated that the constitutive behavior of Cold Lake oil sands is quite different from that of Athabasca oil sands. This research has been conducted on Cold Lake Lower Grand Rapids Formation oil sands. The objectives of the research is composed of three aspects:

- 1) Geomechanical properties and behavior of the Lower Grand Rapids Formation oil sands will be measured through laboratory triaxial testing that simulates the stress conditions during in situ recovery processes. The behavior of this specific Cold Lake oil sand deposit will be determined following a series of stress paths.

- 2) The previous geomechanical tests on oil sands were mostly performed in the high effective confining stress range. There is little information on how oil sands behave at low effective confining stresses which most often occur during in situ recovery processes, such as steam and hot water injection, in situ combustion, and hydraulic fracturing. In this testing program, therefore, attention is paid to the low effective stress range. It is hypothesized that the oil sands may behave differently at low and high effective stresses in terms of compressibility and stress-strain-strength behavior because of dilatancy and grain crushing.

- 3) The triaxial test results will be fitted to a hyperbolic model to determine if the stress-strain relationships of the Grand Rapids oil sands can be represented by this form of model.

To determine the effect of different stress conditions on Grand Rapids oil sands, the laboratory tests are divided into series in which different stress paths are followed. According to the stress path, five types of triaxial testing will be conducted in the

research, isotropic cyclic consolidation (ICC) tests, isotropically consolidated drained compression (CID) tests, isotropically consolidated undrained compression (CIU) tests, isotropically consolidated drained compression with mean effective stress constant (CIP) tests and anisotropically consolidated pore pressure injection (CAI) tests.

1.2 Organization of the Thesis

The thesis consists of seven chapters which follow the conventional thesis format starting with Chapter One in which the objective of the thesis is stated.

Chapter Two reviews the general behavior of sands, grain crushing and the present research achievements on oil sands. As well, some soil stress-strain models and oil sands models are summarized. The geologic background of the Cold Lake oil sands is outlined in Chapter Three. This chapter includes the general geology of this area and the detailed stratification and mineralogy of the Grand Rapids oil sands deposit tested. The test apparatus and procedures are described in Chapter Four. Chapter Five and Chapter Six present the test results and their discussions. Conclusions are given at the end of each section in these chapters. Chapter Seven summarizes the conclusions and raises questions for future study.

Chapter 2

Stress-Strain Behavior of Sands and Oil Sands

2.1 Shear Strength and Dilatancy of Sands

In engineering practice, soils are sometimes assumed to be ideal elastic materials. The principle of elasticity therefore, is directly applied to solve problems of soils by use of the deformation modulus and the Poisson's ratio. In fact, soils are not elastic materials and their mechanical behavior can not be totally represented by elastic theory. To obtain more reasonable solutions to engineering problems, many assumptions have been made to meet the needs in soil analyses. For example, the problems of stability or limiting equilibrium have generally been solved on the basis of a rigid plastic soil whose properties are defined by a single value of strength. The solution of the bearing capacity problem involves elastic-plastic idealization which is more close to reality (Yassin and Gibbison 1953).

Bishop (1972) stated that most real soils depart from elastic-plastic idealization in one important respect. With a few exceptions (loose sand under drained conditions), real soils do not continue to yield at a constant stress after the point of failure is reached. Strain softening behavior after failure is commonly observed. The stress decreases until an ultimate or residual value is reached. Therefore, the strength of a soil should be described by two values τ_f , the peak or failure stress and τ_r , the residual stress. The brittleness index I_B (Bishop 1967) which relates τ_f to τ_r , is often used to evaluate the behavior of a soil.

$$I_B = \frac{\tau_f - \tau_r}{\tau_f} \quad (2.1.1)$$

By use of the brittleness index, some empirical criteria for choosing assumptions, rigid plastic or elastic-plastic, in soil analyses have been established (Bishop 1971, Rowe 1969). If I_B is less than 30 %, the rigid plastic analysis based on a single value of strength (peak) is little in error, but if I_B exceeds 70%, the average stress (considering progressive failure in the stability analysis) may lie closer to the residual than to the peak.

For cohesionless soils, the stress dependent strength is the most significant characteristic. Also, in the drained condition, dense sands show dilatancy during shear at low stresses which increases the strength of the sands considerably. In undrained condition, the tendency to dilate results in a decrease in pore pressure or increase in the effective confining stress which also strengthens the sand specimen. This behavior characterizes the difference of sands from other engineering materials. The Mohr-Coulomb failure criterion is widely used to determine the shear strength of sands.

$$\frac{\sigma_1' - \sigma_3'}{\sigma_1' + \sigma_3'} = \sin \phi' \quad \text{or} \quad \frac{\sigma_1'}{\sigma_3'} = \tan^2 \left(45^\circ + \frac{\phi'}{2} \right) \quad (2.1.2)$$

In which, σ_1' and σ_3' are the major and minor principal effective stresses, and ϕ' is the effective friction angle. As mentioned before, two values of strength, peak and residual, characterize soil behavior. In the case of cohesionless soils, the residual state may be identified with the critical state which was clearly defined by Hvorslev (1937): " Eventually a condition is reached under which a continued flow does not cause further changes in the shearing resistance and void ratio. This ultimate value of the shearing resistance as well as the ultimate value of the void ratio are equal in both cases (i.e. the loose and dense states) and therefore independent of the initial state of consolidation of the soil". The convenient way to determine the residual or critical state strength of cohesionless soils is to plot strength against the rate of volume change at failure $\left(\frac{d\varepsilon_v}{d\varepsilon_1} \right)_f$ for series of samples of

different initial densities tested in triaxial compression and by extrapolation find the strength of the sample failing at zero rate of volume change.

Bishop (1950) has derived an expression to separate the strength of a sand sample according to the frictional and dilatancy components. The shear box test results presented indicated that the difference in shear strength between dense sand and loose sand was mainly due to dilation. In other words, the work done in overcoming frictional forces is almost unchanged for both dense and loose sands in shear.

$$\tan \phi_f = \frac{\tau - \tau_d}{\sigma_n} = \tan \phi_{\max} - \frac{\delta v}{\delta \Delta} \quad (2.1.3)$$

In which, ϕ_f = friction angle between particle surfaces, σ_n = normal stress, τ = shear strength and τ_d = shear necessary to cause sample to dilate against the normal stress. δv = expansion per unit area and $\delta \Delta$ = the shear displacement in which δv occurs. The concept of dilatancy was later extended by Bishop (1954) to an expression for the stress condition in the triaxial compression test.

$$\tan^2 \left(45 + \frac{\phi_f}{2} \right) = \left(\frac{\sigma_1'}{\sigma_3'} \right)_f = \left(\frac{\sigma_1'}{\sigma_3'} \right)_{\max} - \sigma_3' \frac{d\varepsilon_v}{d\varepsilon_1} \quad (2.1.4)$$

Where $d\varepsilon_v$ is the rate of unit volume change and $d\varepsilon_1$ is the rate of major principal strain change.

The dilatancy is, somehow, controlled by the effective confining pressure. The suppression of dilatancy which accompanies an increase in effective normal stress gives a dense sand the behavior characteristic of a loose sand at lower stresses. This suppression of dilatancy can be accompanied by very marked particle fracture in natural sands.

Dilatancy implies that particle movements during deformation and failure are not necessarily in the direction of the applied shear stress. Rowe (1962) studied the stress-

dilatancy relation for static equilibrium of an assembly of particles in contact. It was found that the dilatancy and strength of an assembly of individual particles in contact when subjected to a deviatoric stress system depend on the angle of friction, ϕ_u , between particle surfaces, on the geometrical angle of packing, α , and on the degree of energy loss during remoulding. The Mohr-Coulomb criterion of failure which is strictly applicable to a continuum was shown not to have general application to a discontinuous assembly of particles. A new expression was presented

$$\frac{\sigma_1'}{\sigma_3'(1 + \frac{d\varepsilon_v}{d\varepsilon_1})} = \tan^2 (45 + \frac{\phi_u}{2}) \quad (2.1.5)$$

It is evident (Roscoe 1970) that soil in rupture zones will dilate fully to achieve a critical state, at which shear deformation can continue in the absence of a volume change. At peak strength, usually, the maximum rate of dilation defined as $(-d\varepsilon_v/d\varepsilon_1)_{\max}$ is achieved, where ε_v is the volumetric strain and ε_1 is the major principal strain (both defined positive in compression). Barden et al (1969) derived the expressions for the peak angles of shearing resistance ϕ'_{\max} and dilation ψ_{\max} by using Mohr circles based on a drained plane strain compression test. They are

$$\sin \phi'_{\max} = \left(\frac{\tau_{13}}{(\sigma_1' + \sigma_3')/2} \right)_p = \frac{(\sigma_1'/\sigma_3')_{\max} - 1}{(\sigma_1'/\sigma_3')_{\max} + 1} \quad (2.1.6)$$

$$\sin \psi_{\max} = \left(-\frac{d\varepsilon_v}{d\varepsilon_1} \right) = \frac{(d\varepsilon_1/d\varepsilon_3)_{\max} + 1}{(d\varepsilon_1/d\varepsilon_3)_{\max} - 1} \quad (2.1.7)$$

Bolton (1986) employed a less rigorous approach to develop an expression which deviates only slightly from Rowe's stress-dilatancy theory in its estimate of ϕ' appropriate

to a plane shear test. The angle of shearing ϕ' is composed of the two components ϕ'_{crit} and ψ . That is

$$\phi' = \phi'_{\text{crit}} + \psi \quad (2.1.8)$$

The critical angle ϕ'_{crit} and dilation angle ψ can be calculated using equations 2.1.6 and 2.1.7 respectively. Compared with Rowe's stress-dilatancy relation of plane strain (equation 2.1.5), equation 2.1.7 overestimates the dilation angle by 20%. Practically, the expression indistinguishable from Rowe's theory is given by

$$\phi' = \phi'_{\text{crit}} + 0.8\psi \quad (2.1.9)$$

The advantage of developing this expression is that any angle of shearing in excess of the friction angle of loose sand is seen to be due solely to the geometry of the volumetric expansion which is necessary before shearing can take place. Bolton (1986) introduced a new parameter, relative dilatancy index, to relate dilatancy to the relative density of sand and mean effective stress imposed on the specimen tested.

$$I_r = I_d (10 - \ln p') - 1 \quad (2.1.10)$$

Where I_r is the dilatancy index; I_d is relative density and p' is mean effective stress. It is found that I_r changes between 0 and 4. For the plane strain test

$$\phi'_{\text{max}} - \phi'_{\text{crit}} = 0.8\psi = 5 I_r$$

For triaxial strain,

$$\phi'_{\max} - \phi'_{\text{crit}} = 0.8\psi = 3 I_r$$

For both test configurations

$$\left(-\frac{d\varepsilon_v}{d\varepsilon_1}\right)_{\max} = 0.3 I_r$$

Negative values of I_r indicate that large contractile strains will occur before ϕ'_{crit} can be mobilized.

Lee and Seed (1967) studied the drained behavior of Sacramento River sand. It was concluded that the drained shear resistance of sand is composed of three components: sliding friction, dilatancy and grain crushing, and particle rearranging. In the test program, the effective confining stress was up to 14 MPa. For each effective confining stress, volume change together with shear deformation tended to cause the same void ratio in the specimen at failure regardless of the initial void ratio. This void ratio is the critical void ratio. If there is no volume change or little volume change in the drained condition, the drained strength would be the same as the undrained strength. It was found that for each void ratio after consolidation, there exists a critical effective confining stress at which the volume change in drained shear is zero. The critical effective confining stress decreases with an increase in the void ratio. The critical void ratio is a function of the critical effective confining stress and decreases with an increase in the critical effective confining stress.

2.2 Grain Crushing

Clough and Vesic (1968) investigated the behavior of sands under high stresses. There is a basic difference in the behavior of dense sand at high stresses (10 to 100 MPa), as compared with the behavior of the same material at low stresses (0 to 1.0 MPa). At high stresses, dense sand samples fail as ductile materials (by bulging) without any of the pronounced rupture planes normally seen at low stresses. The stress-strain curves from high stress tests bear a close resemblance to the analogous curves for loose sand at low stresses. Failures occur at large strains, followed by an insignificant drop of the strength after failure. Volume changes distinctly show only contraction, regardless of the initial void ratio of the samples. Thus, the initial void ratio does not have any effect on the behavior of samples consolidated to high stresses (greater than 20 MPa). The rate of volume change at failure $(\frac{d\varepsilon_v}{d\varepsilon_1})_f$, is equal to zero. It is conceivable that for any density there would be a high enough stress to prevent dilation at failure. From this point of view, Vesic et al (1968) suggested a correction for the concept of conventional critical void ratio of sand. Depending on the initial relative density, there may exist for any granular material a critical mean normal stress at which there is no volume change at failure in pure shear; and for any mean normal stress lower than critical, there exists a critical void ratio at which there is no volume change at failure in pure shear.

There exists a mean normal stress beyond which the influence on the shear strength of its initial void ratio vanishes. This stress is defined as the breakdown stress (σ_B). It represents the stress level at which all dilatancy effects disappear and beyond which particle breakage becomes the only mechanism, in addition to simple slip, by which shearing displacement in the slip planes becomes possible. It appears that this stress is affected by the mineral composition and the gradation and shape of the particles of the granular material. The mineral composition should affect this stress through two parameters, namely crushing strength of the mineral at particle contacts and the mineral's angle of physical friction. The lower this crushing strength and the higher the physical friction angle of the

mineral, the lower should be the breakdown stress. Also the poorer the gradation and the smaller the particle sphericity, the lower should be the breakdown stress. The nature of sand deformation varies with the stress range. Below the breakdown stress, in the low and elevated stress range (below 10 MPa) the modulus of deformation of sands increases as a power function of the mean normal stress. The strength envelope is curved and depends on the initial void ratio of the material. Beyond the breakdown stress, sand behaves essentially as a linearly deformable solid, with a modulus of deformation E which is proportional to the mean normal stress. The curvature of the strength envelope disappears. Its failure characteristics are defined by a constant angle of internal friction.

Lee and Farhoomand (1967) performed a series of consolidation tests in which the stress ratio, $K_c = \sigma'_1/\sigma'_3$, varied from 1.0 to 2.8. Crushed granitic gravel samples formed with angular and subrounded particles were used. It was found that the samples comprised of angular particles were more compressible and breakable than that of subrounded particles. The anisotropic stress condition causes more grain crushing than the isotropic stress condition. They suggested a parameter, "relative breakage", $R_b = D_{15i}/D_{15a}$, to quantitatively evaluate the magnitude of particle breakage in which D_{15i} is the initial 15 percent size finer soil and D_{15a} is the 15 percent finer after testing. "Relative crushing", R_b , is a function of stress ratio, shape of grains and major principal consolidation stress. At the same stress condition, the "relative crushing" would be higher for angular particles than for subrounded particles. If the shape of particles is the same, the "relative crushing" would increase with the increase in stress ratio and major principal consolidation stress. Hardin (1985) studied the behavior of grain crushing and summarized that particle breakage is related to particle size, shape and hardness, void ratio, state of stress and stress path. The occurrence of water also strongly influenced the amount of grain crushing. The tests conducted on Antioch sands showed that water greatly increased the crushability or decreased the particle hardness. A parameter, breakage potential was defined to quantify the particle breakage. That is

$$B_p = \int_0^1 b_p df \quad (2.2.1)$$

Where B_p =breakage potential, df =differential of "percent passing" divided by 100, and b_p =the potential for breakage of a particle of a given size, D ,

$$\begin{aligned} b_p &= \log_{10} \left[\frac{D}{0.074} \right] & \text{for } D \geq 0.074 \text{ mm} \\ b_p &= 0 & \text{for } D < 0.074 \text{ mm} \end{aligned} \quad (2.2.2)$$

The amount of grain crushing is measured by total breakage B_t

$$B_t = \int_0^1 (b_{po} - b_{pl}) df \quad (2.2.3)$$

in which b_{po} =original b_p , b_{pl} =the value of b_p after loading. It was found that the total breakage is approximately proportional to B_p , when a soil element with the same particle material and shape, at a given void ratio is subjected to the same state of stress following a specific stress path. In addition, the effective stress ratio, particle hardness, particle shape and void ratio are also embedded in the evaluation of grain crushing.

2.3 Stress-Strain Behavior of Oil Sands

Oil sands possess a special fabric which was identified as locked sands by Dusseault (1977). Because of the locked structure, the strength of oil sands is significantly higher than that for other dense sands. Dusseault and Morgentern (1979) conducted studies on Athabasca oil sands, Swan River Sandstone and St. Peter Sandstone, all of which were locked sands. Test results showed that the rate of dilatancy at failure is a function of normal stress. Dilatancy causes a high shear strength at a low stress level. As test stress level increases, the effective confining stress suppresses the dilatancy. Grain surface asperity

shear occurs. The behavior at different stress levels results in a curved failure envelope. The angles of shear resistance of locked sands are much higher than that of very dense sands with the same composition. The strain to failure of locked sands is usually very small.

The shear strength and stiffness of oil sands at low stress levels are very sensitive to the sample disturbance. Dusseault and Morgenstern (1978,1979) found that the strength and the rate of dilatancy of Athabasca oil sands drop greatly if the sample is disturbed. Agar (1984) intensively studied the effect of sample disturbance on Athabasca oil sands. Two failure envelopes showing the strength of high grade or undisturbed oil sands and remoulded or totally disturbed oil sands are defined in Figure 2.3.1, which give the upper and low limits of the strength. The shear strength of oil sands with a certain level of disturbance lay between these two envelopes. With the same effective confining stress of 8.0 MPa in drained triaxial compression, Agar (1984) observed that the shear strengths of two specimens differed by 3.5 MPa with an initial porosity difference of only 0.012 due to sample disturbance. Therefore, a relatively small increase in initial porosity of a specimen may reduce the shear strength of oil sands dramatically. Dusseault and Domselaar (1982) suggested a method to evaluate the quality of specimens. The Index of Sample Disturbance is defined as

$$I_D = \frac{n_e - n}{n} \quad (2.3.1)$$

In which I_D = Index of Sample Disturbance, n_e = laboratory porosity and n = in situ porosity.

Although the shear strength of oil sands is higher than for other dense sands, it appears to be totally cohesionless. The existence of bitumen does not contribute to the shear strength. Dusseault and Morgenstern (1978) performed a series of triaxial and shear box tests on undisturbed and recompacted Athabasca oil sands. The failure envelopes are highly

curved with a very steep slope at the beginning and pass through the origin. They showed that cohesion, viscosity of bitumen, negative pore pressure and interfacial tension do not significantly influence the strength of the oil sands. Agar (1984) also concluded that Athabasca oil sand is a cohesionless material whose shear strength is primarily frictional. Dusseault (1977) investigated the characteristics of natural slopes in the Athabasca oil sands. It was noted that bitumen alone does not contribute to the long term stability of the slopes. There is no mechanical resistance to failure provided by bitumen. The occurrence of viscous resistance is based on the initiation of failure and on the movement at a relatively rapid strain rate. Scott and Kosar (1984) conducted research on Athabasca oil sands. It was found that the presence of bitumen does not have a significant influence on the compressibility, shear strength and elastic parameters of oil sands. The bitumen, however, has a controlling effect on the permeability of the oil sands. Since the viscosity of bitumen increases with temperature, the permeability of oil sands also increases with temperature. The test results showed that when the temperature varied from 5 °C to 200 °C, the permeability increased by 7 orders of magnitude.

The bulk compressibility of Athabasca oil sands has been studied by a number of researchers. It can be measured either by confined compression in an oedometer or by isotropic compression in a triaxial cell. The important finding is that, under an isotropic cyclic stress condition, the oil sands behave elastically. Agar (1984) found that the relationship between effective confining stress and volumetric strain upon unloading and reloading in isotropic cyclic consolidation are repeatable. Kosar (1989) carried out a series of constrained compression tests and isotropic compression tests with Athabasca McMurray Formation oil sands and Athabasca Clearwater Formation oil sands. Figure 2.3.2 shows one of the isotropic cyclic consolidation test results. It is seen that the volumetric strains in stress cycling after the initial loading vary along the same path. The repeatability of the results indicates the elastic behavior of the oil sand in stress cycling. Assuming a constant Poisson's ratio of 0.3, the bulk and constrained moduli were

calculated using the theory of elasticity. The calculated values of the bulk modulus from the constrained modulus had a reasonable agreement with the measured values. This fact contributed more evidence to the view that the oil sands behave in an elastic manner in the testing stress range. Au (1983) summarized the previous results for the compressibility of Athabasca oil sands. By establishing the relationship between the compressibility and void ratio of specimens, an estimation of the in situ compressibility for Athabasca oil sands was given, which ranges from 0.3 to $0.7 \times 10^{-3} \text{ MPa}^{-1}$. The bulk compressibility is related to the stress range in which it is measured. A different stress range would generate a different compressibility. Based on test results, Kosar et al (1987) suggested a value of compressibility of $1.4 \times 10^{-3} \text{ MPa}^{-1}$ in the stress range of 1.0 to 4.5 MPa for Athabasca McMurray Formation oil sands and $0.98 \times 10^{-3} \text{ MPa}^{-1}$ for Cold Lake Clearwater Formation oil sands.

The shear strength of oil sands is dependent on effective confining stress, stress path and temperature. Dusseault and Morgenstern (1978) suggested using a power law to express the failure criterion for Athabasca oil sands because the test results illustrated that a gradual curvature of the failure envelope is more consistent with the test data than the bimodal postulate proposed by Brooker (1975). The high shear strength of oil sands at low effective confining stress is primarily due to the energy required for dilation because of the locked fabric. When the fabric is damaged, the oil sands will behave similar to other dense sands. Agar (1984) found that the strength of undisturbed oil sands at low effective confining stress is much greater than that of dense Ottawa sands. When the test is conducted raising the effective confining stress over 8.0 MPa , the strength of oil sands appears to be close to that of Ottawa sand. Oil sands exhibit a strain-weakening behavior when subjected to shear. Continuous straining disrupts the fabric gradually until failure occurs and the fabric is destroyed. There is a sudden reduction in shear strength after peak strength is reached. Au (1983) analyzed the strain-weakening behavior of oil sands. It was found that the tendency of strain-weakening is governed by the effective confining stress.

The oil sands are more strain weakened at low effective confining stresses than at high effective confining stresses. The strain weakening will eventually disappear with the increase in effective confining stress. For the influence of temperature on the strength of oil sands, Agar (1984) observed that at low elevated temperatures, heating Athabasca McMurray Formation oil sands results in a small amount of densification which increases the stiffness and dilatancy of the specimen. But when the temperature is raised to 200 °C, the heating effect on the strength is relatively insignificant. Kosar (1989) pointed out that the heating effect on the strength and deformation behavior of Athabasca oil sands is strongly related to the fines contents of the oil sands. The shear strength and deformation behavior of rich, low fines oil sands are almost independent of heating. An elevated temperature (up to 225 °C) may cause an increase in shear strength and elastic modulus for oil sands with high fines contents. On the other hand, the shear strength is also affected by the rate of temperature increase and the rate of pore pressure dissipation. Heating increases the pore pressure in a specimen. If the rate of pore pressure dissipation is smaller than that of temperature increase, the effective confining stress would drop, and the shear strength consequently decreases.

Wong et al (1993) studied the stress-strain behavior of Cold Lake Clearwater Formation oil sands following different stress paths. It was found that, during isotropic stress cycling, the behavior of the oil sands can be represented by the theory of elasticity in a stress range between 3.0 to 14.0 MPa . The volume change with effective confining stresses has a best fit with the following expression

$$\varepsilon_v = C_1 P_a \left(\frac{\sigma_3'}{P_a} \right)^m \quad (2.3.2)$$

Where ε_v = volumetric strain, C_1 = a constant, P_a = normalization pressure, σ_3' = effective stress and m = exponent. After isotropic cyclic consolidation, the void ratio of a specimen was close to the in situ void ratio and no significant grain crushing occurred up to an

effective confining stress of 14 MPa. Isotropic stress cycling appeared to bring a specimen back to a physical state close to the in situ state. It was noted that the state parameter (Been and Jeffery 1985) does not have a controlling effect on the geomechanical behavior of Cold Lake Clearwater Formation oil sands. The critical state line determined from undrained triaxial compression tests is a unique line and can be used as a reference property. When simulating a field stress path in triaxial tests, it was suggested that grain rolling and shear dilation are the dominant mechanisms during steam stimulation in field recovery processes.

2.4 Soil Models

2.4.1 Hyperbolic Model

The hyperbolic model is the most popular model employed in the analysis of soil stress-strain relationships. It was first developed by Kondner et al (1963), and studied by many researchers. Duncan and Chang (1970) applied this model to a few tests which were performed using uniform fine silica sand specimens. The model showed satisfactory results in stress-strain response for both dense and loose sands. The main idea of the model is based on the hyperbolic simulation of a stress-strain relationship represented by a hyperbolic equation proposed by Kondner (1963).

$$(\sigma_1 - \sigma_3) = \frac{\epsilon}{a + b\epsilon} \quad (2.4.1)$$

Where $(\sigma_1 - \sigma_3)$ = deviator stress (major principal stress minus minor principal stress); ϵ = axial strain ; a, and b = constants which can be obtained from testing.

Fig 2.4.1 shows a hyperbolic stress strain relationship. The physical meaning of a and b is obvious as given in the plot.

$$a = \frac{1}{E_i} \quad (2.4.2a)$$

$$b = \frac{1}{(\sigma_1 - \sigma_3)_{ULT}} \quad (2.4.2b)$$

Transforming equation (2.4.1), we have

$$\frac{\epsilon}{\sigma_1 - \sigma_3} = a + b\epsilon \quad (2.4.3)$$

It can be noted that equation 2.4.3 represents a straight line. The parameters a and b are the intercept and the slope of the line respectively. Graphically, they are shown in Fig 2.4.2.

However, it has been found that a soil failure compressive strength $(\sigma_1 - \sigma_3)_f$ is always smaller than the asymptotic value $(\sigma_1 - \sigma_3)_{ULT}$ by a small amount, because $(\sigma_1 - \sigma_3)_{ULT}$ is the upper limit of the hyperbolic curve. Therefore, a factor R_f is employed in the formulation to accommodate the difference of these two strengths.

$$(\sigma_1 - \sigma_3)_f = R_f (\sigma_1 - \sigma_3)_{ULT} \quad (2.4.4)$$

Where $(\sigma_1 - \sigma_3)_f$ = deviator stress at failure and $(\sigma_1 - \sigma_3)_{ULT}$ = the asymptotic value of the deviator stress. R_f is the failure ratio whose value is related to soil type and is independent the of confining stress imposed on the soil. It varies between 0.75 and 1.00.

Summarizing equation (2.4.1) to (2.4.4), the hyperbolic relationship can be expressed as

$$(\sigma_1 - \sigma_3) = \frac{\epsilon}{\frac{1}{E_i} + \frac{\epsilon R_f}{(\sigma_1 - \sigma_3)_f}} \quad (2.4.5)$$

Duncan et al (1970) pointed out that both the tangent modulus and the compressive strength of soils are stress dependent. They vary with the effective confining pressure used in the tests. The experimental relationship between initial tangent modulus and confining stress determined by Janbu (1963) was suggested as follows.

$$E_i = K_m p_a \left(\frac{\sigma_3'}{p_a} \right)^{n_m} \quad (2.4.6)$$

In which, p_a = atmospheric pressure expressed in the same units as E_i , E_i = the initial tangent modulus, K_m = a modulus number, n_m = the exponent determining the rate of variation of E_i with σ_3' , the values of K_m and n_m can be determined by plotting the values of E_i against σ_3' on a log-log scale and fitting a straight line. On this plot, K_m is the intercept and n_m is the slope.

The relationship between failure strength and effective confining pressure is governed by the Mohr - Coulomb failure criterion which can be expressed as

$$(\sigma_1 - \sigma_3)_f = \frac{2 c' \cos \phi' + 2 \sigma_3' \sin \phi'}{1 - \sin \phi'} \quad (2.4.7)$$

The instantaneous slope of the stress strain curve, the tangent modulus E_t , can now be derived by differentiating equation (2.4.1), that is

$$E_t = \frac{d(\sigma_1 - \sigma_3)}{d\varepsilon}$$

as a result,

$$E_t = \frac{\frac{1}{E_i}}{\left(\frac{1}{E_i} + \frac{R_f \varepsilon}{(\sigma_1 - \sigma_3)_f}\right)^2} \quad (2.4.8)$$

From equation 2.4.5,

$$\varepsilon = \frac{\sigma_1 - \sigma_3}{E_i \left(1 - \frac{R_f (\sigma_1 - \sigma_3)}{(\sigma_1 - \sigma_3)_f}\right)} \quad (2.4.9)$$

Substituting equation 2.4.9 into 2.4.8, in combination with equation 2.4.6 and 2.4.7, E_t is finally expressed as

$$E_t = \left(1 - \frac{R_f (1 - \sin \phi') (\sigma_1 - \sigma_3)}{2 c' \cos \phi' + 2 \sigma_3'^2}\right)^2 K_m p_a \left(\frac{\sigma_3'}{p_a}\right)^{n_m} \quad (2.4.10)$$

In equation 2.4.10, the tangent modulus E_t is a function of stress only. It provides a convenient measure for incremental stress analyses. But the friction angle ϕ' generally is not a constant. It varies with the effective confining stress. The relationship between these two may be experimentally established. Duncan et al (1980) suggested that the variation of friction angle with confining stress may be represented by the following expression.

$$\phi = \phi_0 - \Delta \phi \log\left(\frac{\sigma_3'}{p_a}\right) \quad (2.4.11)$$

where ϕ_0' is the value ϕ' when $\sigma_3' = p_a$, $\Delta \phi$ is a reduction factor in ϕ' for a 10 fold increase in σ_3' .

The values of Poisson's ratio for drained tests are calculated in an incremental manner. They are not constant for a soil tested and change with different stress levels.

$$v = \frac{\Delta\varepsilon_1 - \Delta\varepsilon_v}{2\Delta\varepsilon_1} \quad (2.4.12)$$

In which, v = Poisson's ratio, ε_1 = axial strain (compression positive), ε_v = volumetric strain. Duncan (1970) found that the values of Poisson's ratio generally increase with increasing stress level on primary loading for dense sands. The value, however, for loose sands does not change too much with stress level during testing.

Duncan (1981) improved the hyperbolic model by using values of bulk modulus which vary with effective confining pressures. According to the theory of elasticity, the value of bulk modulus is defined by,

$$K = \frac{\Delta\sigma_1 + \Delta\sigma_2 + \Delta\sigma_3}{3\varepsilon_v} \quad (2.4.13)$$

where K =bulk modulus; $\Delta\sigma_1$, $\Delta\sigma_2$ and $\Delta\sigma_3$ are the changes in principal stresses; and ε_v is the corresponding change in volumetric strain. In the triaxial test, where $\sigma_1 = \sigma_3$, when the effective confining stress is held constant, equation 2.4.13 has the following form,

$$K = \frac{\sigma_1 - \sigma_3}{3\varepsilon_v} \quad (2.4.14)$$

This equation shows that the value of bulk modulus for a conventional triaxial compression test may be calculated using the value of deviator stress $\sigma_1 - \sigma_3$ corresponding

to any point on the stress-strain curve, and the corresponding point on the volume change curve.

2.4.2 Bulk Modulus and Shear Modulus

The modulus of deformation, or tangent modulus (Duncan 1970), analogous to Young's modulus, as determined from a triaxial compression test has been found to be a function of the density of the soil, the magnitude of confining pressure, and the shear stress level (Chen, 1948). Evaluation of the modulus by plate bearing tests has shown that the plate size has a significant influence on the modulus (Benkelman and Williams, 1959). For Poisson's ratios, another parameter in the theory of elasticity also used in soil analyses, studies have shown that the value is influenced considerably by the method used to obtain it. Therefore, there are difficulties to characterize the stress-strain behavior of cohesionless soil by use of Young's modulus and Poisson's ratio because of variations caused by soil properties and test conditions.

Domaschuk et al (1969) suggested that the response of a soil to an imposed stress system is better characterized by the use of a bulk modulus and a shear modulus, each of which can be associated with a separate physical component of soil behavior.

Based on the theory of elasticity, the state of stress is divided into two components, hydrostatic and deviatoric components. The hydrostatic component is related to the volumetric strain, while the deviatoric component to the shear strain. The stress strain relationship is given as follow.

$$\sigma_{ij} = K\epsilon_{ij}\delta_{ij} + 2G(\epsilon_{ij} - \frac{1}{3}\epsilon_{kk}\delta_{ij}) \quad (2.4.15)$$

Where σ_{ij} , ϵ_{ij} are stress and strain tensors; K =bulk modulus; ϵ_{kk} =volumetric strain; δ_{ij} =Kronecker delta, and G =shear modulus.

For a hydrostatic condition, $i = j$,

$$\sigma_{ii} = 3K\varepsilon_{ii} \quad (2.4.16)$$

For pure shear,

$$s_{ij} = 3G(\varepsilon_{ij} - \frac{1}{3}\varepsilon_{kk}\delta_{ij}) \quad (2.4.17)$$

Equations 2.4.16 and 2.4.17 indicate that only the deviatoric stress causes deviatoric strain, while the volumetric stress causes volumetric strain. The stress-strain relationships are related by shear modulus, G , and bulk modulus, K , respectively.

The advantage of using G and K rather than E and ν in soil mechanics solutions based on the theory of elasticity is that the former moduli may be evaluated independently and may be more readily related to the state of stress (Domaschuk et al 1969, 1975). Practically, the bulk modulus can be obtained in laboratory testing by running isotropic consolidation tests, and the shear modulus, G , by triaxial compression tests with the mean effective stress, p' , constant.

Since a soil does not exhibit a linear stress-strain relationship, K and G are not a single value. They both change with the magnitude of stress imposed on the soil. Domaschuk et al (1969) found that the bulk modulus has a linear relationship with mean normal stress over a limited stress range. It is a function of both mean normal stress and relative density. That is, the bulk modulus increases with the increase of both density and mean normal stress.

The shear modulus G , as mentioned before, can be investigated by means of triaxial compression tests with constant mean normal stress. If the soil is assumed to be isotropic, the stress-strain tensor directions are coaxial and the expression of shear modulus obtained from a triaxial test with constant mean normal stress may be written

$$G = \frac{s_d}{\epsilon_d} = \frac{\sigma_1 - \sigma_3}{2(\epsilon_1 - \epsilon_3)} \quad (2.4.18)$$

Since s_d does not have a linear relationship with ϵ_d , a hyperbolic relationship is also employed to express the stress strain relationship.

$$s_d = \frac{\epsilon_d}{a + b\epsilon_d} \quad (2.4.19)$$

Where $a = 1/G_i$; G_i = initial shear modulus; $b = 1/(s_d)_{ULT}$. Equation 2.4.19 can be rewritten as

$$s_d = \frac{\epsilon_d G_i}{1 + b\epsilon_d} \quad (2.4.20)$$

The shear modulus G is defined as the instantaneous slope of the stress-strain relationship, the differentiation of Equation 2.4.20 gives the equation for the shear modulus.

$$G = G_i(1 - bs_d) \quad (2.4.21)$$

The shear modulus was found to be dependent on the mean normal stress, the relative density of the soil, and the magnitude of the deviatoric stress.

2.4.3 Three Moduli Hypoelastic Model

This model was proposed by Yin et al in 1990 based on tests conducted on the sand-bentonite "buffer" specimens. It is comprised of three moduli, bulk modulus K , shear

modulus G and coupling modulus J which can all be determined from the results of isotropic consolidation and consolidated undrained shear tests.

The basic stress-strain relationships proposed by Yin et al (1990) is

$$d\epsilon_v = \frac{1}{K} dp' + \frac{1}{J} dq \quad (2.4.22)$$

$$d\epsilon_s = \frac{1}{J} dp' + \frac{1}{3G} dq \quad (2.4.23)$$

Where K =bulk modulus; G =shear modulus and J =coupling modulus which is, assumed, the same in coupling dp' , $d\epsilon_s$ and dq , $d\epsilon_v$; q =deviator stress and p' =mean effective stress.

As mentioned in sections 2.4.1 and 2.4.2, the CID test is used to find the modulus E and poisson's ratio ν (Duncan and Chang 1970). Isotropic consolidation is used to find the bulk modulus K and the constant p' test is used to find the shear modulus G (Domaschuk et al 1969). All the parameters are not single values but functions of p' , q or σ_3' . In the three moduli model, isotropic consolidation and consolidated undrained shear tests are required. The former is used to find the bulk modulus K , which is the same measure used by Domaschuk et al (1969), and the latter, relatively easy to run (Yin et al 1990), is employed to determine G and J .

In isotropic consolidation, $dq=0$, the volumetric strain ϵ_v is only a function of p' , that is

$$\epsilon_v = \frac{\lambda}{v_i} \ln p' + \epsilon_{vo} \quad (2.4.24)$$

Where $v_i=1+e_o$, the initial specific volume. The equation (2.4.22) gives

$$K = \frac{dp'}{d\epsilon_v} \quad (2.4.25)$$

Differentiating the equation (2.4.24),

$$K = \frac{p'}{\lambda_v} \quad (2.4.26)$$

In undrained shear, $d\varepsilon_v=0$, the equation (2.4.22) becomes

$$J = \frac{dq}{d(-p')} K \quad (2.4.27)$$

Where $-p'=u-p$. K can be obtained from an isotropic consolidation test, and then the coupling modulus J can be calculated using equation (2.4.27) in which q is a function of $p'(p'-q$ plot in undrained shear).

Undrained shear also provides the relationship between deviator stress and shear strain.

$$q = f(\varepsilon_s) \quad (2.4.28)$$

Transforming equation (2.4.27),

$$dp' = - \frac{K}{J} dq \quad (2.4.29)$$

Substituting 2.4.29 into 2.4.23 gives,

$$\frac{dq}{d\varepsilon_s} = \frac{3GJ^2}{J^2-3GK} \quad (2.4.30)$$

The left side of the equation is the derivative of the equation 2.4.28 which can be obtained from the stress-strain relationship of the undrained shear test. Equation 2.4.30 can be rewritten as

$$G = \frac{\frac{dq}{d\varepsilon_s} J_2}{3(J_2 + \frac{dq}{d\varepsilon_s} K)} \quad (2.4.31)$$

It can be seen, in the three moduli model, that although equations 2.4.22 and 2.4.23 show very simple forms, a few nonlinear relationships, such as $p' - \varepsilon_v$, $p' - q$ and $q - \varepsilon_s$, are involved in the formulations. As a matter of fact, all three moduli have functional expressions.

2.4.4 Oil Sands Models

Wan et al (1989) proposed a non-associated generalized plasticity model to simulate the effective stress-strain behavior of Athabasca McMurray Formation oil sands. In this model, the important behavior; hardening, softening, and dilatancy and contraction are considered. The influence of temperature is also evaluated by changing material properties. The Ramberg-Osgood function which characterizes the hardening and softening behavior, the Matsuoka-Nakai failure criterion which describes the failure condition, and Rowe's theory of dilatancy which quantifies the behavior of dilatancy at low stress levels, are embedded in the formulation. A good agreement between the predicted and measured stress-strain and volume change relationships is reached in applying the model to test results for Athabasca oil sands.

Vaziri (1989) suggested another constitutive stress-strain model to simulate the geomechanical behavior of oil sands. This model tries to minimize the number of parameters encountered in soil analysis and to use the parameters which are easily obtained from routine tests. The model contains three assumptions: hyperbolic non-linear elastic

behavior before yielding occurs, critical-state elastoplastic behavior after yielding is achieved, and Mohr-Coulomb criterion at failure. In the model, the stress-strain relationship is divided into three regions:

1) Nonlinear elastic hyperbolic region in which Duncan's (1970, 1980) hyperbolic model is directly applied;

2) Critical-state elasto-plastic region in which the sub-critical region characterizes the behavior of oil sands in a loose state that could originate from either depositional conditions or from external forces such as steam injection. The upper critical region characterizes the behavior of oil sands in a dense state;

3) Failure region in which the post failure behavior is governed by the Mohr-Coulomb criterion.

2.5 Summary

The stress-strain behavior of sands and oil sands has been briefly discussed in this chapter.

It is noted that the brittleness index, I_p , suggested by Bishop (1967) is a good parameter to apply to engineering materials for soil stability and foundation analyses. The shear strength of sands includes two components; one is caused by the intergranular friction and the other is caused by dilation. The occurrence of dilation during shear is a significant characteristic of dense sands. Bishop (1950) separated the friction and dilation components based on shear box tests. Rowe (1962) formulated a more accurate expression into Mohr-Coulomb criterion taking dilation into account. Bolton (1986) developed a less rigorous expression to estimate the dilation rate.

However, when a dense sand is sheared at a high effective confining stress, dilation is suppressed. A dense sand will show the stress-strain behavior of a loose sand. In this case, dilation disappears and grain crushing dominates the stress-strain behavior. Clough

and Vesic (1968) defined a parameter, "break down" stress to represent the stress level beyond which grain crushing is the dominant mechanism in shear. Hardin (1985) suggested a parameter, breakage potential, B_p , to quantify the particle breakage.

With a locked fabric, oil sands are distinguished from other sands. The tests conducted on Athabasca McMurray Formation oil sands indicated that the oil sands show a significant elastic behavior when subjected to an isotropic cyclic stress condition and the shear strength is generally much higher than for other dense sands with the same void ratios. When the locked fabric is destroyed, oil sands will behave like other dense sands. Dusseault and Domselaar (1982) defined an index of sample disturbance to assess the quality of an oil sand sample. Bitumen does not contribute to the high shear strength of oil sands. Its viscous resistance can only be mobilized when a failure is initialized and the rate of movement is relatively large. The shear strength of oil sands is a function of effective stress, stress path and temperature.

Several constitutive soil models were presented in Section 2.4. Formulating a constitutive soil model for the Lower Grand Rapids Formation oil sands is beyond the scope of this thesis. The review of soil modeling was for the purpose of determining how the measured soil parameters should be presented so they can be readily used in the development of a constitutive soil model for the Lower Grand Rapids Formation oil sands. The hyperbolic model, however, is used in the stress-strain analyses in Chapter 6.

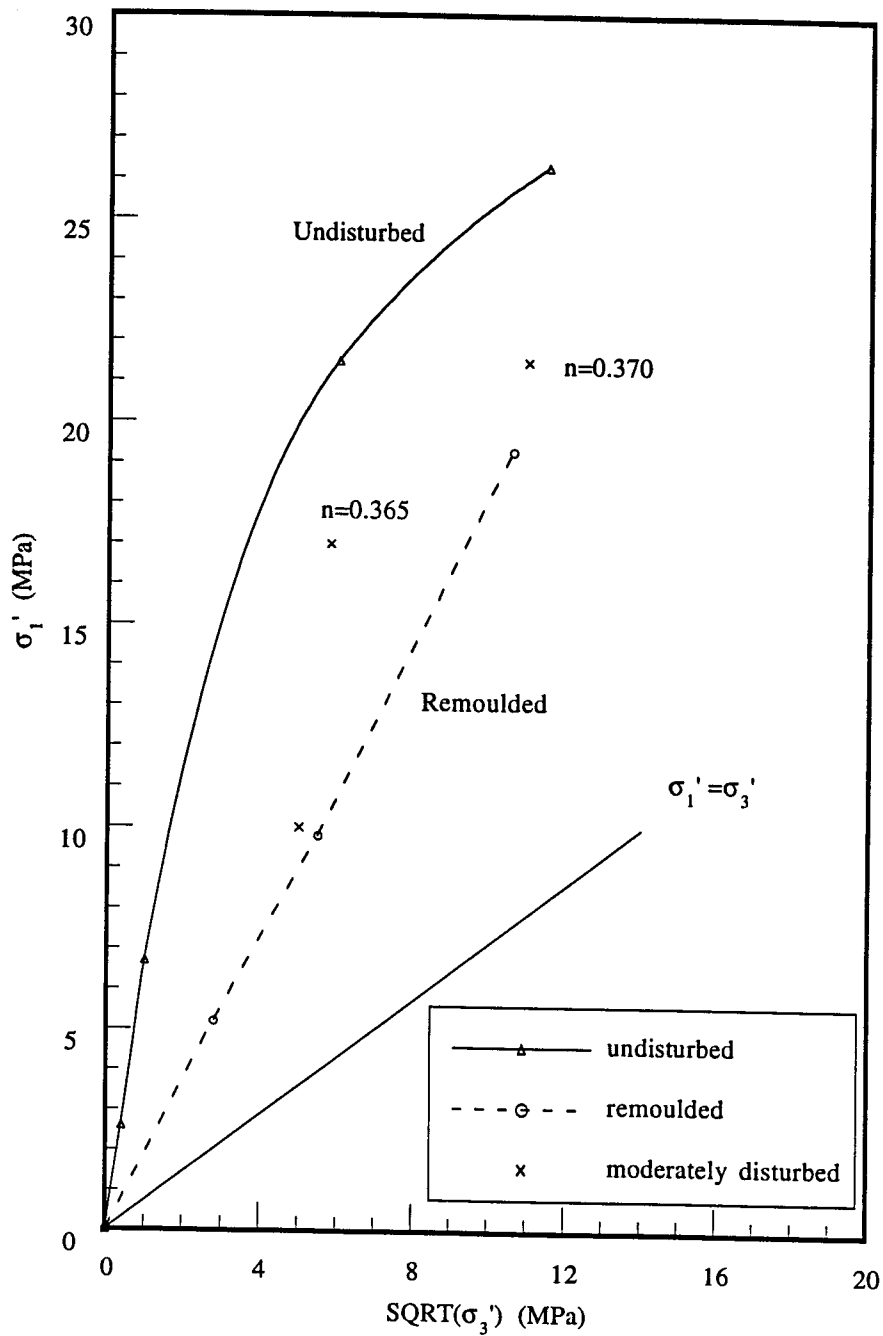


Fig 2.3.1 Failure Envelopes of Athabasca Oil Sands (After Agar, 1984)

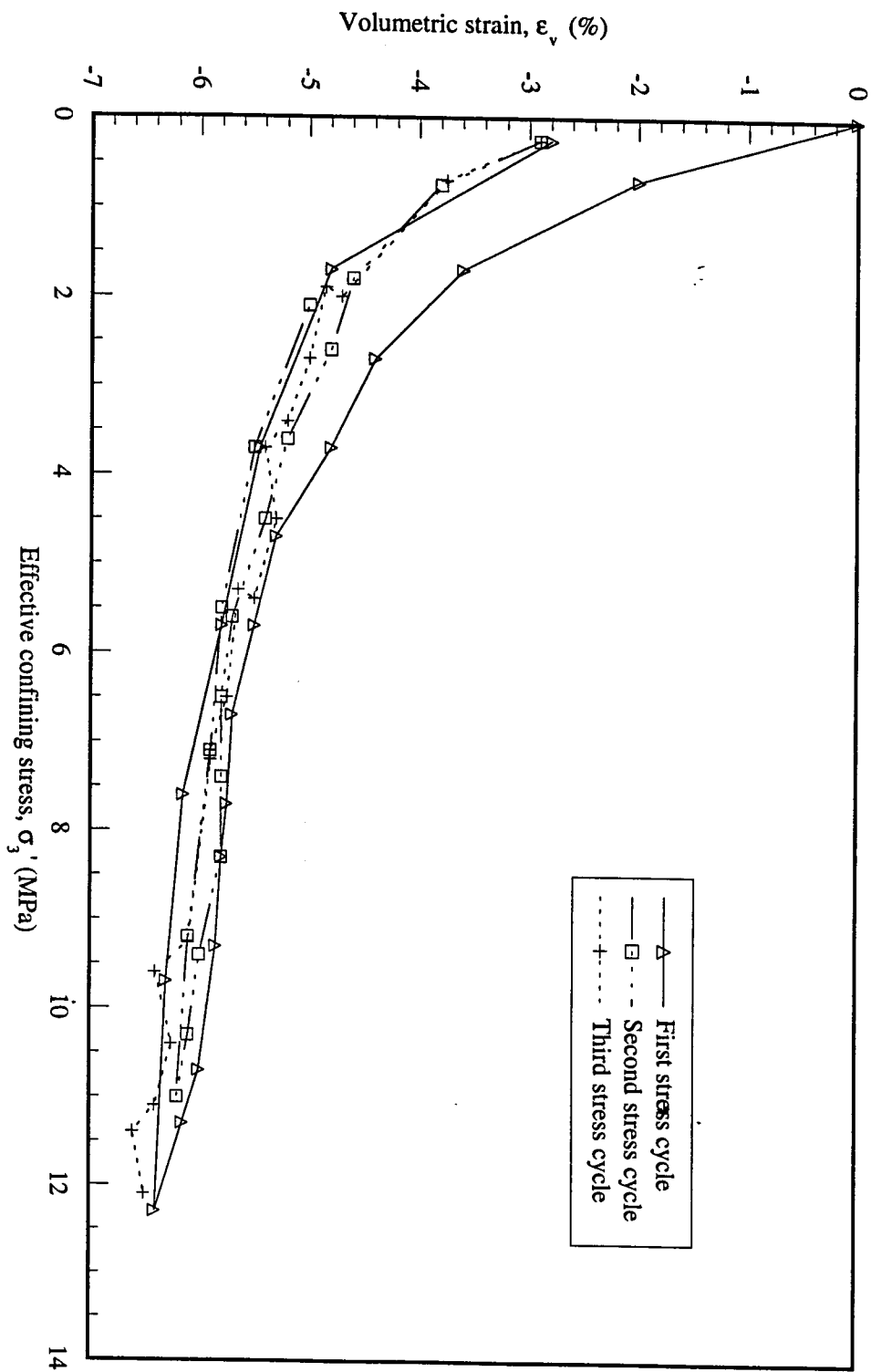


Fig 2.3.2 Isotropic Cyclic Consolidation Test on Athabasca McMurray Formation Oil Sand (After Kosar, 1989)

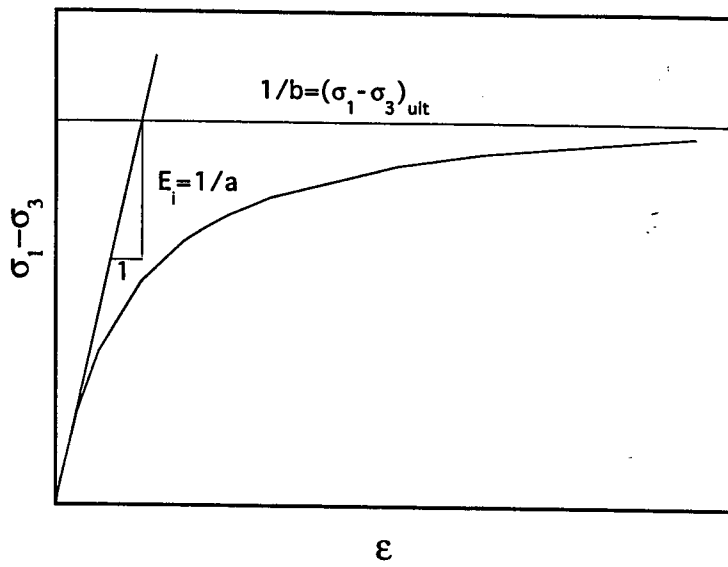


Fig 2.4.1 Hyperbolic Stress-Strain Relationship

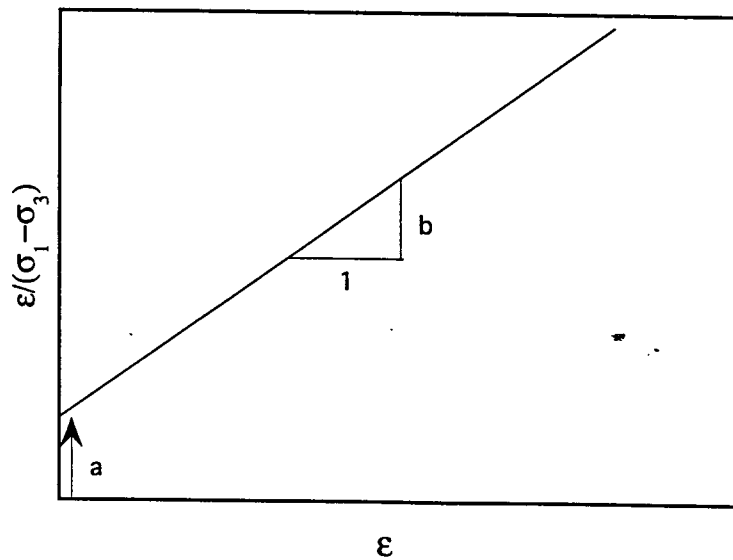


Fig 2.4.2 Transformed Stress-Strain Relationship

Chapter 3

Geology of the Cold Lake Oil Sands

3.1 General Geology

Alberta's bitumen and heavy oil deposits are generally classified into three categories (Mossop et al 1979), Lower Cretaceous oil sand deposits, Lower Cretaceous heavy oil deposits and bitumen-bearing Paleozoic rocks, "Carbonate Trend". As shown in Figure 3.1.1, the oil sands are grouped in three deposits; Athabasca-Wabasca, Cold Lake and Peace River areas, while the heavy oil deposits are located in the Lloyminster area and extend south to the Suffield region. The bitumen-bearing carbonate rocks are hidden beneath the Pre-Cretaceous unconformity in a huge area throughout north central Alberta.

The oil sand deposits in Alberta are contained in the Lower Cretaceous Mannville Group which is divided into lower and upper sections. It rests unconformably on the Middle Devonian argillaceous limestone (Beckie and McIntosh 1991). The stratigraphy of the Lower Cretaceous Mannville Group varies in different locations. Relatively different formations were developed in the same geological time. Figure 3.1.2 illustrates the major stratigraphy of the bitumen bearing geological formations in Alberta.

In Cold Lake, the Lower Mannville section consists of the McMurray Formation which is generally 30 to 70 m thick and up to 125 m thick in one erosional low on the Middle Devonian surface (Beckie 1991). The Upper Mannville section consists of the Clearwater Formation and the overlying Lower and Upper Grand Rapids Formation. These stratigraphies extend throughout central and north Alberta. In the Lloyminster area, the Lower Mannville is formed from the Dina Formation and the Upper Mannville section is

divided into eight formations which are relevant in geologic time to the Clearwater and the Grand Rapids Formations as shown in Figure 3.1.2.

The distribution of oil sand reservoirs is related to the facies patterns controlled by the depositional environments (Mossop et al 1979). Athabasca oil sands are mainly contained within the Lower Mannville Group, McMurray Formation. Only limited oil reserves exist in the overlying Clearwater Formation. The McMurray Formation in the Athabasca oil sands area consists of very fine to median grained quartz sand with interbedded shales and silts. The sand grains are uncemented. Porosity in the clean sands varies from 25 to 35 percent (Mossop et al 1979). The McMurray Formation is believed to be derived from sediments from the erosion of the Precambrian Shield to the east. The lower part of the formation was deposited in a fluvial and deltaic depositional environment and the upper part is interpreted to be coastal and floodplain deposits (Beckie and McIntosh 1991).

Cold Lake oil sands are contained within all three Mannville Group Formations; McMurray, Clearwater and Grand Rapids. Considering individual reservoirs, the lateral extent of reservoirs is very limited in the McMurray Formation which is, therefore, not considered to be an important bitumen reserve. The Clearwater Formation has been interpreted to be a marine deltaic sequence (Harrison et al 1979). It is a marine wedge of salt and pepper sandstones containing some glauconite. The sandstone grades to a shaly facies near the southern limit of the area (Minkeni 1974). The Clearwater Formation has a basal member called the Wabiskaw which consists of fine grained sandstones and gradually disappears towards the south. This member is interpreted to be deposited in a restricted marginally marine environment (Dekker et al 1987). The depositional model for the Clearwater Formation has been studied by Wightman and Berezniuk (1991). The basic feature is the coarsening up sequence which is the typical characteristic in deltaic depositional environments. The formation contains one or more coarsening up sequences corresponding to different locations. The porosity of the oil sand reservoirs in the

Clearwater Formation varies from 18 to 35 percent and the oil saturation can be as high as 16 percent by weight (Mossop et al 1979). The deposition of the formation was not controlled by basin topography. The relative thickness of the sand layers are parallel to the regional trend of the basin (Menkeni 1979). The Grand Rapids Formation overlies the Clearwater Formation. It consists of sequences of interbedded sands and shales which were deposited in mixed nearshore marine and continental environments (Mossop et al 1979). The sands are mixtures of grains of quartz, feldspar, rock fragments and chert. The Grand Rapids Formation is divided into a lower member and an upper member. The Lower Grand Rapids reflects a regressive sequence. It is interpreted to represent a prograding delta. The deposition appears not to be controlled by basin topography. The Upper Grand Rapids represent a transgressive sequence. The deposition seems to be governed by basin topography (Minkeni 1974). The Grand Rapids Formation possesses most of the bitumen reserves at Cold Lake, but the oil accumulation is very variable. The reservoirs are commonly related to water-bearing sands. In the Upper Grand Rapids, free gas occasionally occurs in some sand layers (Harrison 1979).

The Mannville Group which contains heavy oil deposits in the Lloyminster region has a different stratigraphy from central and northern Alberta. It is composed of a series of sand-shale cycles (Hulten and Smith 1991). The detailed stratigraphy is presented in Figure 3.1.2. The Mannville Group in Lloyminster is divided into nine subdivisions, which are agreed on by many researchers. The only dispute is that the geological units in the Mannville Group are, sometimes, considered to be members (Vigrass 1977) and sometimes, to be formations (Orr et al 1977, Hulten and Smith 1991). The Lower Mannville Dina Formation is related to the McMurray Formation to the north. The other formations from Cummings to Colony correlate with the Upper Mannville Group in the other oil sands areas, that is the Clearwater and Grand Rapids Formations (Mossop et al 1979). Concerning heavy oil reserves, the Sparky and Waseca Formations are the best reservoirs. Almost no oil exists in the Cummings and Colony Formations. The General

Petroleum, Rex and Lloyminster Formations are heavy oil reservoirs with an intermediate magnitude of bitumen.

3.2 Oil Sands Tested

The oil sand cores used in this testing program came from the Cold Lake region, Wolf Lake field, and were recovered by Mobil Oil Canada Ltd. The geographic location in which the cores were taken is Townships 63 and 64 and Range 6 W4M. The core laboratory reports provided by Mobil Oil Canada characterize the geological units of the cores as that occurring in the Lloyminster area and this terminology has been maintained in this thesis. Therefore, the Mannville Group contains nine formations designated from Dina to Colony in the sequence of geologic time. Some formations are further divided into a few subdivisions. For instance, the Sparky Formation has three subunits, the lower, middle and upper members. The core specimens were selectively chosen from the Rex, General Petroleum and Sparky Formations by visual examination with the help of X-ray interpretation to avoid shale layers and to ensure a relatively undisturbed, low fines sand sample was obtained. The core specimens were prepared in a cold room. The techniques for preparing core specimens for triaxial testing will be discussed in Chapter 4.

Minkeni (1974) investigated the geology and oil sand reserves in the Cold Lake region including the Wolf Lake field from which the cores used in this testing program were obtained. In Minkeni's study, one geological cross section cuts through Range 1 to Range 7 within Township 64, W4M which embodies the Wolf Lake field. The geological units are classified as the Lower Mannville Group which consists of both the McMurray and Clearwater Formations, and the Upper Mannville Group which is divided into the Lower and Upper Grand Rapids Formations. It should be noted that three geological cross sections are presented in Minkeni's paper. The Clearwater Formation is incorporated into the Lower Mannville Group in two cross sections and into the Upper Mannville Group in

one cross section. There appears to be a mistake in printing in the one section. Harrison et al (1979) conducted research on the oil sand reservoirs of the Clearwater Formation in Cold Lake and gave a detailed reservoir description. The study area covers from Township 64 to 66 and Range 3 to 5, W4M which is adjacent to the area involved in this testing program. In Harrison's study, the geological units in the Mannville Group are categorized into the McMurray, Clearwater, Lower Grand Rapids and Upper Grand Rapids Formations. The Lower Mannville Group only contains the McMurray Formation. The other formations belong to the Upper Mannville Group. Visser et al (1985) analyzed the geological depositional history and patterns, and the mineral compositions of the Clearwater reservoir sands in the Wolf Lake field. Although most of the attention was paid to the interpretation of the depositional environment and mineralogy analysis of the Clearwater Formation, the geological units were classified the same as by Harrison et al (1979). Wightman et al (1991) conducted a study on the quality and extent of the bitumen reservoirs and on the depositional model of the Clearwater Formation in Cold Lake. This study involved Townships 60 to 66 and Ranges 1 to 10, W4M. Within Range 1 to 5, the area extends north to Township 68. The Mannville Group in the study is divided into three formations, McMurray, Clearwater and Grand Rapids. The Grand Rapids has two subdivisions, lower and upper members which are not considered to be formations. The different categorization of the geological units in the Cold Lake area by various investigators indicates the complexity of the geological deposits.

Geographically, the Cold Lake oil sand deposits extend from Township 52 to 68, Range 1 to 10, W4M. It is inevitable that the stratigraphy and geological depositional environment changes from place to place in this broad area. However, referring to the abundant information provided by different researchers, the various formations encountered in this testing program can be related to the relevant geological units whose categorization is commonly accepted by geologists who conducted studies in the Cold Lake region. That is, the Rex, General Petroleum and Sparky Formations are equivalent to the

Lower Grand Rapids Formation and the Waseca Formation to the Upper Grand Rapids Formation. The existing titles of the formations used by Mobil Oil Canada will be maintained in the testing program. However, in detailed stress-strain analyses, the Rex, General Petroleum and Sparky Formations will be dealt with as various depositional sequences in the same formation, referred to as the Lower Grand Rapids Formation.

3.3 Mineralogy of Cold Lake Oil Sands

The geologic depositional environment has a controlling effect on the mineral composition of the Cold Lake oil sands which, therefore, shows a significant difference among different formations. The mineralogy also varies with the location and depth within a formation. Quartz, feldspar and rock fragments are the main components in the mineral composition, usually making up more than 95% of the grains. The other minerals, such as clay and heavy minerals, only provide a very limited amount of the total composition.

Harrison et al (1979), Vessic et al (1991), and Beckie and McIntosh (1991) conducted research on the Cold Lake oil sands. Attention to the mineralogy was paid to different formations by different researchers. Figure 3.3.1 and Table 3.3.1 present the results of the mineral composition of the Cold Lake oil sands determined in these studies. It can be seen that the mineral composition changes considerably from one formation to another. The McMurray Formation consists primarily of quartz whose percentage varies from 88 percent reported by Beckie and McIntosh (1991) to 93 percent reported by Harrison et al (1979). Feldspar and rock fragments take less than 10 percent. The variation of quartz is related to the geographic locations. It is noted that the mineral composition of the McMurray Formation in the Cold Lake oil sands area is quite similar to that of Athabasca McMurray Formation oil sands in which the quartz percentage varies between 90 to 98 percent (Dusseault and Morgenstern 1978). Although the mineralogy fluctuates with location within a formation, there is a consistency in the mineral composition throughout a

formation deposited in one geologic time. As the mineralogy, in turn, strongly influences the constitutive behavior of the oil sands, it would be expected that different formations would exhibit different geotechnical properties.

The mineralogy of the Clearwater Formation is relatively consistent with depth and location. Harrison et al (1979) reported that the quartz, feldspar and rock fragments are 21, 28 and 51 percent respectively. The results presented by Beckie and McIntosh (1991) were achieved from different locations. The quartz content varies within a limited range from 22 to 25 percent with an average of about 23.5 percent. The quartz content reported by Vessic et al (1991) varies from 22 to 36 percent but the maximum value of 36 percent is exceptional. The average fraction of quartz is about 24.5 percent which coincides with the others.

The mineral compositions of the oil sands in this testing program are also presented in Figure 3.3.1 and Table 3.3.1. The information is quoted from the Core Laboratory Reports provided by Mobil Oil Canada. The measurements listed in the table are the minimum and the maximum values which occur in the petrographic analyses reports for wells 13-6-64-6 W4M and 14-6-64-6 W4M. Since the quartz composition is about 50%, the sands in the formations change from feldspathic litharenite to lithic arkose. Generally, the Lower Waseca and Upper Sparky units are all feldspathic litharenite in which there exists a coarsening up sequence from the base to the top. In the Middle Sparky, when the quartz increases and the ratio of the rock fragments to feldspar decreases, the sands are classified as subarkose. When the quartz content decreases and the ratio of R/F increases, the Middle Sparky falls into the category of feldspathic litharenite. Therefore, the classification of the Middle Sparky sands change from feldspathic litharenite to subarkose and sublitharenite. The Lower Sparky also shows a coarsening up sequence and it is mainly characterized as feldspathic litharenite. The General Petroleum unit has a large variation in mineral compositions with depth. The quartz composition changes from 38 to 85 percent, which causes a large variation in its classification ranging from lithicarkose to

sublitharenite.

To show a clear overview of the mineralogy of Cold Lake oil sands, the mineral compositions of the different formations are presented in Figure 3.3.1, a ternary composition plot. From the available information, the specimens involved in this testing program are mainly feldspathic litharenite sands. Such sands contain relatively weak minerals and are susceptible to stress induced grain crushing.

The maximum permeability of the oil sands tested is generally smaller than that of the Clearwater Formation as shown in Table 3.3.1. Permeability is controlled by the mean grain size and porosity of the sands. It increases with an increase in the mean grain size and the porosity. There exists an approximately linear relationship on a semi-log plot between permeability and mean grain size. The oil sands do not deviate from the relationship unless the sands contain a high calcite cement content and with high matrix or carbonaceous material content (Mobil Oil Canada Lab Report, 1987). The relationship, however, is not unique for all the geological units involved. A permeability relationship is established for each formation.

3.4 Summary

The oil sand cores used in this testing program were obtained in the Cold Lake region, Wolf Lake field at a depth from 300 and 400 meters and were recovered by Mobil Oil Canada Ltd. Three geologic formations; the Rex, General Petroleum and Sparky Formations were involved in the testing program. These formations are equivalent to the Lower Grand Rapids Formation.

The petrophysical analyses showed that the mineralogy of the oil sands tested is mainly feldspathic litharenite and the grain composition is about 50% quartz, 25% feldspar and 25% chert and rock fragments. Therefore, a considerable percentage of the sand grains are relatively weak and susceptible to stress induced grain crushing. It can be expected that

the stress-strain behavior of these oil sands will be different from that of the Athabasca McMurray Formation oil sands due to the different mineral composition. Their mineralogy, however, is similar to the Cold Lake Clearwater Formation oil sands and their geotechnical behavior may be similar to the oil sands from this formation.

Table 3.3.1 Mineral Compositions of Cold Lake Oil Sands

Formation	Source of Information	Number of Petrographic Tests	Quartz (%)	Feldspar (%)	Chert and Rock Fragments (%)	Others (%)	Median Grain Size (mm)	Maximum Permeability (md)	Maximum Porosity (%)
Clearwater	Harrison et al (1979)		21	28	51		0.16		
	Beckie and McIntosh (1991)		22 -- 25	5 -- 6	53 -- 68	1 -- 5	0.155 -- 0.250	2467 -- 11500	
	Vissic et al (1991)	10	20 -- 36	6 -- 32	24 -- 54				
Wabiskaw Member	Dekker et al (1987)		40	10	48	2			
	Beckie and McIntosh (1991)		50	18	25	7	0.15		
McMurray	Harrison et al (1979)		93	5	2				
	Dekker et al (1987)		88	7	2	3			
	Beckie and McIntosh (1991)		88	6	3	3	0.11		
(Oil sands tested)* Lower Waseca Upper Sparky Middle Sparky Lower Sparky General Petroleum Rex		4	29 -- 36	23 -- 32	27 -- 30	1 -- 3	0.07 -- 0.16	334 -- 1490	28
		6	42 -- 66	6 -- 22	7 -- 30	0 -- 2	0.03 -- 0.12	191 -- 867	29
		5	25 -- 81	4 -- 17	4 -- 21	1 -- 3	0.03 -- 0.12	522 -- 1760	34
		6	42 -- 63	8 -- 18	21 -- 26	1 -- 3	0.03 -- 0.08	76 -- 1320	30
		7	38 -- 85	6 -- 22	7 -- 26		0.08 -- 0.16	436 -- 7570	35
		3	35 -- 53	18 -- 30	16 -- 24	1 -- 3	0.08 -- 0.21		31

* From core lab report provided by Mobil Oil Canada

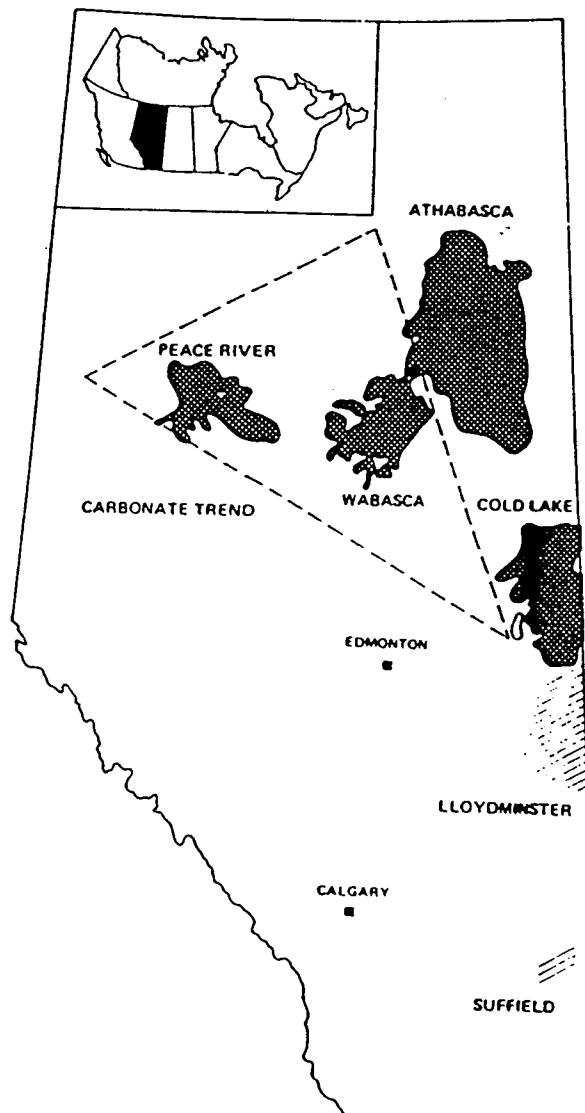
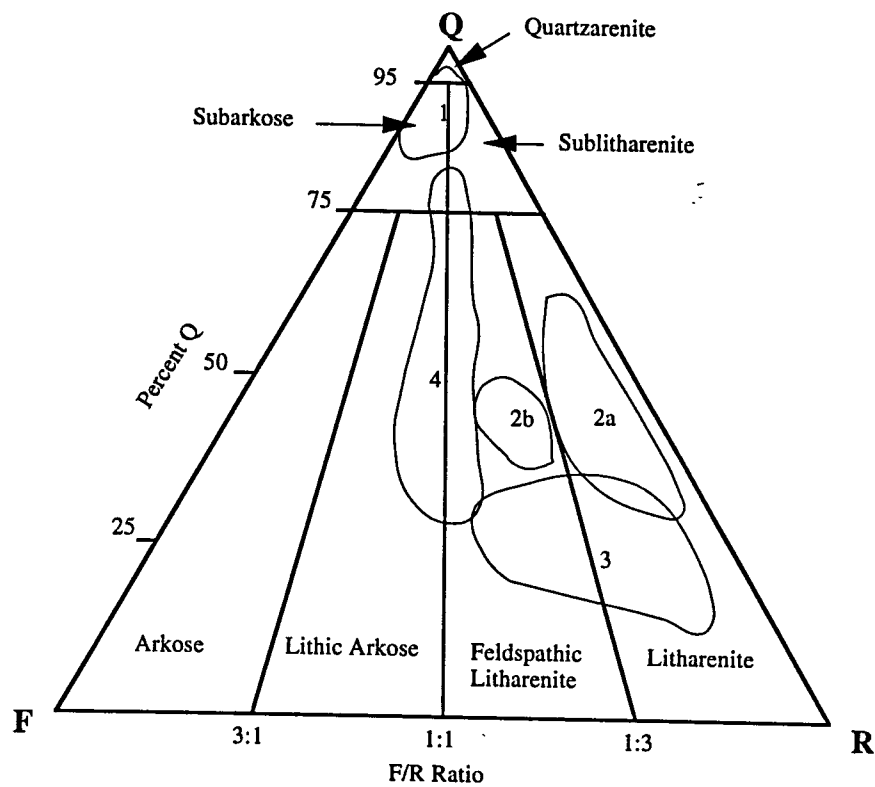


Fig 3.1.1 Oil Sand Deposits in Alberta

Lower Cretaceous Mannville Group		Peace River	Wabasca	Athabasca	Cold Lake	Lloydminster
Albian	Upper Mannville	Spirit River	Grand Rapids	Grand Rapids	Upper Grand Rapids	Colony
					Lower Grand Rapids	McLaren
Apitan and older	Lower Mannville	Bluesky	Clearwater	Clearwater	Wabiskaw Mbr	Waseca
		Gething	Wabiskaw Mbr	Wabiskaw Mbr		Sparky
		Cadomin	McMurray	McMurray	McMurray	General Petroleum
			Pre-Cretaceous Unconformity			Rex
						Lloydminster
					Cummings	
						Dina

Fig 3.1.2 Stratigraphic Correlation of the Lower Cretaceous Mannville Group
(After Wightman et al 1991, and Beckie et al 1991)



1. McMurray Formation (Dekker et al 1987)
2. Wabiskaw Member (2a. Dekker et al 1987 2b. Beckie et al 1991)
3. Clearwater Formation (Harrison et al 1979 and Beckie et al 1991)
4. Oil Sands tested (Mobil Oil Canada 1987)

Fig 3.3.1 Mineral Composition of Cold Lake Oil Sands

Chapter 4

Test Apparatus and Procedures

4.1 Test Apparatus

4.1.1 Pressure Systems

Two pressure sources were used in the testing program. Low pressure is supplied by the existing water pressure line installed in the geotechnical laboratories which could serve pressure as high as 0.4 MPa and high pressure was provided by two compressed nitrogen bottles which had a capacity of 25 MPa. The pressure was adjusted using two pressure control panels which controlled the cell pressure and the back pore pressure.

Fig 4.1.1 illustrates the pressure control system for the cell pressure. The back pore pressure control system has the same configuration. On the pressure control panel, there are two water reservoirs. Reservoir No. 1 containing a water-oil interface is subjected to a high pressure and connected to the triaxial cell to provide the required testing cell pressure. Reservoir No. 2 being full of water is connected to the building water pressure system (low pressure) and used to refill Reservoir No. 1. During testing, the connection between these two reservoirs is shut off and Reservoir No. 2 is not in use. The cell pressure is adjusted by the regulator No. 1 on the control panel. The pressure from the nitrogen bottle is stabilized in the pressure accumulator in which there exists an air-oil interface and then applied to the cell through Reservoir No. 1. Regulator No. 2 controls the magnitude of pressure from the nitrogen bottle.

4.1.2 Triaxial Cell

To meet the pressure requirement in the testing program, a triaxial cell, Wykeham Farrance, WF 40010 which had a capacity of 14 MPa was chosen. Figure 4.1.2 shows the diagram of the triaxial cell. It consists mainly of two parts, the triaxial base and the cell chamber which are fastened together through six bolts and sealed with an o-ring. The cell is made of stainless steel. A piston used to apply a vertical load to a specimen passes through the top of the cylindrical chamber. Three glass windows are built into the side of the chamber through which the specimen can be observed. The specimen pedestal, 40 mm in diameter, is located at the center of the base. A specimen cap with the same diameter sits on the top of the sample. Two small porous stones, 12.5 mm in diameter, are inlaid into the pedestal and the cap respectively. The back pore pressure line is connected to the cap through a brass tubing coil. The cell pressure line comes into the base and opens to the inside of the chamber. The pore pressure line passes through the central axis of the pedestal to reach the bottom of a specimen and comes out of the base to the pore pressure measurement transducer. After mounting a specimen, the cell chamber and the base are bolted together, and then the cell is filled with water from the cell pressure inlet. An air bleed valve at the top of the chamber remains open until the cell is full of water.

4.1.3 Volume Change Measuring Device

The change in volume of a specimen in a triaxial test was measured with a bellows volume change measuring device which is schematically shown in Figure 4.1.3. The device is a cylindrical steel chamber which contains a metal bellows mounted on the base. The chamber and the bellow are sealed to each other and both filled with water. The chamber is connected to the back pore pressure supply and the bellows to the specimen cap in the triaxial cell. The back pore pressure in a test is applied to the specimen through the volume change measuring device. The metal bellows can vertically extend and compress when water enters or leaves the bellows. Three steel rods are fastened on the base to prevent possible buckling

damage when the bellows is fully compressed. A piston seated on the top of the bellows holds a LVDT which records the vertical displacement of the bellows which is calibrated to the specimen volume change. A maximum of 100 cm^3 change in volume can be measured when the bellows is fully extended or compressed. The device can measure volume change to 0.01 cm^3 .

4.1.4 Axial Loading

Two types of loading frames were involved in the testing program, strain controlled and stress controlled frames. Most tests were conducted using the strain controlled vertical loading system as shown in Figure 4.1.4. In this system, the vertical force is mobilized by raising the loading piston to compress the specimen vertically. The loading piston can be adjusted to the required elevation manually before testing commences. The strain rate is preset by adjusting the corresponding gears in a gear box. The vertical load is recorded by a load cell transducer located at the top of the loading frame. The vertical displacement is measured by a Linear Vertical Displacement Transducer (LVDT) which is held in place by a LVDT clamp fixed to the top of the cell piston. The core of the LVDT is seated on the cell chamber. The displacement of a specimen is actually determined by measuring the relative movement between the cell chamber and the cell piston. A Wykeham Farrance loading frame which has a capacity of 200 KN was engaged in the tests.

The stress controlled loading frame, a bellofram, is shown in Figure 4.1.5. It was only used in the pore pressure injection tests to provide an anisotropic stress condition. In this system, the bellofram acting on the cell piston in conjunction with the cell pressure provides the vertical stress imposed on the specimen. The bellofram connected to the building air pressure system can supply a vertical force as high as 20 KN.

4.1.5 Data Logging

The measurements of cell pressure, back pore pressure, change in pore pressure, vertical displacement and volume change are collected with a Fluke 2240 Datalogger connected to an IBM computer through LVDTs and pressure transducers. Readings are taken at chosen time intervals, and then are imported to a Lotus 1-2-3 program in the computer or transferred to a Macintosh computer for further analysis.

4.1.6 Configuration of the Testing System

The diagram of the testing system is presented in Figure 4.1.6. As described above, the cell pressure and the back pressure are supplied by two high pressure nitrogen bottles through two pressure control panels. The bellows volume change measuring device connected to the back pore pressure line records the amount of the water flowing into or out of a specimen to indicate the change in volume during a test. The vertical loading frame provides a shear force with a constant strain rate. The Fluke Datalogger and IBM computer collect the data simultaneously from three pressure transducers measuring cell, back and pore pressures, one load cell transducer showing the axial force, and two LVDTs displaying the axial displacement and volume change of a specimen.

Since the tests were conducted over a large stress range, the effective confining stress varies from 0.1 to 9.5 MPa, pressure transducers with high capacities are required. As a result, the accuracy of the pressure measurement in the low stress range decreases. The effective confining stress is determined by subtracting the back pore pressure from the cell pressure. If an effective stress of 0.1 MPa is required in a test, the error in determination of the effective confining stress becomes significant. To solve this problem, an innovation in the pressure measurement has been made. Instead of using two pressure transducers to monitor the cell and the back pressures simultaneously, one transducer is employed to monitor both of them separately. In this case, the effective stress is determined by the subtraction of cell and back pressures observed with the same transducer. Therefore, the accuracy is highly

improved. Figure 4.1.7 shows the installation of the measurement system. A brass tubing connecting the cell and the back pressure inlets and a few valves are added to the base of the triaxial cell. With this addition, either the cell pressure transducer or back pore pressure transducer can be used to observe both the cell and back pressures. For example, closing valve No. 5 in this figure, the back pressure is monitored by the back pressure transducer. By closing valve No.s 3 and 4, and leaving No. 5 open, the cell pressure would be monitored by the back pressure transducer. The same measurement can also be performed as a check with the cell pressure transducer by adjusting the valves properly.

4.2 Specimen Preparation

4.2.1 Trimming Specimens

The cores used in the testing program were obtained from the Cold Lake region, Wolf Lake Field, and were recovered by Mobil Oil Canada Ltd. Three types of core were encountered in preparation of the specimens. They were frozen tube cores, slabbed frozen cores and slabbed unfrozen cores, each of which required a different trimming technique. Specimens were prepared in a cold room in which the temperature was below -20°C . To ensure the core was not thawed by the trimming generated heat, dry ice was used to chill the core frequently during the process of trimming.

a). Frozen tube core

Frozen tube core has the best quality among the three types of cores. It was sealed and frozen as soon as it was recovered. The degree of disturbance is relatively small.

The core is first cut into a 100 to 120 mm long piece as shown in Figure 4.2.1. An electric diamond saw is used to cut lengthwise through the PVC casing from two opposite sides in order to take off the casing. The core is installed on a lathe in the cold room and the middle part of the core is trimmed to the required diameter, 38 mm, and length, 76 to 80 mm, with a diamond bit. During trimming, care is taken that thaw does not occur. After trimming

off a thin layer from the core, it is dismounted and put into dry ice for about 15 minutes to chill. When the diameter of 38 mm is achieved, the two large ends are cut off with an electric diamond saw located in the cold room. The sample is then installed on the lathe again to trim the ends to obtain the required length with flat ends perpendicular to the specimen axis.

b). Slabbed frozen core

This type of core is not in cylindrical form. One-third of the core was cut off along its axis after recovery for petrophysical laboratory analyses. The remaining two-thirds was kept sealed and frozen until it was used in this testing program. Since the core was no longer circular, it could not be directly trimmed on the lathe. To obtain a satisfactory specimen, a new method was employed.

Specimens were prepared on a milling machine. Figure 4.2.2a shows the machine set-up. A coring barrel is installed on the milling machine. At the top end of the barrel, a rotating bushing sits which is connected to the air pressure through a brass tubing. The cold pressurized air flows through the rotating bushing into the barrel and blows out the drilling debris during coring to enable the barrel to proceed without damaging or thawing the specimen. The oil sand cores are mounted on the machine table. The specimen is cored by either raising the machine table or lowering the barrel on the milling machine.

To mount the oil sands sample to be cored on the machine table, a special procedure is required. As shown in Figure 4.2.2b, a PVC cylinder, 154 mm in diameter, and 120 mm in length, is chosen. The diameter is a little greater than that of the oil sand core which is 127 mm. The PVC cylinder is fixed on a plate temporarily. Two pieces of the slabbed core, 100 mm in length, are cut and wrapped with a thin plastic sheet to prevent moisture loss, and then put into the cylinder face to face. The space left inside the cylinder is filled with fine Ottawa sand mixed with 10 to 15% water. The cylinder containing the oil sand cores is left in the cold room for 24 hours to freeze completely so that the oil sand cores are frozen into the

Ottawa sand and the PVC cylinder. After freezing, the cylinder can be mounted on the machine table to core the specimens.

The cored specimen is removed from the milling machine and mounted on the lathe to trim the ends.

c). Slabbed unfrozen core

This type of core was extremely disturbed, because it was left unsealed and unfrozen for a period of four years. It was allowed to expand freely and was completely desiccated.

A core was first put into the moisture room to absorb some water and then two small pieces were cut from the core with their casings attached. Being face to face, the two pieces were bonded together tightly with a strong fiber tape. The cores were mounted vertically on a loading frame. Two lubricated Shelby tubes were positioned on the top of the cores. A vertical force was applied with a very slow strain rate to push the tubes into the cores until the samples were trimmed into the Shelby tubes. The Shelby tubes with the samples inside were then left in the cold room for 24 hours to freeze. After freezing, each Shelby tube was mounted on a sample extruder to push the sample out of the tube. The final step was to trim the ends of the specimen on the lathe.

4.2.2 Sample Disturbance

Many factors contribute to sample disturbance of oil sands core. Generally, the effects of disturbance are involved in the process of sampling, transportation, storage and trimming. As mentioned in Section 2.3, Dusseault and Domselaar (1982) suggested a parameter, the index of sample disturbance, I_D , to evaluate the degree of disturbance. This index has proven to be very useful and has been adopted in this research work.

$$I_D = \frac{n_e - n}{n} \quad (2.3.1)$$

The in situ porosity, n , is determined from an extraction test in which the mass fractions of solids, water and bitumen are measured. It is assumed that there is no free gas in situ. According to the mass fractions obtained from the extraction test, the in situ volume, V_i , of the specimen tested in laboratory can be calculated.

$$V_i = \frac{M_s}{G_s} + \frac{M_w}{G_w} + \frac{M_b}{G_b} \quad (4.2.1)$$

Where M_s , M_w and M_b are the masses of solids, water and bitumen of the specimen respectively, G_s , G_w and G_b are their specific gravities. Knowing the in situ volumes of the different fractions, the in situ porosity can be determined by use of the following expression (Scott and Kosar 1984)

$$n = \frac{\frac{M_w}{G_w} + \frac{M_b}{G_b}}{\frac{M_s}{G_s} + \frac{M_w}{G_w} + \frac{M_b}{G_b}} \quad (4.2.2)$$

Obviously, the greater the I_D , the more disturbed is the sample. To obtain high quality core, sampling techniques have been developed, but the core used in this research was taken with a standard coring barrel which allows considerable expansion and disturbance of the core. Frozen storage and cyclic compression of the core, to some degree, aids in reducing I_D . The technique of trimming a specimen in a cold room, as mentioned above, minimizes the amount by which the sample can be disturbed during specimen preparation.

In this study, another factor that may have an impact on the amount of sample disturbance is the bitumen content. A higher bitumen content appears to cause more disturbance probably due to greater gas evolution. The relationship between the index of sample disturbance and the bitumen content is plotted in Figure 4.2.3. These results clearly show the tendency that the index of sample disturbance increases with an increase in the bitumen content. The high bitumen contents imply that the oil sands contain a large amount of

gas that is in solution in the bitumen in situ. When it is cored and brought to the surface, the in situ pressure is released immediately. As a result, the gas comes out of solution. The sand particles are pushed apart by gas bubbles evolving in the bitumen and the voids are highly increased, even though the core is frozen as soon as the core tube is taken out of the sampling barrel. A lower bitumen content, therefore, will cause less disturbance as less gas evolution can occur.

4.3 Test Procedures

The specimen set-up for all the triaxial tests in the program is illustrated in Figure 4.3.1. The diameter of the specimen is designed to be 38 mm. The ratio of length to diameter (L/D) is 2. Because of the difficulties encountered in specimen trimming, the length and diameter of a specimen in each test vary. The dimensions of the specimens are shown in Table 5.1.1 in Chapter 5. To minimize the influence of end restraint on the oil sands behavior, a frictionless cap and pedestal (Plewes 1987) are used in the tests. It is made of three layers of latex membrane lubricated with vacuum grease with a hole, 12.5 mm in diameter, in the center. Side filter paper drains and paper filters are also installed around the circumference and on ends of the specimen to increase the rate of drainage or dissipation of pore pressure. The specimen is sealed with two standard triaxial rubber membranes and three rubber o-rings are clamped on the cap and on the pedestal. A coiled brass tubing connects the back pore pressure line to the cap.

After mounting a specimen on the pedestal, the cell chamber is bolted to the triaxial base, and then the cell is filled with water. The triaxial cell is then mounted on the loading frame and connected to the pressure system. A 500 kPa cell pressure is immediately applied to the specimen with the back pore pressure line closed to prevent the expansion of the specimen during thawing. At this confining stress, the specimen is allowed to thaw for at least 12 hours. A subsequent test is then performed following a specific stress path.

To minimize the possibility of sample disturbance during installation of a test specimen, no thawing is allowed. The installation was carried out at room temperature in the test laboratory. It took no more than 15 minutes from taking a specimen out of the cold room to apply the cell pressure to the specimen.

4.4 Test Program

The testing program is organized following six stress paths illustrated in Figure 4.4.1. The stress paths are presented in a p' - q plot. For the purpose of a better interpretation of the test results, the stress paths will be illustrated also in s' - t plots, at times, in later chapters. Symbols p' , q , s' and t are defined as follows.

$$p' = \frac{\sigma_1' + \sigma_2' + \sigma_3'}{3}$$

$$q = \sigma_1 - \sigma_2 \quad (4.3.1)$$

$$s' = \frac{\sigma_1' + \sigma_3'}{2}$$

$$t = \frac{\sigma_1 - \sigma_2}{2} \quad (4.3.2)$$

Each test does not necessarily follow only one stress path. In most cases, a specimen first experiences isotropic cyclic consolidation and then is subjected to a deviatoric stress to failure following one of the other stress paths. The stress paths shown in Figure 4.4.1 are briefly described as follows.

Path A. Isotropic cyclic consolidation (ICC)

This stress path was used to investigate the bulk compressibility of the oil sands. In the triaxial test, $\sigma_1' = \sigma_2' = \sigma_3'$, the mean normal effective stress,

that is, effective confining stress, is raised step by step until the maximum (up to 9.5 MPa) is reached. When consolidation is completed for the maximum stress increment, the effective stress is reduced decrementally. The expansion of the specimen is allowed to finish for each decrement until the effective confining stress decreases to 0.1 MPa. The stress cycling is repeated two or three times. The bulk compressibility is an important parameter to show the constitutive behavior of oil sands. It is used in most of the soil models discussed in Chapter 2. Isotropic stress cycling is part of the in situ stress path when oil sands are subjected to cyclic steam injection and oil production.

Path B. Consolidated drained triaxial compression (CID)

This stress path was followed to measure the drained stress-strain-strength and volume change of the oil sands. After isotropic cyclic consolidation, the effective confining stress is kept constant and the major principal stress σ_1' (axial stress) increases at a constant strain rate until the specimen fails and the post peak strength is reached. Free drainage is allowed. There is no pore pressure built up when a deviatoric stress is imposed on the specimen. This stress path is used to define a reference failure criterion for the oil sands. Some parameters for use in the hyperbolic model are measured. Since this is the most frequent stress path reported in the literature, it allows comparison of behavior with other sands.

Path C. Consolidated undrained triaxial compression (CIU)

The procedure is similar to Path B, but the drainage is prohibited when a deviatoric stress is applied. The pore pressure changes during shear and the volume change is zero. This stress path will give an indication if the oil sands

follows the failure criterion established from Path B. As well, the parameters required in the three moduli model are measured in this test procedure.

Path D. Consolidated drained triaxial compression with p' constant (CIP)

This stress path is also known as a J_1 constant test, because the first invariant J_1 does not change in the test. It creates a pure shear stress condition. After isotropic cyclic consolidation, σ_1' increases at a constant strain rate, while σ_2' and σ_3' ($\sigma_2' = \sigma_3'$ in the triaxial test) decreases to keep $p' = (\sigma_1' + \sigma_2' + \sigma_3')/3$ constant. Free drainage is allowed during shear. Following this stress path, the pure shear behavior of the oil sands is investigated and the shear modulus of the oil sands is determined.

Path E. Anisotropic consolidation (CID)

This stress path is the same as Path B. The only difference is that the major principal stress, σ_1' , is raised to a level where the failure of the specimen does not occur, while the effective confining stress is held constant. Following this stress path, an anisotropic stress condition is established for the pore pressure injection test (CAI).

Path F. Pore pressure injection (CAI)

This stress path works in conjunction with Path E which creates a deviatoric stress acting on the test specimen. In Path F, the deviatoric stress is held constant, the mean normal effective stress is reduced decrementally by increasing the pore pressure. The specimen is allowed to fully drain and dilate at each pore pressure increment. The pore pressure keeps increasing incrementally until failure occurs to the specimen. This stress path simulates the in situ production processes of steam injection and hydraulic fracturing.

The maximum in situ vertical effective stress, σ_v' , at the depth where samples were recovered is about 5 MPa and the horizontal effective stress is less than 5 MPa. Therefore, the maximum effective confining stress in the testing program was established at 5 MPa. Considering that in situ recovery processes could create an effective stress as low as zero and that the accuracy of the test equipment requires a positive contact stress, the minimum effective confining stress in the testing program was established at 0.1 MPa.

A pore pressure parameter B test was conducted on each specimen to insure full saturation of the specimen before commencing a stress path.

As mentioned above, isotropic cyclic consolidation was conducted on every specimen to measure isotropic bulk compressibility of the oil sands prior to the application of any other stress path. For stress paths CID, CIU, CIP and CAI a minimum of five specimens with effective confining stresses of 0.1, 0.5, 1.0, 3.0 and 5.0 MPa respectively were tested. A failure envelope for the CID stress path was first determined and used as a reference to predict the failure stress conditions and design the test procedures for the other stress paths.

Based on the designed program, a total of thirty tests were performed following different stress paths. The results are presented in Chapter 5 and Chapter 6.

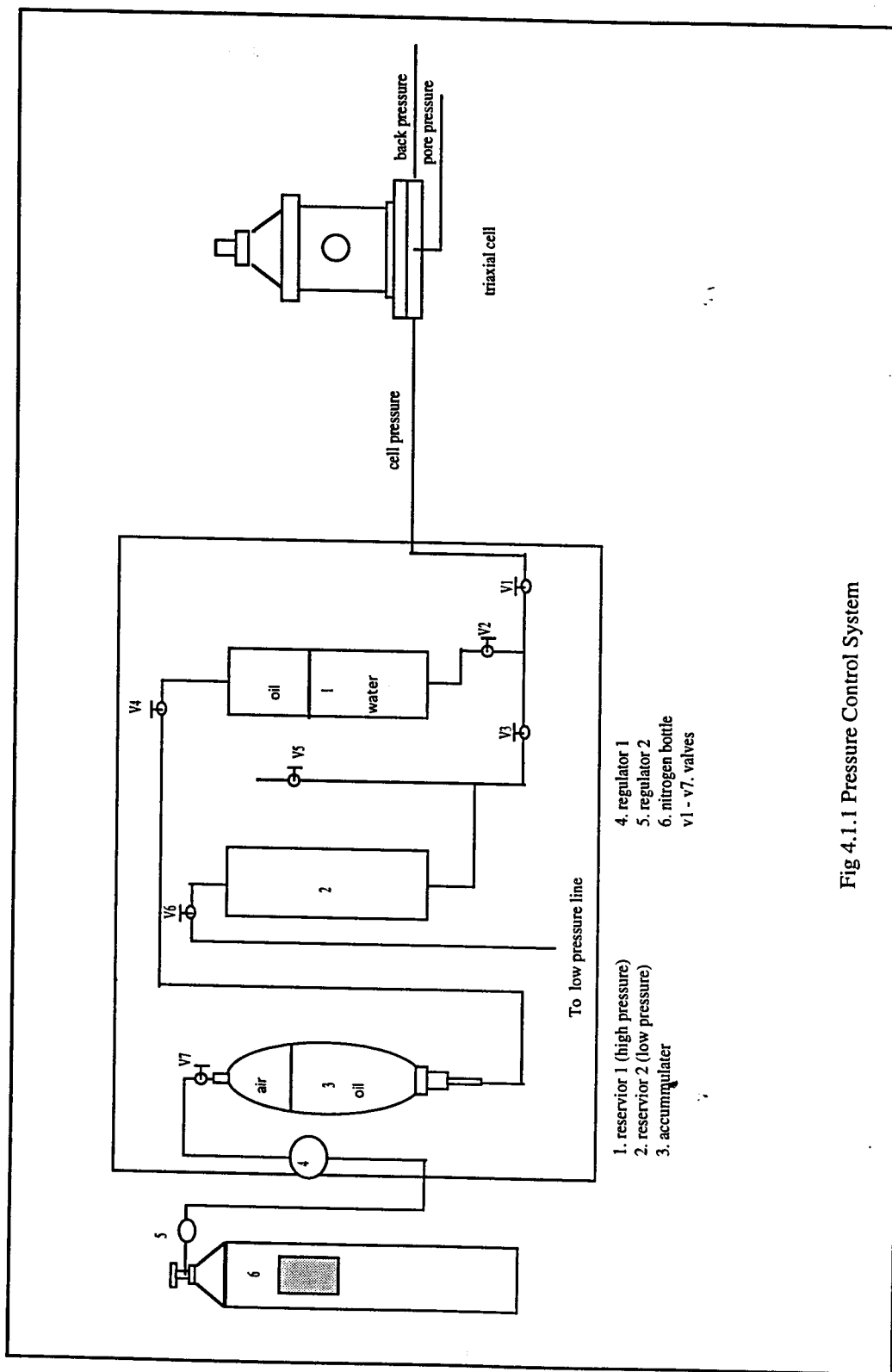


Fig 4.1.1 Pressure Control System

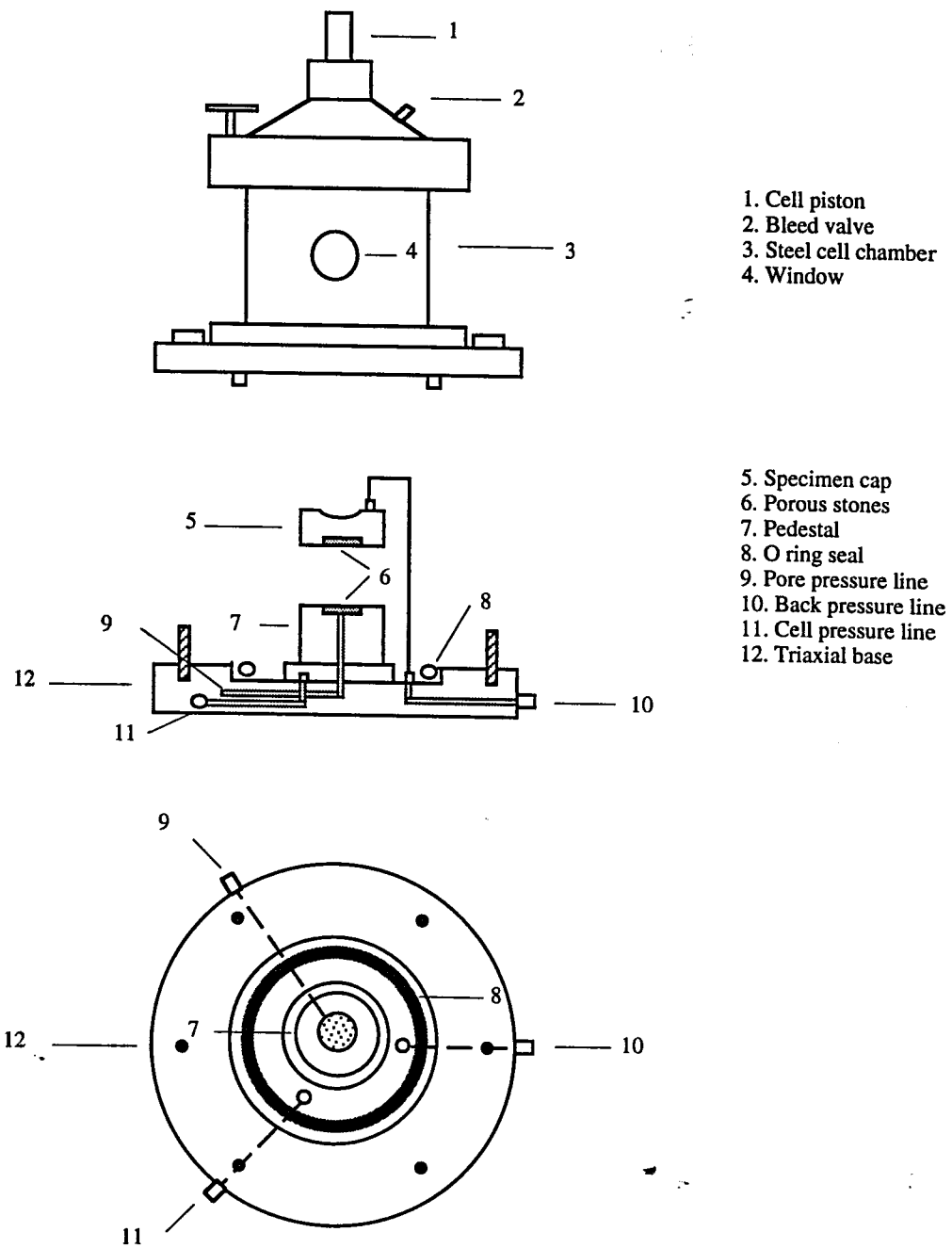


Fig 4.1.2 Diagram of Triaxial Cell

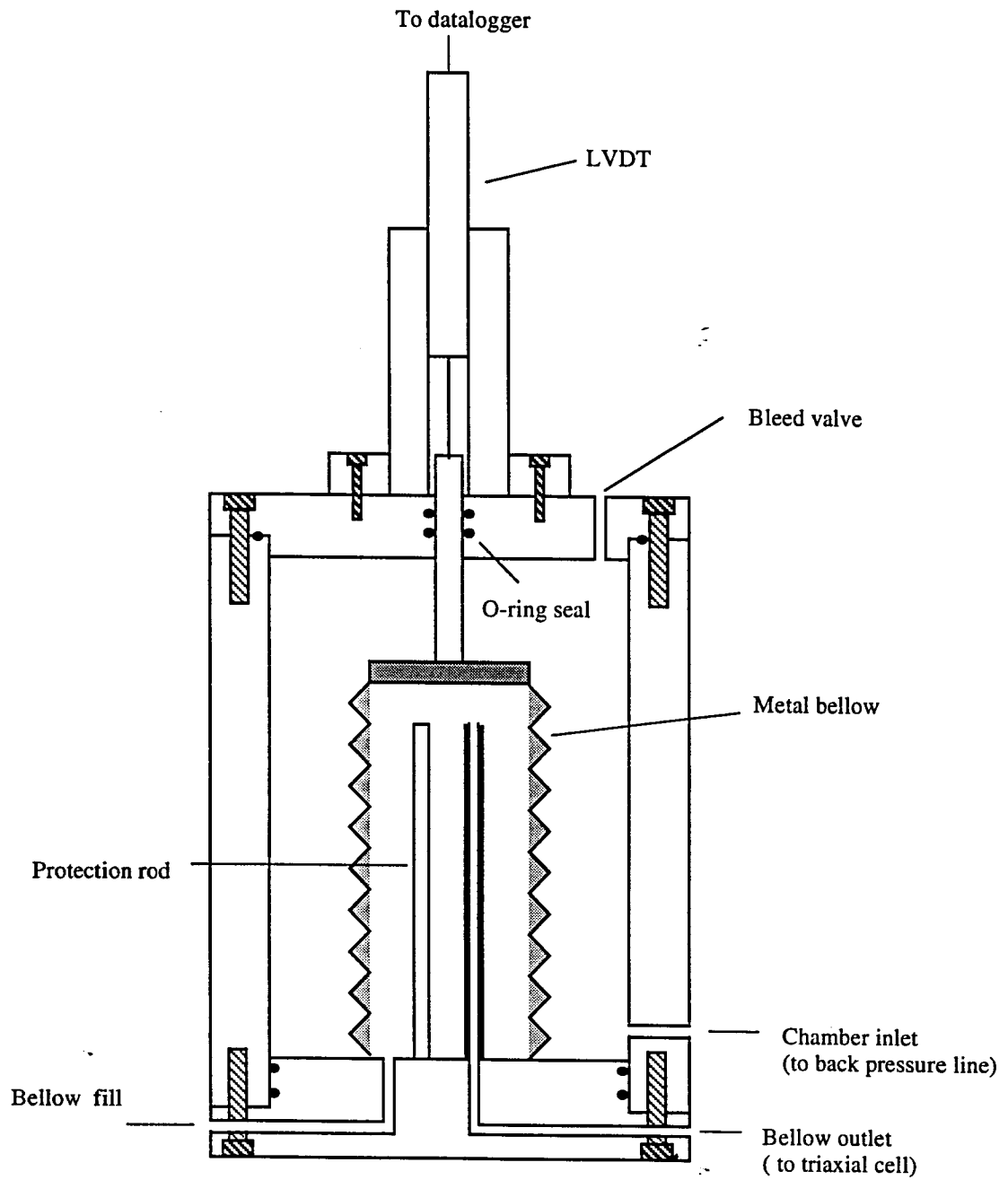
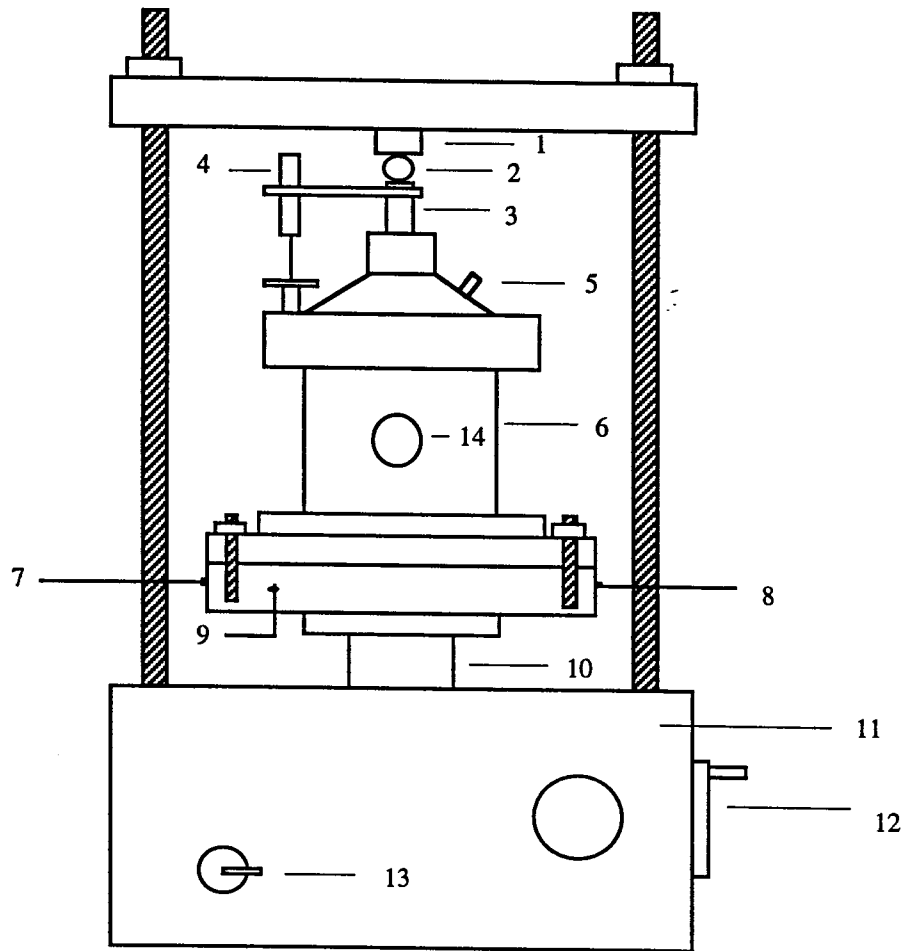
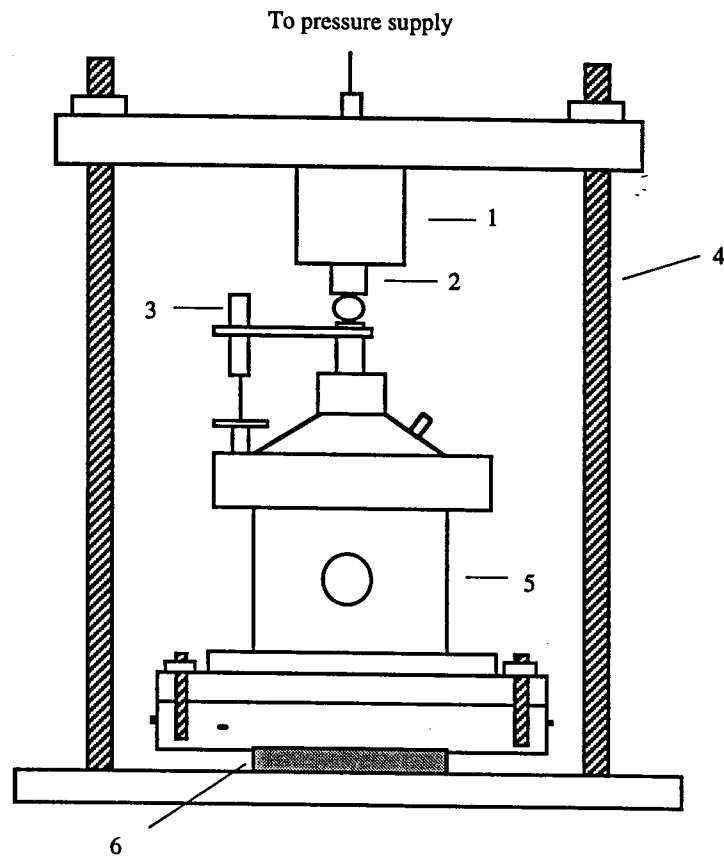


Fig 4.1.3 Bellow Volume Change Measuring Device



- | | |
|-------------------------|-----------------------|
| 1. Load cell transducer | 8. Back pressure line |
| 2. Ball | 9. Pore pressure line |
| 3. Cell piston | 10. Loading ram |
| 4. LVDT | 11. Loading frame |
| 5. Bleed valve | 12. Control handle |
| 6. Triaxial cell | 13. Switch |
| 7. Cell pressure line | 14. Window |

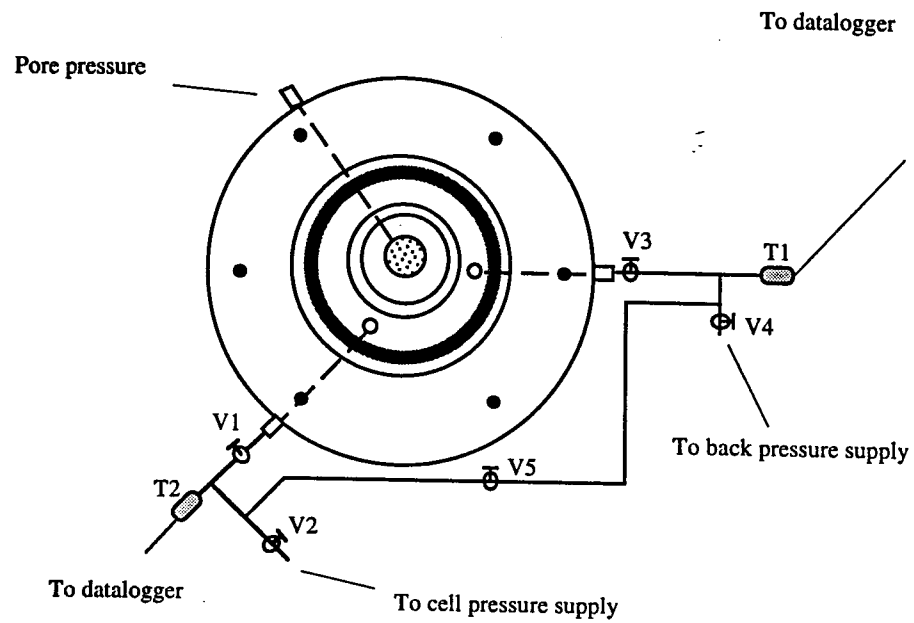
Fig 4.1.4 Strain Controlled Vertical Loading System



- 1. Pressure bellow
- 2. Load cell transducer
- 3. LVDT

- 4. Bellofram
- 5. Triaxial cell
- 6. Steel block

Fig 4.1.5 Stress Controlled Vertical Loading Frame -- Bellofram



T1. Back pressure transducer
 T2. Cell pressure transducer
 V1-V5. Valves

Fig 4.1.7 Innovation of The Triaxial Cell

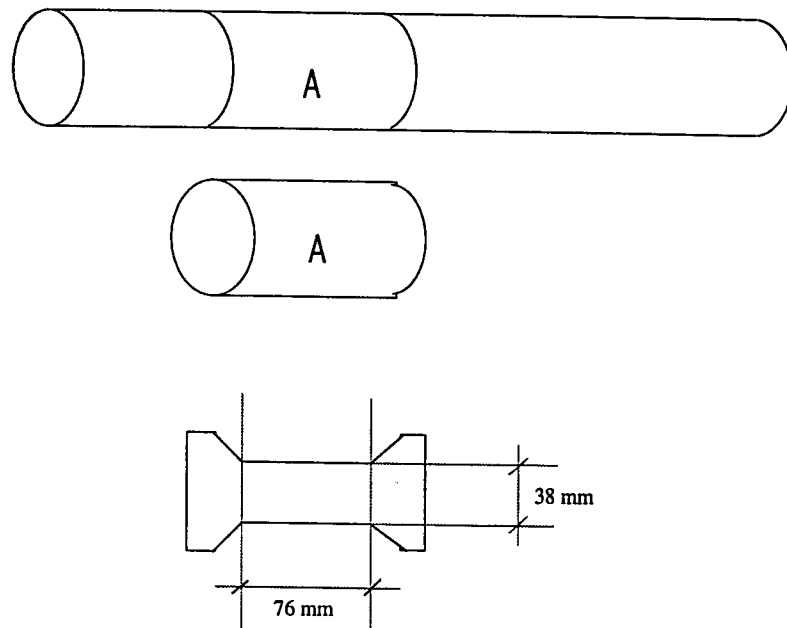


Fig 4.2.1 Trimming Specimen Using Tube Core

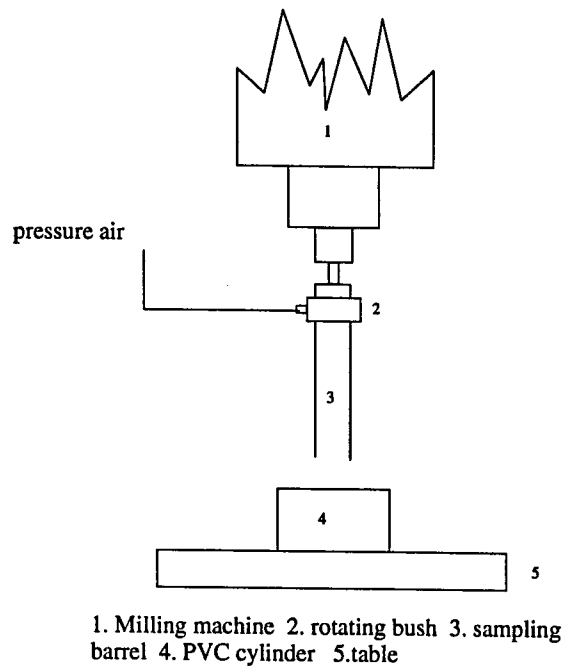


Fig 4.2.2a Coring Specimen on Milling Machine

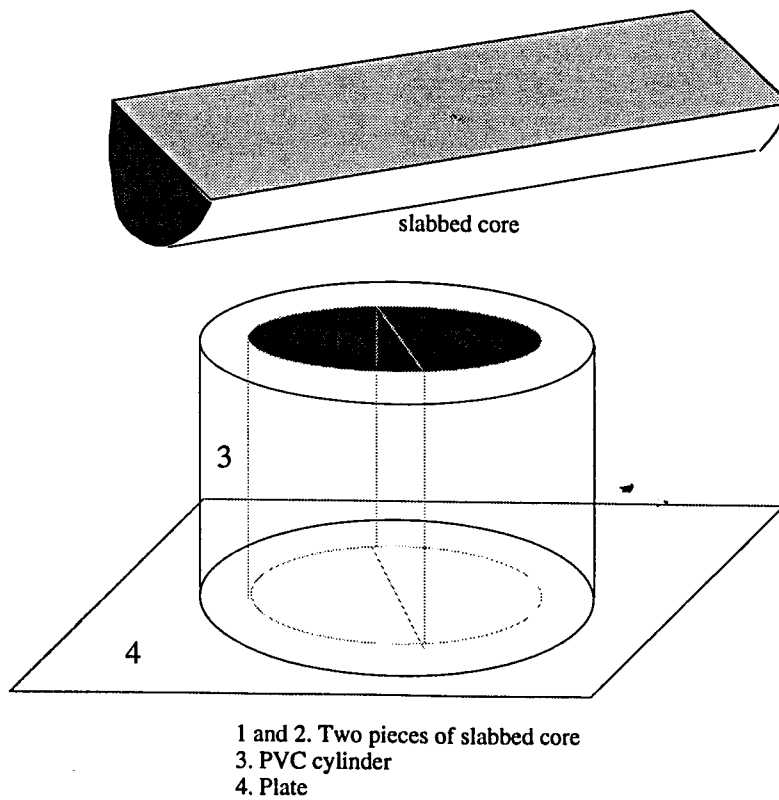


Fig 4.2.2b Freeze Slabbed Cores In The Cylinder

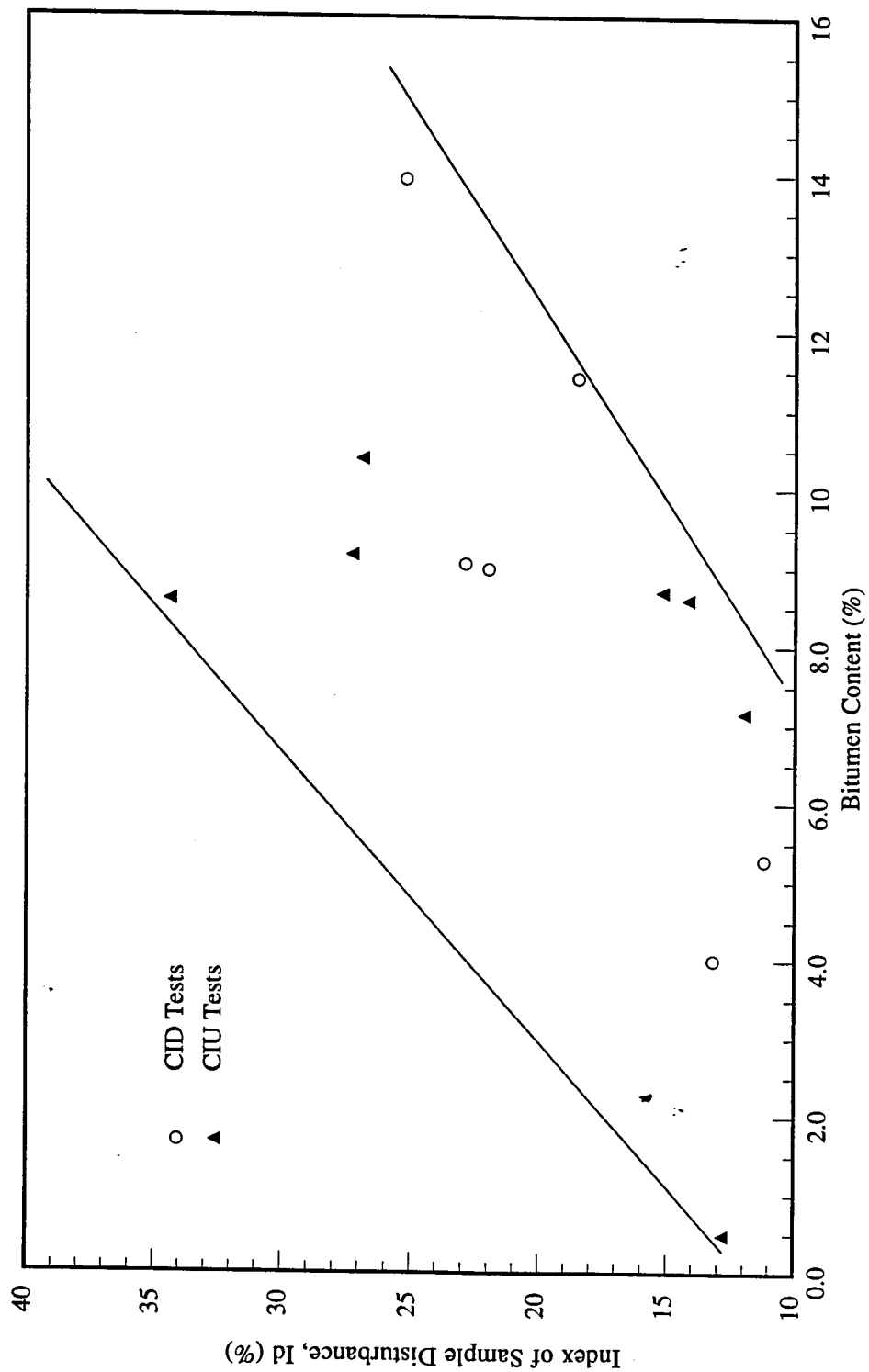


Fig 4.2.3 The Relationship Between Index of Sample Disturbance and Bitumen Content

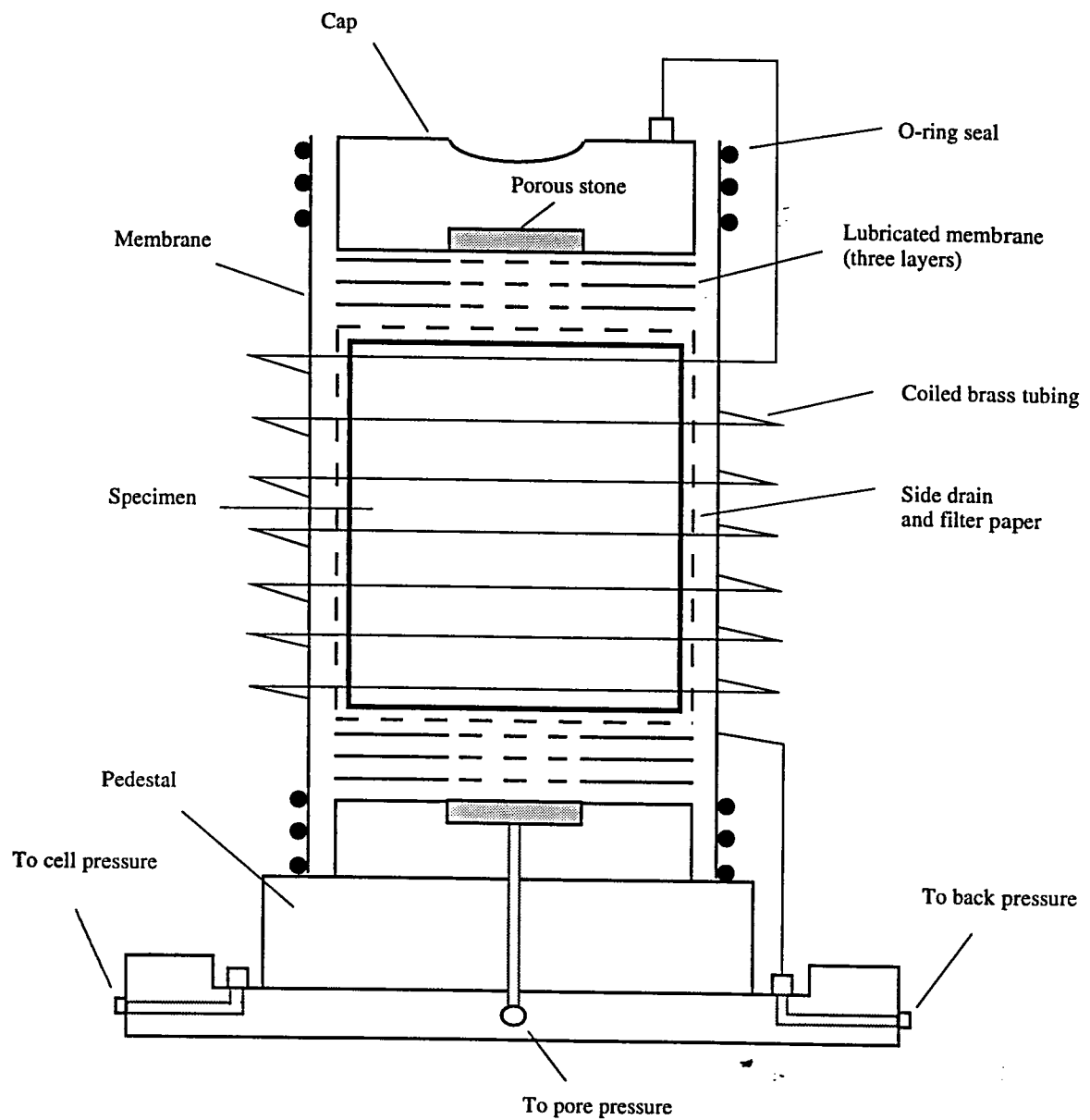
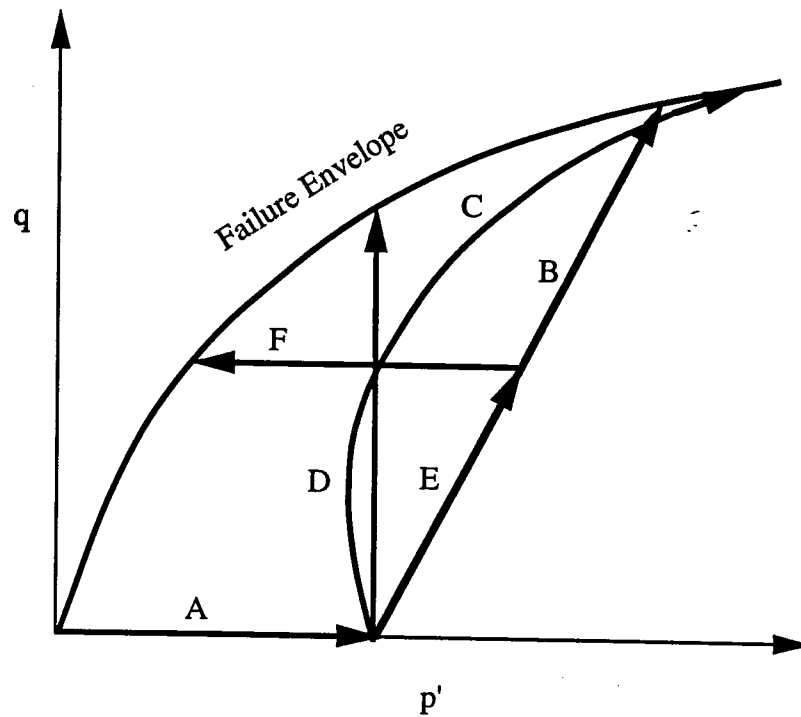


Fig 4.3.1 Test Specimen Set Up



- A. Isotropic cyclic consolidation
- B. Consolidated drained triaxial compression
- C. Consolidated undrained triaxial compression
- D. Consolidated drained triaxial compression with p' constant
- E. Anisotropic consolidation
- F. Pore pressure injection

Fig 4.4.1 Stress Paths In Testing Program

Chapter 5

Isotropic Bulk Compressibility

Of Cold Lake Lower Grand Rapids Formation Oil Sands

5.1 General Description

The isotropic bulk compressibility C_b (Settari et al 1988, Chalaturnyk and Scott 1992) of the oil sands was measured by performing cyclic isotropic consolidation tests (stress path A in figure 4.4.1). Generally, this test was conducted on all the specimens prior to the other testing stress paths CID, CIU, CIP and CAI.

In total, twenty two tests were conducted to measure the isotropic bulk compressibility of the Cold Lake Lower Grand Rapids oil sands. Tests CD1 and CD2 followed a procedure of not applying a back pressure during consolidation. The drainage line was connected to a burette which was full of water and whose end opened to the atmosphere to measure volume change. This procedure was used to measure both the liquid and gas volumes flowing out or into the specimen during loading and unloading. However, the gas appeared to be trapped in the specimen and its volume change could not be measured. Especially, this procedure did not show the volume change of the specimen during unloading.

For the rest of the tests, the procedure was changed. A 500 kPa or higher back pore pressure, according to the pore pressure parameter B test, was applied to saturate the specimen first. All the air and gas would be dissolved in solution under this pressure and then a cyclic consolidation test was conducted. This procedure proved to be satisfactory for the rest of the tests.

In test CU2, bitumen clogged the porous stone and the drainage was impaired during consolidation. Therefore, the results were not acceptable. Similar conditions occurred in Tests CP8, CI4, CI4A and CI5A. Their results were not used to evaluate the bulk compressibility.

The oil sands specimens were taken from the Cold Lake region, Wolf Lake field at depths between 347.0 and 394.0 m. Table 5.1.1 lists the detailed specimen data including well number, core number, specimen dimensions and the depth at which the cores were recovered.

In the isotropic cyclic consolidation test, the effective confining stresses varied from 0.1 to 9.5 MPa. Two or more full cycles of loading and unloading were completed. The completion of the consolidation in each loading or unloading step is determined by monitoring the change in volume and pore pressure. Both of these changes cease when consolidation is completed.

5.2 Test Results and Analyses

A typical isotropic consolidation curve, that is, the relationship between volumetric strain and effective confining stress, is presented in Figure 5.2.1. For convenience, the terminologies used in the interpretation of consolidation results are also defined in this figure. The results of isotropic cyclic consolidation for all the specimens tested are given in Appendix C.

It can be seen that the initial loading causes a large deformation which can be considered to be the influence of sample disturbance (Kry et al 1989). The bulk compressibility upon initial loading can not represent the in situ compressibility. Its magnitude is related to the index of sample disturbance I_D . In other words, a high I_D will result in a large deformation upon initial loading. Whereas, the bulk compressibility

measured in the unloading and reloading cycles, to some degree, can approximately simulate the in situ compressibility which will be discussed later.

After initial loading, the specimen was unloaded decrementally to the effective confining stress of 0.1 MPa (unloading #1 curve in Figure 5.2.1). During the process of unloading, the specimen did not experience a large amount of expansion (pore fluid flowed back into specimen) until the stress dropped to about 2.0 MPa. Between 8.0 and 2.0 MPa, the magnitude of the volumetric strain is relatively small. It is shown in the figure that, when the effective confining stress changes from 8.0 MPa to 2.0 MPa, the volumetric strain only increases by 0.4%. That is about 0.07% per MPa on average. Below 2.0 MPa, when the effective confining stress changes from 2.0 MPa to 0.1 MPa, the volumetric strain increases by 1.6%, about 0.84% per MPa. The average change in magnitude is 12 times as large as that between 2.0 and 8.0 MPa. The rate of change in volume increases with the decrease in effective confining stress and accelerates quickly with each decrement of effective confining stress reaching a maximum at the effective confining stress of 0.1 MPa. Reloading recompresses the specimen (reloading #1 curve in Figure 5.2.1) and the rate of change in volume decreases with the increase in effective confining stress. The process is repeated in the second cycle of unloading and reloading. From Figure 5.2.1, two facts can be observed. First of all, the unloading and reloading curves in the two cycles do not fall on the same path. A hysteresis loop is created. Secondly, each cycle of unloading and reloading causes a certain amount of unrecoverable deformation. In other words, the accumulative volumetric strain in the second stress cycle is greater than that in the first stress cycle. The other test results given in Appendix C show the same behavior. These two facts imply that the oil sand tested does not behave elastically during stress cycling. The behavior differs from that of Athabasca McMurray Formation oil sands, which show an elastic behavior in isotropic cyclic consolidation (Kosar 1989).

Agar (1984) reported similar results on Athabasca oil sands, which indicated that they behaved in an elastic manner during stress cycling. Kosar (1989) performed both constrained consolidation and isotropic consolidation in which the constrained modulus D and bulk modulus K had a reasonable agreement in conjunction with the theory of elasticity. Figure 2.3.2 in Chapter 2 is a typical isotropic cyclic consolidation result achieved by Kosar (1989). Except for the initial loading, the stress-strain curves follow approximately the same paths in three stress cycles. This elastic behavior during isotropic stress cycling was also observed by Kosar (1989) on Cold Lake Clearwater Formation oil sands which, however, did not show elastic behavior in one-dimensional constrained consolidation. Wong et al (1993) also reported the elastic behavior of Cold Lake Clearwater Formation oil sands in stress range between 3.0 and 14.0 MPa during isotropic stress cycling. Obviously, the Cold Lake Lower Grand Rapids Formation oil sands behave differently from the other oil sands in the test stress range used in these tests. The main reason is that isotropic cyclic consolidation can cause grain crushing in the testing stress range due to the weak mineral composition of the Grand Rapids oil sands. Petrophysical analyses show that quartz grains compose only about 50% of the sands, unlike Athabasca oil sands which consist of almost 100% quartz grains. Grain crushing does not occur in Athabasca oil sands in both isotropic and anisotropic consolidation tests. For Cold Lake Clearwater Formation oil sands, Kosar (1989) found that grain crushing only occurred in one dimensional consolidation in which shear stress was triggered due to the constrained condition. The oil sands still behaved in an elastic manner without grain crushing in isotropic cyclic consolidation. Hardin's (1985) test results on granular materials indicated that grain crushing occurs in both isotropic and anisotropic stress conditions. The magnitude of crushing caused by isotropic consolidation is relatively smaller than that of other stress paths tests in which an anisotropic stress condition was involved.

It is noted that, in Figure 5.2.1, the two unloading curves are approximately parallel to each other, so are the reloading curves. All the consolidation curves in Appendix C show the same results. As the bulk compressibilities for unloading and reloading are quite different, they should be evaluated separately. However, the bulk compressibilities for the first cycle and the second cycle of unloading or reloading bear the same magnitude. Figures 5.2.2 and 5.2.3 show the unloading compressibility and reloading compressibility for the two cycles respectively. In figure 5.2.2, the solid line represents the bulk compressibility in the first cycle of unloading, and the dashed line is the compressibility in the second cycle of unloading. The lines are superposed. In figure 5.2.3, the same results are observed for reloading bulk compressibility. It is evident that the two curves in each figure can be represented by one curve statistically.

The isotropic bulk compressibility, C_b , is calculated in an incremental manner. It is the average value in each stress increment and can be expressed as

$$C_b = \frac{\Delta \epsilon_v}{\Delta \sigma'_3} \quad (5.2.1)$$

Where $\Delta \sigma'_3$ is the increment of effective confining stress, and $\Delta \epsilon_v$ is the corresponding volumetric strain caused by $\Delta \sigma'_3$.

A relationship exists between compressibility and effective confining stress which has a good agreement with a power function, expressed as

$$C_b = a \sigma'^3_b \quad (5.2.2)$$

where

C_b = Isotropic bulk compressibility (MPa^{-1})

σ'_3 = Effective confining stress (MPa)

a, b = Constants

By curve fitting, the constant a and the exponent b in equation (5.2.2) can be determined. Figures 5.2.4 and 5.2.5 show the curve fitted relationship between bulk compressibility and effective confining stress for unloading and reloading in Test CU6 respectively. The two equations shown in the figures relating the compressibility to the effective confining stress display a significant difference in compressibility between unloading and reloading. Table 5.2.1 summarizes the results of compressibility tests in terms of constant a and exponent b . It can be seen that a and b for unloading compressibility or reloading compressibility vary within a limited range. The bulk compressibility in unloading or reloading on all the specimens tested does not diverge significantly from one another. The constant a varies between 2.74 and 6.23 with an average of 4.83, and b between -0.97 and -1.65 with an average of -1.26 upon unloading, while the constant a changes between 2.98 and 6.92 with an average of 5.02, and b between -0.53 and -0.78 with an average of -0.65 upon reloading. The average values indicate that the difference between unloading compressibility and reloading compressibility depends on the exponent b more than on the constant a . The absolute value of b in unloading is almost twice as large as that in reloading, whereas the value of a in unloading is almost equal to that in reloading.

Previous studies on Athabasca McMurray Formation oil sands and Cold Lake Clearwater Formation oil sands, as mentioned before, found that the oil sands exhibit elastic behavior in isotropic stress cycling. The relationship between volumetric strain and effective confining stress is the same in all the stress cycles experienced by a specimen. The volumetric strain, generally, has a linear relationship with effective confining stress within a certain stress range. The bulk modulus K or the bulk compressibility C_b of the oil sands, therefore, can be represented by a single value in that stress range. Kosar et al (1987) summarized the research achievements and presented the value of bulk compressibility, $C_b = 1.4 \times 10^{-3} \text{MPa}^{-1}$, in the stress range of 1.0 to 4.5 MPa for Athabasca oil sands and $C_b = 0.98 \times 10^{-3} \text{MPa}^{-1}$ in the stress range of 4.0 to 9.0 MPa for

Cold Lake oil sands. Kosar (1989) also conducted some one-dimensional and triaxial isotropic consolidation tests and recognized the differences between unloading compressibility and reloading compressibility. The results for each stress cycle were also represented by single values. For Cold Lake Clearwater Formation oil sands, the bulk compressibility varied between 0.60 and 0.93 10^{-3}MPa^{-1} in reloading (8 tests) and between 0.88 and 0.99 10^{-3}MPa^{-1} in unloading (3 tests) in the stress range of 5.0 to 9.0 MPa. However, the results shown in previous studies were mainly obtained in high stress ranges. The behavior of oil sands in a low effective confining stress range was not measured.

The tests, in this study show that, in a low effective confining stress range, the bulk compressibility changes dramatically with a small variation in effective confining stress. The compressibility for different stress levels is summarized in Table 5.2.2. The variation of compressibility with effective confining stress shows that the compressibility can not well be represented by a single value over the entire testing stress range. Plewes (1987) had the same comment on the behavior of Athabasca McMurray Formation oil sands. It is noted in Table 5.2.2 that even in the stress range over 4.0 MPa, the change in the compressibility with the effective confining stress is not constant, which is illustrated in figures 5.2.6 and 5.2.7. It can be seen that in the elevated stress range between 2.0 and 8.0 MPa, the bulk compressibility still changes about two orders of magnitude.

These figures also show that the unloading or reloading compressibilities for the two stress cycles follow the same paths except for a few points at high stresses, even though the differences in the two stress cycles in the elevated stress range are exaggerated due to the nature of the semi-log scale. The results given in Appendix C for all the other tests show the same results.

When a very low effective confining stress is experienced by a specimen in a triaxial test, the theory of elasticity will no longer dominate the stress-volume change behavior in isotropic stress cycling. It is possible that unloading to a low effective

confining stress could create a stress-strain condition in which particle rolling or reorientation is allowed. As a result, the stress-volume change mechanism changes and more grain crushing or shear displacement occurs in stress cycling. In other words, a low effective confining stress can change the geomechanical behavior of the oil sands from that postulated by Wong et al (1993).

The oil sands generally exhibit similar compressibility, provided the grain size distributions of different specimens do not have much difference. Table 5.2.1 indicates the impact of grain size on the bulk compressibility of Cold Lake oil sands in terms of parameters **a** and **b**. The specimens in Test CI1 through CI5 have similar grain size distribution, the effective grain size d_{10} changes from 0.078 to 0.080 mm. All the five specimens experienced the same process of sampling, storage, transportation and trimming, and tested in the same stress range, 0.10 to 8.00 MPa. Table 5.2.1 displays that in unloading, the constant **a** varies between 5.23 and 6.04, and the exponent **b** between -0.97 and -1.09. In reloading, the constant **a** changes between 5.21 and 6.65, and the exponent **b** between -0.56 and -0.64. The variations fluctuate within a very limited range. However, the variation of the bulk compressibility among the specimens with different grain size distributions is relatively large. Generally, the finer grained specimens are less compressible than the coarser grained.

Another factor which largely influences the compressibility of the oil sands is sample disturbance. The three types of oil sand cores involved in specimen preparation experienced a different degree of sample disturbance because of different storage conditions. The frozen tube core was the least disturbed, whereas the slabbed unfrozen core was the most disturbed. The slabbed frozen core stayed in a state of moderate disturbance. The average bulk compressibility for each type of oil sand core is summarized in Table 5.2.3. A clear trend of variation of compressibility with the magnitude of sample disturbance is illustrated. The less disturbed frozen tube oil sands demonstrate the smallest values of compressibility and the more disturbed slabbed

unfrozen oil sands show the largest values of compressibility in the stress range between 0.5 and 8.0 MPa.

In figures 5.2.4 and 5.2.5, it is noted that the bulk compressibility increases slowly with the decrease in effective confining stress in the high stress range. When the effective stress drops to a certain value, a small decrement will cause a large increment in the bulk compressibility. The value of effective confining stress below which the compressibility changes dramatically with variation of effective confining stress is about 2.0 MPa in these figures. Since the bulk compressibility is a function of effective confining stress, there exists a point on the isotropic compressibility curve at which the curvature is the maximum. This point can be considered to be the boundary separating high rate and low rate of change in bulk compressibility. The boundary may be determined using a mathematical measure. In calculus (Swokowski, 1975), the curvature of a curve $f(x)$ is determined by the following equation,

$$K(x) = \frac{f''(x)}{[1+(f'(x))^2]^{3/2}} \quad (5.2.3)$$

Where $f(x)$ is the equation of a curve, $f'(x)$ and $f''(x)$ are the first and the second derivatives of the curve, and $K(x)$ is the curvature. Let the first derivative of the curvature $K(x)$ be equal to zero and by trial and error, the value x at which the maximum curvature exists can be determined. Making use of this method, a specific value of the effective confining stress on an isotropic compressibility curve above or below which oil sands may have a different behavior can be found. Since a significant change in bulk compressibility of the oil sands tested with effective confining stress mainly appears at a low stress range, this stress, designated as boundary stress σ_b' , may be used to define the stress range on an analytical basis. That is, stresses lower than this value would be called the low effective stress range, and higher than this called the high or elevated stress range.

In figures 5.2.4 and 5.2.5, the effective confining stress of 2.25 MPa is the boundary for both unloading and reloading bulk compressibility. Other values of the boundary stresses for all the specimens tested are listed in Table 5.2.1. The average value of the boundary stresses is 2.24 MPa for unloading and 2.00 MPa for reloading.

5.3 Estimation of In Situ Bulk Compressibility

Compressibility of oil sands is inevitably influenced by sample disturbance. Generally, the value increases with the increase in the index of sample disturbance. From this point of view, a relationship between compressibility and index of sample disturbance can possibly be found. Such relationships for all tests are plotted in figures 5.3.1 to 5.3.4. The disturbance of samples is unavoidable. It usually starts with sampling in the field and develops throughout handling and testing. Poor sampling techniques and handling processes will result in high sample disturbance. Whereas, at initial in situ conditions, the oil sands are not disturbed. Therefore, the index of sample disturbance is zero. By extrapolating the relationships with a best fit straight line in figures 5.3.1 to 5.3.4, that is, extending the lines to the C_b axis, the intercepts at $I_D=0$ would approximate the in situ compressibility. It can be seen that, in figures 5.3.1 to 5.3.4, the relationship between compressibility and the index of sample disturbance has a very small slope for both unloading and reloading. It implies that stress cycling does help minimize the influence on compressibility caused by disturbance. This linear extrapolation may not be the best relationship between compressibility and sample disturbance. As compressibility has a power relationship with effective confining stress, it may also have a similar relationship with sample disturbance. Not enough test results at very low indices of disturbance are available, however, to evaluate which extrapolation technique would be the best.

Closely examining the relationships, it seems that the influence of sample disturbance on reloading compressibility is more than on unloading compressibility. Upon unloading, the relationships expressed as straight lines are almost horizontal to the C_b axis. The slope increases from 0.001 to 0.013, when the effective confining stress drops from 8.0 to 0.5 MPa. In the same stress range, the slope for reloading compressibility changes from 0.01 to 0.09, which is greater than that in unloading by more than one order of magnitude. The estimated in situ compressibility values for different stress levels are listed in Table 5.3.1. They are also presented in figure 5.3.5. It should be pointed out that these values are the averages for all the specimens tested. The data in the figure are highly scattered and the influences of the grain size distribution and geological background are not considered. Since all the geological units associated with the specimens are in the Lower Grand Rapids Formation, the influence on the compressibility would mainly come from the grain size distribution. The average values can be used to quantify the in situ compressibility for the oil sand layers in this formation. Dusseault (1980) suggested in situ compressibility values of 0.4 to $1.0 \cdot 10^{-3} \text{ MPa}^{-1}$ in the stress range of 7.0 to 13.0 MPa for Cold Lake Clearwater Formation oil sands, which has a similar mineral composition as the oil sands tested. This compressibility coincides with the estimated reloading compressibility in this testing program, which is about $1.2 \cdot 10^{-3} \text{ MPa}^{-1}$ in the same stress range.

5.4 Conclusions

From the analyses above, the following conclusions can be drawn for the Cold Lake Lower Grand Rapids Formation oil sands tested:

- 1) The oil sands tested do not behave in an elastic manner in isotropic cyclic consolidation tests. Shear displacement usually occurs during the stress cycling and

unrecoverable deformation appears in each stress cycle. Grain crushing causes the unrecoverable deformation due to the weakness of the mineral composition.

2) The isotropic bulk compressibility of the oil sands tested is a function of effective confining stress. It is not governed by the theory of elasticity. Since the bulk compressibilities for unloading and reloading do not follow the same path they must be evaluated separately. It was found that the bulk compressibilities for unloading or for reloading in different stress cycles bear the same magnitude. They may be represented by one curve statistically which can be expressed as a power function.

$$C_b = a \sigma_3'^b \quad (5.2.2)$$

Where the average **a** and **b** for unloading are 4.83 and -1.26 respectively and for reloading 5.02 and -0.65 respectively. The difference in bulk compressibility between unloading and reloading is mainly shown in exponent **b** not in constant **a**.

3) Two important factors, grain size distribution and sample disturbance, significantly influence the compressibility of the oil sand deposits. The constants **a** and **b** vary within a very limited range, provided that the grain size distribution is similar. The finer grained oil sands are less compressible than the coarser grained oil sands. The greater the sample disturbance, the higher the compressibility value even after isotropic stress cycling.

4) The in situ bulk compressibility of the oil sands can be estimated using the relationship between compressibility and index of sample disturbance by extrapolating to the in situ porosity. The estimated in situ compressibility for the oil sands tested can be expressed as

$$\text{Unloading: } C_b = 4.83 \sigma_3'^{-1.24} \quad 10^{-3} \text{MPa}$$

$$\text{Reloading: } C_b = 4.41 \sigma_3'^{-0.66} \quad 10^{-3} \text{MPa}$$

5) The bulk compressibility of the oil sands tested varies dramatically in the low stress range. In most cases, when the effective confining stress is lower than 2.0 MPa, a small variation of effective confining stress will result in a significant change in bulk compressibility. The boundary stress, σ_b' , which separates the low stress range and the high stress range for all specimens tested was calculated to be about 2.0 MPa.

Table 5.1.1 Specimen Data

Test	Well No.*	Core No.	Length mm	Diameter mm	Depth m	Geologic Unit	Core Type
CD1	10-18-63-6	22	77.5	37.8	387.50-387.58	Rex	Slabbed
CD2	10-18-63-6	22	65.1	37.8	387.94-388.01	Rex	Slabbed
CD3	10-18-63-6	22	77.2	37.8	388.17-388.25	Rex	Slabbed
CD4	10-18-63-6	22	70.0	37.4	388.50-388.57	Rex	Slabbed
CD5	10-18-63-6	22	80.6	36.3	388.57-388.65	Rex	Slabbed
CD6	10-18-63-6	22	63.6	37.2	388.82-388.88	Rex	Slabbed
CU1	11-06-64-6	8	72.0	37.5	374.50-374.58	Middle Sparky	Slabbed
CU2	10-18-63-6	3	71.0	39.0	347.22-347.30	Upper Sparky	Tube
CU2	10-18-63-6	3	68.6	38.0	347.30-347.37	Upper Sparky	Tube
CU4	10-18-63-6	14	67.0	38.2	363.70-363.77	Middle Sparky	Tube
CU5	10-18-63-6	14	64.3	38.3	363.80-363.87	Middle Sparky	Tube
CU6	10-18-63-6	8	50.3	39.0	355.30-355.36	Upper Sparky	Tube
CU7	10-18-63-6	10	69.4	39.6	358.70-358.77	Upper Sparky	Tube
CU8	10-18-63-6	3	62.4	39.5	347.70-347.77	Upper Sparky	Tube
CP1	10-18-63-6	14	67.6	38.0	364.00-364.07	Middle Sparky	Tube
CP2	10-18-63-6	14	64.4	38.8	364.20-364.27	Middle Sparky	Tube
CP3	10-18-63-6	14	62.2	38.5	364.40-364.47	Middle Sparky	Tube
CP4	10-18-63-6	8	65.2	38.2	356.00-356.07	Upper Sparky	Tube
CP5	10-18-63-6	8	76.3	38.3	355.10-355.18	Upper Sparky	Tube
CP6	14B-6-64-6	1	49.2	37.6	362.38-362.43	Upper Sparky	Slabbed
CP7	14B-6-64-6	1	56.2	37.4	362.18-362.24	Upper Sparky	Slabbed
CP8	14B-6-64-6	4	72.8	37.5	392.50-392.60	General Petroleum	Slabbed
CI1	14B-6-64-6	4	78.0	37.5	393.25-393.33	General Petroleum	Slabbed
CI2	14B-6-64-6	4	71.0	37.3	393.18-393.25	General Petroleum	Slabbed
CI3	14B-6-64-6	4	70.6	37.8	393.10-393.18	General Petroleum	Slabbed
CI4	14B-6-64-6	4	69.5	37.4	392.93-393.00	General Petroleum	Slabbed
CI4A	14B-6-64-6	4	76.2	37.2	393.34-393.42	General Petroleum	Slabbed
CI4B	14B-6-64-6	4	65.2	37.4	393.57-393.64	General Petroleum	Slabbed
CI5	14B-6-64-6	4	69.4	37.3	392.83-392.90	General Petroleum	Slabbed
CI5A	14B-6-64-6	4	68.4	37.4	393.50-393.57	General Petroleum	Slabbed

*All wells are in Cold Lake region, Wolf Lake field

Table 5.2.1 Compressibility Parameter a and b

Test	Reloading			Unloading			d10 (mm)	Stress Range (MPa)	Geological Unit
	a	b	σ_b' (MPa)	a	b	σ_b' (MPa)			
CD3	3.86	-0.58	1.60	3.93	-1.18	2.05	0.085	0.10-9.35	Rex
CD4	6.78	-0.78	2.50	6.23	-1.37	2.55		0.10-9.50	Rex
CD5	6.75	-0.68	2.40	6.04	-1.12	2.50	0.085	0.10-9.40	Rex
CD6	6.92	-1.34	2.65	5.50	-1.04	2.35		0.10-9.50	Rex
CU1	3.80	-0.67	1.70	3.69	-1.07	1.95	0.065	0.10-9.50	M.S.*
CU3	5.03	-0.68	2.05	4.06	-1.65	2.10	0.100	0.10-9.50	M.S.
CU4	5.27	-0.65	2.05	5.46	-1.04	2.35	-	0.10-9.50	M.S.
CU5	4.24	-0.53	1.60	2.74	-1.63	1.85	-	0.10-8.00	M.S.
CU6	6.13	-0.66	2.25	4.78	-1.51	2.25	0.048	0.10-8.00	U.S.**
CU8	4.59	-0.58	1.75	3.79	-1.41	2.05	0.100	0.10-7.74	U.S.
CP1	4.13	-0.72	1.85	4.35	-1.20	2.15	-	0.10-9.00	M.S.
CP2	4.91	-0.77	2.05	4.47	-1.41	2.20	-	0.10-9.00	M.S.
CP3	2.98	-0.58	1.35	3.48	-1.23	1.95	-	0.10-9.00	M.S.
CP4	4.83	-0.79	2.05	4.91	-1.42	2.30	0.050	0.10-8.00	U.S.
CP5	4.35	-0.71	1.85	4.33	-1.38	2.15	0.050	0.10-8.00	U.S.
CP6	5.90	-0.65	2.15	5.03	-1.32	2.30	0.070	0.10-8.00	U.S.
CP7				4.91	-1.34	2.30	0.074	0.10-8.00	U.S.
CI1	5.79	-0.59	2.05	5.64	-0.97	2.35	0.080	0.10-8.00	G.P.***
CI2	6.29	-0.63	2.20	5.86	-1.09	2.45	0.080	0.10-8.00	G.P.
CI3	6.12	-0.64	2.20	5.68	-1.07	2.40	0.080	0.10-8.00	G.P.
CI4B	6.65	-0.57	2.20	6.04	-1.01	2.45	0.078	0.10-8.00	G.P.
CI5	5.21	-0.56	1.85	5.23	-1.08	2.30	0.078	0.10-8.00	G.P.
Average	5.02	-0.65	2.00	4.83	-1.26	2.24			

*Middle Sparky

**Upper Sparky

***General Petroleum

Table 5.3 Summary of Compressibility Measurements (10-3/MPa) For Different Effective Confining Stress

Cb Test	Reloading (MPa)					Unloading (MPa)								
	0.1	0.5	1.0	2.0	4.0	6.0	8.0	0.1	0.5	1.0	2.0	4.0	6.0	8.0
CD3	14.67	5.77	3.86	2.58	1.73	1.37	1.15	59.48	8.90	3.93	1.73	0.76	0.47	0.34
CD4	40.85	11.64	6.78	3.95	2.30	1.68	1.34	146.05	16.10	6.23	2.40	0.93	0.54	0.36
CD5	32.31	10.81	6.75	4.21	2.63	2.00	1.64	79.62	13.13	6.04	2.78	1.28	0.81	0.59
CD6	151.39	17.52	6.92	2.73	1.08	0.63	0.43	60.30	11.30	5.50	2.67	1.30	0.85	0.63
CU1	17.77	6.05	3.80	2.39	1.50	1.14	0.94	43.35	7.75	3.69	1.76	0.84	0.54	0.4
CU3	24.08	8.06	5.03	3.14	1.96	1.49	1.22	181.35	12.74	4.06	1.29	0.41	0.21	0.13
CU4*	23.54	8.27	5.27	3.36	2.14	1.64	1.36	59.87	11.23	5.46	2.66	1.29	0.85	0.63
CU5*	14.37	6.12	4.24	2.94	2.03	1.64	1.41	116.88	8.48	2.74	0.89	0.29	0.15	0.09
CU6	28.02	9.69	6.13	3.88	2.46	1.88	1.55	154.67	13.60	4.78	1.68	0.59	0.32	0.21
CU8	17.45	6.86	4.59	3.07	2.05	1.62	1.37	97.42	10.07	3.79	1.43	0.54	0.30	0.2
CPI*	21.67	6.80	4.13	2.51	1.52	1.14	0.92	68.94	9.99	4.35	1.89	0.82	0.51	0.36
CP2*	28.91	8.37	4.91	2.88	1.69	1.24	0.99	114.90	11.88	4.47	1.68	0.63	0.36	0.24
CP3*	11.33	4.45	2.98	1.99	1.33	1.05	0.89	59.10	8.16	3.48	1.48	0.63	0.38	0.27
CP4	29.78	8.35	4.83	2.79	1.62	1.17	0.93	129.15	13.14	4.91	1.83	0.69	0.39	0.26
CP5	22.31	7.12	4.35	2.66	1.63	1.22	0.99	103.87	11.27	4.33	1.66	0.64	0.37	0.25
CP6	26.35	9.26	5.90	3.76	2.40	1.84	1.53	105.09	12.56	5.03	2.01	0.81	0.47	0.32
CP7								107.42	12.43	4.91	1.94	0.77	0.44	0.3
CI1	22.53	8.72	5.79	3.85	2.56	2.01	1.70	52.64	11.05	5.64	2.88	1.47	0.99	0.75
CI2	26.83	9.73	6.29	4.06	2.63	1.03	1.70	72.09	12.47	5.86	2.75	1.29	0.83	0.61
CI3	26.71	9.54	6.12	3.93	2.52	1.94	1.62	66.73	11.92	5.68	2.71	1.29	0.84	0.61
CI4B	24.70	9.87	6.65	4.48	3.02	2.39	2.03	61.81	12.16	6.04	3.00	1.49	1.00	0.74
CI5	18.92	7.68	5.21	3.53	2.40	1.91	1.63	63.12	11.10	5.25	2.48	1.17	0.76	0.56

* Contains a high percentage of fines

Table 5.2.3 Average C_b (10^{-3} /MPa) For The Different Oil Sands Cores

C_b Stress Core Type	Reloading (MPa)						Unloading (MPa)					
	0.5	1.0	2.0	4.0	6.0	8.0	0.5	1.0	2.0	4.0	6.0	8.0
Tube Frozen	7.41	4.65	2.92	1.84	1.41	1.16	11.06	4.24	1.65	0.65	0.38	0.26
Slab Frozen	10.36	5.62	3.17	1.85	1.36	1.10	11.44	5.08	2.27	1.02	0.64	0.46
SlabUnfrozen	9.13	5.99	3.94	2.59	1.85	1.70	11.96	5.49	2.54	1.18	0.76	0.56

Table 5.3.1 Estimated In Situ Bulk Compressibility

Stress Level (MPa)	Unloading Stress Path C_b (10^{-3}/MPa)	Reloading Stress Path C_b (10^{-3}/MPa)
8.0	0.38	1.11
6.0	0.53	1.31
4.0	0.86	1.80
2.0	1.99	2.86
1.0	4.68	4.49
0.5	11.13	6.88
0.1	87.42	20.06

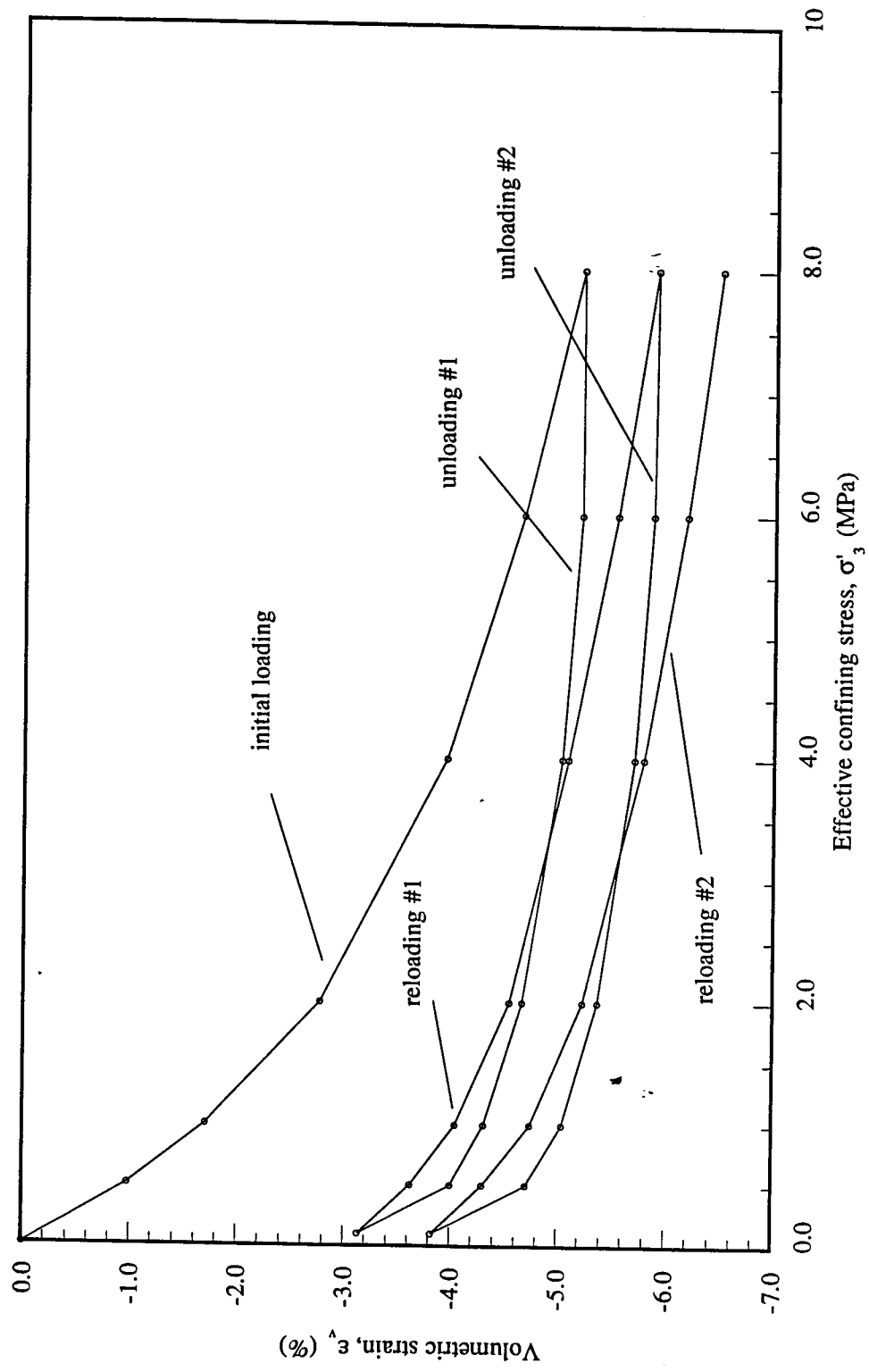


Fig 5.2.1 Test CU6: Isotropic Cyclic Consolidation

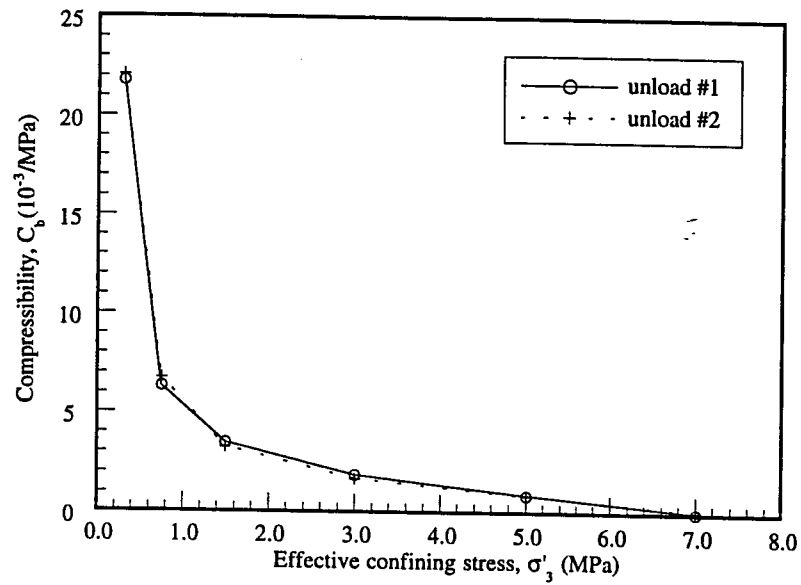


Fig 5.2.2 Test CU6: Isotropic Compressibility Unload #1 and #2

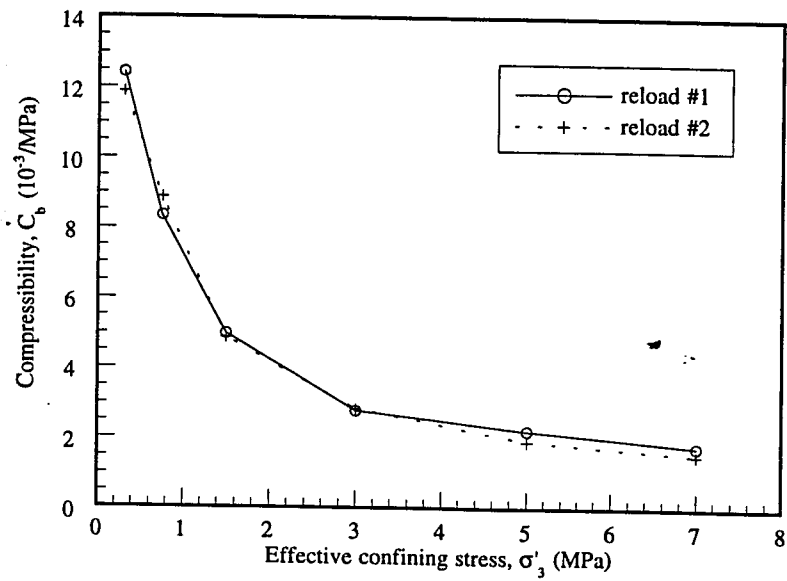


Fig 5.2.3 Test CU6: Isotropic Compressibility Reload #1 and #2

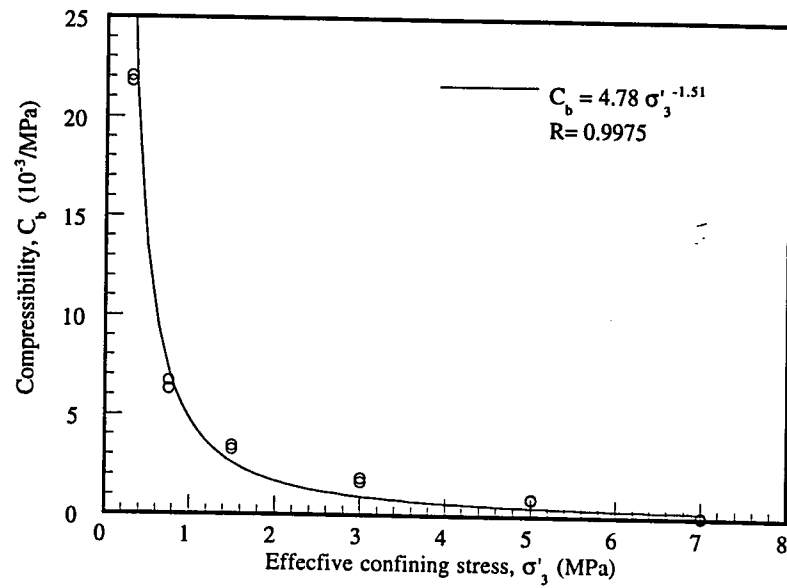


Fig 5.2.4 Test CU6: Isotropic Compressibility Unloading

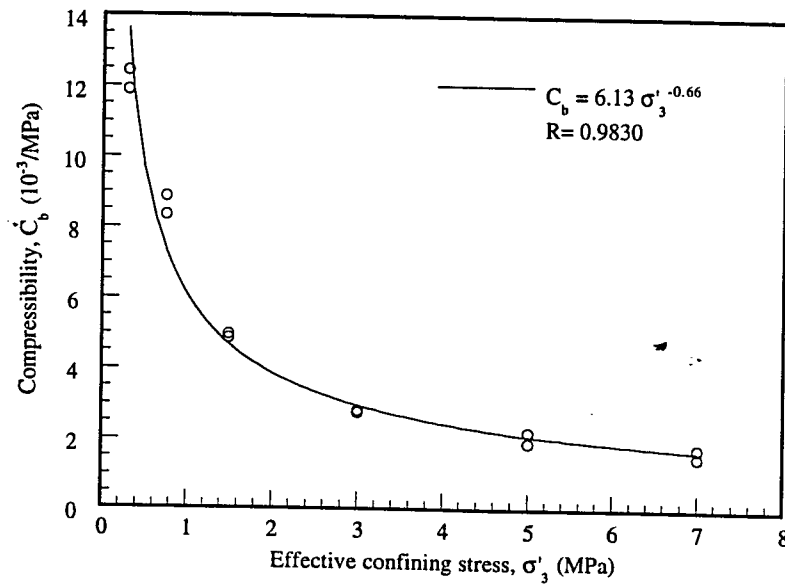


Fig 5.2.5 Test CU6: Isotropic Compressibility Reloading

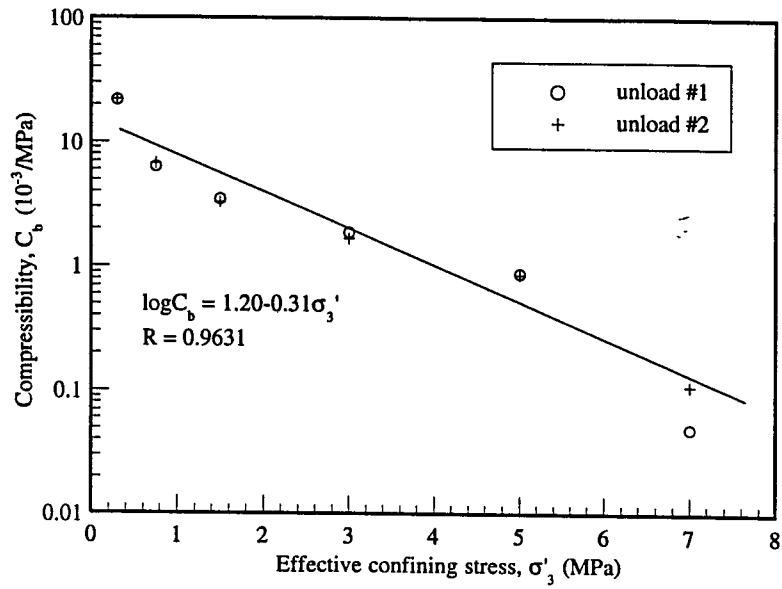


Fig 5.2.6 Test CU6: Isotropic Compressibility
Unloading #1 and #2 (Semilog scale)

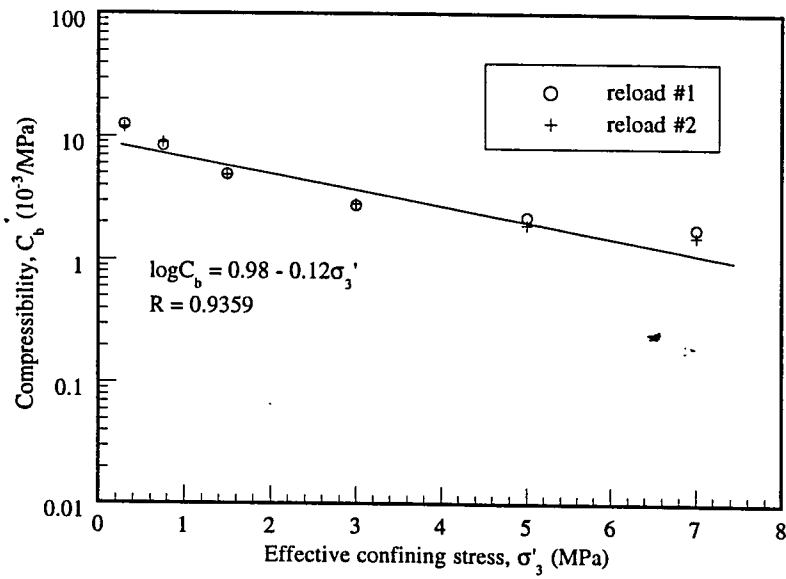


Fig 5.2.7 Test CU6: Isotropic Compressibility
Reloading #1 and #2 (Semilog Scale)

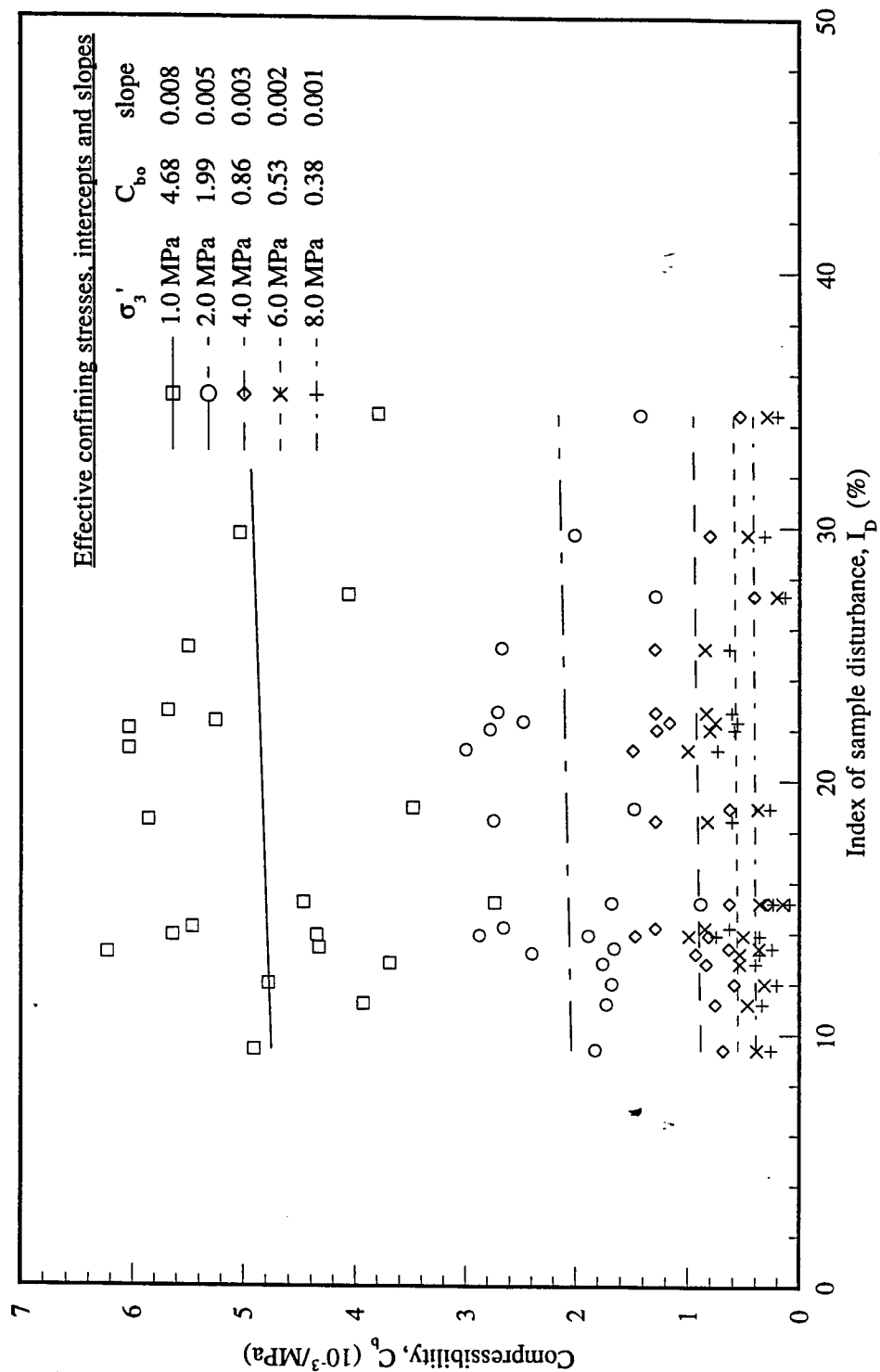


Fig 5.3.1 The Relationship Between Unloading Compressibility and Index of Sample Disturbance (Stress Range 1.0 to 8.0 MPa)

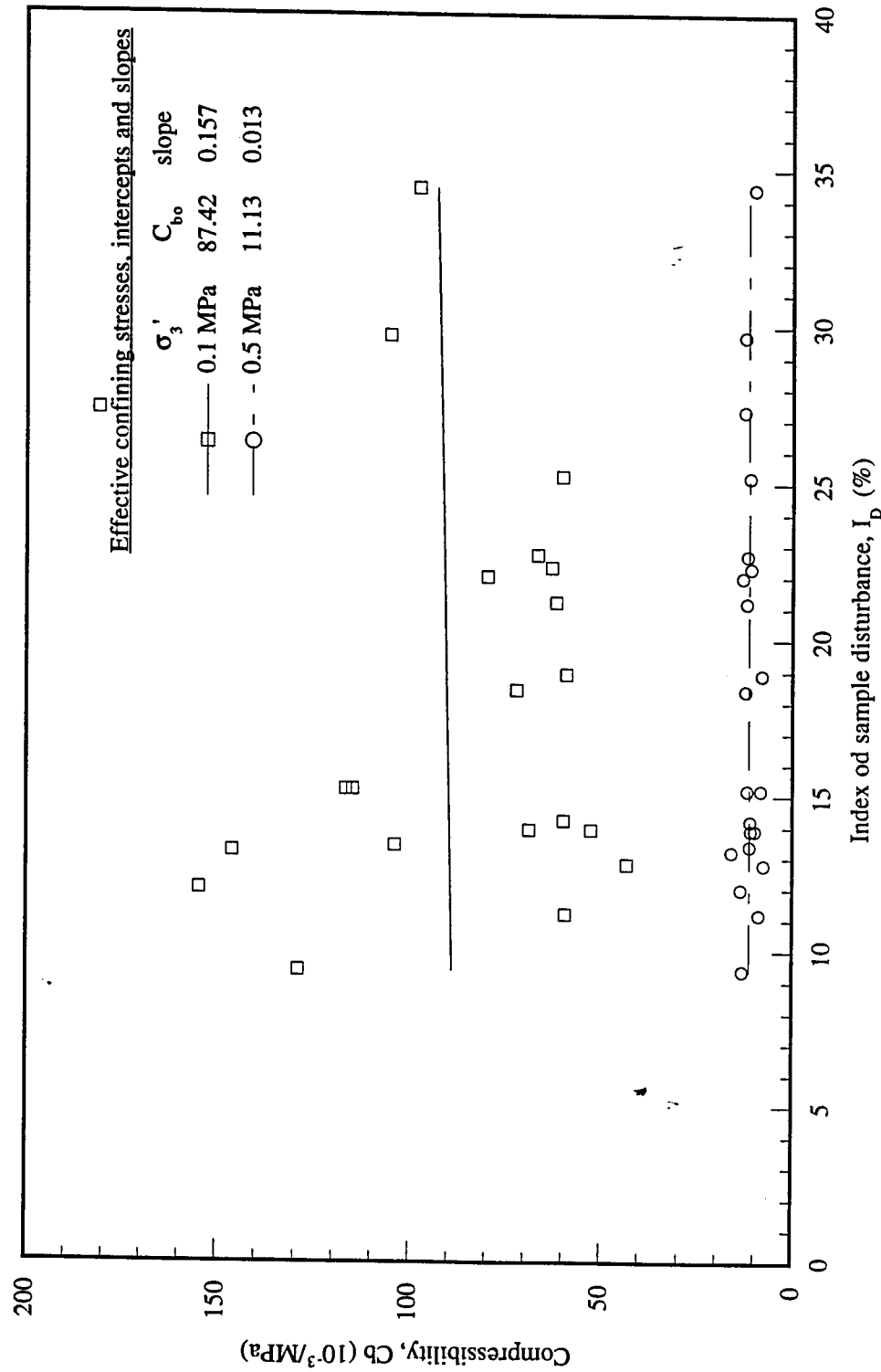


Fig 5.3.2 The Relationship Between Unloading Compressibility and Index of Sample Disturbance (Stress Range 0.1 to 0.5 MPa)

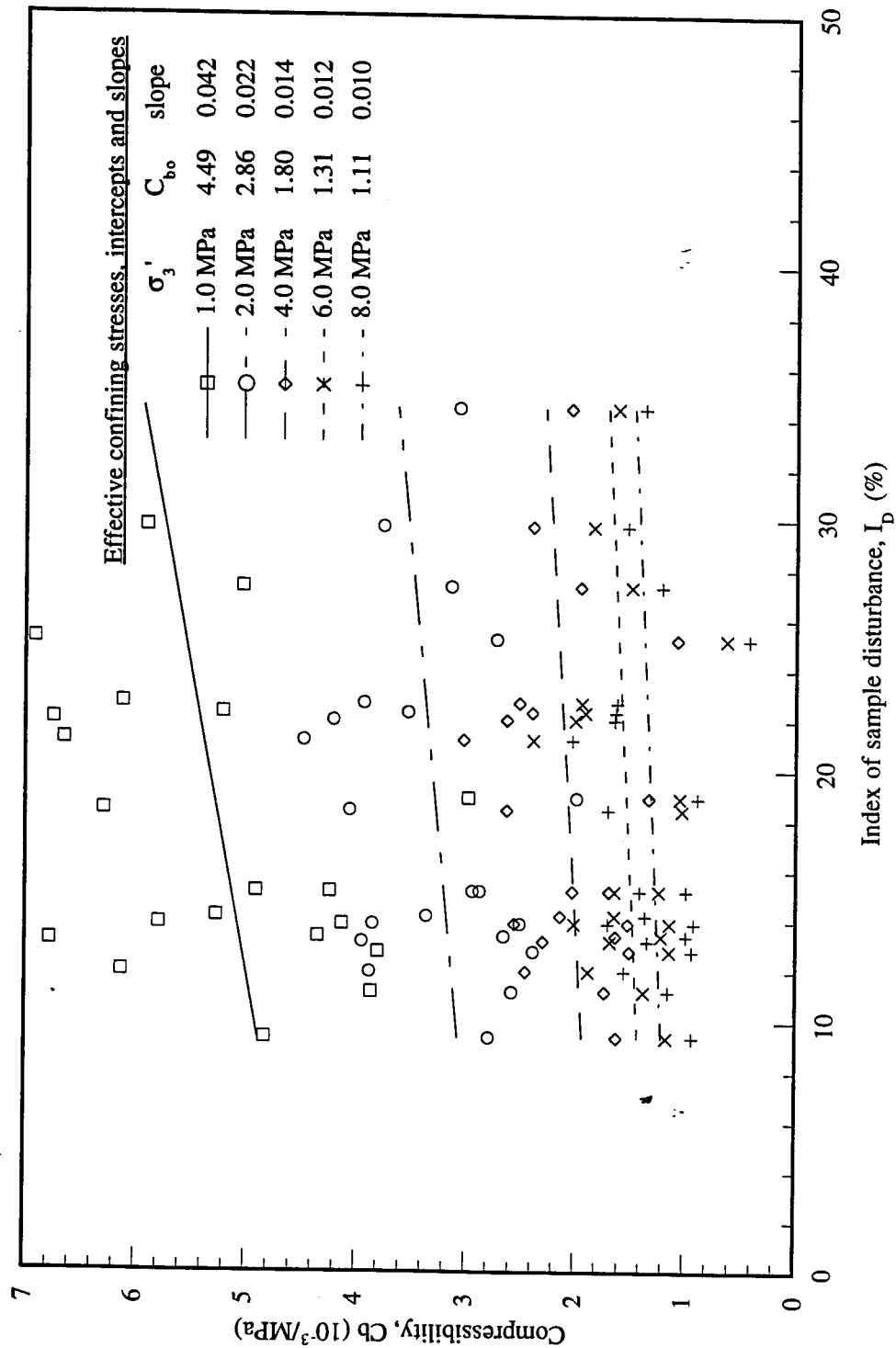


Fig 5.3.3 The Relationship Between Reloading Compressibility and Index of Sample Disturbance (Stress Range 1.0 to 8.0 MPa)

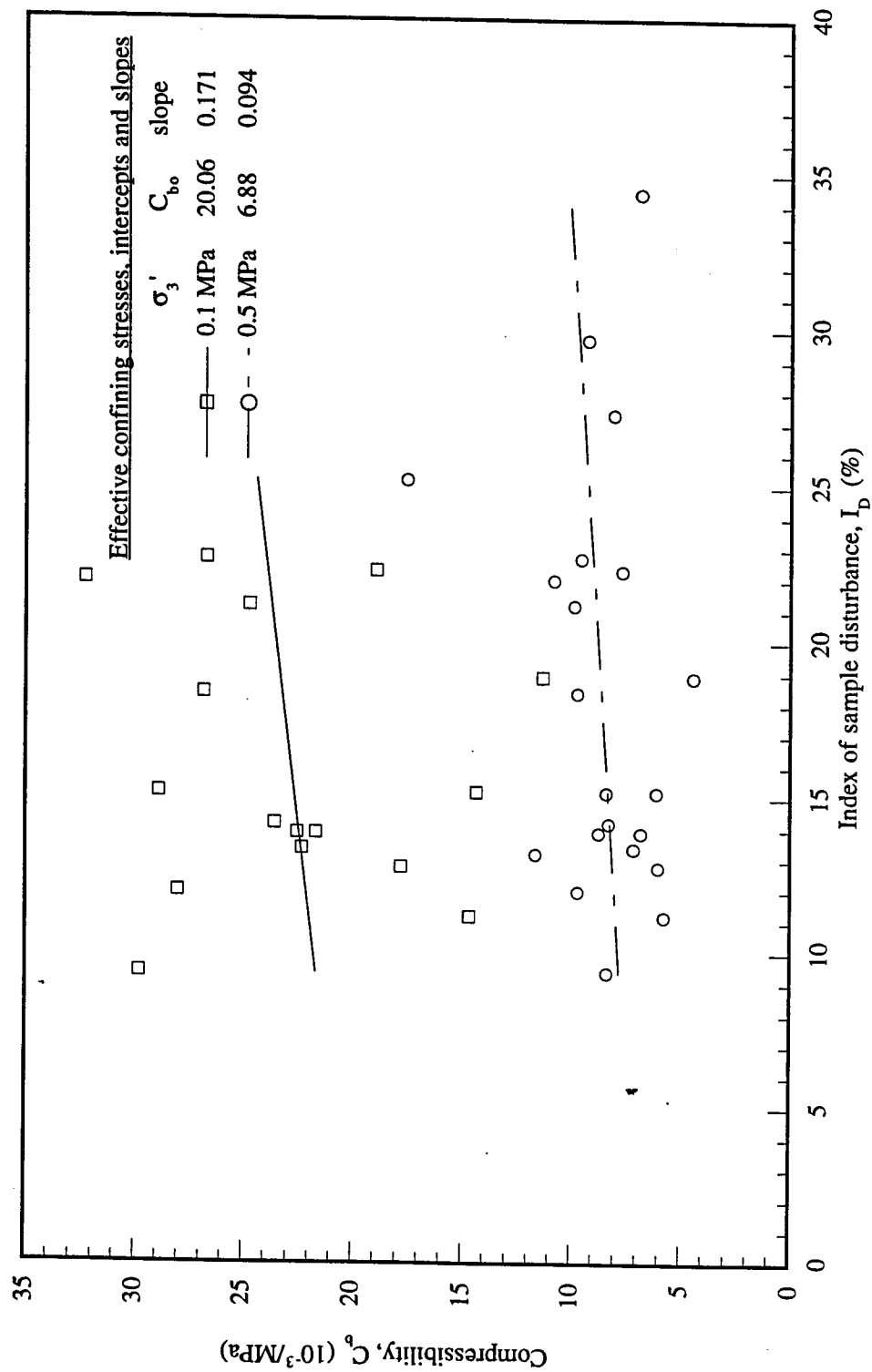


Fig 5.3.4 The Relationship Between Reloading Compressibility and Index of Sample Disturbance (Stress Range 0.1 to 0.5 MPa)

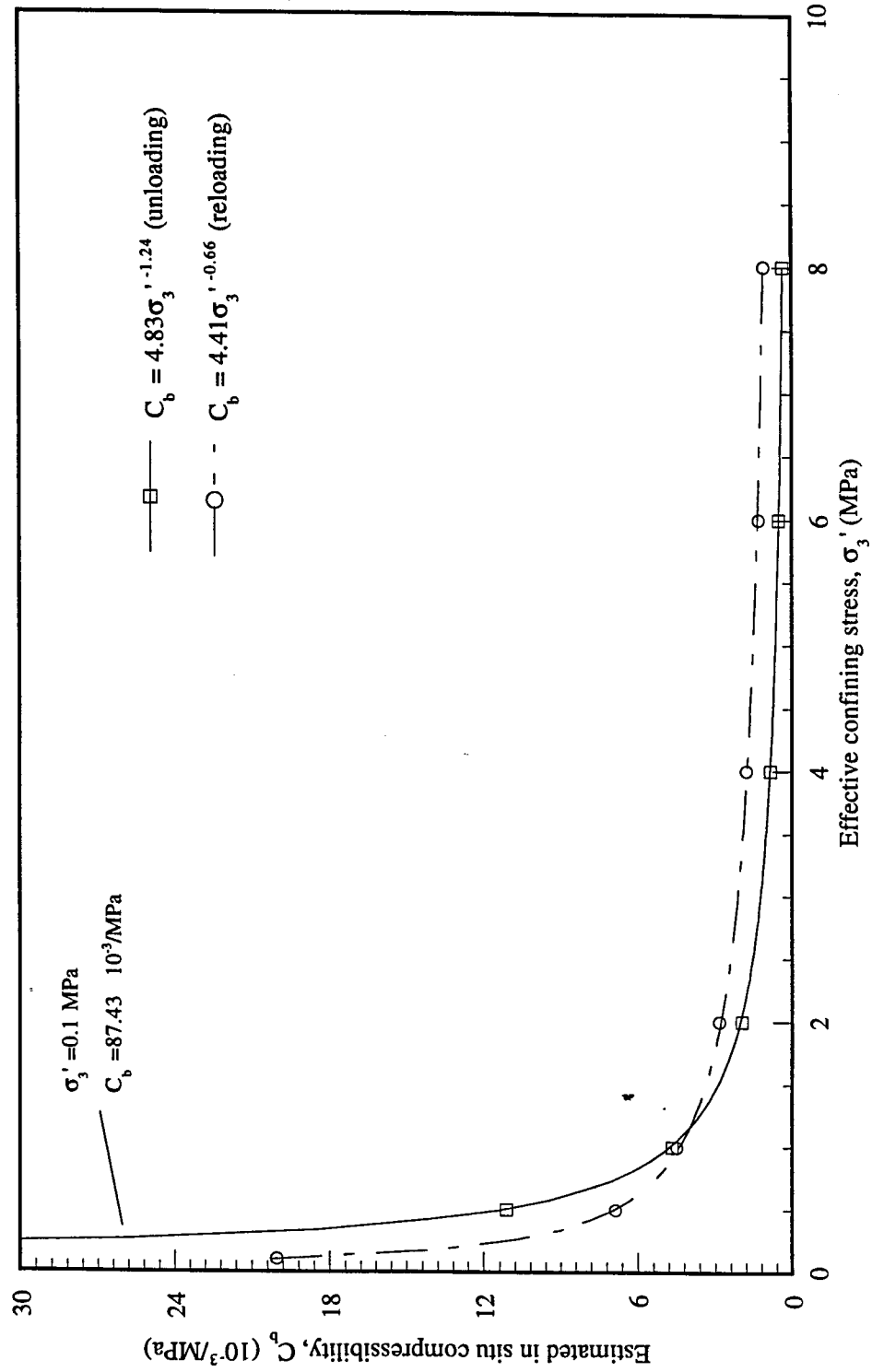


Fig 5.3.5 Estimated In Situ Isotropic Bulk Compressibility

Chapter 6

Stress-Strain Behavior

Of the Lower Grand Rapids Formation Oil Sands

6.1 Drained Triaxial Compression

Following stress path B (CID) in Fig 4.4.1, drained triaxial compression tests were performed with effective confining stresses of 0.1, 0.5, 1.0, 3.0 and 5.0 MPa. A total of six tests were conducted. Test CD4 was not successful because of leakage of the membrane during shear. Its result was excluded. The results of the five successful isotropically consolidated drained shear tests are summarized in Table 6.1.1 and the stress-strain-volume change curves are plotted in Fig. 6.1.1.

6.1.1 Stress-Strain Behavior

From Fig. 6.1.1, it is noted that the effective confining stress controls the stress-strain behavior, shear strength, volume change behavior and failure mode of the oil sands. At effective confining stresses of 3.0 MPa and lower, brittle failure behavior is observed, that is, the deviatoric stress decreases after the peak shear strength is reached. For brittle failure, the axial strain at peak strength is generally less than 2.5%, and the critical state (residual strength) is reached with an axial strain of about 6%. A ductile failure behavior occurs at the effective confining stress of 5.0 MPa. Bishop (1967) suggested a method to evaluate the brittleness of soils. As mentioned in Chapter 2, the brittleness index is expressed as

$$I_B = \frac{\tau_f \tau_r}{\tau_f} \quad (6.1.1)$$

If I_B is less than 30%, a soil can be treated as a rigid plastic material (Bishop 1971). From this point of view, $I_B=30\%$ can be used as the boundary to separate brittle behavior and ductile behavior. In the triaxial condition, τ_f would be $(\sigma_1 - \sigma_3)_f$ and τ_r is $(\sigma_1 - \sigma_3)_r$. The brittleness indexes for the five specimens tested are listed in Table 6.1.1. It is noted that, at the effective stress of 3.0 MPa or lower, I_B is about 50 % which indicates a significant brittle behavior at failure. At the effective confining stress of 5.0 MPa, I_B is only about 10%. The brittle behavior vanishes and instead, ductile behavior takes over. Since there is a considerable difference in the brittleness index which changes from 50% to 10% between the effective confining stresses of 3.0 and 5.0 MPa, the boundary of effective stress which separates brittle and ductile failure is in this stress range. Failure modes for the specimens tested are illustrated in Appendix C.3. It can be seen that most specimens failed along a shear band which was developed following a bedding plane or a defect. In Test CD5 ($\sigma_3' = 5$ MPa), the failure plane did not extend through the specimen even at an axial strain over 12%. It indicates that the axial deformation during shear was generally accommodated by bulging which resulted in a ductile stress-strain behavior.

Kosar (1989) conducted three drained triaxial compression tests on Athabasca McMurray Formation oil sands in which brittle failure was observed at an effective confining stress of 2.5 MPa or lower. Since the specimens used in Kosar's tests were almost entirely composed of quartz, grain breakage could not be significant at this effective confining stress (2.5 MPa). Compared with Agar's (1984) test result in which a high quality specimen was involved, and a much higher shear strength and brittle behavior were observed, Kosar (1989) pointed out that the ductile stress-strain relationship and contractive volume change behavior were due to sample disturbance.

When a disturbed oil sands specimen is subjected to a relatively high effective confining stress, the grain contacts may alter from an interlocking to a tangential configuration which reduces shear strength and results in a ductile stress-strain response. For the Athabasca Clearwater Formation oil sands, a brittle failure appeared to require an even lower effective confining stress. Among four tests performed by Kosar (1989), brittle behavior only occurred at the lowest effective stress of 1.0 MPa. Furthermore, for the Cold Lake Clearwater Formation, Location No. 2, oil sands (Kosar 1989) which has similar mineral composition and fine contents to the oil sands tested in this program, no brittle failure was observed at effective confining stresses of 1.0 MPa and higher. Wong et al (1993) showed similar test results of failure modes on Cold Lake Clearwater Formation oil sands. Six drained triaxial compression tests were conducted in the effective confining stress range between 0.6 and 12 MPa. Brittle failure occurred only in the tests with 0.6 and 0.7 MPa effective confining stresses which were the lowest effective confining stresses used.

For the oil sands tested and Clearwater Formation oil sands, both of which have weak mineral composition, brittle and ductile failure modes appear to be related to both shear mechanism in a test and the amount of sample disturbance. If the effective confining stress is low enough to allow particle rolling and sliding during shear, dilation occurs. As a result, brittle behavior will be the dominant mechanism. If the effective confining stress is high enough to partially suppress the particle rolling, less dilation or contraction occurs. Consequently, ductile behavior caused by grain crushing will be the dominant mechanism.

The deviatoric stress at failure increases with the increase in effective confining stress. Table 6.1.2 compares the test results for Athabasca McMurray Formation, Athabasca Clearwater Formation, Cold Lake Clearwater Formation and the Cold Lake Lower Grand Rapids Formation oil sands tested in this program. In the same effective confining stress range, the peak shear strengths of the Clearwater

Formation and the Grand Rapids Formation oil sands are much lower than that of Athabasca McMurray Formation oil sands. The internal friction angles for the oil sands from different formations are shown in Table 6.1.2. It can be seen that at an effective confining stress of 4.0 MPa, the internal friction angle of Athabasca McMurray Formation oil sand is 43° (Agar 1984), while the friction angle of the Cold Lake Clearwater Formation (Kosar 1989) and the Lower Grand Rapids Formation oil sands is about 28° . The difference in the internal friction angle is mainly due to the variation in mineral composition. McMurray Formation oil sands are comprised primarily of quartz grains, which are much stronger than the minerals in the other oil sands. Since sample disturbance strongly influences the strength of oil sands, the strength of the McMurray oil sands reported by Agar (1984) is significantly higher than that reported by Kosar (1989) due to different quality specimens being used in their testing programs. The shear strengths of Cold Lake Clearwater Formation and Athabasca Clearwater Formation oil sands are very similar to the strengths of the Lower Grand Rapids Formation oil sands tested in this program.

6.1.2 Volume Change Behavior

As well, the volume change which reflects dilatancy and contraction is also related to the effective confining stress. In Fig. 6.1.1, the positive change in volume means dilation and the negative change in volume means contraction. Generally, at the beginning of shear, all the tests show a slight contraction and then dilation or contraction with an increase in axial strain depending on the magnitude of the effective confining stress. Under a very low effective confining stress (0.1 MPa), the specimen dilates in shear. On the other hand, no dilation occurs, if a high confining stress is imposed on the specimen. At 5.0 MPa effective confining stress, contraction continues throughout shear. For confining stresses from 0.5 to 3.0 MPa, there is no significant volume change throughout shearing. This behavior indicates that grain

crushing is involved in the shearing process. After isotropic cyclic consolidation, the densities of the specimens are relatively high. The specimens should behave as other dense sands do, that is, dilation should dominate the volume change behavior during shear. The test results, however, indicate that the volume change behavior is highly dominated by the magnitude of the effective confining stress. A low effective confining stress allows dilation and a high effective confining stress results in contraction. This behavior occurs because of particle crushing during shearing. When the effective confining stress is small, the particles can roll and ride over one another during shear, which results in an increase in volume. In other words, dilation occurs. If the effective confining stress is high during shear, the particles can not overcome the confining stress to ride over one another. Consequently, the particles will be broken by the shear force. The particles become smaller with the shearing process and the broken particles fill the small voids which could not be filled before breakage. As a result, the volume of the specimen decreases and contraction occurs.

Carefully examining the individual volume change curves in the tests, it is found that, at effective confining stresses of 0.5 MPa and 1.0 MPa, the specimens first experienced contraction and then dilation whose magnitude, however, is relatively small. It implies that grain crushing has taken place during shear and has reduced the potential magnitude of dilation. Since the intensity of grain crushing at this effective confining stress is not large, dilation still plays a dominant role in the volume change behavior. It is also noted that there is almost no volume change throughout shearing at an effective confining stress of 3.0 MPa. In this case, the dilation caused by grain rolling and sliding and the contraction caused by grain crushing reach an equilibrium. Grain crushing tends to control the volume change behavior during shear. The effective confining stress of 3.0 MPa can be considered to be the 'break down' stress (Vesic and Clough 1968) for an oil sand with this grain size and mineralogy. As dilation and grain crushing are at a balance at this stress level, it may be better to call

this the 'balance' stress but Vesic and Clough's term will be used here. The test results presented by Wong et al (1993) show that the 'break down' stress for the Cold Lake Clearwater Formation oil sands is about 4.5 MPa. It appears that the mineral composition of the Clearwater Formation oil sands in Wong's test program is a little stronger than that of the oil sands tested.

6.1.3 Initial Tangent Modulus and Poisson's Ratio

The tangent modulus, E_t , analogous to the Young's modulus, E , is calculated for each specimen from its stress-strain relationship and volume change. Since the stress-strain curves in most of the tests have initial linear portions, the initial tangent modulus is taken as E_t . Because of dilatancy, Poisson's ratio, ν , can not always be measured during triaxial testing. It is valid only upon contraction at the beginning of shear before grain crushing or dilation occurs. Therefore, Poisson's ratio is determined using a small axial strain ($\epsilon_a=0.25\%$) before dilation significantly affects the sand volumetric strain behavior. The expressions for the tangent modulus, E_t , and the Poisson's ratio, ν , are given as follow.

$$E_t = \frac{(\sigma_1 - \sigma_3)_t}{\epsilon_a} \quad (6.1.2)$$

$$\nu = \frac{\epsilon_a - \epsilon_v}{2\epsilon_a} \quad (6.1.3)$$

Where $(\sigma_1 - \sigma_3)_t$ = tangent deviatoric stress, ϵ_a = axial strain and ϵ_v = volumetric strain at an axial strain of 0.25%.

The tangent modulus and Poisson's ratio values are shown in Table 6.1.1. The initial tangent modulus for the Cold Lake oil sands tested and the results from previous studies are presented in Figure 6.1.2. Among all the moduli for different oil

sands, the initial moduli of the Lower Grand Rapids Formation oil sands tested make up the lower boundary.

6.1.4 Axial and Volumetric Strains

Figures 6.1.3 and 6.1.4 show the axial strain and the volumetric strain respectively at peak and at residual shear strength with the effective confining stresses. The axial strain increases with an increase in effective confining stress, which reflects the transition from brittle to ductile behavior. It can be seen that the volumetric strain decreases with the increase in the effective confining stress. When the effective confining stress is smaller than 0.5 MPa, volumetric strains at peak and at residual are positive, that is, the volume increases in shear. When the effective confining stress is greater than 3.0 MPa, volumetric strains at peak and at residual are negative, that is, the volume decreases in shear. This behavior indicates that dilation is dominant at low confining stresses, while contraction from grain crushing is dominant at high confining stresses. When the confining stress is between 0.5 and 3.0 MPa, the volumetric strains at both peak and residual are very close to zero. It can be concluded that at a low effective confining stress, the Cold Lake Lower Grand Rapids Formation oil sands behave as ordinary dense sands similar to the Athabasca McMurray Formation oil sands. The particle rearrangement during shear causes the volume to increase, that is, dilation occurs. At a high effective confining stress, the Grand Rapids Formation oil sands behave as loose sand unlike the Athabasca McMurray Formation oil sands, because the high stress causes particle crushing during shear. The volume decreases, that is, contraction occurs. For comparison, the axial strains at failure measured on Athabasca McMurray Formations oil sands (Kosar 1989, and Agar 1984), Athabasca Clearwater Formations oil sands and Cold Lake Clearwater Formations oil sands (Kosar 1989, Wong et al 1993) are plotted together with the results from the oil sands tested in Fig 6.1.5. The axial strains at failure for the Grand

Rapids oil sands tested are similar to that for the Cold Lake Clearwater Formation oil sands at an effective confining stress below 3.0 MPa. Above 3.0 MPa, the axial strains at failure vary due to a ductile stress-strain response.

6.1.5 Failure Envelope

Figure 6.1.6 shows the stress path for each test and the $s' - t$ failure envelope for the CID tests. There is a good polynomial relation between t and s' expressed as

$$t = 0.0420 + 0.7896s' - 0.0435s'^2 \quad \text{MPa} \quad (6.1.4)$$

The curved failure envelope is typical for dense sands, whose curvature is mainly caused by grain crushing at the higher confining stresses. Figure 6.1.7 shows the shear strength for Athabasca McMurray Formation and Clearwater Formation oil sands, Cold Lake Clearwater Formation oil sands and the Lower Grand Rapids Formation oil sands tested. The failure envelope presented in the figure is that defined from this program's test results. It can be seen that the strengths of the Clearwater Formation from both Athabasca and Cold Lake are close to this envelope when the effective confining stress is below 5.0 MPa. It indicates that similarities do exist between the Clearwater oil sands and the oil sands tested because of the similar mineral composition and grain size distribution. As mentioned above, however, the initial tangent moduli are significantly different. The Clearwater Formation oil sands are stiffer than that of the oil sands tested. This may be attributed to the sample disturbance, overconsolidation stress applied, as well as to different geologic materials. The curved envelope indicates that the secant internal friction angle decreases with an increase in the effective confining stress. The values of the friction angles are listed in Table 6.1.2. The results achieved from previous studies and from this program are shown in Figure 6.1.8. In this figure, the effective confining stress is

normalized to the atmospheric pressure. The relationship between secant angle of internal friction and the effective confining stress can be expressed as

$$\phi' = \phi'_0 - \Delta\phi \log(\sigma'_3/p_a) \quad (6.1.5)$$

Where ϕ' = angle of internal friction; ϕ'_0 = intercept at $\log(\sigma'_3/p_a)=1$; σ'_3 = effective confining stress and p_a = atmospheric pressure. The solid line is the results from Agar (1984), which can fairly represent the strength of Athabasca McMurray Formation oil sands and the dashed line shows the results of the Cold Lake Lower Grand Rapids Formation oil sands tested. The Cold Lake and Athabasca Clearwater Formation oil sands tested by Kosar (1989) the Cold Lake Clearwater Formation oil sands tested by Wong et al (1993) are also presented in the figure. It is noted that the secant angle of internal friction of Clearwater Formation oil sands from both Athabasca and Cold Lake scatter just above the dashed line obtained from these test results. Since the grain size distribution and mineral compositions of these oil sands are similar to the oil sands tested, their shear strengths are also similar. This similarity indicates that the grain size distribution and the mineralogy control the shear strength after isotropic cyclic consolidation. Compared to the angles of internal friction of Athabasca McMurray Formation oil sands reported by Agar (1984), the slopes of the two lines are almost the same, the difference only being in the intercepts at $\log(\sigma'_3/p_a)=1$. The intercept of the Lower Grand Rapids Formation oil sands and Clearwater Formation oil sands is 60 degrees which is 12 degrees lower than that of Athabasca McMurray Formation oil sands. This much lower peak strength would appear to be due to grain crushing in the Cold Lake materials. The mineralogical differences of the sands in the different formations would have little effect on peak friction angle (Lambe and Whitman 1969). The degree of sample disturbance may also have an influence on this difference in strength but cyclic compressibility tests on the

Grand Rapids specimens generally recompressed the specimens close to their in situ void ratios.

6.1.6 Conclusions

Several conclusions can be reached from the test results.

1) In CID tests, the effective confining stress controls the stress-strain -volume change behavior of the Grand Rapids Formation oil sands tested. Ductile behavior in stress-strain response does not occur until the effective confining stress exceeds 3.0 MPa. The CID shear strength is a function of the effective confining stress. The $s' - t$ stress path curve which defines the failure envelope can be fit using the polynomial relationship:

$$t = 0.0420 + 0.7896s' - 0.0435s'^2 \quad \text{MPa}$$

2) At low effective confining stresses, below 0.5 MPa, the Grand Rapids oil sands behave as other dense sands similar to the McMurray oil sands. At effective confining stresses above 0.5 MPa, grain crushing during shear starts to affect the stress-strain-volume change behavior, unlike the McMurray oil sands. At stresses above 3.0 MPa, grain crushing dominates the behavior of Grand Rapids oil sands during shear. An effective confining stress of 3.0 MPa can be considered to be the 'break down' stress.

3) The shear strength of the Grand Rapids oil sands tested is significantly lower than that of Athabasca McMurray oil sands because of the weak mineral compositions. However, the shear strength of the oil sands tested is similar to that of Clearwater Formation oil sands from both Athabasca and Cold Lake due to the similar mineralogy and grain size distribution.

4) The tangent modulus of the oil sands is stress dependent increasing with an increase in the effective confining stress. The initial tangent moduli are relatively small. They make up the lower boundary of all the test results reported by Agar (1984), Kosar (1989) and Wong et al (1993). The Poisson's ratio varies from 0.14 to 0.42 with an average of 0.26.

5) The secant internal friction of the oil sands tested has a linear relationship with the effective confining stress normalized to the atmospheric pressure in a semi-log plot

$$\phi' = 59.86 - 19.41 \log(\sigma_3'/\text{pa})$$

The slope of the line is almost the same as that for Athabasca McMurray Formation oil sands reported by Agar (1984) but the intercept is smaller by 12 degrees. The secant internal friction angle of Clearwater Formation oil sands from both Athabasca and Cold Lake are very close to the test results for the Lower Grand Rapids Formation oil sands.

6.2 Undrained Triaxial Compression

Undrained triaxial compression tests following stress path C in Fig 4.4.1 were conducted after isotropic cyclic consolidation. A total of eight specimens were tested but test CU7 was not completed because of membrane leakage and test CU4 failed eccentrically and the results of these two tests are not plotted. From grain size analyses shown in Appendix C, specimens CU4 and CU5 may be identified as silty sands. Test CU5 is plotted with the other tests on sand specimens. The initial effective confining stresses during shear were 0.1, 0.5, 1.0, 3.0 and 5.0 MPa. The tests were strain controlled with a strain rate of 0.013 mm/min. Changes in pore pressure, axial strain

and vertical load were simultaneously recorded with a data logger, pressure and displacement transducers.

6.2.1 Stress-strain Relationship

The stress-strain relationships are plotted in Fig 6.2.1 with deviatoric stress, $\sigma_1 - \sigma_3$, against deviatoric strain, $\frac{2}{3}(\epsilon_1 - \epsilon_3)$.¹ The changes in pore pressures are also shown in this figure. The test results are summarized in Table 6.2.1.

At the beginning of shear, all specimens show a positive change in pore pressure, and then depart from each other with the increase in axial strain. It is obvious that the pore pressure change which shows the tendency for contraction or dilation is controlled by the initial effective confining stress. A high initial effective confining stress causes a positive change in pore pressure. The specimens are attempting to contract. However, a low initial effective confining stress results in a negative change in pore pressure. The specimens are attempting to dilate. The changes in pore pressure shown in Fig 6.2.1 match the volume change in the drained triaxial compression tests presented in Section 6.1. It can be noted that, when the initial effective confining stress is between 1.0 and 3.0 MPa, the changes in pore pressure are not significant. This behavior indicates that the specimens are not attempting to either dilate or contract. Significantly, the change in pore pressure is almost zero if the initial effective confining stress is about 3.0 MPa. This stress, therefore, verifies the 'break down' stress (Vesic and Clough, 1968) that was obtained in the CID tests which separated the volume change behaviors of contraction and dilation. The failure modes for the CIU tests are

¹. In undrained shear, $\epsilon_v = 0$,

$$\epsilon_v = \epsilon_1 + 2\epsilon_3 = 0$$

$$\epsilon_3 = -\frac{1}{2}\epsilon_1$$

$$\text{As a result, } \frac{2}{3}(\epsilon_1 - \epsilon_3) = \epsilon_1 = \epsilon_a$$

shown in Appendix C.3. A shear band failure generally occurred along a bedding plane or a defect. No significant bulging effect was observed.

6.2.2 Pore Pressure Parameter A

Fig 6.2.2 shows the variation of pore pressure parameter A with axial strain in each test, and the relationship between effective stress ratio and axial strain during the undrained triaxial compression tests. Pore pressure parameter A is defined as the ratio of the change in pore pressure to the change in total vertical stress (total major principle stress) in an undrained triaxial compression test (Appendix A.3). Since pore pressure is gradually induced in a test, the pore pressure parameter A varies with axial straining. Shear failure, in CIU tests, is defined as the stress condition at the maximum effective stress ratio.

The induced pore pressure at failure and pore pressure parameter A at failure also reflect the controlling effect of the initial effective confining stress. As shown in Fig 6.2.3 and 6.2.4, both u_f and A_f increase from negative to positive with an increase in the initial effective confining stress. It indicates that a low initial effective confining stress results in a negative change in pore pressure which represents the tendency for dilation, and a high initial effective stress results in a positive change in pore pressure which reflects the tendency for contraction. At 1.0 and 3.0 MPa, both u_f and A_f are about zero. An equilibrium is reached between positive and negative changes in pore pressure.

Fig 6.2.5 shows another interpretation of the change in pore pressure parameter A at failure. A_f decreases with an increase in the overconsolidation ratio which is defined as the ratio of the maximum preconsolidation stress to the initial effective confining stress. The variation of pore pressure parameter A in a triaxial test can give a clear indication of the stress history experienced by the soil tested (Skempton, 1954). As mentioned before, a specimen was usually cyclically consolidated to 9.5 MPa (some

lower than this) and then unloaded to the required effective confining stress to start shear. In this procedure, a specimen actually experiences a process of over consolidation. A high initial effective confining stress in shear results in a small OCR because of the relatively small decrement in effective confining stress from the maximum consolidation stress. A low initial effective confining stress in shear results in a large OCR.

Plewes (1987) examined the change in A_f with initial effective confining stress. It was found that the critical effective confining stress, where $A_f = 0$, for Athabasca McMurray Formation oil sands is between 5.0 and 6.0 MPa. Adopting this concept, the critical effective confining stress for the Lower Grand Rapids Formation oil sands is between 1.0 and 3.0 MPa.

6.2.3 Axial Strain at Failure

Fig 6.2.6 shows the relationship between axial strain at failure and the initial effective confining stress where failure is defined as the maximum effective stress ratio. It can be noted that axial strain at failure almost linearly increase with the increase in initial effective confining stress. It shows the significant role played by initial effective confining stress in the stress-strain behavior of the oil sands tested.

6.2.4 Stress Paths

The stress paths that the specimens experienced in the undrained triaxial compression tests are shown in Fig 6.2.7. The black dots in the figure are the maximum effective stress ratios which define the CIU failure envelope. The CID failure envelope defined by the drained triaxial compression tests is also shown in the figure. It can be seen that, the CIU failure envelope is not similar to the failure envelope obtained in the CID tests. At the effective confining stresses at and below 3.0 MPa, a stress path reaches the undrained failure envelope at the maximum effective stress ratio.

Afterwards, it approximately travels along the envelope towards the peak deviatoric stress, and then both s' and t drop gradually to the residual state. At an initial effective confining stress of 5.0 MPa (Test CU6), the stress path shows a significant difference from the others. It is highly curved because of the large positive pore pressure generated. Most specimens had not reached their steady states when the tests were stopped between 8% and 12% strain.

The stress paths shown in this figure differ significantly from that reported by Wong et al (1993) on the Cold Lake Clearwater Formation oil sands in which the stress paths experienced in the tests show typical dense sand behavior. That is, at the high effective confining stresses used in Wong's tests, the pore pressure generated in shear was high enough for a stress path to turn to the left to hit the steady state line.

Plewes (1987) observed similar stress paths in undrained triaxial compression tests on Athabasca McMurray Formation oil sands as Wong's et al (1993) on Clearwater Formation oil sands. Two tests conducted on Saline Creek oil sands achieved the same ultimate state after reaching the maximum effective stress ratio and traveling along the failure envelope.

Since grain crushing is involved in the process of shear, its magnitude inevitably has an impact on the stress-strain and pore pressure change behavior. The magnitude of grain crushing is a function of particle size, shape and hardness, void ratio, state of stress and stress path (Hardin 1985). The physical conditions of specimens used in both CID and CIU tests are similar, especially after isotropic cyclic consolidation. Therefore, the state of stress and the stress path are the most important factors governing the magnitude of grain crushing in these tests. As the stress path controls the state of stress in the process of shear, a different state of stress will be developed following a CID stress path where volume change takes place or following a CIU stress path where volume change cannot occur. The magnitude of grain crushing is consequently different

in the two different test procedures. It is hypothesized that less grain crushing occurs in the CIU tests which results in a higher shear strength.

Fig 6.2.8 shows the comparison of the stress paths between CID and CIU tests. It can be seen that, when the initial effective confining stress is lower or equal to 3.0 MPa, the CIU tests approximately follow the same stress paths as the CID tests. As shown in Table 6.1.1, the axial strains at failure in CID tests are less than 2.2 % within which most CIU tests reach their maximum effective stress ratio. The pore pressures in CIU tests within this range of axial strain are not significantly mobilized. With a further increase in axial strain, the pore pressure in CIU tests is gradually developed and the CIU stress paths depart from the CID stress paths. Since there is almost no pore pressure change in CIU tests when the initial effective confining stress is below or equal to 3.0 MPa, the CIU and CID stress paths are almost superposed. At 5.0 MPa, the stress paths experienced by CIU and CID tests are totally different because of the large pore pressure increase in the CIU test.

6.2.5 Effect of Fines (Silt) Content

It is realized that the grain size of specimens has a significant influence on the effective shear strength. Several specimens tested had only 50% sand sizes with most of the finer material being silt size. Tests CU5 and CU8 started with the same initial effective confining stress of 0.1 MPa. The deviatoric stress at failure in Test CU5 is more than twice that in Test CU8. Grain size analyses in Appendix C indicate that specimen CU5 contains about 50% silty fines (< 0.045 mm) while specimen CU8 contains only 3.1% silty fines. It is evident that fine grains tend to strengthen the test specimen. Compared with coarse grains, fine grains are difficult to break when subjected to shear stress (Lee and Farhoomand 1967, Hardin 1985). Consequently, the tendency for dilation with a silty sand specimen in undrained triaxial compression is much higher than that with a sand specimen. A negative change in pore pressure is

developed quickly during axial straining for fine grained specimens which, in turn, increases the undrained shear strength.

6.2.6 Steady State Behavior

Wong et al (1993) suggested that the critical state of the Cold Lake Clearwater Formation oil sands measured in undrained triaxial compression tests can be used as a reference property since it is unique for the oil sands. A critical state line is defined in $p' - q$ stress space. The critical state here is an ultimate state at a large strain at which pore pressure and deviatoric stress are constant. This state is, sometimes, termed as steady state (Poulos 1981).

The steady state parameters for the Lower Grand Rapids Formation oil sands tested are shown in Table 6.2.2. There does not exist an unique relationship in either $p' - q$ stress space or $e - p'$ space. Although the shear strength and pore pressure tend to become constant at a large strain in each test as shown in Fig 6.2.1 and 6.2.2, an unique ultimate state is not achieved in terms of stress path. In Fig 6.2.7, the stress paths with initial effective confining stresses of 0.1 and 0.5 MPa appear to reach their ultimate states. All the other stress paths continue to change with axial strain. Grain crushing may cause this behavior. The ultimate state may be reached at large strains after completion of grain crushing.

6.2.7 Conclusions

A few conclusions can be drawn from the undrained triaxial compression tests.

- 1) The specimens in the undrained triaxial compression tests (CIU) did not fall on the failure envelope defined by the drained triaxial compression tests (CID). The failure envelope following the CID stress path, therefore, does not represent the failure criteria for the CIU tests. A new failure envelope for the CIU tests was established, which is above the CID failure envelope. Grain crushing whose magnitude is controlled

mainly by state of stress and stress path was the reason for the variation in the failure criteria.

2) The pore pressure in the CIU tests varied in direction depending on the initial σ_3' . Below an initial σ_3' of 3 MPa, the pore pressures at large strains were negative while above 3 MPa they were positive. This difference in direction mirrored the direction of change in volume in the CID tests. Therefore, the CID test results and the CIU test results agreed with each other.

3) The change in pore pressure which reflects the tendency for dilation and contraction in shear is stress dependent and associated with the magnitude of grain crushing. The initial effective confining stress of 3.0 MPa is found to be the 'break down' stress at which there is almost no change in pore pressure throughout shearing. This agrees with the CID test results. Below the 'break down' stress, rotation of the grains caused by shear plays a dominant role in the failure mechanism. Above the 'break down' stress, grain crushing dominates the failure mechanism.

4) The stress paths experienced in the undrained triaxial compression tests resemble the drained triaxial compression test stress paths before failure occurs, provided the initial effective confining stress is less or equal to 3.0 MPa. Since there is almost no change in pore pressure at the 'break down' stress of 3.0 MPa, the CIU stress path is superposed on the CID stress path. At an initial effective confining stress above 3.0 MPa, the pore pressure increases dramatically with axial strain. In this case, the CIU stress path is totally different from the CID stress path.

5) Fine grains appear to increase the undrained shear strength of the oil sands. With a similar bulk density, less grain crushing is mobilized for a fine grained specimen than a coarse grained specimen. A more negative change in pore pressure at a low initial effective confining stress or a less positive change in pore pressure at a high initial effective confining stress is induced by an increase in the fines content. As a

result, the undrained shear strength of a fine grained specimen is higher than that of a coarse grained specimen.

6) There does not exist an unique steady state for the Lower Grand Rapids Formation oil sands based on the rest results. Further study may be needed to explore the behavior at steady state.

6.3 Drained Compression With J_1 Constant

6.3.1 Theory of "Pure Shear"

Drained compression with J_1 constant tests follow the stress path D in Figure 4.4.1, which is a simulation of "pure shear". The influence on oil sands behavior by a change in mean normal effective stress is eliminated in the process of shearing. Consequently, the oil sands behavior can be represented with two separate physical parameters, bulk modulus K and shear modulus G . In a strain controlled loading system, to conduct this test, increase the vertical stress σ_1' and simultaneously reduce the effective confining stress σ_3' by adjusting the cell pressure. The detailed calculations to determine the cell pressure required for maintaining J_1 constant is shown in Appendix A.

In the theory of elasticity, the relationship between deviatoric stress and deviatoric strain is

$$\epsilon'_{ij} = \frac{S_{ij}}{2G} \quad (6.3.1)$$

Where ϵ'_{ij} = strain deviator tensor, S_{ij} = stress deviator tensor and G = shear modulus. The state of stress is the sum of two components, deviatoric stress and hydrostatic stress, that is,

$$\sigma_{ij} = S_{ij} + \sigma''_{ij} \quad (6.3.2)$$

$$\text{or } S_{ij} = \sigma_{ij} - \sigma''_{ij} = \sigma_{ij} - \frac{1}{3} \sigma_{kk} \delta_{ij} \quad (6.3.3)$$

Where σ_{ij} = stress tensor, $\sigma''_{ij} = \frac{1}{3} \sigma_{kk} \delta_{ij}$ is the hydrostatic stress tensor, and σ_{kk} is the mean hydrostatic stress

$$\sigma_{kk} = \frac{1}{3} (\sigma_{11} + \sigma_{22} + \sigma_{33}) \quad (6.3.4)$$

In the triaxial test, only principal stresses exist in the vertical and horizontal planes. The state of stress can be expressed as

$$[\sigma_{ij}] = \begin{bmatrix} -\sigma_1 & 0 & 0 \\ 0 & -\sigma_3 & 0 \\ 0 & 0 & -\sigma_3 \end{bmatrix} \quad (6.3.5)$$

The hydrostatic stress is

$$\sigma = \frac{1}{3} \sigma_{kk} = -\frac{1}{3} (\sigma_1 + 2\sigma_3) \quad (6.3.6)$$

The deviatoric stress has the following form

$$[S_{ij}] = \begin{bmatrix} -\sigma_1 & 0 & 0 \\ 0 & -\sigma_3 & 0 \\ 0 & 0 & -\sigma_3 \end{bmatrix} + \frac{1}{3} \begin{bmatrix} \sigma_1 + 2\sigma_3 & 0 & 0 \\ 0 & \sigma_1 + 2\sigma_3 & 0 \\ 0 & 0 & \sigma_1 + 2\sigma_3 \end{bmatrix}$$

$$= \begin{bmatrix} -\frac{2}{3}(\sigma_1 - \sigma_3) & 0 & 0 \\ 0 & \frac{1}{3}(\sigma_1 - \sigma_3) & 0 \\ 0 & 0 & \frac{1}{3}(\sigma_1 - \sigma_3) \end{bmatrix} \quad (6.3.7)$$

Therefore, the deviatoric stresses in the principal directions are determined,

$$S_{11} = -\frac{2}{3}(\sigma_1 - \sigma_3) \quad \text{and}$$

$$S_{22} = S_{33} = \frac{1}{3}(\sigma_1 - \sigma_3) \quad (6.3.8)$$

Similarly, the deviatoric strain in major principal direction is

$$\epsilon_{11} = -\frac{2}{3}(\epsilon_1 - \epsilon_3) \quad (6.3.9)$$

Plotting the stress-strain relationship with $(\sigma_1 - \sigma_3)$ against $(\epsilon_1 - \epsilon_3)$ in the major principal direction, the slope of the curve is $2G$.

6.3.2 Test Results

A total of eight tests were conducted following this stress path. Specimens CP1 to CP3 were high in fines content. Their behavior differed from the other specimens and these test results are treated separately. The results from tests CP4 to CP8 are plotted in Figure 6.3.1 with deviatoric stress against deviatoric strain. The summary of the test results is shown in Table 6.3.1. Since shear modulus, G , is not a constant in each test, and decreases with the increase in deviatoric stress, only the initial shear modulus, G_i , is given in Table 6.3.1.

It is shown in Table 6.3.1 that, after isotropic cyclic consolidation, the bulk density of the specimens is close to the in situ condition. Specimens CP6, CP7 and

CP8 were trimmed from the core which dried out during storage. Their laboratory bulk density was only 1.67 to 1.72 Mg/m³ and the index of sample disturbance was as high as 30.9. The extraction tests cannot be used to evaluate the in situ physical parameters of the specimens because of loss of water content. The in situ physical parameters were determined from the core laboratory report provided by Mobil Oil Canada. Isotropic cyclic consolidation greatly improved the specimen quality. It can be seen that the bulk density of most specimens is about 2.0 Mg/m³ after consolidation.

In the J_1 constant test, the effective confining stress at failure is related to the initial effective confining stress, that is J_1 . Compared to one another, a high initial effective confining stress results in a relatively high effective confining stress at failure. Tests CP4 to CP8 were conducted with initial effective confining stress ranging from 0.17 to 5.0 MPa. Their effective confining stress at failure varied from 0.00 to 2.92 MPa respectively.

Figure 6.3.1 shows the stress-strain relationship and volume change behavior of the oil sands in J_1 constant tests. It is obvious that the shear strength of the oil sands tested is a function of J_1 . That is, high J_1 results in a relatively high shear strength and low J_1 causes a relatively low shear strength. The stiffness of the stress-strain relationship is also a function of J_1 . The initial shear modulus G_i increases with an increase in J_1 . It can also be noted that the volume change behavior is controlled by J_1 . Among the five test results presented in this figure, the volume change behavior varies from dilation to contraction with the increase in J_1 . When J_1 is below 3.0 MPa, dilation dominates. Above 3.0 MPa, contraction dominates. At $J_1 = 3.0$ MPa, there is almost no volume change throughout the test. The volume change characteristics of the oil sands indicate that a mean normal effective stress of 3.0 MPa has a special effect on the volume change behavior. It appears to be the break down stress beyond which grain crushing becomes a dominant mechanism during shearing. At this mean

effective stress, grains no longer ride over each other when a shear strain is imposed on a specimen. Instead, the shear stress breaks the grains.

The failure modes for the CIP tests are presented in Appendix C (Fig C.49). A shear band was developed in each specimen. A failure occurred along a shear plane which was inclined by 20° to 70° to the horizontal direction.

6.3.3 Comparison of the Geomechanical Behavior in CIP and CID Tests

In a CID test, the mobilized shear stress by shear straining is composed of both an increase in mean normal effective stress which creates a contractive component in volume change and an increase in deviatoric or shear stress whose influence on volume change depends on the effective confining stress. The total volume change is a joint effect generated by the changes in deviatoric stress and mean normal effective stress. Keeping J_1 constant during shear eliminates the influence on volume change behavior by an increase in the mean normal effective stress. The volumetric strain measured in the test is a pure effect caused by a change in deviatoric stress only.

To compare the results in a CIP test with that in a CID test, the stress-strain relationships following different stress paths for tests CD3 and CP4 are plotted together in Figure 6.3.2 with deviatoric stress against axial strain. The volume changes are also included. The initial effective confining stresses are 0.5 MPa in both tests. It can be seen that the shear strength in the CID test is higher than that in the CIP test. The first invariant J_1 is constant in the CIP test and the only change in the process of shear is the deviatoric stress. The mobilized shear strength, therefore, is a function of the deviatoric stress only. In the CID test, however, the process of shearing involves a change in both deviatoric stress and mean normal effective stress. As a result, consolidation occurs along with the increase in deviatoric stress due to the increase in J_1 . The specimen tends to densify during shearing. In other words, the average

effective confining stress gradually increases until the peak strength is reached. Consequently, the shear strength becomes high.

It is also noted that there is a significant difference in the volume change behavior between the CID and CIP tests. The oil sands are more dilative in a CIP test, and more contractive in a CID test. The difference between these two is that caused by an increase in mean normal effective stress which causes contraction. In other words, the effect of consolidation is also appearing during the process of shearing.

In Chapter 5, an expression for isotropic bulk compressibility is developed. Combining equations (5.2.1) and (5.2.2), it gives

$$C_b = \frac{d\varepsilon_v}{d\sigma_3'} = a \sigma_3'^b \quad (6.3.10)$$

Where, in this case, σ_3' is the mean principal effective stress.

The volume change caused by an increase in mean principal effective stress during shear can be assumed to be the same as the volume change in isotropic consolidation with an all round effective confining stress when these are equal. This volume change can be determined by integrating equation (6.3.10) between the initial effective confining stress and the mean normal effective stress at which the volume change is to be calculated.

$$\Delta\varepsilon_v = \int_{p_0}^{p_1} a \sigma_3'^b d\sigma_3' \quad (6.3.11)$$

Where $\Delta\varepsilon_v$ is the change in volumetric strain caused by the change in mean normal effective stress, and p_0 and p_1 are the integral limits. Ideally, the total volume change at a given axial strain in a CID test is the sum of volume change caused by an increase in mean normal effective stress and the volume change caused by an increase in deviatoric stress. The first component is the same as that in an isotropic

consolidation test in which there is no change in the deviatoric stress and the second component is the same as that in a CIP test in which there is no variation in the mean normal effective stress. In other words, the volumetric strain in a CID test minus the volumetric strain in a CIP test should be equal to the volumetric strain in an isotropic consolidation at the same stress level and strain level. At the same axial strain, the calculated volumetric strain with equation 6.3.11 and the measured volumetric strain are listed in Tables 6.3.2 and 6.3.3.

Table 6.3.2 shows the comparison between tests CD3 and CP4. In these two tests, the initial effective confining stress is 0.5 MPa. Because of the low effective confining stress, grain crushing cannot be significant in the volume change behavior during shear. The table shows that the calculated volumetric strain caused by a change in mean normal effective stress does not match the measured values in tests CD3 and CP4. At 0.5% axial strain, the calculated volumetric strain is greater than the measured. At 1.0% axial strain, the calculated is smaller than the measured. A few reasons may have caused the difference. The major reason is that although the test results are compared at the same strain level, they are not at the same stress level. Several minor reasons may also be influencing the comparisons. First of all, the grain size distributions of these two specimens are quite different. Specimen CP4 contains more fines passing the No. 200 (0.074 mm) sieve which influences the volume change behavior of the oil sands. Secondly, the specimens were taken from different depths at which the oil sands have different bulk compressibility as discussed in Chapter 5. Thirdly, the consolidation occurring during shear in the CID test is actually an anisotropic consolidation which is simplified to an isotropic consolidation by making use of the mean effective confining stress. This simplification may create some error which could be evaluated by performing some laboratory tests with artificial specimens in which the physical conditions are controlled. Finally, the measuring accuracy may influence the calculations.

Table 6.3.3 shows the comparison between tests CD5 and CP8. The tests were conducted with an initial effective confining stress of 5.0 MPa. The calculated $\Delta\epsilon_v$ at both 0.5% and 1.0% axial strain is smaller than the measured values. This variation between the calculated and the measured values, besides the reasons mentioned above, may also be attributed to the different grain crushing mechanism in shear. Obviously, the intensity of grain crushing in Test CP8 is weaker than that in Test CD5 because of the continuous decrease in effective confining stress to insure a constant J_1 . That is, the stress condition in CP8 causes less grain breakage.

6.3.4 Stress Paths

Figure 6.3.3 presents the real stress paths the specimens experienced. The failure envelope defined in the CID tests is also shown for the purpose of comparison. It can be seen that the stress paths are vertical straight lines in the $p' - q$ plot which indicate the J_1 constant stress condition throughout testing. To be consistent with the stress path plots in the other sections, the stress paths are also presented in a $s' - t$ plot in Figure 6.3.4. Both CID and CIP failure envelopes are shown in Figures 6.3.3 and 6.3.4. It can be seen that the CID failure envelope and CIP failure envelope are the same. The failure stress conditions of the CIP tests can be represented by the CID failure envelope.

6.3.5 Effect of Fines Content

The test results for specimens CP1 to CP3 which contain more than 50% grains passing the No. 200 (0.074 mm) sieve are plotted in Figure 6.3.5. Compared with tests CP4 to CP8, it is apparent that, with the same J_1 , the shear strength of oil sands containing more fines is higher than that containing less fines. Tests CP1 and CP7 were performed with a constant J_1 of about 3.0 MPa. The shear strength of Test CP1 is twice as high as that of Test CP7. The same results are achieved in tests CP3

and CP8 with $J_1 = 5.0$ MPa. It may be concluded that the fine grains increase the shear strength of the oil sands tested following the CIP stress path because the fines are less susceptible to breakage during shear (Hardin 1985). This is also the reason that tests CP4 and CP5 failed above the CID failure envelope with a higher shear strength. The fines contents in specimens CP4 and CP5 are somewhat higher than in specimens CP6 to CP8.

6.3.6 Conclusions

Five conclusions can be reached from the CIP test results:

- 1) The shear strength of the oil sands is dependent on J_1 . It increases with an increase in J_1 . The shear modulus of the oil sands with a constant J_1 is dependent on deviatoric stress. It decreases with the increase in the deviatoric stress. The shear modulus of the oil sands is also a function of J_1 . The initial shear modulus increases with an increase in J_1 .
- 2) The shear strength of the oil sands following a CIP stress path is smaller than that following a CID stress path when the initial stress conditions are the same because the CID stress path incorporates consolidation into the process of shear to further densify the specimen, while the CIP stress path only reflects the effect of pure shear.
- 3) Compared with the CID stress path, the volume change behavior is more dilative than contractive in CIP tests. The difference between the two volume changes measured in CID and CIP tests is the result of changes in mean effective normal stress.
- 4) The CID failure envelope can represent the failure criteria for the CIP tests.
- 5) Fines content appears to strengthen the oil sands during shear. Following the CIP stress path, the shear strength of oil sands containing more fine grains is greater than that containing less fine grains. Less breakage of the fine grains is probably the cause of this behavior.

6.4 Pore Pressure Injection

6.4.1 Introduction

A pore pressure injection test simulates steam or water injection in the process of in situ recovery or in hydraulic fracturing. The stress paths followed in the testing program are Paths E and F (CAI) in Fig 4.4.1. In this type of test, isotropic cyclic consolidation is first performed on a specimen to measure isotropic bulk compressibility and reconsolidate the specimen. After consolidation, an anisotropic stress condition is imposed on the specimen where the major principal effective stress in the vertical direction is greater than the minor principal effective stress in the horizontal direction. The specimen undergoes initial shear strains from the anisotropic stressing applied to create this initial effective stress ratio. The pore pressure is then increased through the back pressure reservoir by increasing the back pressure gradually. This increase in pore pressure reduces the major and minor principal effective stresses by the same amount which results in an increase in the effective stress ratio. The increase in effective stress ratio from pore pressure injection results in axial shear strain and volumetric strain.

Following these stress paths, a total of eight tests were conducted with initial effective stress ratios of 1.13, 1.25, 1.39, 1.50 and 1.63. The initial effective confining stress was 8.0 MPa. During the tests, a high initial effective stress ratio appeared to cause clogging of the drainage system. With a high initial effective stress ratio, the vertical stress, σ_1' , is much higher than the effective confining stress, σ_3' and the amount of compression in the vertical direction is greater than that in the horizontal direction. The permeability in the σ_1' direction usually is smaller than that in the σ_3' direction due to horizontal stratification. As well, the large vertical stress causes the filter paper between the specimen and the loading cap to be less permeable. If bitumen

intruded into the filter paper or porous stone, the influence of clogging would be larger. These conditions created difficulties in the pore pressure injection tests and a few tests were repeated because of these problems.

In test CI4, the pore pressure had not equalized with the back pressure at the beginning of the pore pressure injection. Before the back pressure was raised to 8.2 MPa, the pore pressure inside the specimen, recorded by the pore pressure transducer, had changed very little. A break through occurred at a back pressure of 8.2 MPa. Equilibrium of the pore pressure was finally achieved, and the specimen failed at an effective stress ratio of 6.0. A similar condition occurred in Test CI4A, but pore pressure equilibrium was never obtained because of clogging of the drainage system and the specimen did not reach shear failure. Test CI5 was not completed because the volume change measuring device started to leak at a back pressure of 6.6 MPa. These three test results are not included in the test analyses but their results are given in Table 6.4.1.

6.4.2 Test Procedure

Test specimens were obtained from the General Petroleum Sands Formation and trimmed from slabbed cores. The detailed specimen data are listed in Table 5.1.1 in Chapter 5. The oil sand cores used to prepare the test specimens had been stored for about five years since recovery without sealing or being frozen and as a result, they were desiccated. Without a casing confinement, the cores were in a condition of free expansion and had a high index of disturbance. Extraction test results showed that the water content for most specimens was less than 1%. Therefore, to determine the in situ physical parameters for the specimens, the information provided in core laboratory reports (Mobil Oil Canada Ltd, 1983) was used.

A new procedure was employed to saturate the specimens. After mounting a specimen into a triaxial cell, a 500 kPa cell pressure was applied to the specimen. A

water reservoir was connected to the bottom drainage port or pore pressure measuring port located at the base of the cell. The back pressure line connected to the loading cap of the specimen was left open to the atmosphere. A water pressure of about 350 kPa was then applied to the water reservoir to flush the specimen from the bottom to the top. Water was flushed through the specimen for about one to two hours to replace the air in the voids. A pore pressure parameter B test was then carried out to insure full saturation. The values of B listed in Table 6.4.1 generally indicate complete saturation following this procedure. After consolidation, most specimens had an index of sample disturbance of less than 10% with the bulk density varying between 1.97 and 2.03 Mg/m³.

Grain size distribution and mineral composition of the specimens were similar to the specimens used in the CID tests. The failure envelope defined in the CID tests was used to design the test procedures. Making use of this failure envelope, the failure stress conditions for each test were anticipated (Appendix A). Table 6.4.2 shows the initial stress conditions imposed on the specimens before testing and the failure stress conditions anticipated using the CID failure envelope. The initial effective confining stress was fixed at 8.0 MPa for all tests. The value, $t = \frac{\sigma_1 - \sigma_3}{2}$, was chosen at intervals of 0.5 MPa. Based on a designed initial effective stress ratio, the initial σ_1' was then determined. In a $s' - t$ plot, the stress path of a pore pressure injection test is a horizontal line parallel to the s' axis. Since t is a constant throughout a test, the value s' at failure can be estimated from the CID failure envelope as it is the intercept of the stress path and the envelope. The effective stress ratio at failure for each test was calculated as shown in Table 6.4.2 and the number and magnitude of pore pressure increments was then chosen to provide good strain control during the tests.

6.4.3 Stress Paths and Effective Stress Ratios at Shear Failure

Figure 6.4.1 shows the stress paths that specimens experienced in the CAI tests. Each test started with the initial stress condition given in Table 6.4.2. An increase in pore pressure during a test reduces both major and minor principal effective stresses by the same amount. In a $s' - t$ plot, s' keeps dropping with a constant t until failure occurs. It is obvious that, in Figure 6.4.1, the failure points converge close to the CID failure envelope. The stress conditions at failure in the tests were very close to the anticipated stress conditions shown in Table 6.4.2. The test results are summarized in Table 6.4.1. For most of the tests, the value s' at failure was only slightly smaller than that anticipated. The failure envelope for the CAI tests is also shown in Figure 6.4.1 and is slightly above the CID failure envelope. For practical purposes the CID failure envelope can represent the CAI failure criteria.

In a pore pressure injection test, the deviatoric stress is a constant. A change in stress condition during the test is best represented by a change in effective stress ratio. Because of the curved failure envelope the effective stress ratio at failure is controlled by the initial effective stress ratio. Figure 6.4.2 shows the change in effective stress ratio during pore pressure injection in Tests CI1 to CI5A. The stress ratios at the effective confining stress of 8.0 MPa were the initial effective stress ratios. During a pore pressure injection test, the effective confining stress decreases and the effective stress ratio increases gradually until shear failure occurs. Test CI1 had the lowest initial effective stress ratio, and failed at the highest effective stress ratio. A small initial effective stress ratio equates to a low deviatoric stress in a test. In other words, the difference between the initial major and the initial minor principal stresses is small. In this case, the magnitude of the pore pressure at failure must be very close to the initial minor principal stress for shear failure to be possible. When the major principal stress is almost equal to the minor principal stress initially, pore pressure

injection results mainly in isotropic unloading and the specimen never reaches shear failure.

6.4.4 Axial Strain and Volume Change Behavior

The axial strain at failure in a pore pressure injection test is associated with the magnitude of the deviatoric stress in the test. The relationship between deviatoric stress and axial strain at failure is shown in Figure 6.4.3. It is noted that a high deviatoric stress requires a large axial strain to fail the specimen.

At the beginning of a pore pressure injection test, an axial extension occurs together with a lateral expansion. With the increase in pore pressure, the axial extension continues until the stress ratio reaches a certain value at which axial compression begins. The change in axial strain with the effective stress ratio is plotted in Figure 6.4.4a in which a negative axial strain stands for axial extension and a positive axial strain represents axial compression. The full stress-strain curves are plotted in Figure 6.4.4b. A negative strain occurred in all the tests but the magnitude in each test was significantly different. The magnitude appeared to be governed by the initial effective stress ratio. Generally, a low initial effective stress ratio causes more negative axial strain.

In each test, the effective stress ratio at which extension axial strain ended and axial compression started was different from one another. This effective stress ratio is termed as 'compression stress ratio', denoted by $(\sigma_1'/\sigma_3')_c$. Its value is not a constant but a function of the initial effective stress ratio as shown in Figure 6.4.5. If the test starts with a low initial effective stress ratio, the axial compression will begin at a high effective stress ratio. The compression stress ratio in the tests ranges from 2 to 5. Wong et al (1993) observed similar volume change behavior in the Cold Lake Clearwater Formation oil sands with axial compression starting at a stress level above 3.

Figure 6.4.6 shows the relationship between stress ratio and volumetric strain in the pore pressure injection tests. All specimens dilated right from the beginning of the tests. The tests were conducted with different initial effective stress ratios as shown at $\epsilon_v=0$ in this figure. It can be seen that the volumetric strain increases with the increase in effective stress ratio but the rate of increase varies significantly in different tests. If a test starts with a high initial effective stress ratio, the volume will expand quickly with the increase in effective stress ratio. At the same effective stress ratio the volume expansion of a specimen with a high initial effective stress ratio is greater than that of a specimen with a small initial effective stress ratio.

Figure 6.4.7 shows the relationship between volumetric strain and axial strain in the pore pressure injection tests. Tests CI1 to CI3 were conducted with lower initial effective stress ratios. Their volumetric expansions were obviously smaller than those in tests CI4B and CI5A performed with higher initial effective stress ratios. Volumetric strain consists of two components; the axial deformation and the lateral deformation. During a pore pressure injection test, lateral expansion always occurs, but the axial deformation is either extension or compression, depending on the stress condition. The volume increases in tests CI1 to CI3 were joint effects from both axial extension and lateral expansion. In tests CI4B and CI5A, the volume increases caused by axial extension were relatively small. Lateral expansion dominated the volume increase behavior from the beginning of the tests. It is evident that the volume increase in a pore pressure injection test with a high initial effective stress ratio is mainly caused by lateral expansion.

6.4.5 Shear Behavior

A shear plane was clearly developed in each pore pressure injection test. Usually, the axial deformation was not significant in a test until the failure stress ratio was reached. As these were stress controlled tests, it was not possible to continue the

tests past shear failure as the specimens exhibited brittle shear behavior. When the effective stress ratio approached the failure effective stress ratio, the rate of deformation increased rapidly and then the specimens collapsed suddenly. The failure angle between the rupture surface and the major principal stress varied between 67 and 75 degrees which gives a secant internal friction angle, ϕ' , of about 50°.

Applying Mohr - Coulomb failure criterion to the failure stress condition, the secant internal friction angle in each test is determined. The values are listed in Table 6.4.1. It varies between 45° and 66° which coincides with the observed values. The secant internal friction angle, ϕ' , at failure is plotted in Figure 6.4.8 against the effective confining stress, σ_3' , at failure which is normalized to the atmospheric pressure, p_a . The secant internal friction angles obtained in the CID tests are also presented in this figure for comparison. The friction angles in the pore pressure injection tests are slightly larger than that in the CID tests, especially at larger confining stresses.

6.4.5 Conclusions

A few conclusions can be reached from the pore pressure injection tests.

1) The initial effective stress ratios which represent in situ stress conditions control the stress-strain behavior of the Cold Lake Lower Grand Rapids Formation oil sands in the pore pressure injection tests. The deviatoric stress which can be represented by the initial effective stress ratio dominates the axial strain at failure. A high deviatoric stress causes a large positive axial strain at failure.

2) The failure envelope for the CAI tests is slightly above the CID failure envelope indicating that the CAI measured shear strengths are greater.

3) The axial deformation starts with an axial extension at the beginning of a pore pressure injection test. Axial compression does not occur until the compression stress ratio is reached. The compression stress ratio decreases with an increase in the

initial stress ratio and ranged from 2 to 5. A lower initial effective stress ratio causes more axial extension.

4) All CAI test specimens increased in volume right from the beginning of the tests regardless of the initial effective stress ratio. The larger the initial effective stress ratio, the greater the increase in volume.

5) The volume change in a pore pressure injection test is a joint effect of axial and lateral deformation. At a low initial effective stress ratio the volume expansion results from both axial extension and lateral expansion at the beginning of the pore pressure injection, and then the lateral expansion controls the volume change after the compression stress ratio is reached. At a high initial effective stress ratio, the lateral expansion dominates the volume change behavior throughout the test with only a small amount of axial extension at the beginning of the test.

6) The secant internal friction angle at failure is a function of the effective confining stress at failure. It decreases with an increase in the effective confining stress. The friction angles in the pore pressure injection tests are slightly larger than those in the CID tests. It may indicate that the shear strength behavior of the oil sands is somewhat stress path dependent.

6.5 Grain Crushing

6.5.1 Introduction

Grain size analysis by sieving has been performed on most of the specimens before and after triaxial testing. The results are summarized in Table 6.5.1. It can be seen in the table that grain crushing occurred in all tests conducted. The table shows the variation of the effective grain size, d_{10} , and the percent passing the No. 200 and the No. 325 sieves before and after the tests. All the tests generated consistent results in that the effective grain size, d_{10} , becomes smaller and the content of fine grains increases. The grain size

distribution curves are presented in Appendix C and display clear evidence of grain crushing.

Grain crushing occurred not only when a deviatoric stress condition was imposed on a specimen, but also when a specimen was subjected to an isotropic stress condition. Grain crushing is generally controlled by the following parameters (Hardin 1985): a) grain size distribution; b) particle shape; c) state of effective stress; d) effective stress path; e) void ratio; f) particle mineralogy or hardness; and g) the presence and absence of water. Examining the factors above, The particle mineralogy, effective stress path and the grain size of the oil sands appear to be the most important parameters that dominated the grain crushing behavior in this testing program.

6.5.2 Influence of Particle Mineralogy

As discussed in Chapter 3, the Lower Grand Rapids Formation oil sands specimens used in this testing program are mainly feldspathic litharenite sands. The grain composition is about 50% quartz, 25% feldspar and 25% rock fragments. The feldspar grains and rock fragments are susceptible to shear induced grain crushing and would appear to be the main reason for the large amount of grain crushing which occurred during the tests.

6.5.3 Influence of Stress Path

As discussed previously, all the specimens had been isotropically and cyclically consolidated up to 9.5 MPa before another stress path was applied. A bulk density and a void ratio close to the in situ values were achieved by the isotropic cyclic consolidation. As the grain mineralogy of all the specimens is approximately the same, the test parameter having the most significant impact on grain crushing can be limited to the stress path followed. Figure 6.5.1 compares the grain size distributions in Tests CD1 and CP6 which followed different stress paths. Test CP6 was conducted with an initial effective confining stress of 1.0 MPa and Test CD1 had an effective confining stress slightly above 1.0 MPa.

The total breakage B_t (Hardin 1985) which is the area enclosed by the grain size distribution curves before and after the test can be determined from the figure. It is obvious that the CID stress path creates more grain breakage than the CIP stress path. Since J_1 is constant throughout the test in Test CP6, the stress mobilized by increasing axial strain only changes the deviatoric stress. Therefore, the grain crushing is the direct result of the deviatoric shear stress acting on the specimen. However, the volume change behavior shown in Figure 6.3.1 illustrates that this specimen dilates under this stress condition and implies that the grain crushing is not the dominant mechanism in shear. The grains roll and slide over one another to cause the increase in volume. In Test CD1, the increase in vertical stress results in an increase in both deviatoric stress and mean effective confining stress. Although the grain breakage has not dominated the mechanism of shear, it certainly has higher intensity than in Test CP6. Although the grain size distributions in Test CD1 and Test CP6 are not exactly the same they are similar enough to make the above comparison. The influence from grain size distribution will be discussed later.

Figure 6.5.2 shows the grain size analyses for Tests CU1 and CU8 which were conducted following the same CIU stress path with an initial effective confining stress of 1.0 and 0.1 MPa respectively. The total breakage in CU8 is obviously greater than that in Test CU1. Carefully examining the stress-strain relationships and changes in pore pressure in these two tests presented in Section 6.2, the result of grain crushing can be expected. Since the initial effective confining stress in Test CU8 was only 0.1 MPa, the specimen tended to dilate during shear and a negative pore pressure gradually built up. As a result, the effective confining stress increased. With an initial effective confining stress of 1.0 MPa, Test CU1 generated a positive change in pore pressure which showed the tendency for contraction. Specimen CU8 failed at an effective confining stress of 1.23 MPa and specimen CU1 failed at an effective confining stress of 0.9 MPa. The higher effective confining stress that developed during shearing resulted in a higher magnitude of grain breakage.

6.5.4 Influence of Grain Size

Grain size distribution has a significant influence on grain crushing. Generally, coarse grains are more breakable and fine grains are less breakable when subjected to the same stress conditions. This behavior is clearly visualized from the grain size distribution curves presented in Appendix C. Tests CP3 and CP8 were both performed with an initial effective confining stress of 5.0 MPa following a CIP stress path. As shown in Fig 6.5.3, the total breakage in Test CP8 which had 7.3% fines passing the No. 200 sieve before testing is much greater than that in Test CP3 which had more than 87% fines passing the No. 200 sieve before testing. Tests CU5 and CU8 were conducted with the same initial effective confining stress of 0.1 MPa following a CIU stress path. Again, as shown in Fig 6.5.4, Test CU8 consisting of less fine grains has more grain crushing than Test CU5.

In CIU tests, a low initial effective confining stress causes a negative change in pore pressure which increases the effective confining stress and the magnitude of grain crushing during shear. A high initial effective confining stress creates a positive change in pore pressure which decreases the effective confining stress and the magnitude of grain crushing during shear. When the initial effective confining stress is 3.0 MPa, the change in pore pressure is almost zero during shear. The positive change caused by grain breakage and the negative change caused by dilation reach an equilibrium and grain crushing starts to play the dominant role in the failure mechanism during shear. As discussed in previous sections, the effective confining stress of 3.0 MPa is determined to be the 'break down' stress for the Cold Lake Lower Grand Rapids Formation oil sands.

Because all the specimens experienced the same isotropic cyclic consolidation, when the grain size analyses are compared with one another, the grain crushing caused by the isotropic consolidation does not influence the comparison. For an individual test, especially with a low effective confining stress, for instance, Test CP5 ($\sigma_3' = 0.17$ MPa), it

is difficult to know whether the grain crushing was a result of shearing or isotropic consolidation.

In the tests following a CAI stress path, each test started with a different stress ratio but they did not exhibit a significant difference in the amount of grain crushing. It suggests that pore pressure injection may not cause serious grain crushing and the grain breakage occurring in these tests is possibly the effect of isotropic cyclic consolidation.

6.5.5 Conclusions

It can be concluded that,

- 1) Grain crushing occurs in all the tests following different stress paths. Since the Lower Grand Rapids Formation oil sands consist of more weak minerals than the Athabasca McMurray Formation oil sands, the grains are easier to break when subjected to an isotropic stress change or a deviatoric stress change.
- 2) The larger amount of feldspar grains and rock fragments in the oil sand specimens are susceptible to shear induced grain crushing and are the main reason for the grain crushing which occurred.
- 3) The magnitude of the effective confining stress controls the grain crushing behavior. The effective confining stress of 3.0 MPa is the 'break down' stress, below which dilatancy dominates the stress-strain and volume change behavior and above which grain crushing becomes the main mechanism.
- 4) Considering that the grain size distribution and mineralogy of all specimens are similar, the CID stress path creates more grain breakage than the CIP stress path. In the CIU test, the change in pore pressure during shear influences the magnitude of grain crushing. A positive change in pore pressure reduces the magnitude and a negative change in pore pressure increases the magnitude.
- 5) Following the same stress path, coarse grains appear to be more vulnerable to breakage than fine grains.

6.6 Application of a Hyperbolic Model To the Test Results

A hyperbolic model (Duncan and Chang 1970) is widely used as a stress-strain curve fitting technique in modeling soil behavior. The principal advantage of the model is its generality (Duncan 1981). It is easy to apply and suitable for a variety of soil types. It can also be used to model the stress-strain behavior of soils following different stress paths or with different physical conditions.

Agar (1984) applied the hyperbolic model to Athabasca oil sands. It was concluded that the model can be used to simulate the non-linear stress-strain relationship of Athabasca oil sands up to 80 percent of the peak deviatoric stress level. Settari et al (1991) employed a generalized hyperbolic model to fit the test results of Athabasca oil sands. The major difference of the generalized model from the standard hyperbolic model is the adjustment of the exponent in the shape function. There was a good match with the test data up to the peak strength.

Since the hyperbolic model is a curve fitting technique and has nothing to do with the failure mechanism and particle interaction, it can not represent the volume change behavior, especially when dilation and grain crushing are encountered. As well, the model is only suitable for simulating strain hardening behavior, in most cases, the stress-strain behavior prior to failure, due to the nature of the hyperbola used in curve fitting. Strain weakening behavior after peak can not be modeled. Therefore, in the application of this model to the test results, the volume change behavior will not be discussed and the curve fitting will be based mainly on the test data before peak and also on a small portion of post peak behavior provided strain weakening is not significant.

The hyperbolic curve fits for stress paths CID, CIU and CIP are plotted in Figures 6.6.1 to 6.6.3 respectively. The model parameters are summarized in Tables

6.6.1 to 6.6.3. In the CID tests, the stress-strain curves with effective confining stresses of 1.0 and 3.0 MPa do not agree very well with the model. The results of tests conducted at effective confining stresses of 0.1, 0.5 and 5.0 MPa have a good match with the model. Based on these tests, the tangent modulus of the Lower Grand Rapids Formation oil sands following a CID stress path is evaluated and expressed as

$$E_t = \left(1 - \frac{0.66(1 - \sin\phi')(\sigma_1 - \sigma_3)}{2\sigma_3' \sin\phi'}\right)^2 1092 \text{ pa} \left(\frac{\sigma_3'}{\text{pa}}\right)^{0.4219} \quad (6.6.1)$$

Where E_t tangent modulus (MPa)

ϕ' secant internal effective friction angle

σ_3' effective confining stress (MPa)

pa atmospheric pressure, generally 0.1 MPa

As indicated in section 6.1, the secant internal effective friction angle, ϕ' , is not a constant, but a function of effective confining stress, σ_3' , expressed as

$$\phi' = 59.86 - 19.41 \log\left(\frac{\sigma_3'}{\text{pa}}\right) \quad (6.6.2)$$

Combining equations (6.6.1) and (6.6.2), the tangent moduli of the oil sands tested can be determined and are shown in Table 6.6.1 with the measured values.

In the CIU tests, the hyperbolic model does not match the test data very well. Among the five tests shown in Fig 6.2.1, only three tests can be matched using the model. For the simulated three tests, the curve fitting is not satisfactory, as shown in Fig 6.6.2. The main reason for the failure of application of the model is that a little concavity exists on the stress-strain curves prior to peak which can not be represented by a hyperbola.

The hyperbolic model has the best fit with the CIP test data. Since the effective confining stress during shear in a CIP test was continuously decreased, the stress-strain relationship did not show a significant strain weakening behavior after the peak deviatoric stress was achieved. This behavior coincides with the characteristics of a hyperbola. It can be seen in Fig 6.6.3 that, although a hyperbola fits the test data in Tests CP6 and CP7 ($J_1=1.0$ and 2.88 MPa) very well, the trend of the curves is different from the others. To determine the shear modulus, G , the test results of CP5, CP4 and CP8 ($J_1=0.17, 0.5$ and 5.0 MPa) were used. Referring to the parameters presented in Table 6.6.3, the shear modulus, G , is expressed as

$$G = \left(1 - \frac{0.46(1-\sin\phi')(\sigma_1-\sigma_3)}{2\sigma_{30}'\sin\phi'}\right)^2 117.6\text{pa} \left(\frac{\sigma_{30}'}{\text{pa}}\right)^{0.6867} \quad (6.6.3)$$

The notations are the same as in equation (6.6.1).

Comparing the modeling results following different stress paths, a hyperbolic model has the best fit with the CIP test results and the worst fit with the CIU test results. Considering a specific stress path, the test data related to initial effective confining stresses of 1.0 and 3.0 MPa, especially 3.0 MPa, do not agree with the model very well or can not fit into the group of fitted curves very well. Grain crushing occurring during shear possibly may be the reason for the disagreement. No matter what stress path is followed in a test, dilation or the tendency for dilation dominates the stress-strain and volume change behavior if the initial effective confining stress is below 3.0 MPa. Grain crushing dominates the behavior, if the initial effective confining stress is above 3.0 MPa. At 3.0 MPa, the 'break down' stress, dilation and grain crushing are in equilibrium. This particular mechanism results in a transformation of the stress-strain relationship which, at times, makes a hyperbolic curve fitting impossible.

It can be seen in Tables 6.6.1 to 6.6.3 that the initial moduli (tangent modulus in the CID tests, elastic modulus in the CIU tests and shear modulus in the CIP tests) determined from curve fitting are usually greater than that from the test data. As a result, the modulus number, K_m , and exponent, n_m , calculated using test data differ from that calculated using curve fitted data. The former is used in the formulation of E_t and G , as shown in Equations (6.6.1) and (6.6.3).

The expression for tangent modulus derived by Duncan and Chang (1970) consists of two components, shape factor and the initial tangent modulus. The shape factor which changes with stress level and effective confining stress applies a deduction number to the initial tangent modulus according to stress level so that the tangent modulus decreases with an increase in stress level. When the stress level is zero, the tangent modulus is the initial tangent modulus. When the stress level is at peak, the tangent modulus is zero. From this point of view, the initial tangent modulus achieved from the test results is more reasonable to use than that obtained from curve fitting.

In the theory of elasticity, the shear modulus and Young's modulus bear the following relationship

$$G = \frac{E}{2(1+\nu)} \quad (6.6.4)$$

Where G =shear modulus, E =Young's modulus and ν =Poisson's ratio. From the CID test results, the average ν is equal to 0.3. Calculation shows that a tangent modulus analogous to Young's modulus obtained from the CID tests does not agree with a shear modulus obtained from the CIP tests in conjunction with this formula. This factor indicates that the oil sands behavior can not simply be dealt with as an elastic behavior.

A few conclusions can be reached in the modeling:

1) Hyperbolic model can only approximately simulate the stress-strain behavior of the Lower Grand Rapids Formation oil sands. It is not considered to be a satisfactory model. The model is suitable for simulating the stress-strain behavior prior to peak and a small portion of post peak, if strain weakening is not significant.

2) Volume change behavior and the change in pore pressure encountered in the tests can not be represented by the model because of the dilation and grain crushing which takes place during shear.

3) For the different stress paths followed in this testing program, the CIP test data had the best agreement with the model, the CIU data had the worst fit with the model because of the shape of the stress-strain curves.

4) Unlike other types of sands, R_f of the oil sands determined from the modeling varies in a relatively large range. It changes from 0.44 to 0.85 in the CID tests, 0.44 to 0.66 in the CIU tests and 0.32 to 0.72 in the CIP tests.

5) Analysis of the test results indicates that the stress-strain behavior of the oil sands is not governed by the theory of elasticity. Shear modulus, G , and tangent modulus, E_t , are not linearly related.

6.7 Comments on Constitutive Modeling

The establishment of a constitutive model for Lower Grand Rapids Formation oil sands is beyond the scope of this thesis. The models discussed in Chapter 2, therefore, were not applied to the test results except for a hyperbolic model which has been used as a curve fitting technique to simulate the stress-strain relationships for the CID, CIU and CIP test data. To meet the needs for geomechanical modeling of this oil sands in the future, the test data were prepared according to the requirements of the models presented in Chapter 2.

The CID test data were plotted with the deviatoric stress against the axial strain. A hyperbolic model (Duncan and Chang 1970) can be applied to the test data to predict the tangent modulus as a function of effective stress as discussed in Section 6.6.

A three moduli hyperelastic model (Yin et al 1990) can be applied to the CIU test results to calculate a coupling modulus, J and a shear modulus, G in order to establish the relationships for the deviatoric strain and the volumetric strain with a change in mean normal effective stress and deviatoric stress.

The CIP test data can also be simulated with the hyperbolic model to find the relationship between shear modulus and deviatoric stress. The oil sands behavior can, therefore, be characterized with two separate parameters, a shear modulus, G and a bulk modulus, K (Domaschuk et al 1969) which are defined in the theory of elasticity.

Since the testing stress range varied from 0.1 MPa to 9.5 MPa, whether dilation or grain crushing dominated the stress-strain and volume change behavior in a test depends on the stress path followed and the stress level reached. When dilation and grain crushing are involved in the stress-strain relationship, there may exist some difficulties in constitutive modeling. Comments on this problem are given in Section 7.2.

Table 6.1.1 Summary of Consolidated Drained Triaxial Compression Results

Initial conditions											
Test	Bulk Density Mg/m3	Dry Density Mg/m3	Mass Fraction			e	n %	Sr %	Calculated in situ n %	B	Id %
			Water (mass)%	Bitumen (mass)%	Solid (mass)%						
CD1	1.85	1.52	6.39	11.41	82.20	0.765	43.3	76.6	36.6	0.99	18.5
CD2	1.76	1.43	9.44	9.05	81.51	0.837	45.6	70.4	37.1	0.97	22.9
CD3	1.90	1.55	13.37	5.29	81.34	0.725	42.0	83.8	37.8	0.74	11.2
CD4	1.86	1.50	15.22	4.01	80.77	0.781	43.8	81.4	38.7	0.93	13.2
CD5	1.80	1.48	9.00	8.98	80.02	0.805	44.6	71.6	36.6	0.66	22.0
CD6	1.79	1.48	3.58	13.94	82.48	0.806	44.6	68.8	35.7	0.97	25.2
After isotropic consolidation											
Test	Volume Change %	Bulk Density Mg/m3	Dry Density Mg/m3	e	n %	Id %					
CD1	-5.23	2.01	1.61	0.672	40.19	10.0					
CD2	-6.43	1.97	1.54	0.719	41.82	12.8					
CD3	0.00	1.90	1.55	0.667	40.02	11.2					
CD4*	-10.24	2.03	1.67	0.595	37.30						
CD5	-8.12	2.01	1.61	0.658	39.70	8.6					
CD6	-8.41	2.02	1.62	0.654	39.55	10.9					
* Negative Id											
Drained shear test results											
Test	Effective Confining Stress MPa	Back Pressure MPa	Deviator Stress at Failure MPa	Axial strain at Failure %	Volumetric Strain at Failure %	Tangent Modulus MPa	Poisson's Ratio	Secant Internal Friction Angle	Brittleness Index %	Deviator Stress at Residual MPa	
CD4*	0.10	0.50	0.13	2.16	1.36	80	0.30	57.5	49.1	0.55	
CD6	0.10	0.50	1.08	1.25	-0.21	325	0.24	49.9	57.2	1.40	
CD3	0.50	0.55	3.27	1.63	-0.28	380	0.20	39.5	52.7	2.00	
CD1	1.21	1.99	4.23	1.95	-0.02	450	0.42	31.4	53.8	3.00	
CD2	2.98	1.99	6.49	7.43	-0.95	430	0.14	24.9	10.3	6.60	
CD5	5.00	0.60	7.25								
*Membrane leak											

Table 6.1.2 Comparison of The Drained Triaxial Compression Test Results

Oil Sand Specimens	Test	Effective Confining Stress MPa	Deviatoric Stress MPa	Axial Strain At Failure %	Volumetric Strain At Failure %	Initial Tangent Modulus MPa	Internal Friction Angle ϕ	Index** of Sample Disturbance %
Athabasca McMurray (Kosar 1989)	AMTOS 2	2.50	8.50	2.2	0.6	616	39.0	7.3
	AMTOS 3	7.00	14.00	4.4	-1.7	1215	30.0	-1.0
Athabasca Clearwater (Kosar 1989)	ACTOS 4	1.00	4.80	1.2	0.3	666	44.9	3.1
	ACTOS 3	2.50	6.50	2.5	-0.7	542	34.4	4.4
	ACTOS 1	5.50	8.50	2.1	-1.1	986	25.8	12.4
	ACTOS 2	7.00	10.00	3.3	-1.4	1335	24.6	7.5
Athabasca McMurray (Agar 1984)	TOS2	4.00	16.90	1.2		2200	43.0	3.0
	TOS5	8.00	17.90	2.0		3600	32.0	8.2
Cold Lake Clearwater Location No.2 (Kosar 1989)	CL2TOS 1	1.00	3.19	2.0	0.1	311	37.9	20.4
	CL2TOS 2	4.00	7.00	2.7	-1.1	677	27.8	11.8
	CL2TOS 3	7.00	10.80	9.0	-5.0	695	25.8	13.5
Cold Lake Clearwater (Wong 1993)	CD01	0.60	5.00	1.3	0.5	233*	53.8	
	CD02	0.70	3.26	0.8	0.7	254	44.4	
	CD03	1.00	4.45	1.8	0.2	310	43.6	
	CD04	4.50	9.63	1.1	0.0	720	31.1	
	CD05	9.00	16.92	1.4	-0.8	1061	29.0	
	CD06	12.00	17.16	1.5	-0.8	1246	24.6	
Cold Lake Lower Grand Rapids	CD6	0.10	1.08	2.2	1.4	80	57.5	10.0
	CD3	0.50	3.27	1.3	-0.2	325	49.9	12.8
	CD1	1.21	4.23	1.6	-0.3	380	39.5	11.2
	CD2	2.98	6.49	2.0	0.0	450	31.4	8.6
	CD5	5.00	7.25	7.4	-1.0	430	24.9	10.9

*Tangent modulus at 0.2% axial strain

**After isotroic consolidation

Table 6.2.1 Summary of Consolidated Undrained Triaxial Compression Test Results

Initial conditions

Test No.	Bulk Density Mg/m ³	Dry Density Mg/m ³	Extraction			e	Lab Porosity n %	Calculated in situ n %	Sr %	B	Id %
			Water (mass) %	Bitumen (mass) %	Solid (mass) %						
CU1	1.98	1.65	15.98	0.49	83.53	0.649	39.4	34.9	82.6	0.99	12.8
CU2	1.82	1.52	5.90	10.38	83.72	0.750	42.9	33.8	68.0	0.97	26.9
CU3	1.81	1.54	5.80	9.16	84.99	0.725	42.0	31.4	63.2	0.96	27.3
CU4	1.95	1.63	7.89	8.6	83.42	0.650	39.4	34.5	81.1	0.90	14.2
CU5	1.95	1.63	7.72	8.7	83.58	0.650	39.4	34.2	80.0	1.00	15.2
CU6	1.87	1.52	11.80	7.15	81.05	0.736	42.4	37.8	82.8	1.00	12.0
CU7*	1.88		15.10	1.9	83.00						
CU8	1.79	1.52	6.38	8.58	85.14	0.715	41.7	31.0	62.9	0.88	34.4

*Membrane broken in consolidation. No data available

Isotropic consolidation

Test No.	Volume Change %	Bulk Density Mg/m ³	Dry Density Mg/m ³	e	n %	Id %	Final Effective Confining MPa
CU1	-2.72	2.07	1.69	0.605	37.7	7.9	1.00
CU2	-8.44	2.05	1.67	0.603	37.6	11.3	3.00
CU3	-8.46	2.05	1.68	0.580	36.7	11.1	0.50
CU4	-4.65	2.10	1.74	0.550	35.5	2.8	5.00
CU5	-4.59	2.10	1.74	0.548	35.4	3.8	0.10
CU6	-6.36	2.01	1.62	0.623	38.4	1.6	5.00
CU8	-4.54	1.99	1.60	0.637	38.9	25.5	0.10

Undrained shear tests

Test No.	Initial Effective Confining MPa	Back Pressure MPa	B	Maximum Stress Ratio	Deviator Stress at Failure MPa	Axial Strain at Failure %	Pore Pressure at Failure MPa	Modulus of Elasticity MPa	Af
CU5	0.10	1.20	0.98	23.38	3.23	0.94	-0.04	415	-0.01
CU8	0.10	1.70	0.89	9.87	1.33	0.89	-0.05	197	-0.05
CU3	0.50	0.80		7.31	4.49	1.53	-0.22	298	-0.05
CU1	1.00	0.70		6.70	5.28	1.50	0.10	400	0.02
CU2	3.00	0.50		3.95	8.51	2.50	0.12	455	0.01
CU4	5.00	2.00		2.32	4.84	1.96	1.34	400	0.28
CU6	5.00	1.50		4.73	9.37	3.55	2.49	406	0.27

Table 6.2.2 Steady States in CIU Tests

Test	σ_{30}' MPa	q MPa	p' MPa	σ_1'/σ_3'	ε_a %	Δu MPa
CU8	0.1	4.1	2.9	3.7	8.6	-1.44
CU3	0.5	4.7	2.6	6.1	3.0	-0.45
CU1	1.0	2.0	1.6	2.7	6.0	-0.13
CU2	3.0	2.0	3.6	1.7	12.0	0.11
CU6	5.0	7.4	4.8	4.0	7.0	2.56

Table 6.3.1 Summary of Triaxial Compression Tests With J1 Constant

Initial condition												
Test NO.	Bulk Density Mg/m3	Dry Density Mg/m3	Extraction			e	Lab Porosity %	Sr %	Calculated Porosity (in situ) %	B	Id %	
			Water (mass) %	Bitumen (mass) %	Solid (mass) %							
CP1	1.96	1.65	5.65	9.95	84.40	0.580	36.7	82.0	32.2	0.79	13.9	
CP2	1.90	1.56	11.37	6.28	82.35	0.718	41.8	79.3	36.3	0.97	15.2	
CP3	1.95	1.65	5.71	9.52	84.77	0.618	38.2	76.6	32.1	0.65	18.9	
CP4	1.91	1.55	11.17	7.56	81.27	0.692	40.9	86.3	37.4	0.96	9.4	
CP5	1.92	1.60	8.94	7.76	83.30	0.626	38.5	82.1	34.0	0.91	13.4	
CP6*	1.72	1.47	3.50	13.30	83.30	0.802	44.5	53.8	34.3	0.92	29.7	
CP7*	1.70	1.46	3.50	13.30	83.30	0.815	44.9	52.9	34.3	0.90	30.9	
CP8*	1.67	1.41	4.60	14.10	81.30	0.890	47.1	52.7	37.4	0.91	26.1	

Isotropic consolidation

Test No.	Volume Change %	Bulk Density Mg/m ³	Dry Density Mg/m ³	e	Porosity %	Id %
CP1	-4.38	2.08	1.74	0.511	33.8	4.9
CP2	-5.36	2.04	1.65	0.626	38.5	6.2
CP3	-4.56	2.09	1.73	0.543	35.2	9.7
CP4	-2.59	1.99	1.59	0.647	39.3	5.2
CP5	-1.42	2.00	1.62	0.603	37.6	10.8
CP6*	-7.36	1.99	1.58	0.669	40.0	16.6
CP7*	-7.34	1.99	1.58	0.669	40.1	18.2
CP8*	-9.88	1.98	1.56	0.704	41.3	10.4

J1 test

Test No.	B	Back Pressure MPa	Initial Effective Confining (J1) MPa	Effective Confining at failure MPa	Deviatoric Stress at failure MPa	Gi MPa	Axial Strain at failure %	Volumetric Strain at failure %
CP2	0.49	1.30	0.87	0.07	2.67	175	1.01	0.93
CP1		1.30	2.70	1.66	8.08	455	1.03	-0.04
CP3		1.30	4.92	0.90	12.01	1000	0.84	0.13
CP5	0.92	1.60	0.17	0.00	0.88	27	0.96	2.00
CP4	0.74	1.70	0.50	0.01	1.77	48	1.15	1.47
CP6*	0.52	2.40	1.00	0.31	2.16	84	1.37	0.81
CP7*	0.72	2.10	2.88	1.40	4.82	220	2.27	0.04
CP8*		2.40	5.00	2.92	6.20	230	5.46	-0.93

* The core dried out during storage. The extraction referred to is from the core lab report.

Table 6.3.2 Comparison of Volumetric Strain in Test CD3 and CP4

Test	CD3	CP4	CD3	CP4
$\epsilon_a(\%)$	0.5		1.0	
$q(\text{MPa})$	1.90	0.70	3.03	1.42
$\epsilon_v(\%)$	-0.17	0.01	-0.26	0.58
Measured $\Delta\epsilon_v(\%)$	0.18		0.84	
$\sigma_3'^*$ (MPa)	1.13	0.50	1.51	0.50
Calculated $\Delta\epsilon_v(\%)$	0.28		0.41	

* σ_3' here is the mean normal effective stress at the given axial strain

$$\sigma_3' = \frac{\sigma_1' + 2\sigma_3'_{0}}{3} = \frac{q + 3\sigma_3'_{0}}{3} \text{ in CID test}$$

$$\sigma_3'_{0} = J_1 = 0.5 \text{ MPa in } J_1 \text{ test}$$

Table 6.3.3 Comparison of Volumetric Strain in Test CD5 and CP8

Test	CD5	CP8	CD5	CP8
$\epsilon_a(\%)$	0.5		1.0	
$q(\text{MPa})$	2.15	0.80	3.80	1.81
$\epsilon_v(\%)$	-0.47	-0.017	-0.61	-0.09
Measured $\Delta\epsilon_v(\%)$	0.45		0.52	
$\sigma_3'^*$ (MPa)	5.72	5.00	6.27	5.00
Calculated $\Delta\epsilon_v(\%)$	0.16		0.27	

* σ_3' here is the mean normal effective stress at the given axial strain

$$\sigma_3'_{0} = J_1 = 5.0 \text{ MPa}$$

Table 6.4.1 Summary of Pore Pressure Injection Test Results

Initial condition		Extraction				e	Lab Porosity %	Sr %	Calculated Porosity (in situ) %	B	Id %
Test No.	Bulk Density Mg/m ³	Dry Density Mg/m ³	Water (mass) %	Bitumen (mass) %	Solid (mass) %						
CI1	1.77	1.52	6.40	12.30	81.30	0.742	42.6	56.1	37.4	1.00	13.9
CI2	1.72	1.48	6.40	12.30	81.30	0.795	44.3	53.8	37.4	1.00	18.4
CI3	1.67	1.43	6.40	12.30	81.30	0.848	45.9	50.2	37.4	1.00	22.7
CI4	1.66	1.43	6.40	12.30	81.30	0.853	46.0	49.1	37.4	1.00	23.1
CI4A	1.75	1.40	7.40	10.30	82.30	0.712	41.6	49.5	35.9	0.99	15.9
CI4B	1.71	1.51	7.40	10.30	82.30	0.770	43.5	45.8	35.9	0.99	21.2
CI5	1.73	1.44	6.40	12.30	81.30	0.845	45.8	61.5	37.4	1.00	22.3
CI5A	1.69	1.49	7.40	10.30	82.30	0.783	43.9	44.5	35.9	0.97	22.3

Note: The core used in the tests dried out during storage. The extraction values were obtained from the core lab report.

Isotropic consolidation

Test No.	Volume Change %	Bulk Density Mg/m ³	Dry Density Mg/m ³	e	Porosity %	Id %
CI1	-7.21	2.03	1.64	0.618	38.2	2.1
CI2	-8.65	2.01	1.61	0.639	39.0	4.3
CI3	-7.50	1.97	1.55	0.709	41.5	10.7
CI4	-7.06	1.97	1.54	0.721	41.9	12.0
CI4A	-5.36	2.02	1.63	0.621	38.3	6.7
CI4B	-9.96	2.04	1.66	0.592	37.2	3.6
CI5	-7.74	1.98	1.56	0.706	41.4	10.6
CI5A	-7.75	1.98	1.59	0.629	38.6	7.5

Pore pressure injection

Test No.	Initial Effective Stress Ratio	Effective Stress Ratio at failure	Deviatoric Stress at failure MPa	Axial Strain at failure %	Volumetric Strain at failure %	Effective Confining stress at failure MPa	Pore Pressure at failure MPa	Back Pressure MPa	s' MPa	t MPa	Secant Internal friction ϕ
CI1	1.13	21.00	1.0	0.49	3.96	0.05	8.95	1.00	0.55	0.50	65.4
CI2	1.25	11.00	2.0	0.59	3.16	0.20	8.80	1.00	1.20	1.00	56.4
CI3	1.39	7.18	3.0	0.65	2.19	0.50	8.50	1.00	1.90	1.50	52.1
CI4	1.50	6.00	4.0	1.27	1.59	2.50	6.50	1.00	4.50	2.00	
CI4A*	1.50	2.30	4.0	0.08	0.02	3.05	5.95	1.00	5.05	2.00	
CI4B	1.50	6.00	4.0	3.29	8.73	0.80	8.20	1.00	2.80	2.00	45.6
CI5*	1.63	2.65	4.3	0.09	0.18	2.60	6.90	1.80	4.75	2.15	
CI5A	1.63	6.00	5.0	3.50	8.80	1.00	8.00	1.00	3.50	2.50	47.7

* The specimen did not fail in the test.

Table 6.4.2 Anticipated Stress Condition In CIA Tests

Test	t MPa	Initial Stress Condition					Failure Stress Condition				
		σ_3^i MPa	$(\sigma_1^i - \sigma_3^i)^i$ MPa	σ_1^i MPa	$(\sigma_1^i / \sigma_3^i)^i$	s^i MPa	$(\sigma_1^i)^f$ MPa	$(\sigma_3^i)^f$ MPa	$(\sigma_1^i / \sigma_3^i)^f$	s^f MPa	
CI1	0.5	8	1	9	1.13	8.5	1.10	0.10	11.0	0.60	
CI2	1.0	8	2	10	1.25	9.0	2.31	0.31	7.5	1.31	
CI3	1.5	8	3	11	1.38	9.5	3.59	0.59	6.1	2.09	
CI4	2.0	8	4	12	1.50	10.0	4.96	0.96	5.2	2.96	
CI5	2.5	8	5	13	1.63	10.5	6.49	1.49	4.4	3.99	

Table 6.5.1 Grain Size Analyses

Test	Before Test			After Test		
	d ₁₀ mm	Fines Grains (%)		d ₁₀ mm	Fine Grains (%)	
		<0.075mm (No.200)	<0.044mm (No.325)		<0.075mm (No.200)	<0.045mm (No.325)
CD1	0.102	4.2	2.0	0.083	5.9	3.2
CD2	0.085	7.3	4.8	0.082	7.7	4.6
CD3*	0.085	10.0	6.7			
CD5	0.085	7.6	4.8	0.064	11.5	6.9
CU1	0.065	12.2	6.2	0.065	12.8	4.5
CU2	0.101	6.1	4.3	0.089	8.2	5.4
CU3	0.100	6.7	4.4	0.082	8.9	6.0
CU4	--	72.2		--	89.4	
CU5	--	88.8	50.6	--	90.6	54.4
CU6	--	42.7	14.1	--	47.2	11.8
CU8	0.100	6.3	3.1	0.055	14.5	8.0
CP1	--	84.4	41.6	--	90.3	50.4
CP2	--	87.4	59.9	--	90.4	59.5
CP3	--	93.3	54.9	--	92.3	52.8
CP4	0.050	47.7	8.3	0.050	55.0	8.6
CP5	0.050	41.6	9.9	0.050	47.8	11.1
CP6	0.070	10.7	4.4	0.060	14.4	6.6
CP7	0.074	9.0	3.8	0.061	12.8	5.6
CP8	0.075	7.3	2.8	0.053	20.7	6.5
CI1	0.078	3.3	1.4	0.075	6.3	2.2
CI2	0.078	3.3	1.1	0.075	6.2	2.6
CI3	0.079	3.5	1.3	0.075	6.3	2.7
CI4	0.078	5.0	1.9	0.055	14.7	8.2
CI4A	0.078	3.8	1.3	0.075	8.5	2.0
CI4B	0.078	4.1	1.7	0.073	10.4	4.4
CI5	0.078	5.6	1.8	0.073	10.5	4.9
CI5A	0.077	4.5	1.7	0.075	6.9	3.0

* There is a conflict in grain size analysis before and after test.
 -- d₁₀ was not measured

Table 6.6.1 Hyperbolic Model In CID Tests

Test	σ_3' MPa	ϵ_{\max} (model) %	a 1/MPa	b 1/MPa	$(\sigma_1 - \sigma_3)_{ult}$ MPa	$(\sigma_1 - \sigma_3)_f$ MPa	E_i (model) MPa	E_i (test data) MPa	R_f
CD6	0.10	2.5	0.0098	0.452	2.43	1.08	102	80	0.44
CD3	0.50	2.1	0.0021	0.214	4.67	3.27	476	325	0.7
CD1	1.21	3.0	0.0020	0.197	5.08	4.23	500	380	0.83
CD2	2.98	4.2	0.0018	0.106	9.43	6.49	555	450	0.69
CD5	5.00	5.0	0.0016	0.115	8.70	7.25	625	430	0.85

$K_m = 1092$ (Test data) and 1438 (Model data)

$n_m = 0.4219$ (Test data) and 0.4313 (Model data)

Table 6.6.2 Hyperbolic Model In CIU Tests

Test	σ_3' MPa	ϵ_{\max} (model) %	a 1/MPa	b 1/MPa	$(\sigma_1 - \sigma_3)_{ult}$ MPa	$(\sigma_1 - \sigma_3)_f$ MPa	E_i (model) MPa	E_i (test data) MPa	R_f
CU8	0.10	6.0	0.004980	0.09569	10.45	4.86	201	197	0.47
CU3	0.50	5.0	0.002299	0.12880	7.76	5.10	344	298	0.66
CU6	5.00	4.0	0.002043	0.04612	21.68	9.54	489	406	0.44

$K_m = 2061$ (Test data) and 2176 (Model data)

$n_m = 0.1814$ (Test data) and 0.2226 (Model data)

Table 6.6.3 Hyperbolic Model In CIP Tests

Test	σ_3' (J1) MPa	ϵ_{\max} (model) %	a 1/MPa	b 1/MPa	$(\sigma_1 - \sigma_3)_{ult}$ MPa	$(\sigma_1 - \sigma_3)_f$ MPa	E_i (model) MPa	E_i (test data) MPa	R_f
CP5	0.17	2.8	0.01569	0.452	2.21	0.88	64	27	0.40
CP4	0.50	3.0	0.00991	0.181	5.53	1.77	100	48	0.32
CP6	1.00	2.0	0.00287	0.331	3.00	2.16	348	84	0.72
CP7	2.88	3.5	0.00355	0.088	11.36	4.82	281	220	0.42
CP8	5.00	6.0	0.00317	0.105	9.5	6.20	315	230	0.65

$K_m = 177.6$ (Test data) and 476.5 (Model data)

$\eta_m = 0.6867$ (Test data) and 0.4989 (Model data)

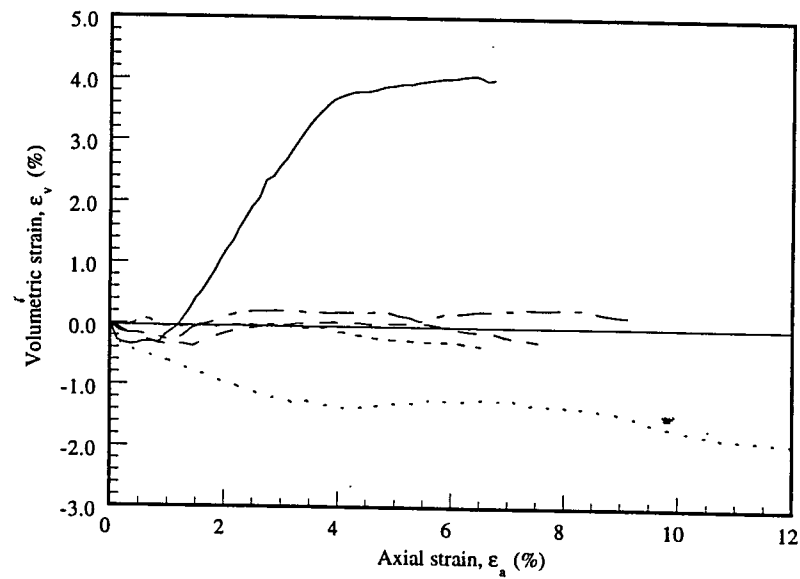
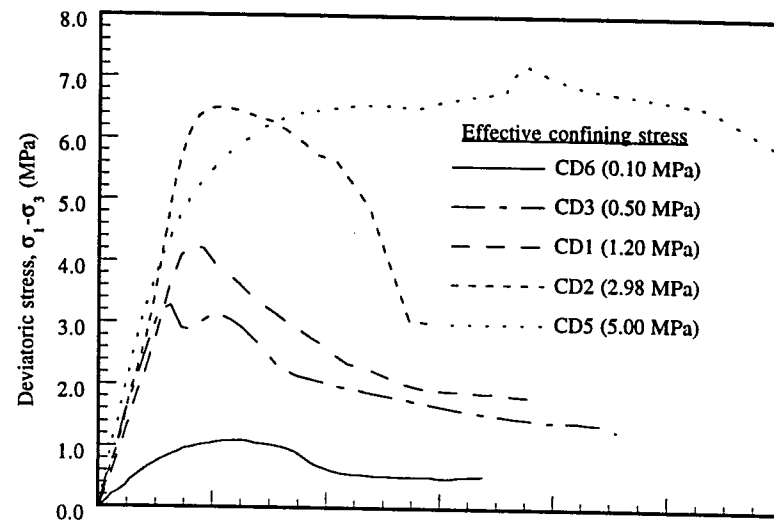


Fig 6.1.1 Stress-strain and Volume Change in CID Tests

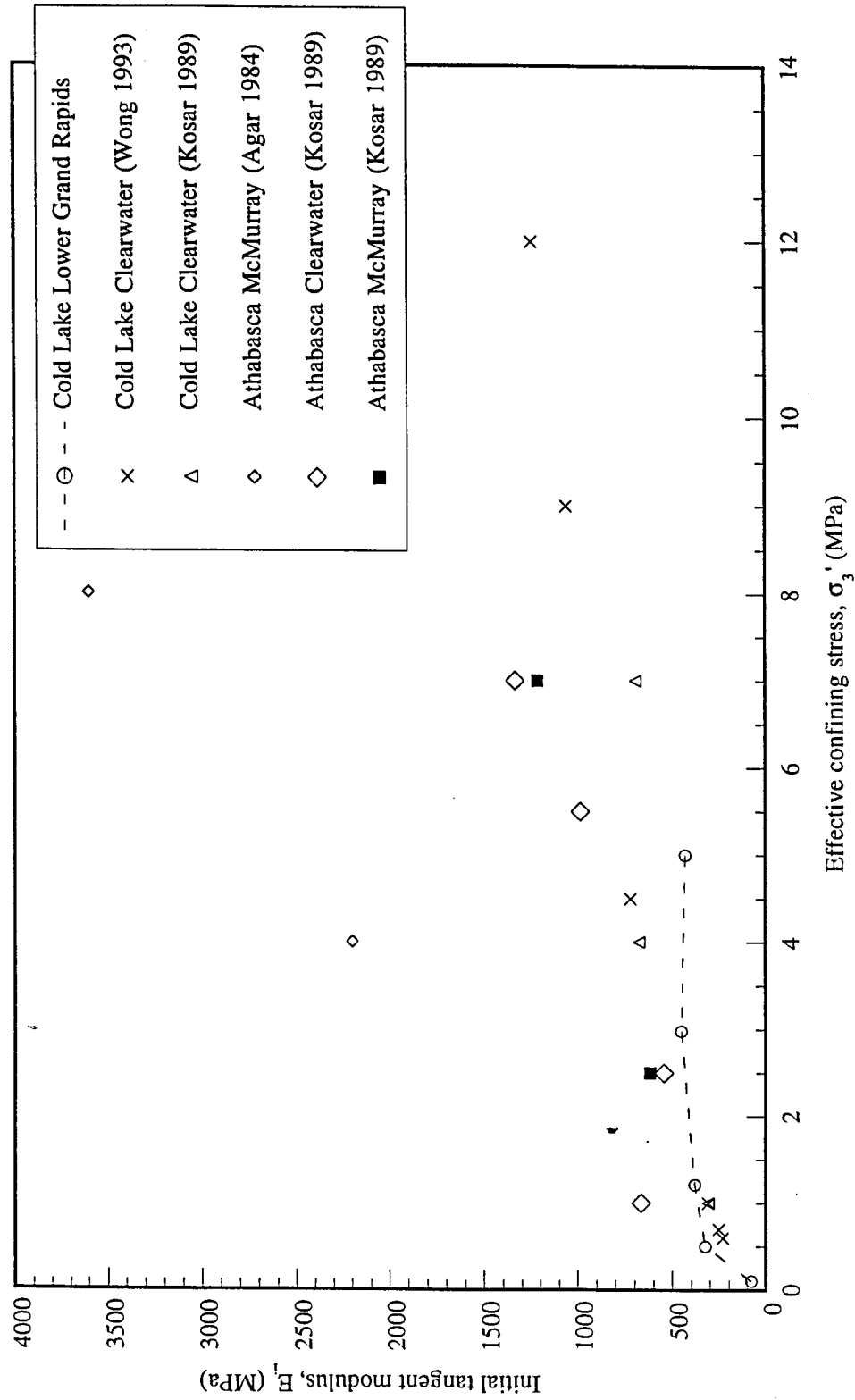


Fig 6.1.2 The Initial Tangent Modulus in Drained Triaxial Compression

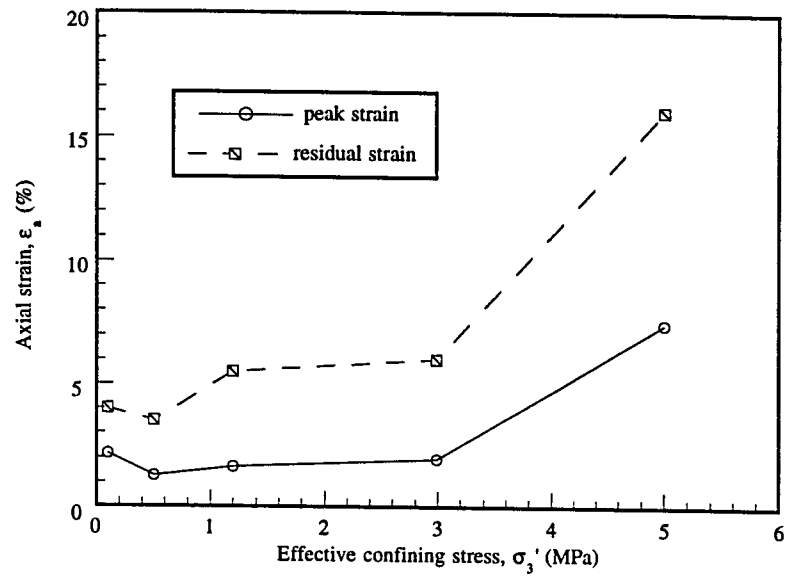


Fig 6.1.3 Axial Strain in CID Tests

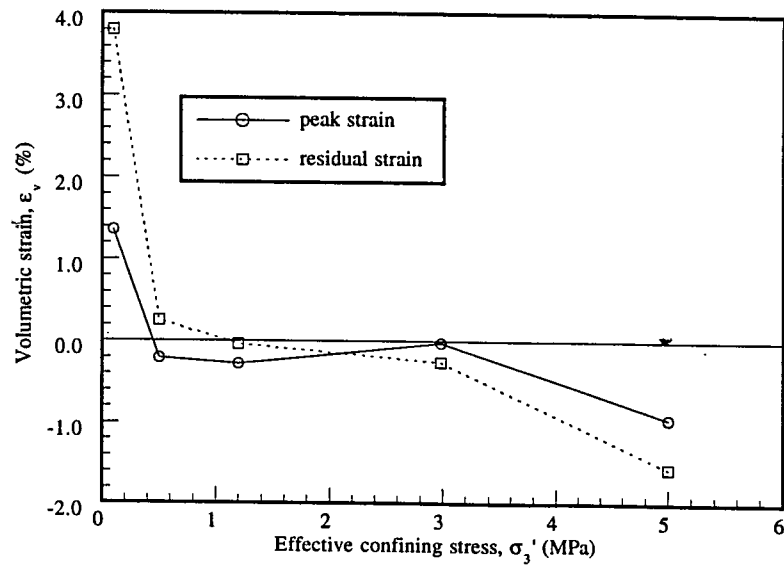


Fig 6.1.4 Volumetric Strain in CID Tests

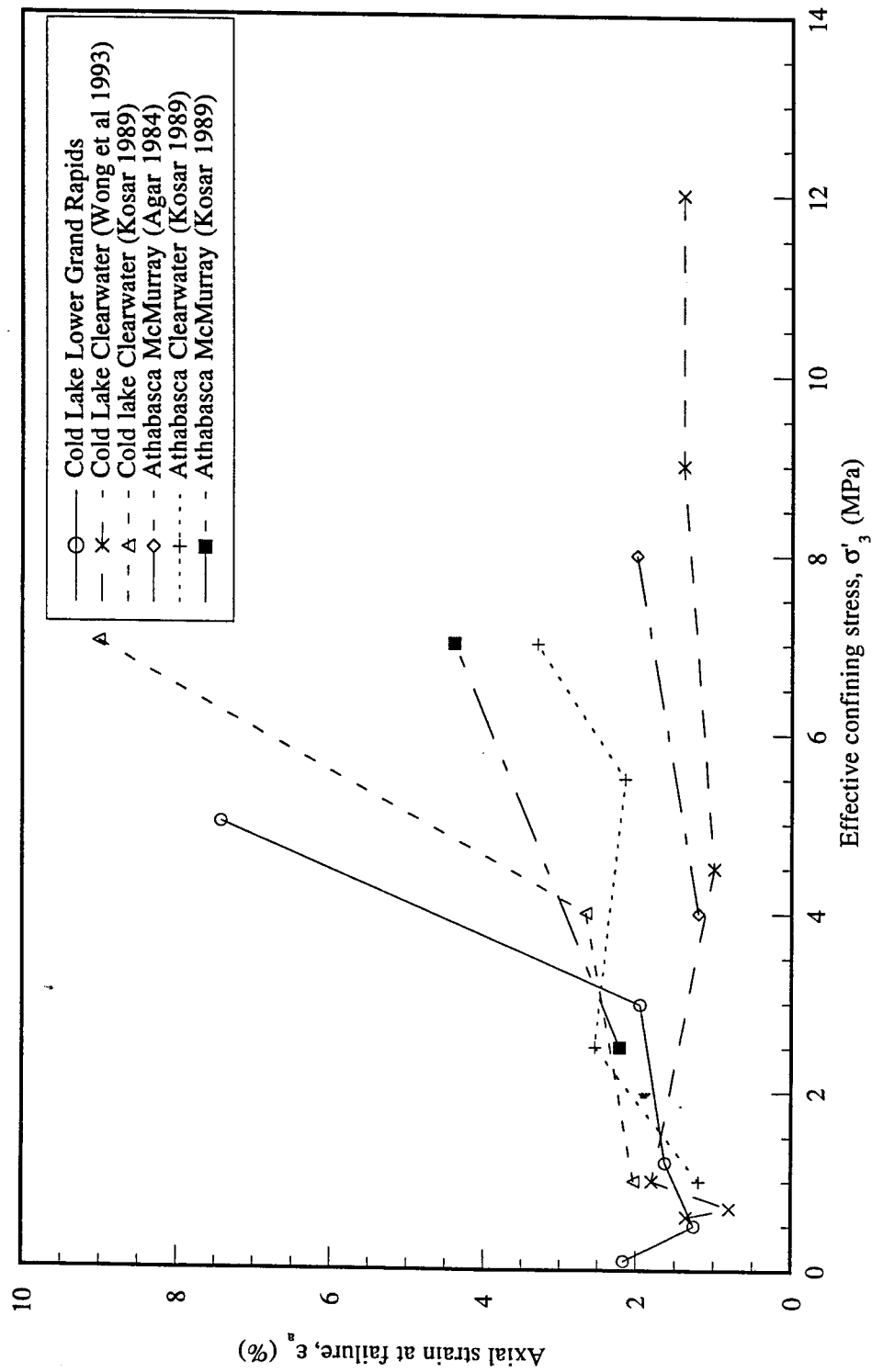


Fig 6.1.5 Axial Strain at Failure in Drained Triaxial Compression

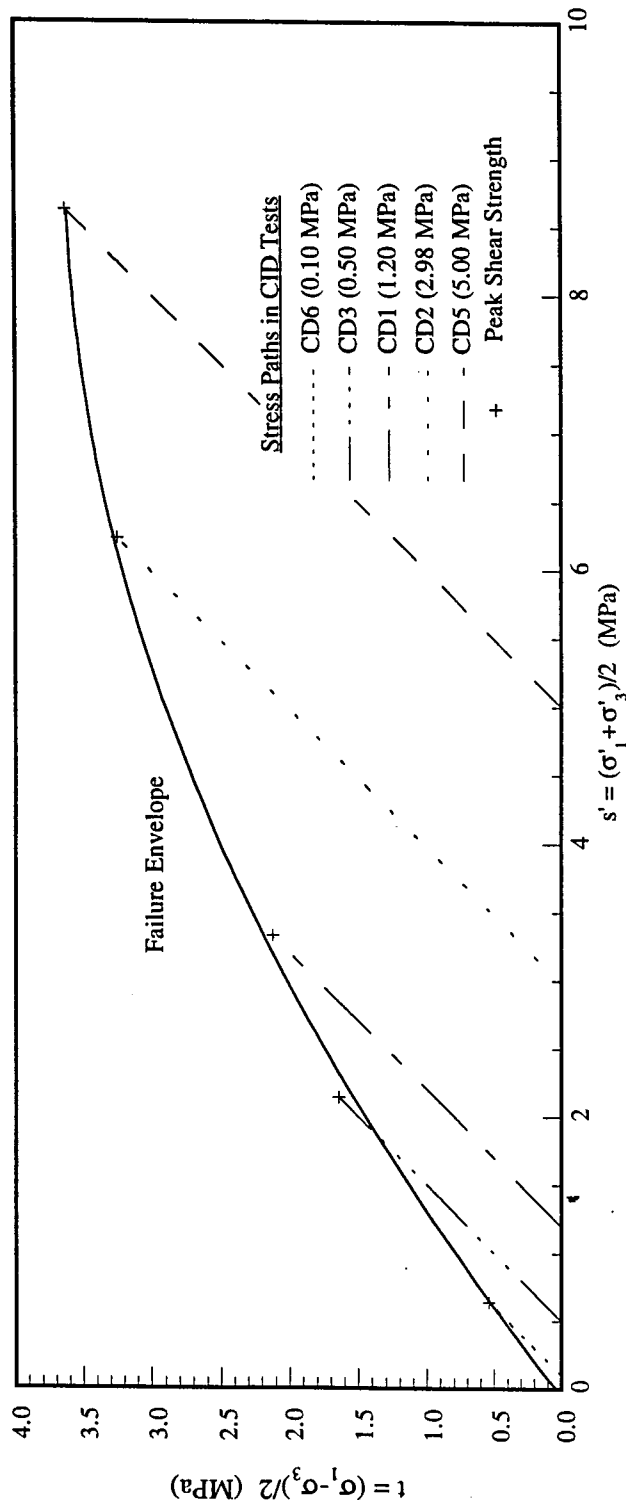


Fig 6.1.6 CID Test Failure Envelope

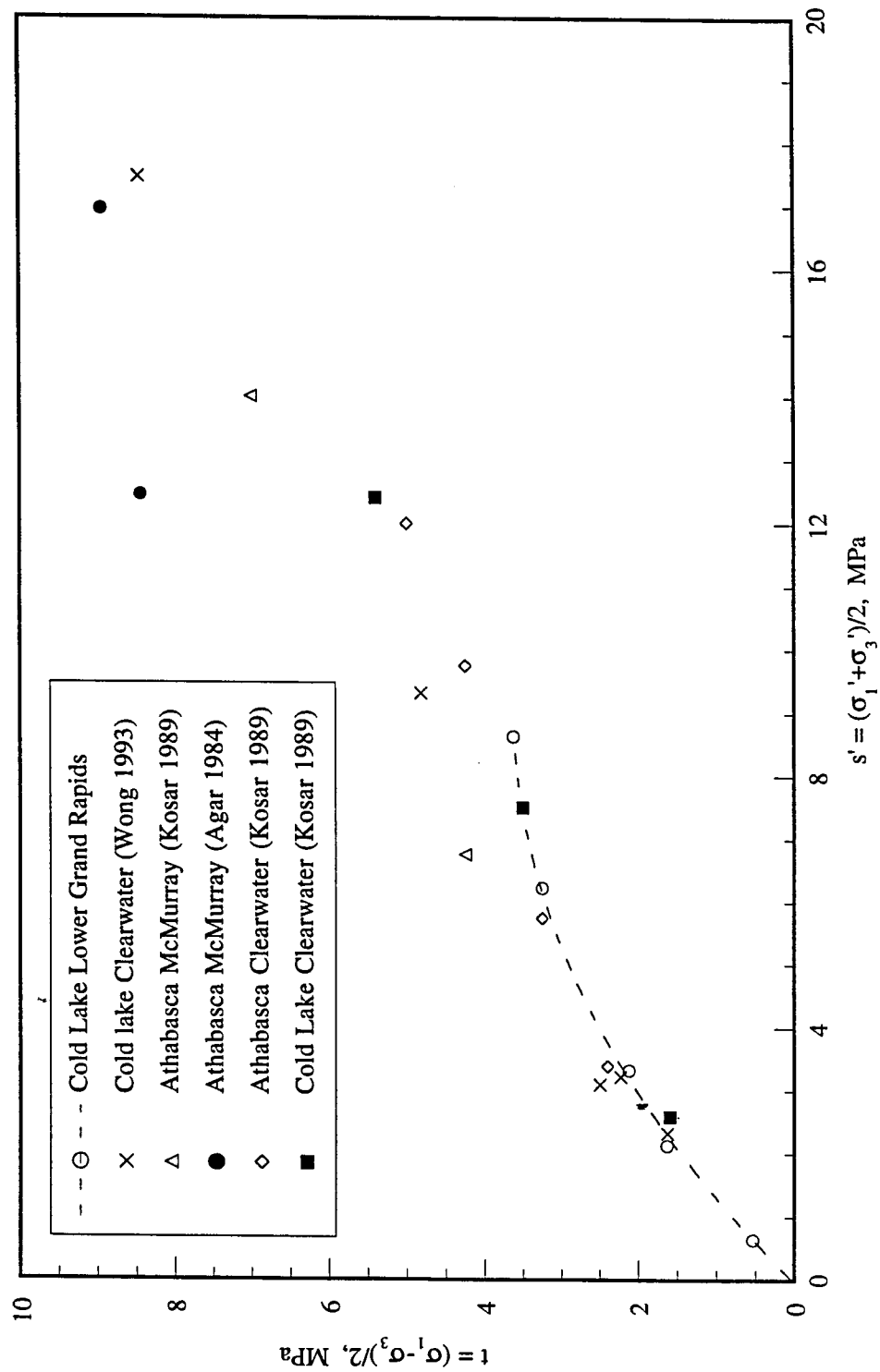


Fig 6.1.7 Shear Strength of Oil Sands In Drained Triaxial Compression

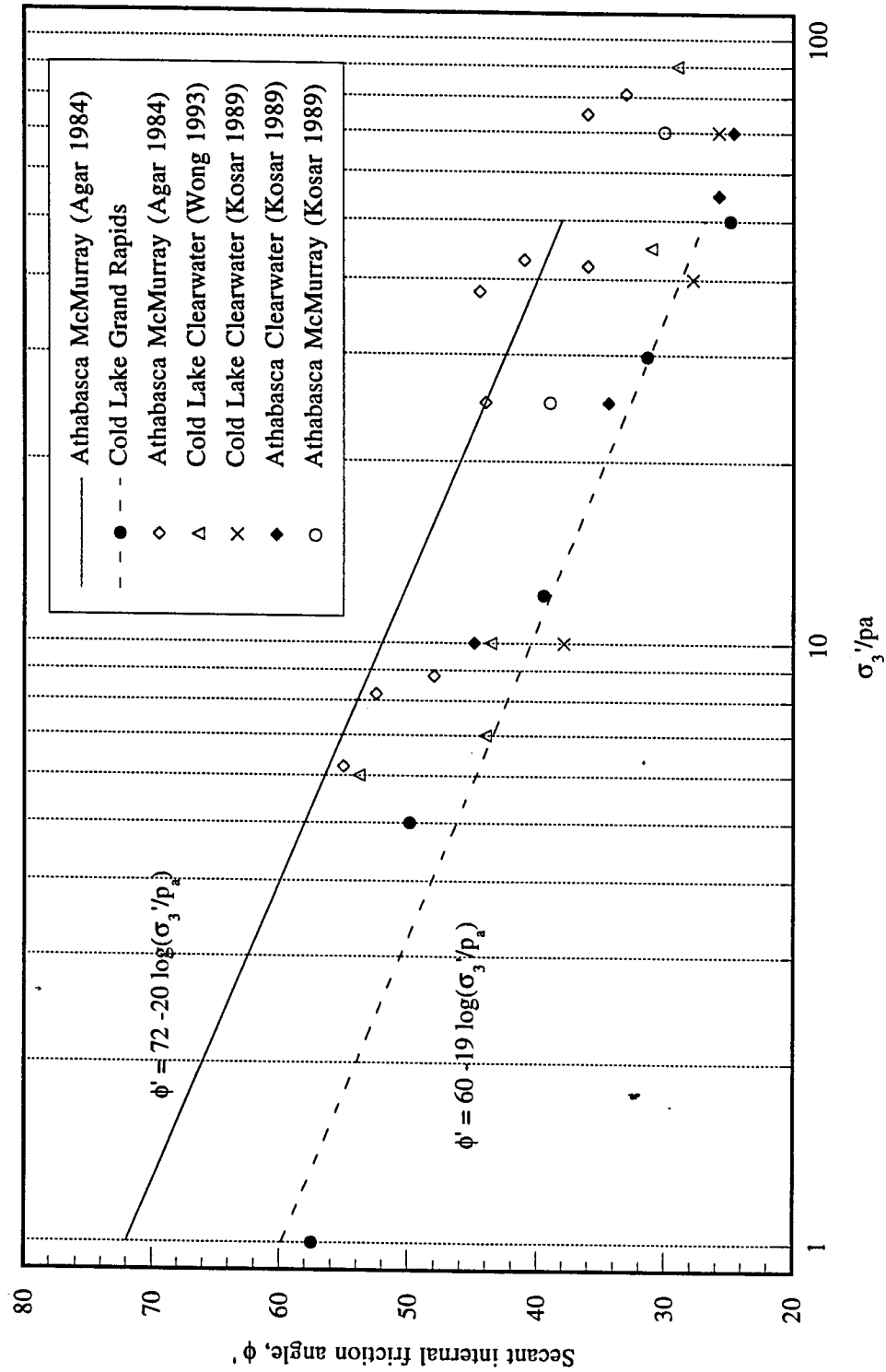


Fig 6.1.8 The Secant Internal Friction Angle In CID Tests

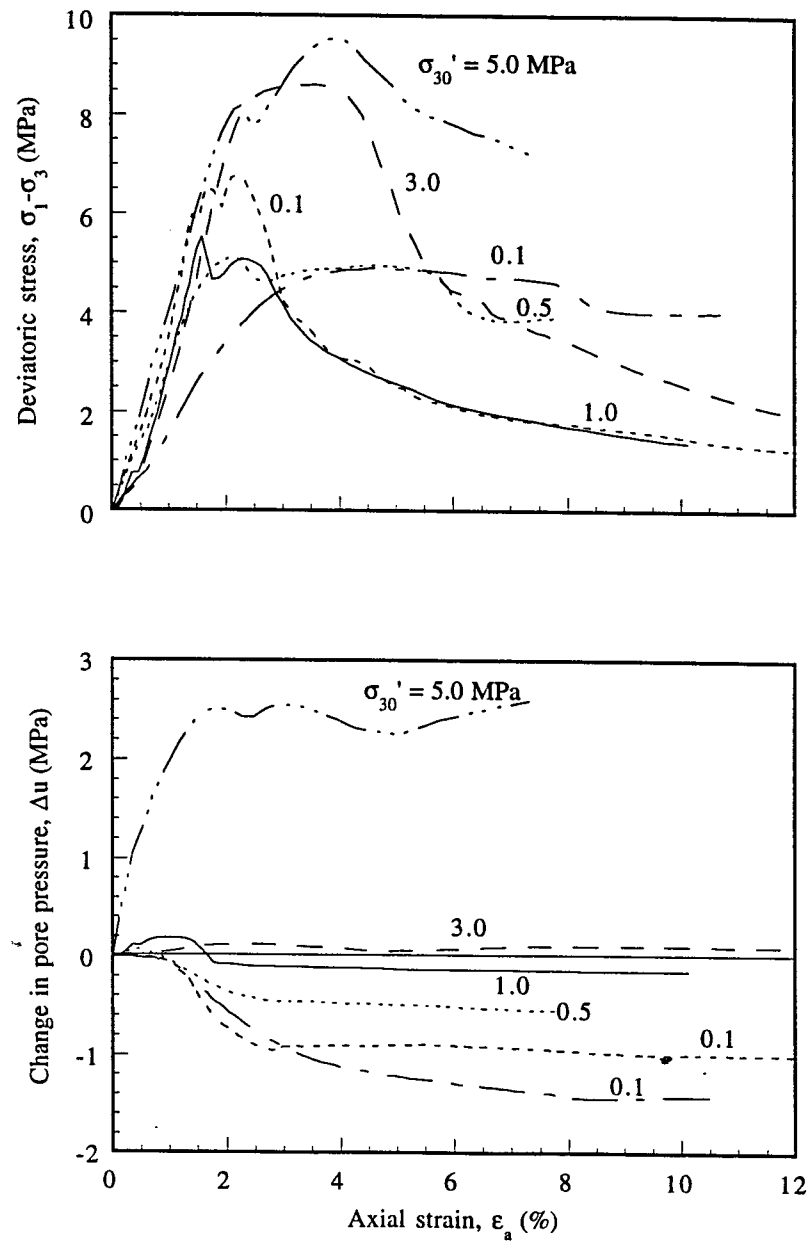


Fig 6.2.1 Stress-Strain Relationship and Pore Pressure Change in CIU Tests

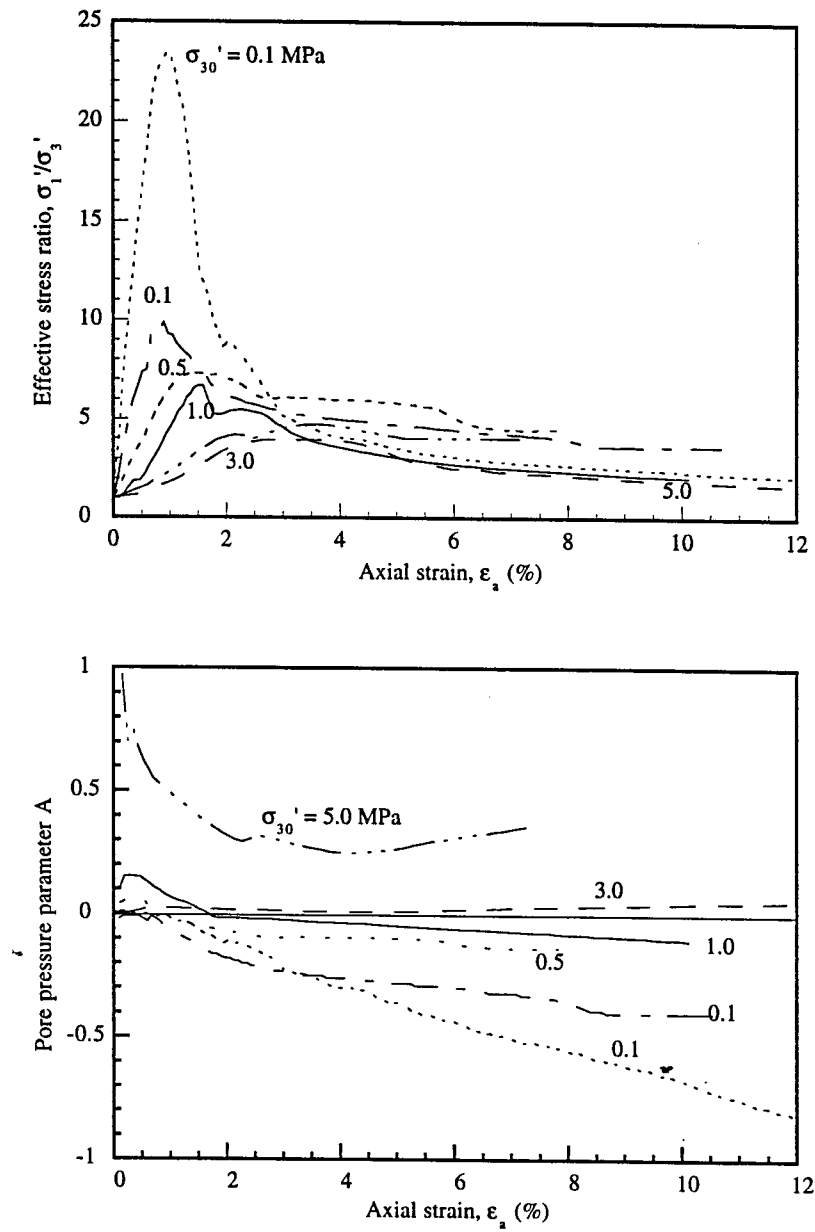


Fig 6.2.2 Stress-Strain Relationship and Change in Pore Pressure Parameter A in CIU Tests

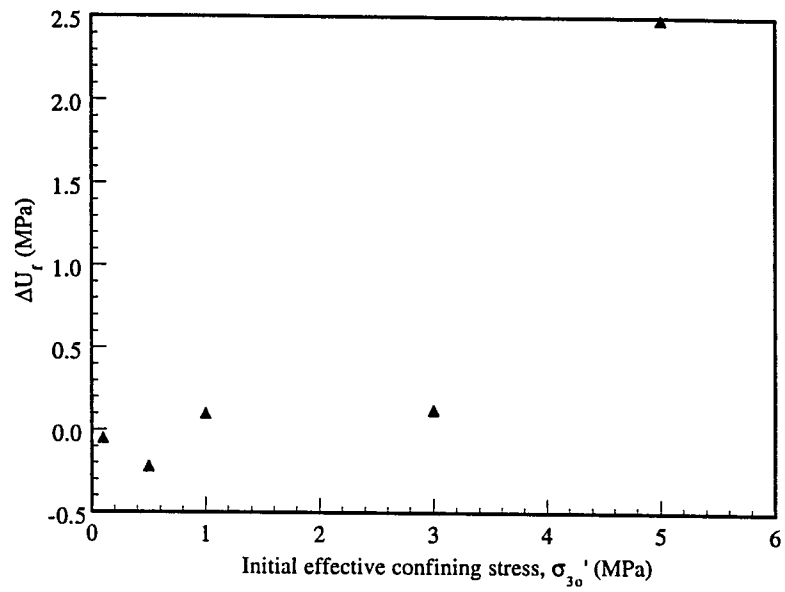


Fig 6.2.3 Pore Pressure Change at Failure in CIU Tests

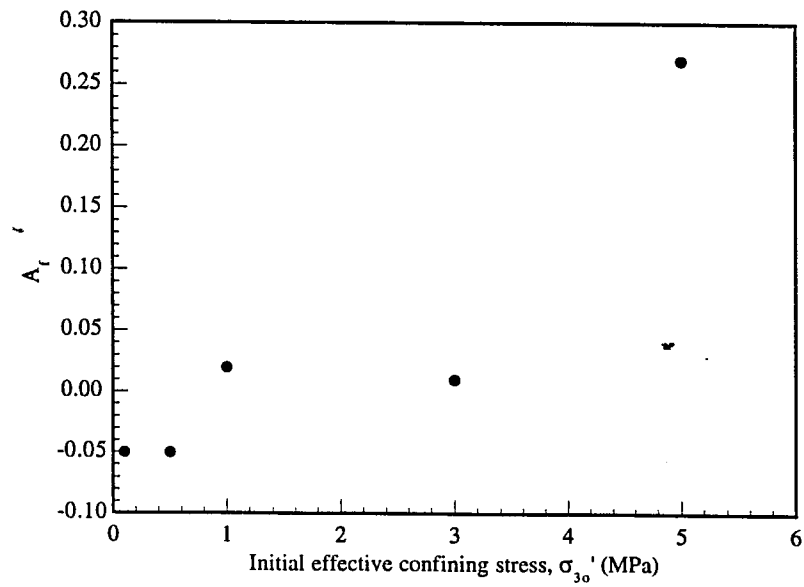


Fig 6.2.4 Pore Pressure Parameter A at Failure in CIU Tests

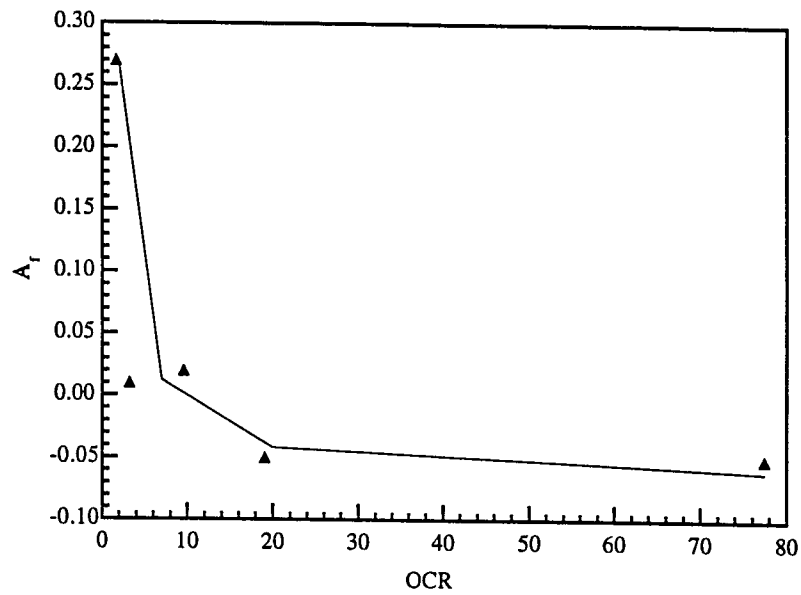


Fig 6.2.5 Relationship Between A_r and OCR In CIU Tests

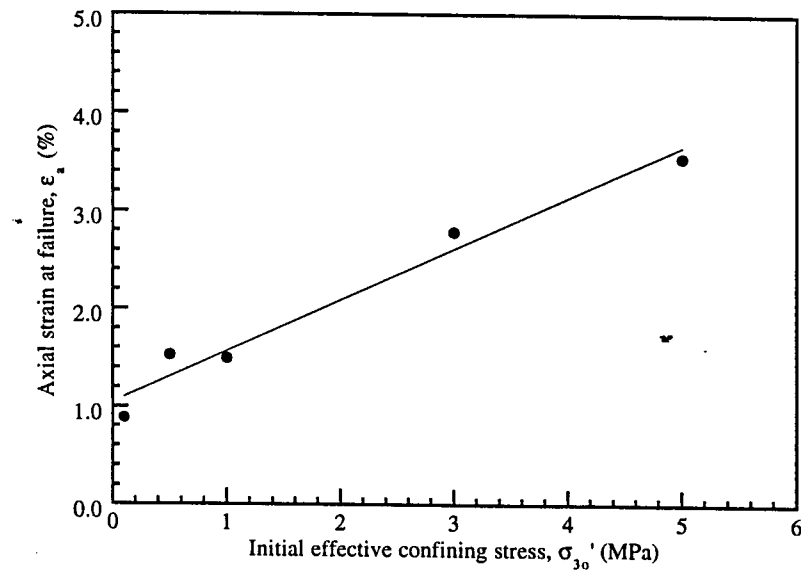


Fig 6.2.6 Axial Strain At Failure In CIU Tests

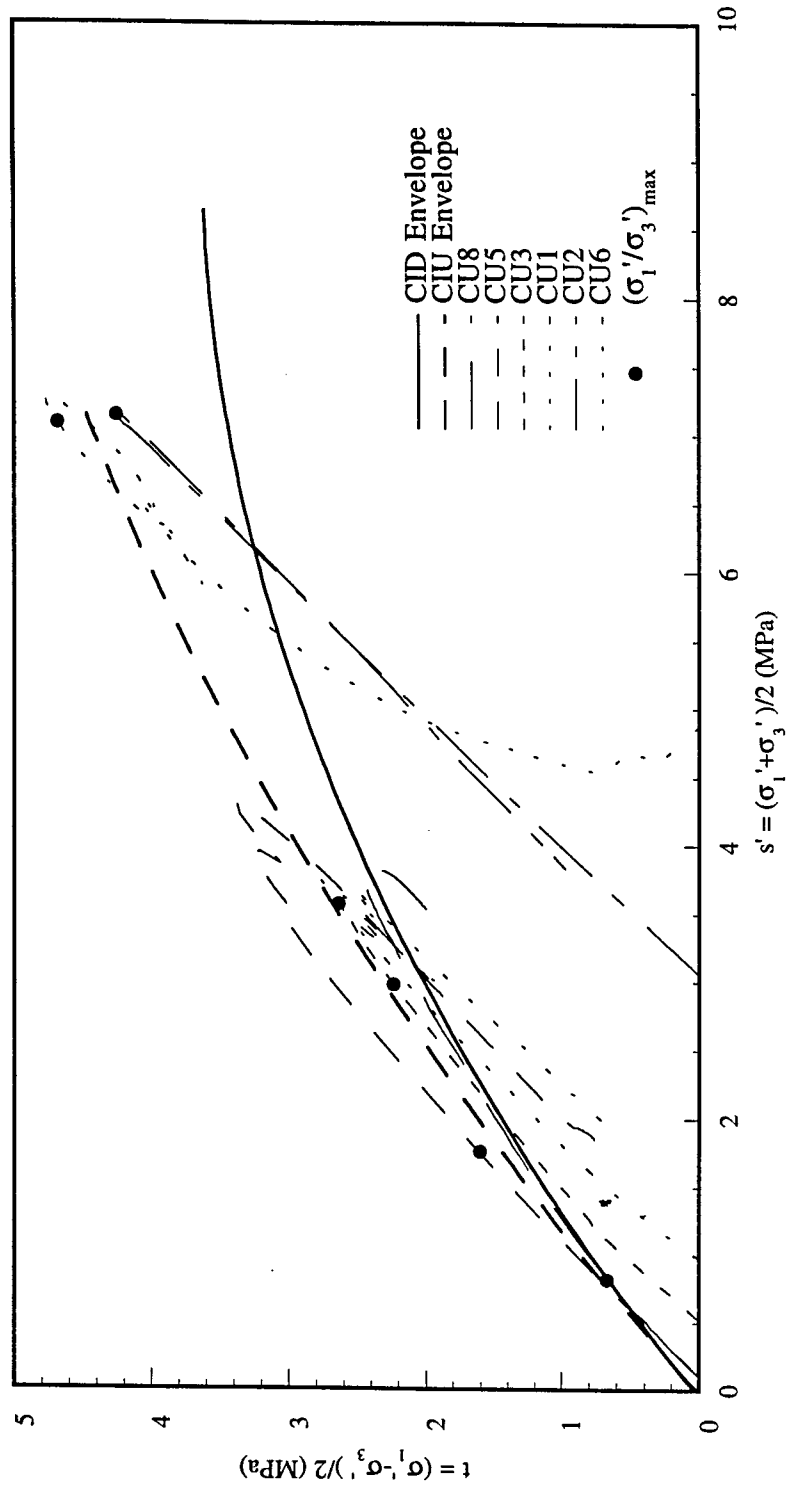


Fig 6.2.7 s' - t Stress Path In CIU Tests

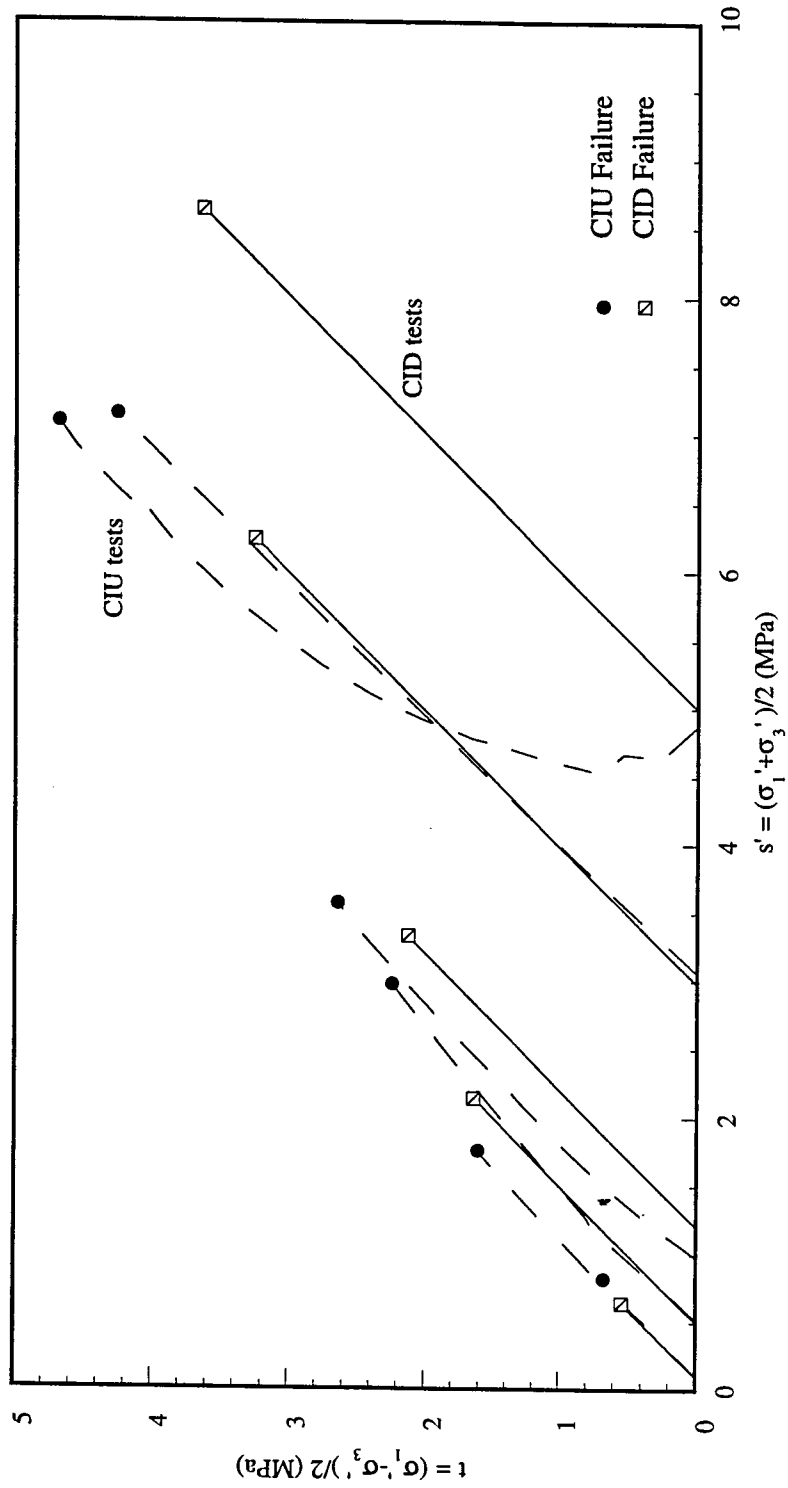


Fig 6.2.8 Comparison of Stress Paths in CID and CIU Tests

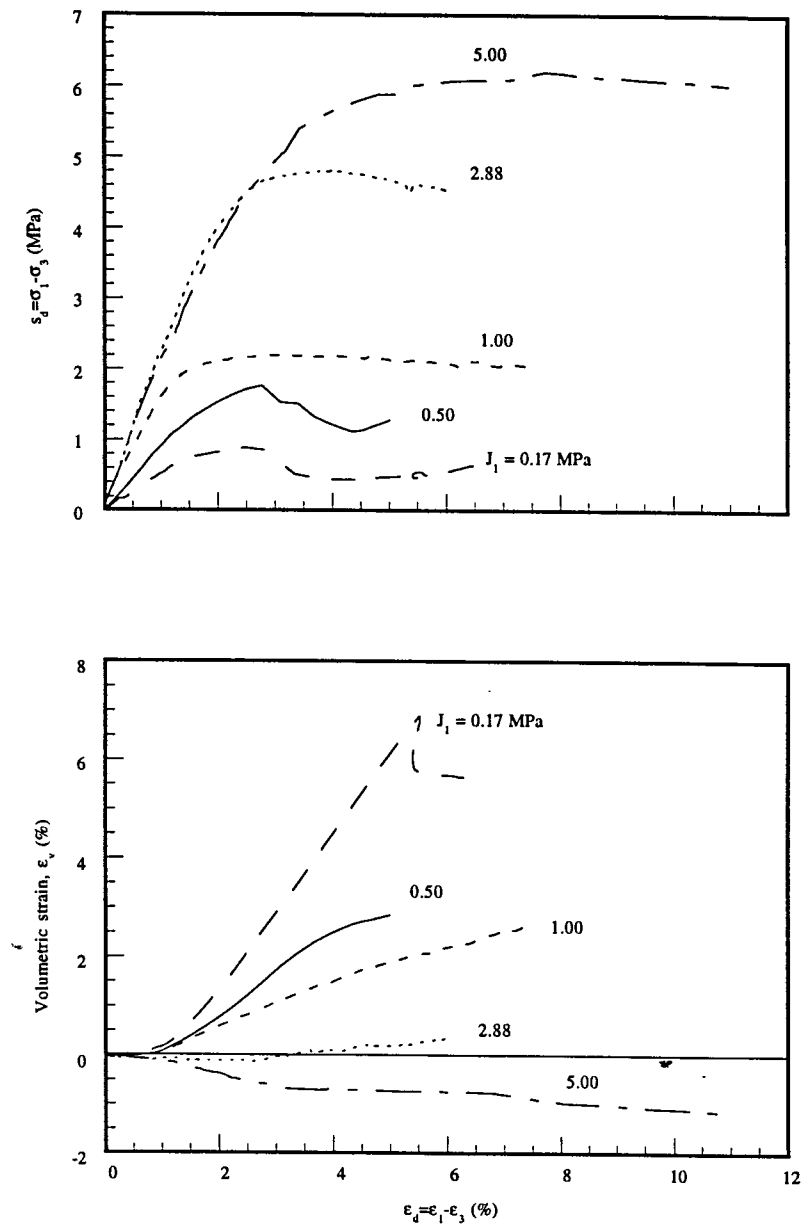


Fig 6.3.1 Stress-Strain Relationship and Volume change in CIP Tests

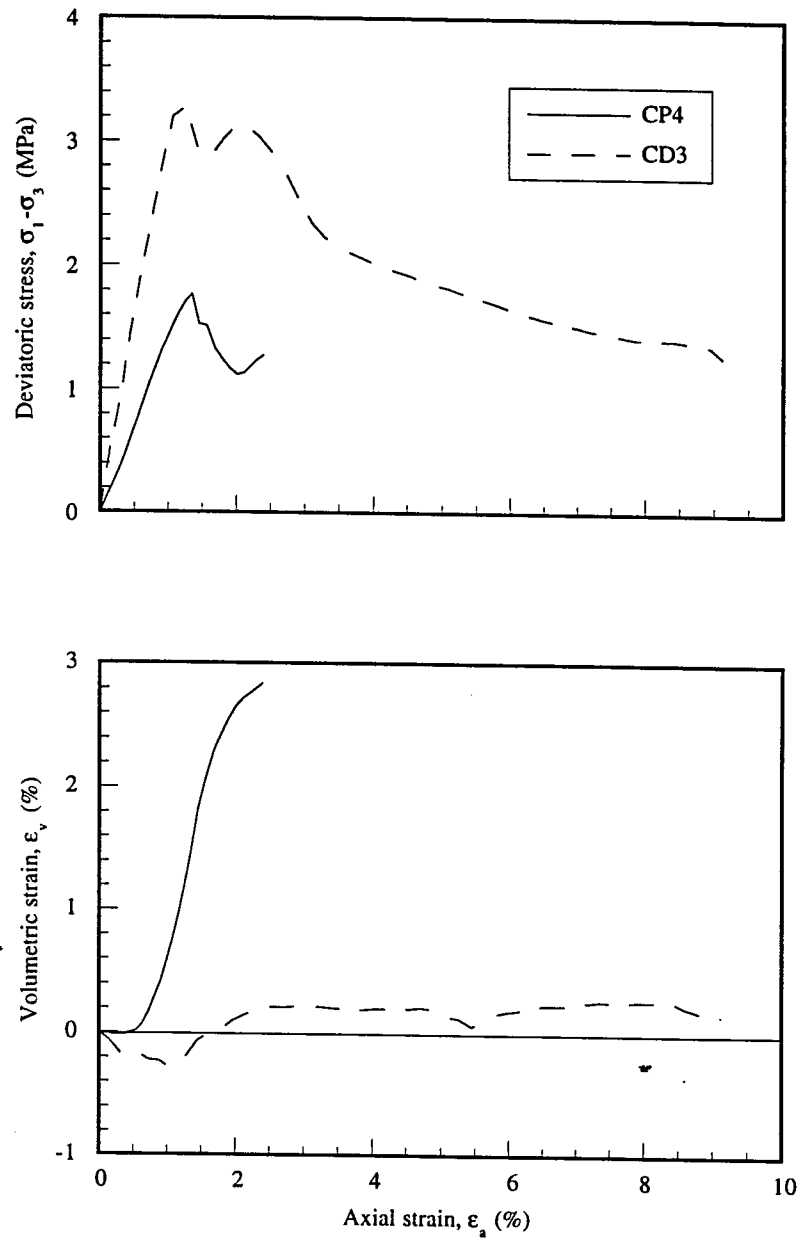


Fig 6.3.2 Stress-Strain Relationship And Volume Change in Tests CD3 and CP4

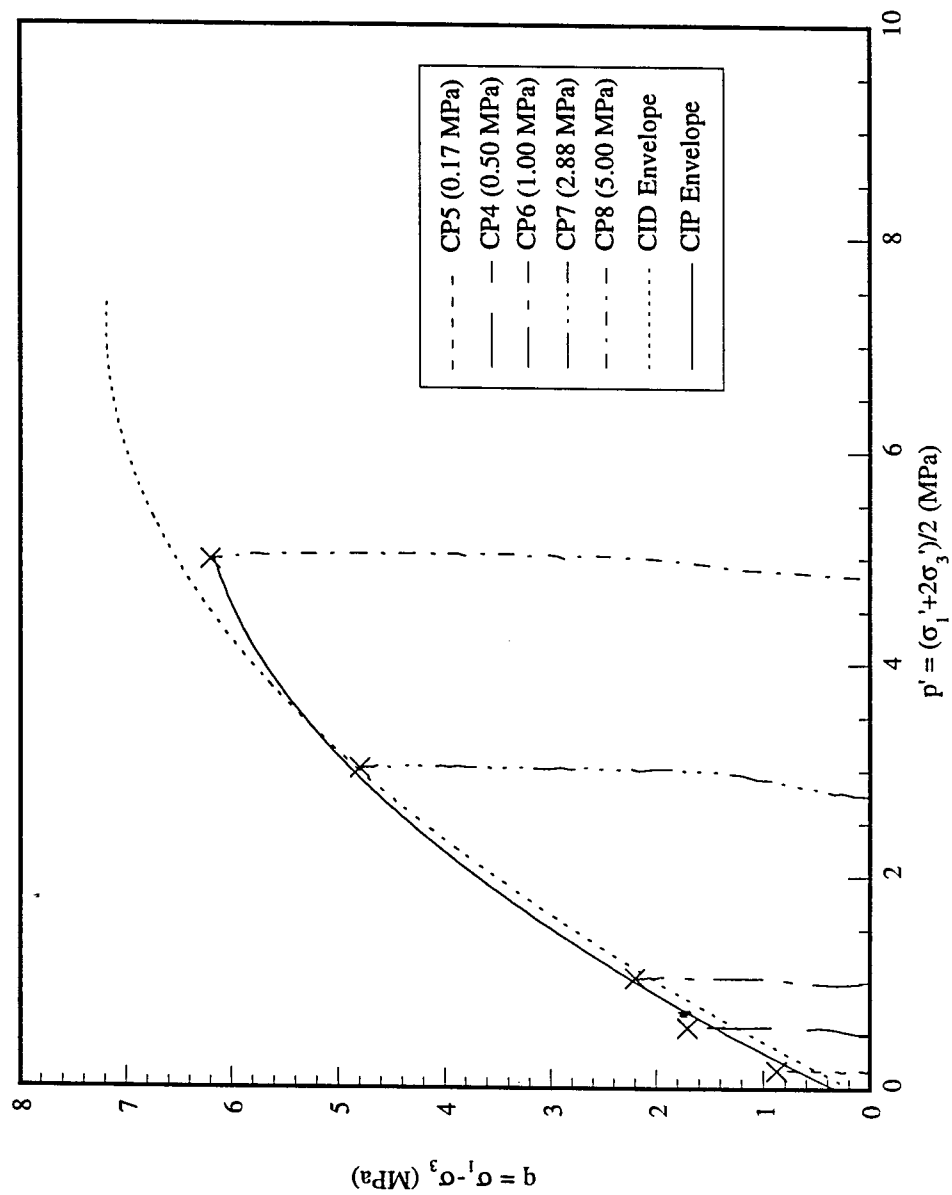


Fig 6.3.3 p' - q Stress Path In CIP Tests

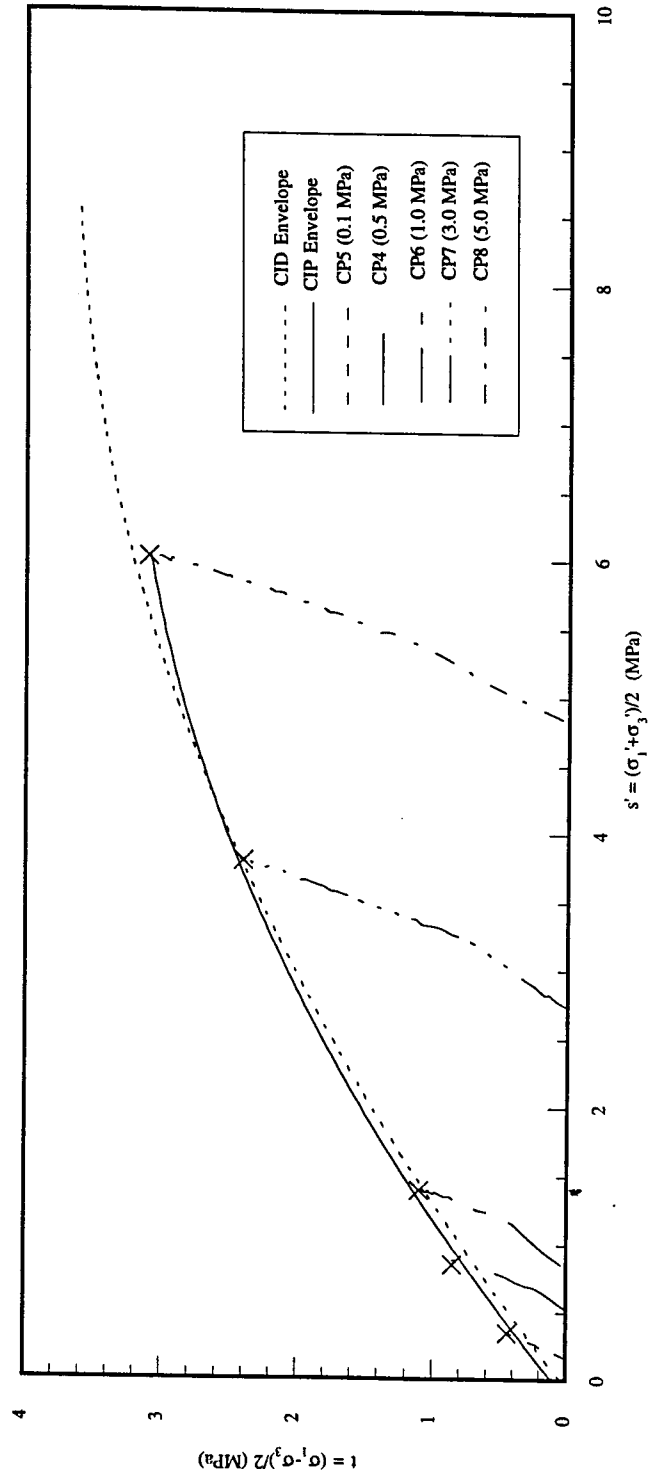


Fig 6.3.4 $s' - t$ Stress Path In CIP Tests

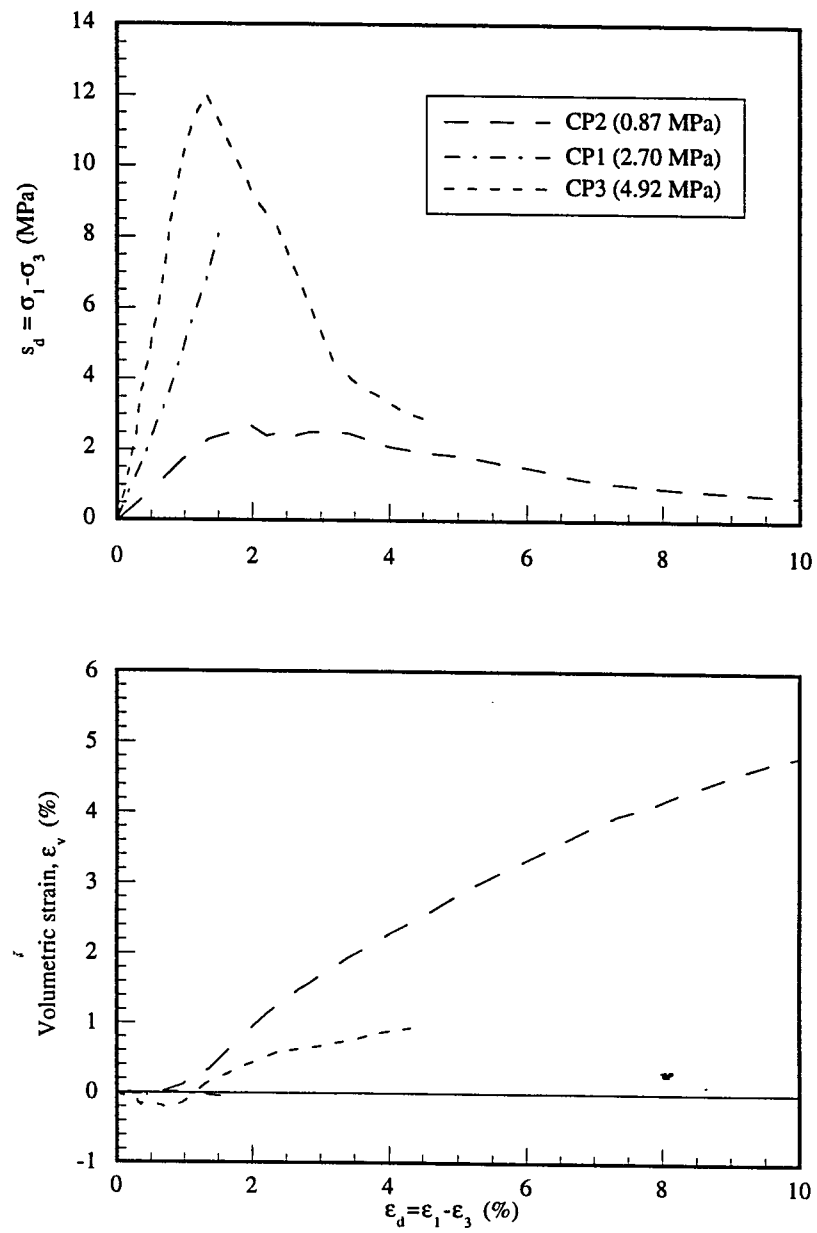


Fig 6.3.5 Stress-Strain Relationship and Volume Change in Tests CP1 to CP3

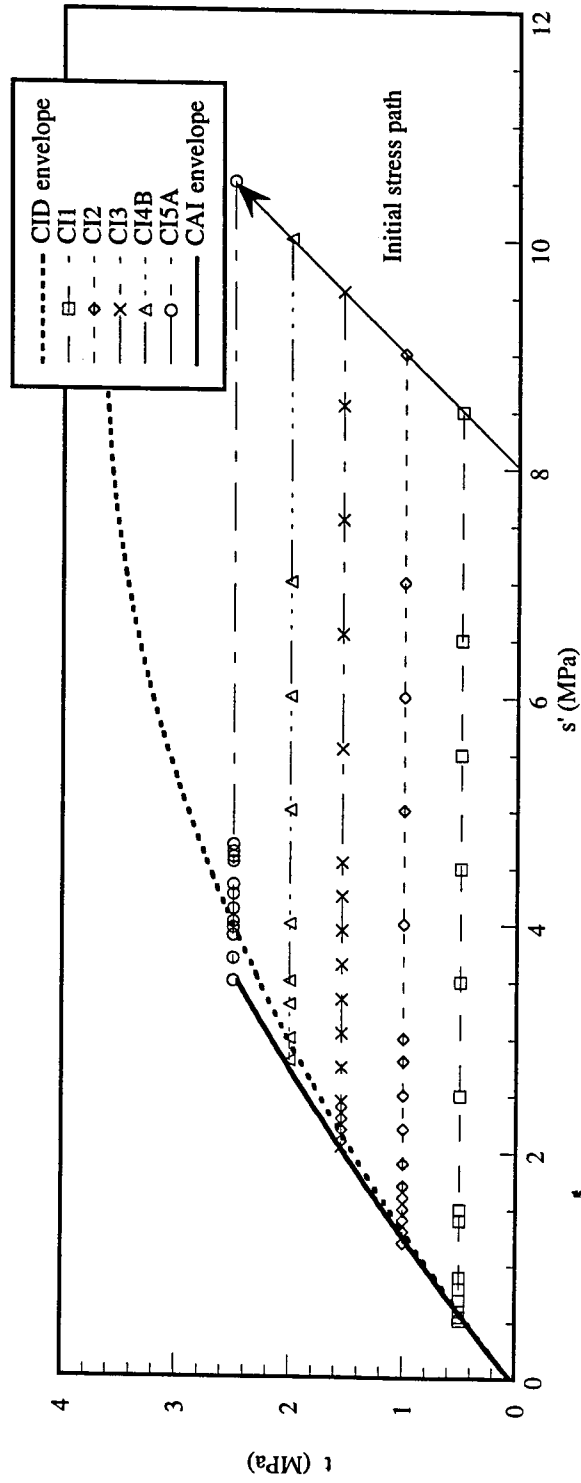


Fig 6.4.1 $s' - t$ Stress Paths in Pore Pressure Injection Tests

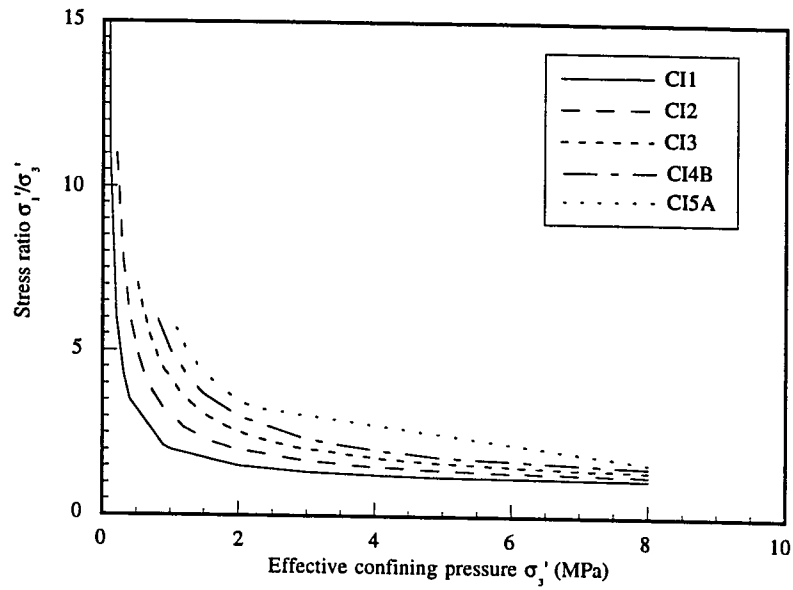


Fig 6.4.2 The relationship between stress ratio and effective confining pressure in CAI Tests

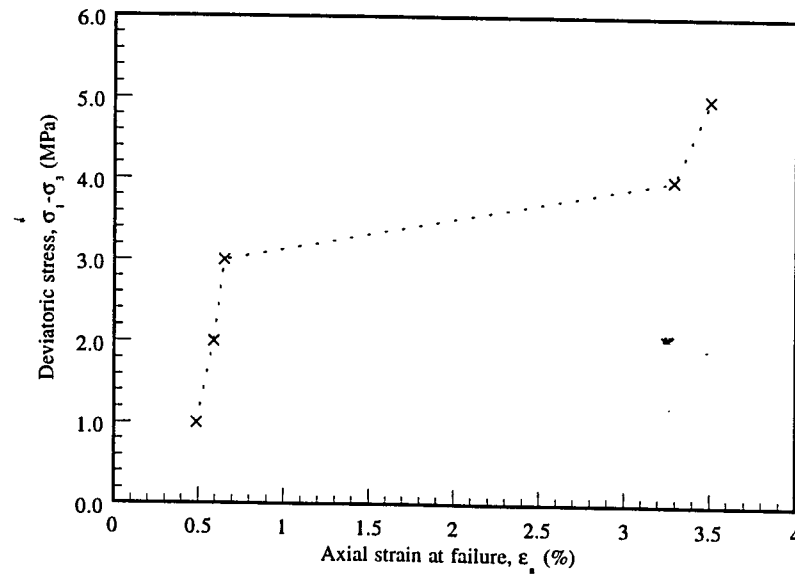


Fig 6.4.3 The Relationship Between Deviatoric Stress and Axial Strain at Failure in CAI Tests

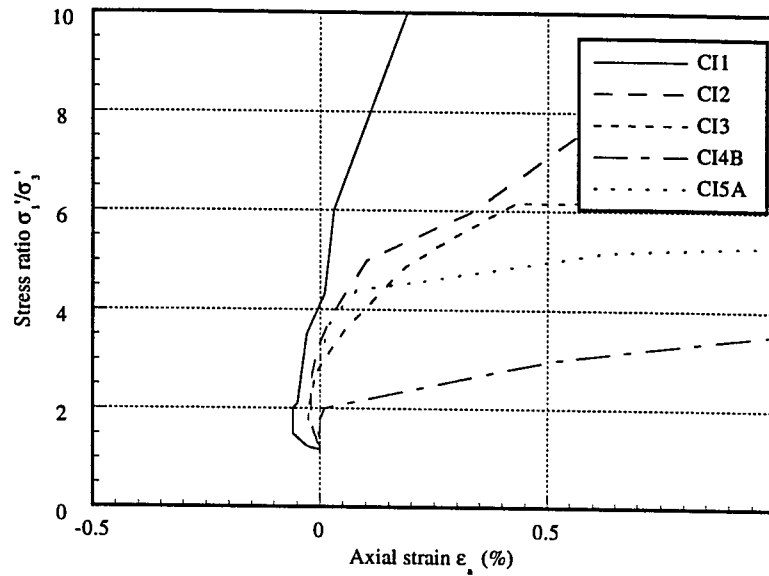


Fig 6.4.4a The Relationship Between Stress Ratio and Axial Strain in Pore Pressure Injection (Small Strain)

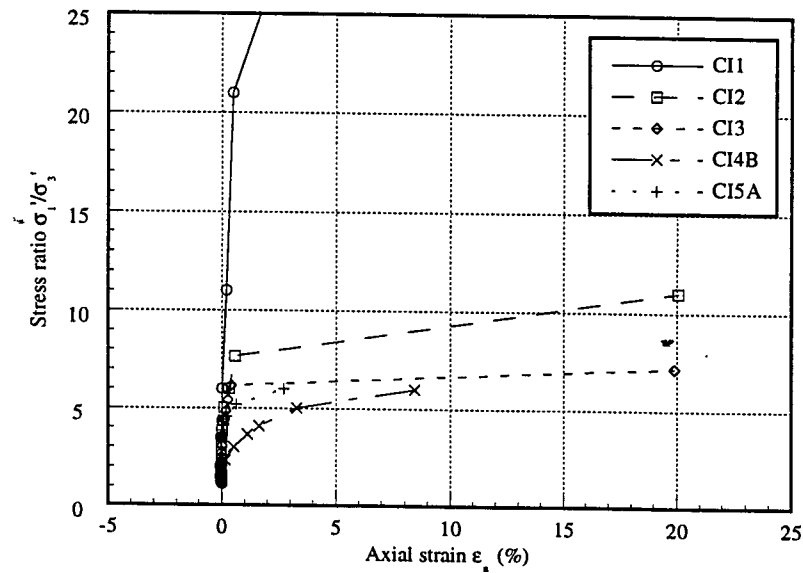


Fig 6.4.4 The Relationship Between Stress Ratio and Axial Strain in Pore Pressure Injection

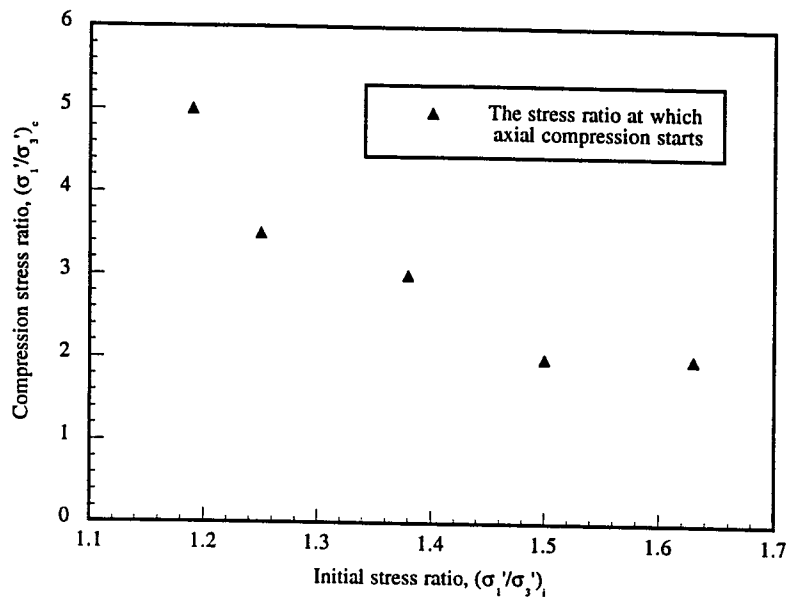


Fig 6.4.5 The Relationship Between Initial Stress Ratio and Compression Stress Ratio

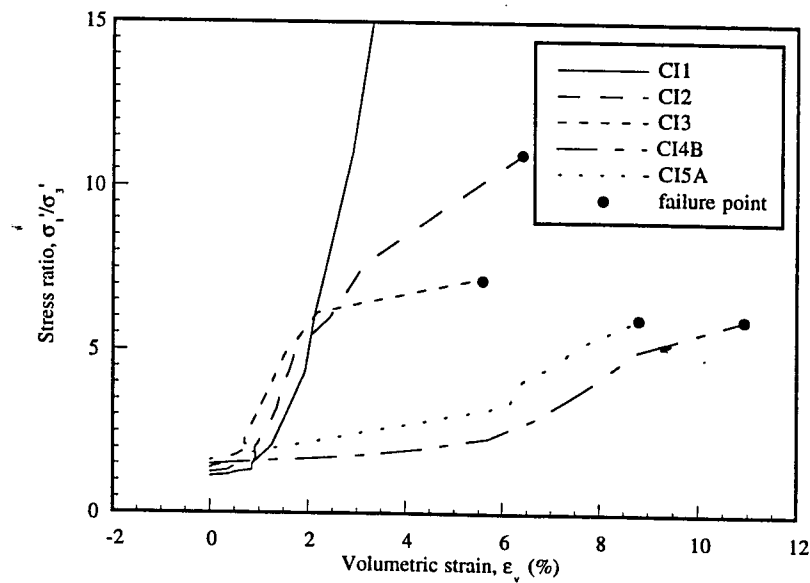


Fig 6.4.6 The Relationship Between Stress Ratio and Volumetric Strain in Pore Pressure Injection

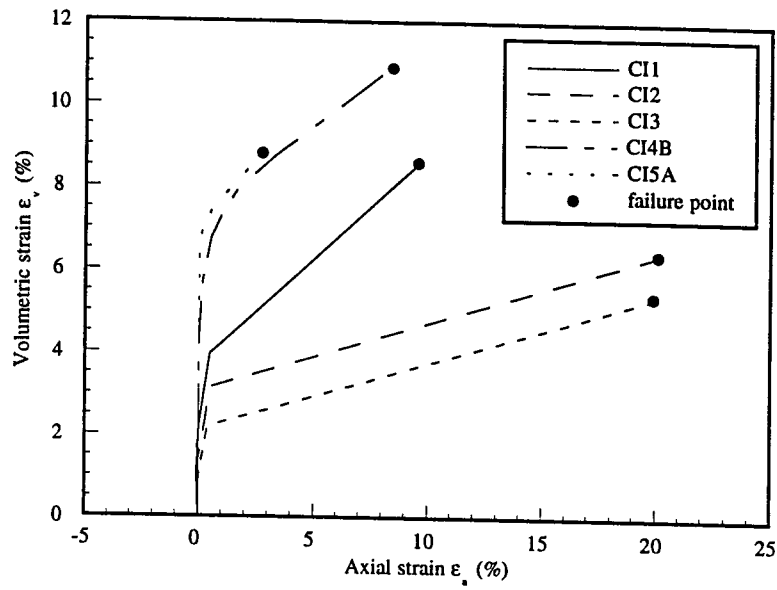


Fig 6.4.7 The Relationship between Volumetric Strain and Axial Strain in Pore Pressure Injection

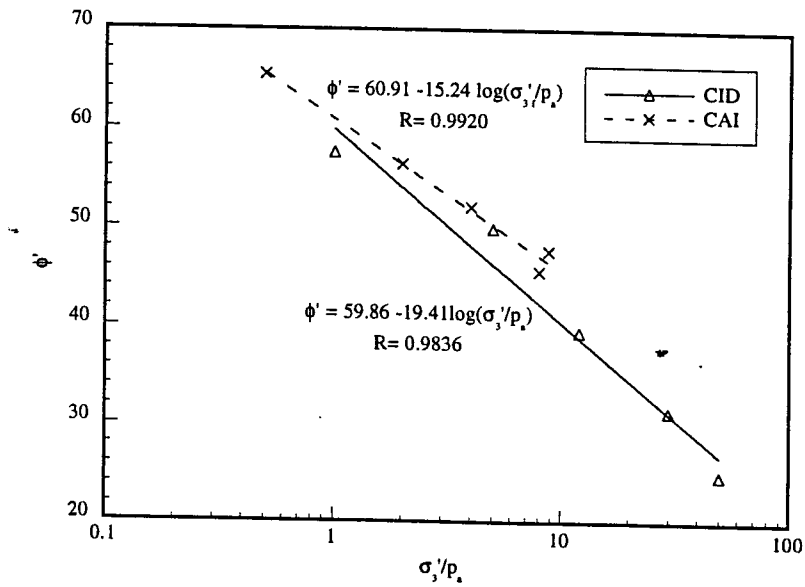


Fig 6.4.8 The Relationship Between Secant Friction Angle and Effective Confining Stress in CID and CAI Tests

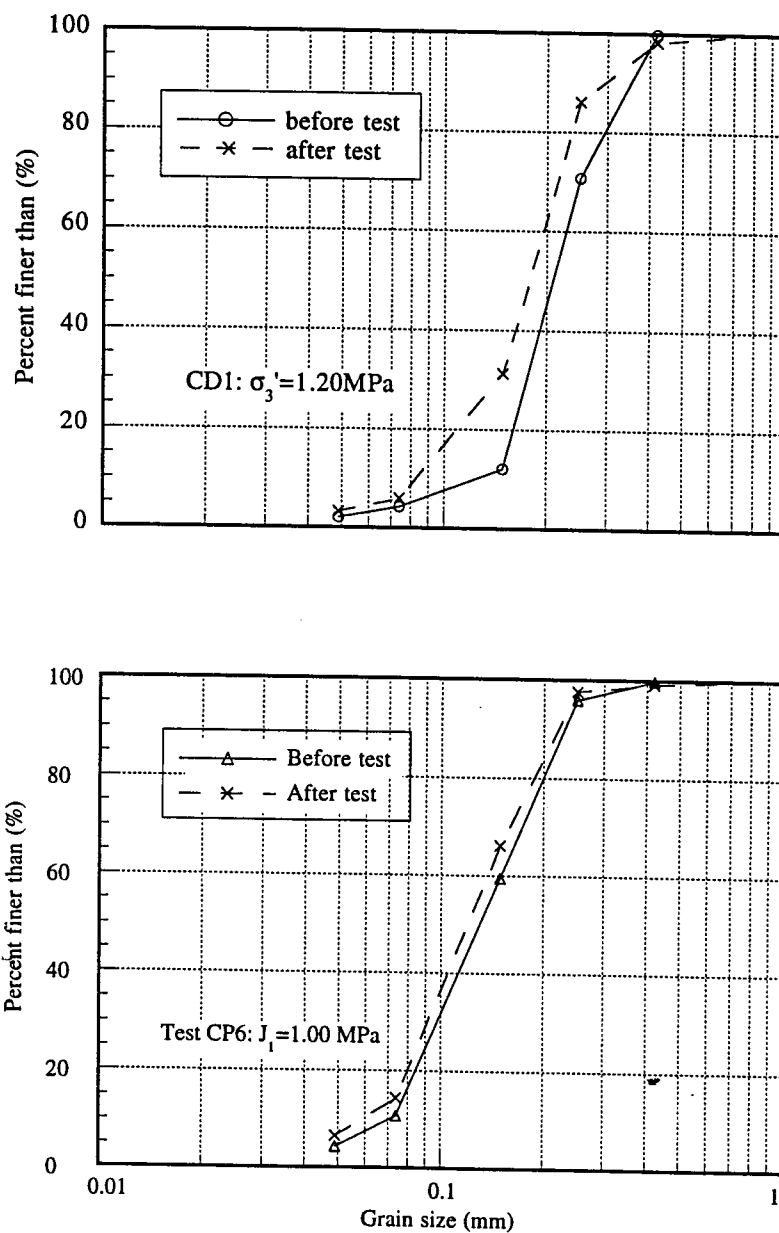


Fig 6.5.1 Comparison of Grain Size Distribution in Tests CD1 and CP6

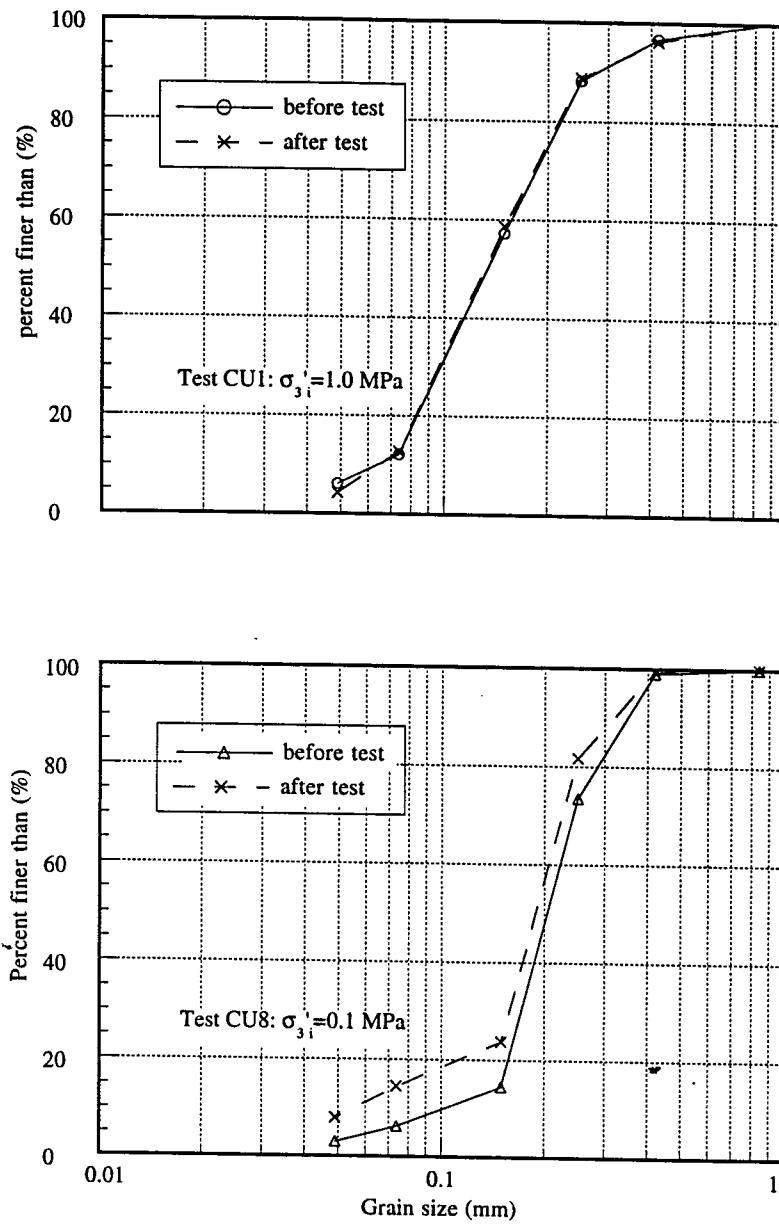


Fig 6.5.2 Comparison of Grain Size Distribution in Tests CU1 and CU8

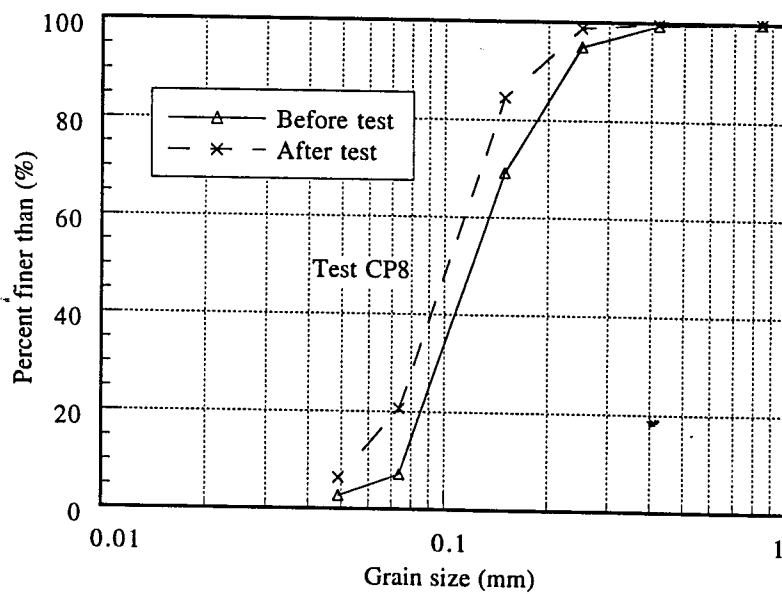
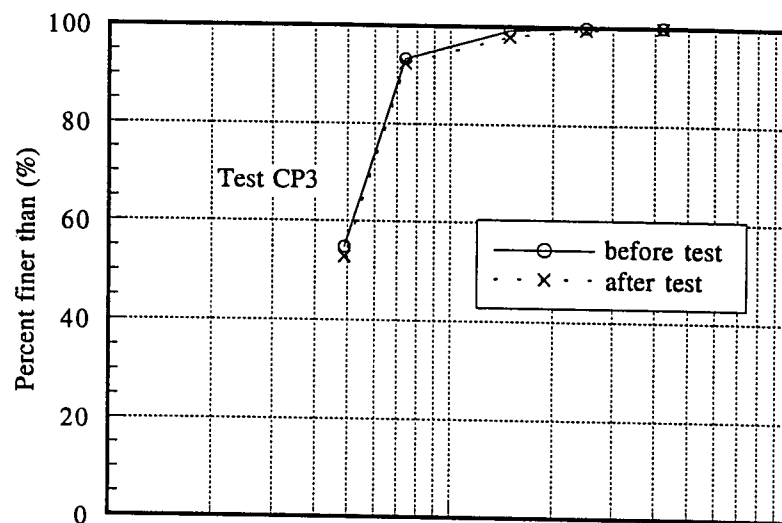


Fig 6.5.3 Comparison of Grain Size Distribution in Tests CP3 and CP8

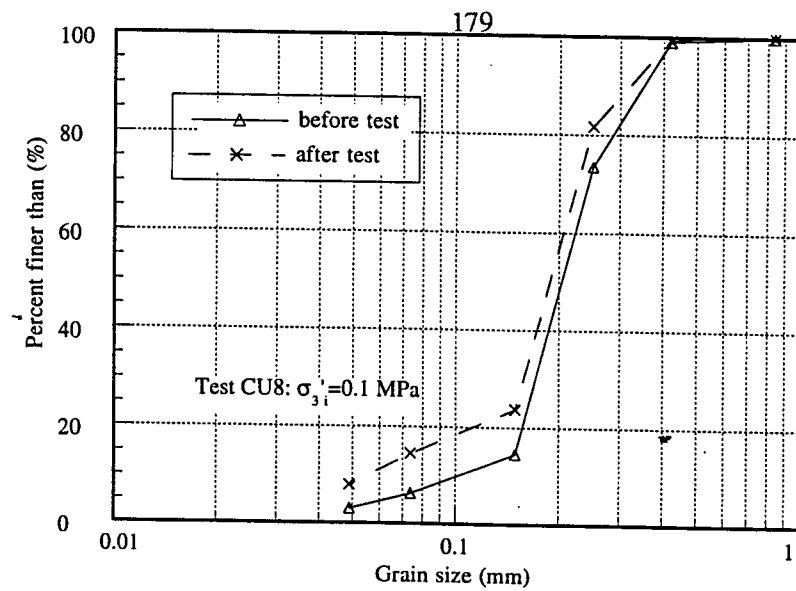
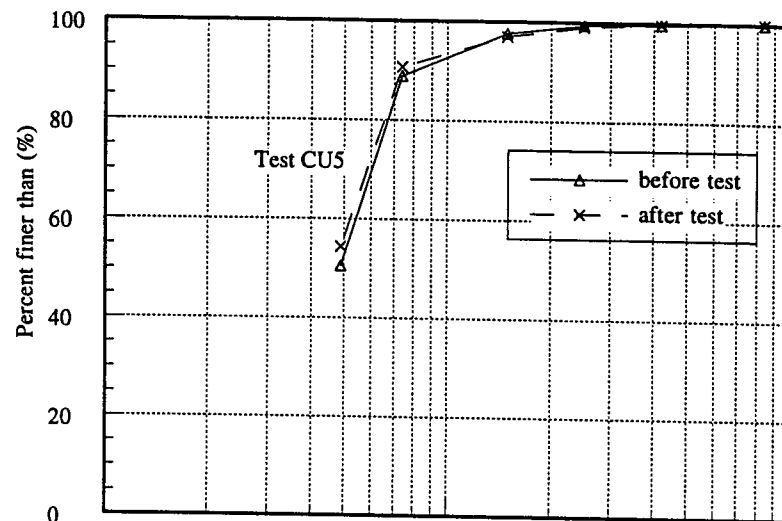


Fig 6.5.4 Comparison of Grain Size Distribution in Tests CU5 and CU8

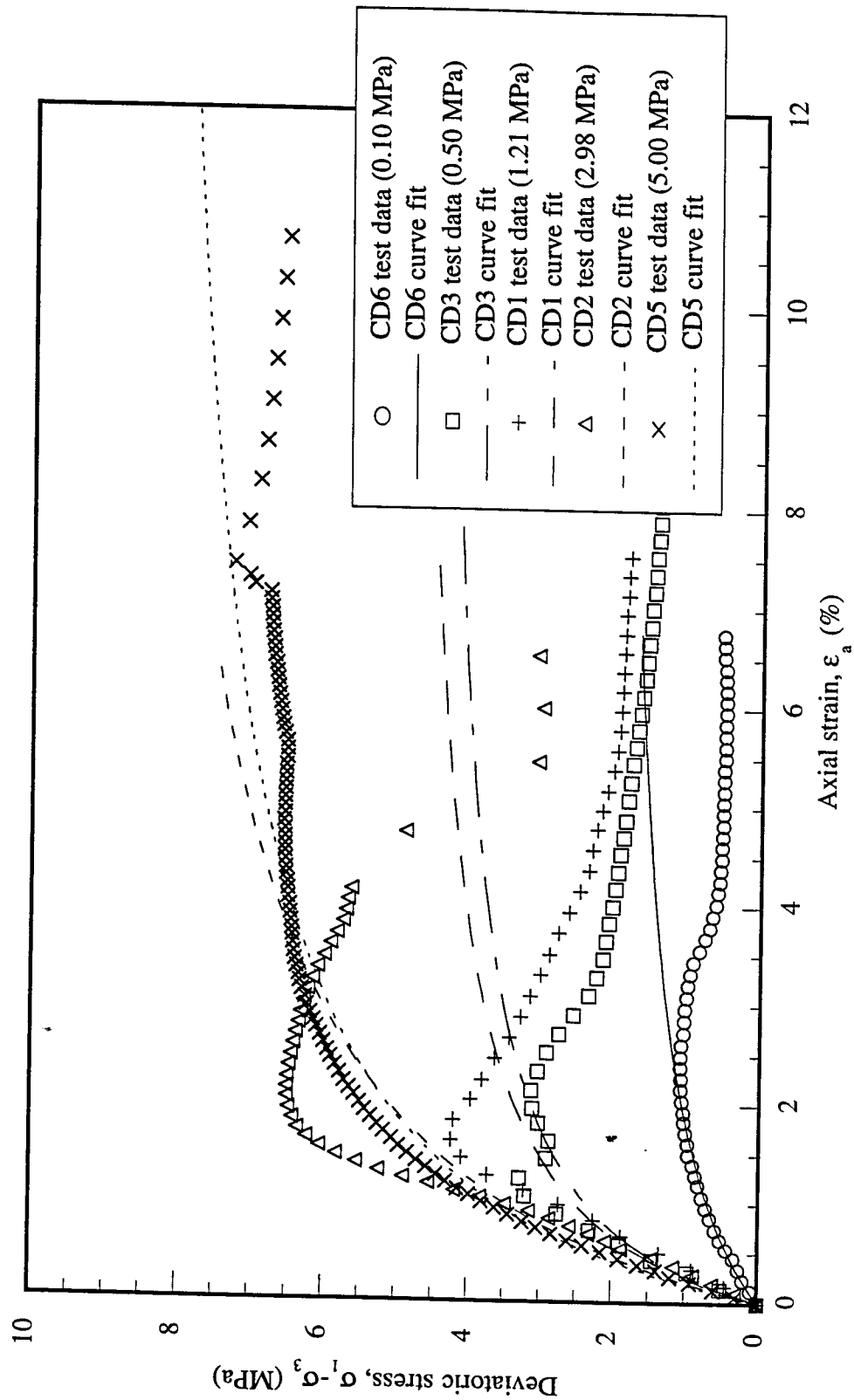


Fig 6.6.1 Stress-Strain Relationship In CID Tests and Hyperbolic Curve Fitting

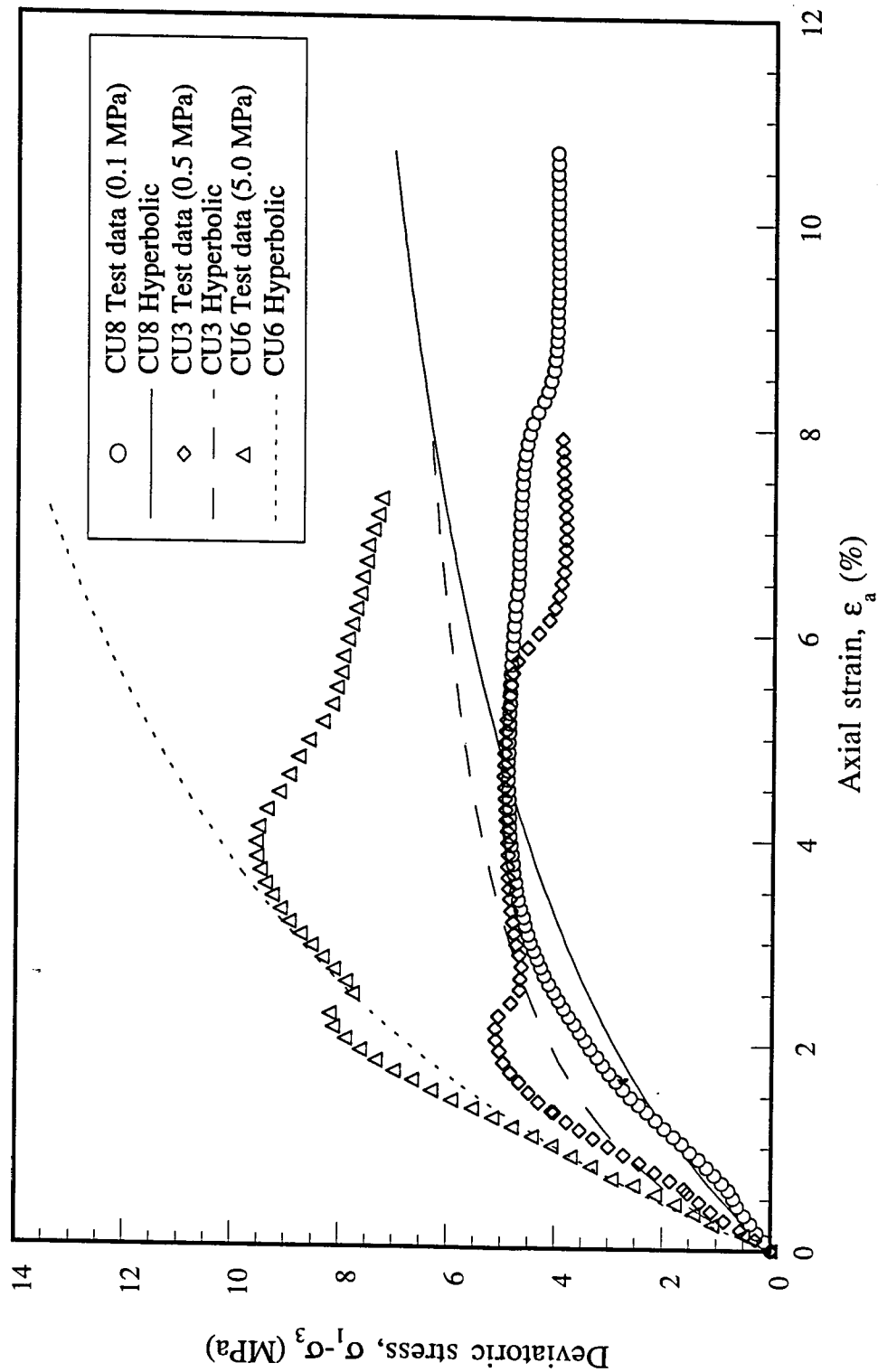


Fig 6.6.2 Stress-Strain Relationship in CIU Tests and Hyperbolic Curve Fitting

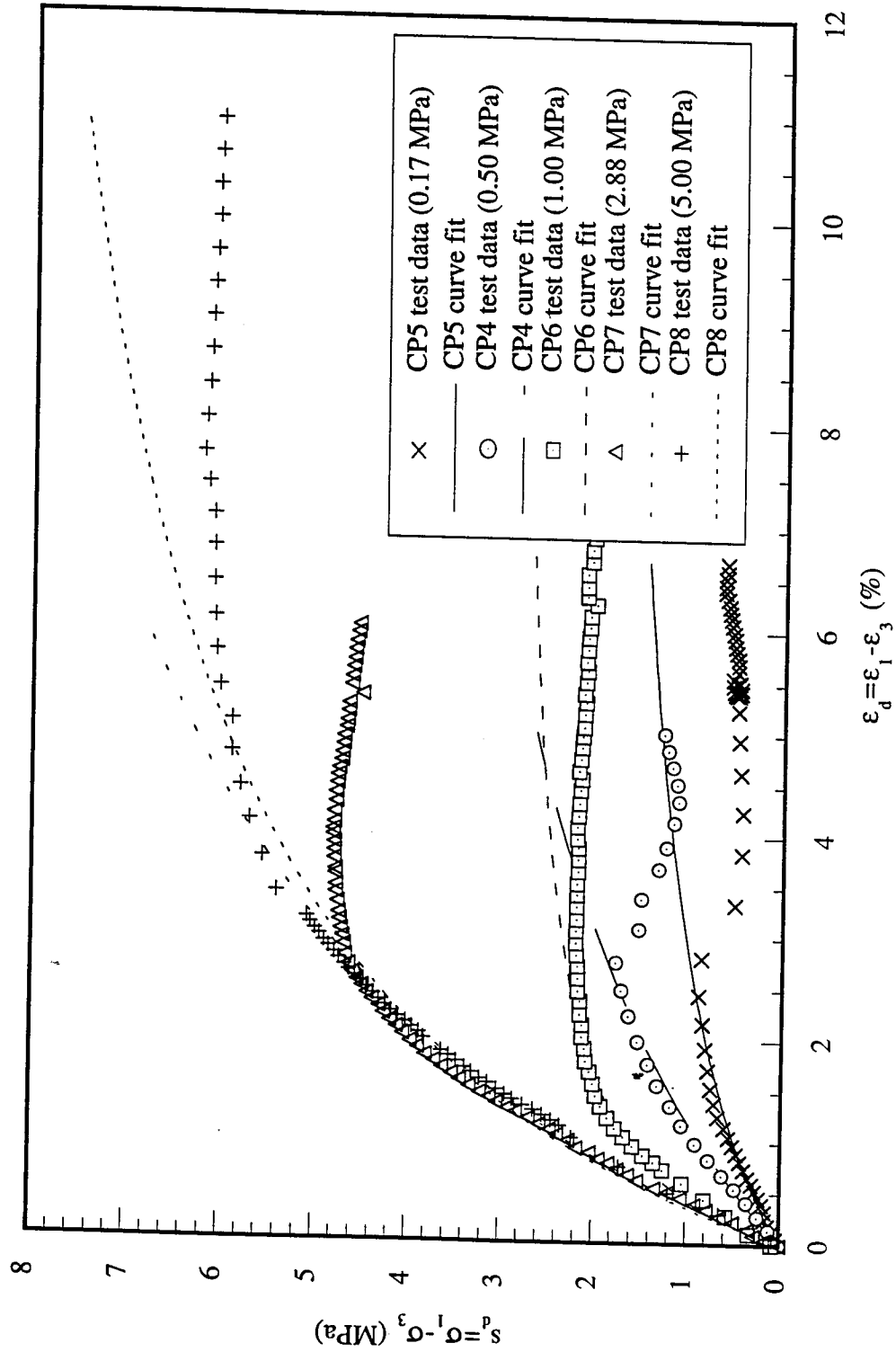


Fig 6.6.3 Stress-Strain Relationships In CIP Tests and Hyperbolic Curve Fitting

Chapter 7

Conclusions

7.1 Summary and Conclusions

Summarizing the test results presented previously, the conclusions are briefly stated as follows.

7.1.1 Isotropic Bulk Compressibility

1) The oil sands tested do not behave in an elastic manner in isotropic cyclic consolidation tests. Shear displacement usually occurs during the stress cycling and unrecoverable deformation appears in each stress cycle. Grain crushing causes the unrecoverable deformation due to the weakness of the mineral composition.

2) The isotropic bulk compressibility of the oil sands tested is a function of effective confining stress. It is not governed by the theory of elasticity. Since the bulk compressibilities for unloading and reloading do not follow the same path they must be evaluated separately. It was found that the bulk compressibilities for unloading or for reloading in different stress cycles bear the same magnitude. They may be represented by one curve statistically which can be expressed as a power function.

$$C_b = a \sigma'_3{}^b \quad (5.2.2)$$

Where the average **a** and **b** for unloading are 4.83 and -1.26 respectively and for reloading 5.02 and -0.65 respectively. The difference in bulk compressibility between unloading and reloading is mainly shown in exponent **b** not in constant **a**.

3) Two important factors, grain size distribution and sample disturbance, significantly influence the compressibility of the oil sand deposits. The constants **a** and **b** vary within a very limited range, provided that the grain size distribution is similar. The finer grained oil sands are less compressible than the coarser grained oil sands. The greater the sample disturbance, the higher the compressibility value even after isotropic stress cycling.

4) The in situ bulk compressibility of the oil sands can be estimated using the relationship between compressibility and index of sample disturbance by extrapolating to the in situ porosity. The estimated in situ compressibility for the oil sands tested can be expressed as

$$\text{Unloading: } C_b = 4.83 \sigma_3'^{-1.24} \quad 10^{-3} \text{MPa}$$

$$\text{Reloading: } C_b = 4.41 \sigma_3'^{-0.66} \quad 10^{-3} \text{MPa}$$

5) The bulk compressibility of the oil sands tested varies dramatically in the low stress range. In most cases, when the effective confining stress is lower than 2.0 MPa, a small variation of effective confining stress will result in a significant change in bulk compressibility. The boundary stress, σ_b' , which separates the low stress range and the high stress range for all specimens tested was calculated to be about 2.0 MPa.

7.1.2 Stress-Strain Behavior Following a CID Stress Path

1) In CID tests, the effective confining stress controls the stress-strain -volume change behavior of the Grand Rapids Formation oil sands tested. Ductile behavior in stress-strain response does not occur until the effective confining stress exceeds 3.0 MPa. The CID shear strength is a function of the effective confining stress. The $s' - t$ stress path curve which defines the failure envelope can be fit using the polynomial relationship:

$$\tau = 0.0420 + 0.7896s' - 0.0435s'^2 \quad \text{MPa}$$

2) At low effective confining stresses, below 0.5 MPa, the Grand Rapids oil sands behave as other dense sands similar to the McMurray oil sands. At effective confining stresses above 0.5 MPa, grain crushing during shear starts to affect the stress-strain-volume change behavior, unlike the McMurray oil sands. At stresses above 3.0 MPa, grain crushing dominates the behavior of Grand Rapids oil sands during shear. An effective confining stress of 3.0 MPa can be considered to be the 'break down' stress.

3) The shear strength of the Grand Rapids oil sands tested is significantly lower than that of Athabasca McMurray oil sands because of the weak mineral compositions. However, the shear strength of the oil sands tested is similar to that of Clearwater Formation oil sands from both Athabasca and Cold Lake due to the similar mineralogy and grain size distribution.

4) The tangent modulus of the oil sands is stress dependent increasing with an increase in the effective confining stress. The initial tangent moduli are relatively small. They make up the lower boundary of all the test results reported by Agar (1984), Kosar (1989) and Wong et al (1993). The Poisson's ratio varies from 0.14 to 0.42 with an average of 0.26.

5) The secant internal friction of the oil sands tested has a linear relationship with the effective confining stress normalized to the atmospheric pressure in a semi-log plot

$$\phi' = 59.86 - 19.41 \log(\sigma_3'/p_a)$$

The slope of the line is almost the same as that for Athabasca McMurray Formation oil sands reported by Agar (1984) but the intercept is smaller by 12 degrees. The secant

internal friction angle of Clearwater Formation oil sands from both Athabasca and Cold Lake are very close to the test results for the Lower Grand Rapids Formation oil sands.

7.1.3 Stress-Strain Behavior Following a CIU Stress Path

1) The specimens in the undrained triaxial compression tests (CIU) did not fall on the failure envelope defined by the drained triaxial compression tests (CID). The failure envelope following the CID stress path, therefore, does not represent the failure criteria for the CIU tests. A new failure envelope for the CIU tests was established, which is above the CID failure envelope. Grain crushing whose magnitude is controlled mainly by state of stress and stress path was the reason for the variation in the failure criteria.

2) The pore pressure in the CIU tests varied in direction depending on the initial σ_3' . Below an initial σ_3' of 3 MPa, the pore pressures at large strains were negative while above 3 MPa they were positive. This difference in direction mirrored the direction of change in volume in the CID tests. Therefore, the CID test results and the CIU test results agreed with each other.

3) The change in pore pressure which reflects the tendency for dilation and contraction in shear is stress dependent and associated with the magnitude of grain crushing. The initial effective confining stress of 3.0 MPa is found to be the 'break down' stress at which there is almost no change in pore pressure throughout shearing. This agrees with the CID test results. Below the 'break down' stress, rotation of the grains caused by shear plays a dominant role in the failure mechanism. Above the 'break down' stress, grain crushing dominates the failure mechanism.

4) The stress paths experienced in the undrained triaxial compression tests resemble the drained triaxial compression test stress paths before failure occurs, provided the initial effective confining stress is less or equal to 3.0 MPa. Since there is almost no change in pore pressure at the 'break down' stress of 3.0 MPa, the CIU stress path is superposed on the CID stress path. At an initial effective confining stress above 3.0 MPa,

the pore pressure increases dramatically with axial strain. In this case, the CIU stress path is totally different from the CID stress path.

5) Fine grains appear to increase the undrained shear strength of the oil sands. With a similar bulk density, less grain crushing is mobilized for a fine grained specimen than a coarse grained specimen. A more negative change in pore pressure at a low initial effective confining stress or a less positive change in pore pressure at a high initial effective confining stress is induced by an increase in the fines content. As a result, the undrained shear strength of a fine grained specimen is higher than that of a coarse grained specimen.

6) There does not exist an unique steady state for the Lower Grand Rapids Formation oil sands based on the test results. Further study may be needed to explore the behavior at steady state.

7.1.4 Stress-Strain Behavior Following a CIP Stress Path

1) The shear strength of the oil sands is dependent on J_1 . It increases with an increase in J_1 . The shear modulus of the oil sands with a constant J_1 is dependent on deviatoric stress. It decreases with the increase in the deviatoric stress. The shear modulus of the oil sands is also a function of J_1 . The initial shear modulus increases with an increase in J_1 .

2) The shear strength of the oil sands following a CIP stress path is smaller than that following a CID stress path when the initial stress conditions are the same because the CID stress path incorporates consolidation into the process of shear to further densify the specimen, while the CIP stress path only reflects the effect of pure shear.

3) Compared with the CID stress path, the volume change behavior is more dilative than contractive in CIP tests. The difference between the two volume changes measured in CID and CIP tests is the result of changes in mean effective normal stress.

4) The CID failure envelope can represent the failure criteria for the CIP tests.

5) Fines content appears to strengthen the oil sands during shear. Following the CIP stress path, the shear strength of oil sands containing more fine grains is greater than that containing less fine grains. Less breakage of the fine grains is probably the cause of this behavior.

7.1.5 Behavior of the Oil Sands in Pore Pressure Injection

1) The initial effective stress ratios which represent in situ stress conditions control the stress-strain behavior of the Cold Lake Lower Grand Rapids Formation oil sands in the pore pressure injection tests. The deviatoric stress which can be represented by the initial effective stress ratio dominates the axial strain at failure. A high deviatoric stress causes a large positive axial strain at failure.

2) The failure envelope for the CAI tests is slightly above the CID failure envelope indicating that the CAI measured shear strengths are greater.

3) The axial deformation starts with an axial extension at the beginning of a pore pressure injection test. Axial compression does not occur until the compression stress ratio is reached. The compression stress ratio decreases with an increase in the initial stress ratio and ranged from 2 to 5. A lower initial effective stress ratio causes more axial extension.

4) All CAI test specimens increased in volume right from the beginning of the tests regardless of the initial effective stress ratio. The larger the initial effective stress ratio, the greater the increase in volume.

5) The volume change in a pore pressure injection test is a joint effect of axial and lateral deformation. At a low initial effective stress ratio the volume expansion results from both axial extension and lateral expansion at the beginning of the pore pressure injection, and then the lateral expansion controls the volume change after the compression stress ratio is reached. At a high initial effective stress ratio, the lateral expansion dominates the volume change behavior throughout the test with only a small amount of axial extension at the beginning of the test.

6) The secant internal friction angle at failure is a function of the effective confining stress at failure. It decreases with an increase in the effective confining stress. The friction angles in the pore pressure injection tests are slightly larger than those in the CID tests. It may indicate that the shear strength behavior of the oil sands is somewhat stress path dependent.

7.1.6 Grain Crushing Behavior

1) Grain crushing occurs in all the tests following different stress paths. Since the Lower Grand Rapids Formation oil sands consist of more weak minerals than the Athabasca McMurray Formation oil sands, the grains are easier to break when subjected to an isotropic stress change or a deviatoric stress change.

2) The larger amount of feldspar grains and rock fragments in the oil sand specimens are susceptible to shear induced grain crushing and are the main reason for the grain crushing which occurred.

3) The magnitude of the effective confining stress controls the grain crushing behavior. The effective confining stress of 3.0 MPa is the 'break down' stress, below which dilatancy dominates the stress-strain and volume change behavior and above which grain crushing becomes the main mechanism.

4) Considering that the grain size distribution and mineralogy of all specimens are similar, the CID stress path creates more grain breakage than the CIP stress path. In the CIU test, the change in pore pressure during shear influences the magnitude of grain crushing. A positive change in pore pressure reduces the magnitude and a negative change in pore pressure increases the magnitude.

5) Following the same stress path, coarse grains appear to be more vulnerable to breakage than fine grains.

7.1.7 Application of a Hyperbolic Model

1) A hyperbolic model can only approximately simulate the stress-strain behavior of the Lower Grand Rapids Formation oil sands. It is not considered to be a satisfactory model. The model is suitable for simulating the stress-strain behavior prior to peak and a small portion of post peak, if strain weakening is not significant.

2) Volume change behavior and the change in pore pressure encountered in the tests can not be represented by the model because of the dilation and grain crushing which takes place during shear.

3) For the different stress paths followed in this testing program, the CIP test data had the best agreement with the model, the CIU data had the worst fit with the model because of the shape of the stress-strain curves.

4) Unlike other types of sands, R_f of the oil sands determined from the modeling varies in a relatively large range. It changes from 0.44 to 0.85 in the CID tests, 0.44 to 0.66 in the CIU tests and 0.32 to 0.72 in the CIP tests.

5) Analysis of the test results indicates that the stress-strain behavior of the oil sands is not governed by the theory of elasticity. Shear modulus, G , and tangent modulus, E_t , are not linearly related.

7.2 Further Studies

The following problems and omissions were encountered in this testing program. First of all, some specimens used in the testing program were trimmed from slabbed cores because of the lack of preserved whole core. Some of the core had dried out during storage. These factors have contributed to some reduction in the accuracy of the measurements and increased the variation in the oil sands behavior. Secondly, the grain crushing behavior in isotropic cyclic consolidation was not measured. Although all the specimens experienced similar isotropic stress cycles and the magnitude of grain breakage

could be assumed to be the same for each specimen, the influence of a stress path on grain crushing after the isotropic cyclic consolidation could not be evaluated separately because the magnitude of grain breakage caused by the isotropic cyclic consolidation remained unknown. Thirdly, the research was limited to the Lower Grand Rapids Formation oil sands. To obtain a general framework of the constitutive behavior of the oil sands in the Cold Lake region, a study on other formations is required, if worthwhile in terms of oil reserves and in situ recovery.

This thesis has been written so that the test results can be used to develop a constitutive model of the Lower Grand Rapids Formation oil sands. Such a constitutive model should be developed within the critical state theoretical framework.

The stress-strain behavior of the Cold Lake oil sands, especially, the behavior at a low effective confining stress, has been studied in this testing program. To model the stress-strain and volume change behavior, some difficulties are encountered. Since both dilation and grain crushing are involved in the shearing process, the volume change behavior is dominantly controlled by dilation at a relatively low effective confining stress and by grain crushing at a relatively high effective confining stress. This makes the volume change behavior unpredictable. The theory of dilation may be used to evaluate the volume change behavior at a low effective confining stress. Furthermore, if the magnitude of grain crushing can be predicted, it may help evaluate the volume change behavior taking the volume contraction caused by grain breakage into account. To develop a mathematical model, a few constitutive relationships are required. Limiting the influence factors on grain crushing to stress state and stress path, first of all, the relationship between effective confining stress and the magnitude of grain crushing following a specific stress path needs to be investigated. Secondly, a relationship between stress path and grain crushing is required. Finally, the relationship between the magnitude of grain crushing and volume contraction needs to be found in order to establish the constitutive relationship for stress-strain-volume change.

As an aid in developing constitutive models, future testing procedures should include close visual observations of the specimens during shear testing. The stress and strain levels when shear bands or other failure mechanisms can first be seen should be noted.

A testing program should be designed, in which the physical conditions of the specimens are controlled. Sand of the appropriate mineralogy with selected grain sizes of the proper diameter should be used to make specimens. The test results should be verified with undisturbed specimens including oil sands and other types of sands with similar mineralogy.

Reference

- Agar, J. G., 1984. Geotechnical Behavior of Oil Sands at Elevated Temperatures and Pressures. Ph.D. Thesis, Department of Civil Engineering, University of Alberta, 472p.
- Agar, J. G., Morgenstern, N. R. and Scott, J. D., 1987. Shear Strength and Stress-strain Behavior of Athabasca Oil Sands at Elevated Temperatures and Confining Pressures. Canadian Geotechnical Journal, Vol. 24, No. 1, pp 1-10.
- Au, K.-S., 1983. The Strength -deformation Properties of Athabasca Oil Sands. M.Eng. Report, Department of Civil Engineering, University of Alberta.
- Barden, L., Ismail, H. and Tong, P., 1969. Plane Strain Deformation of Granular Material at Low and High Pressures. Geotechnique 19, No: 4, pp 441-452.
- Beckie K.M. and McIntosh R. A. 1991. Geology and Resources of the Primrose Crude Bitumen Deposits Northeastern Alberta. Canadian Heavy Oil Association Reservoir Handbook, Published by Canadian Heavy Oil Association, pp 284-298.
- Bishop, A. W., 1954. Discussion on A. D. M. Penman (1953). Geotechnique 4, No. 1, pp 43.
- Bishop, A. W., 1967. Progressive Failure - With Special Reference of the Mechanism Causing it. Proceedings of Geotechnical Conference, Oslo 2, pp 142-150.
- Bishop, A. W., 1971. The Influence of Progressive Failure on the Choice of Method of Stability Analysis. Technique note, Geotechnique 21, No. 2, pp 168-172.
- Bishop, A. W., 1972. Shear Strength Parameters for Undisturbed and Remoulded Soil Specimens. In Stress Strain Behavior of Soils, ed: Parry, R. H. G., London: Poulis, pp 3-58.
- Bolton, M. D., 1986. The Strength and Dilatancy of Sands, Geotechnique 36, No. 1, pp 67-78.

- Chalaturnyk, R. J. and Scott, J. D., 1992. Evaluation of Reservoir Properties From Geomechanical Tests. *The Journal of Canadian Petroleum Technology*. Vol. 31, No. 5, pp 31-40.
- Dekker, R. F. Visser, F. C. and Dankers, P., 1987. The Primrose-kirby Area In The Southern Athabascas, Alberta, Canada: A Detailed Geological Investigation: *American Association of Petroleum Geologists Studies in Geology*, No. 25, pp 507-520.
- Domaschuk, L. and Valliappan, P., 1975. Nonlinear Settlement Analysis By Finite Element. *Journal of the Soil Mechanics and Foundations Division, Proceedings of American Society of Civil Engineers*, Vol. 101, GT7, pp 601-614.
- Domaschuk, L. and Wade, N. H., 1969. A Study of Bulk and Shear Moduli of a Sand. *Journal of the Soil Mechanics and Foundations Division, Proceedings of American Society of Civil Engineers*, Vol. 95, SM2, pp 561-582.
- Duncan, J. M. and Chang, C-Y., 1970. Nonlinear Analysis of Stress and Strain in Soils. *Journal of the Soil Mechanics and Foundations Division, Proceedings of American Society of Civil Engineers*, Vol. 96, SM5, pp 1629-1653.
- Duncan, J. M., 1981. Hyperbolic Stress Strain Relationships. In *Limit Equilibrium, Plasticity, and Generalized Stress-strain in Geotechnical Engineering*. pp 443-460.
- Dusseault, M. B. and Domselaar, H. R., 1982. Unconsolidated Sand Sampling in Canadian and Venezuelan Oil Sands. *The Proceedings of the Second International Conference on the Future of Heavy Crudes and Tar Sands*, United Nations Institute for Training and Research, Caracas, Venezuela, February, pp 336-348.
- Dusseault, M. B. and Morgenstern, N. R., 1977. Sampling and Testing of Athabasca Oil Sands For Stability Studies. *Physical Parameters, in Oil Sands*, pp 260-268.
- Dusseault, M. B. and Morgenstern, N. R., 1978. Shear Strength of Athabasca Oil Sands. *Canadian Geotechnical Journal*, Vol. 15, No. 2, pp 216-238.

- Dusseault, M. B. and Morgenstern, N. R., 1979. Locked Sands. Quarterly Journal of Engineering Geology. Vol. 12, pp 117-131.
- Dusseault, M. B., 1977. Stress State and Hydraulic Fracturing In the Athabasca Oil Sands. Geology and Reserves, Oil Sands, pp 27-35.
- Dusseault, M. B., 1977. The Geotechnical Characteristics of Oil Sands. Ph. D. Thesis. Department of Civil Engineering, University of Alberta, 472p.
- Hardin, B. O., 1985. Crushing of Soil Particles. Journal of Geotechnical Engineering, Vol. 111, No. 10, pp 1177-1192.
- Harrison, D. B., Glaister, R. P. and Nelson, H. W., 1979. Reservoir Description of the Clearwater Oil Sands, Cold Lake, Alberta, Canada. In: The Future of Heavy Crude and Tar Sands, New York. pp 264-279.
- Hulten, F. F. N. and Smith, S. R., 1991. The Lower Cretaceous Sparky Formation, Lloyminster Area: Stratigraphy and Paleoenvironment. Canadian Heavy Oil Association Reservoir Handbook, Published by Canadian Heavy Oil Association, pp 227-238.
- Kondner, R. L., 1963. Hyperbolic Stress-strain Response: Cohesive Soils. Journal of the Soil Mechanics and Foundations Division, Proceedings of American Society of Civil Engineers, Vol. 89, SM1, pp 115-143.
- Kosar, K. M., 1989. Geotechnical Properties of Oil Sands and Related Strata. Ph.D. Thesis, Department Of Civil Engineering, University Of Alberta, 496p.
- Kosar, K. M., Scott, J. D. and Morgenstern, N. R., 1987. Testing to Determine The Geotechnical Properties of Oil Sands. Proceedings of 38th Technical Meeting of Petroleum Society of CIM, June 7-10, Calgary.
- Kry, P. R., Gronseth, and Morgenstern, N. R., 1989. Geotechnical Properties, AOSTRO Technical Handbook on Oil Sands and Heavy Oils. Published by AOSTRA, Edmonton, Chapter 8, pp 185-201.

- Lambe, T. W. and Whitman, R. V., 1969. Soil Mechanics. John Wiley & Sons, Inc., New York, p 147.
- Lee, K. L. and Farhoomand, I., 1967. Compressibility and Crushing of Granular Soil in Anisotropic Triaxial Compression. Canadian Geotechnical Journal, Vol. 4, No. 1, pp 68-86.
- Lee, K. L. and Seed, H. B., 1967. Drained Strength Characteristics of Sands. Journal of the Soil Mechanics and Foundations Division, Proceedings of American Society of Civil Engineers, Vol. 93, SM 6, pp 117-141.
- MacCallum, G. T., 1979. Geology of Lloyminster Play, Alberta. First UNITAR International Conference On Heavy Crude and Tar Sands. Published by McGraw-Hill, New York, June 4-12, pp 223-230.
- Minkeni, D. F., 1974. The Cold Lake Oil Sands: Geology and a Reserves Estimates. In: Hill, L. V. (ed), Oil Sands, Fuel of the Future: Canadian Society of Petroleum Geologists, Memoir 3, pp 84-99.
- Mobil Oil Canada Ltd, 1987. Core Laboratory Reports, Calgary.
- Mossop, G. D., Kramers, P. D., Flach, P. D. and Rottenfusser, B. A., 1979. Geology of Alberta's Oil Sands and Heavy Oil Deposits. First UNITAR International Conference on the Future of Heavy Crude and Tar Sands. Published by McGraw-Hill, New York, June 4-12, pp 197-207.
- Orr, R. D., Johnson, J. R. and Manko, E. M., 1977. Lower Cretaceous Geology and Heavy-oil Potential of the Lloyminster Area, Bulletin of Canadian Petroleum Geology, 30, pp 1187-1221.
- Plewes, H. D., 1987. Undrained Strength of Athabasca Oil Sands. M. Sc. Thesis , Department of Civil Engineering, University Of Alberta, 261p.
- Poulos, S. J., 1981. The Steady State of Deformation. Journal of Geotechnical Engineering, ASCE. Vol. 107, No. GT5, pp 553-560.

- Roscoe, K. H., 1970. The Influence of Strains in Soil Mechanics. *Geotechnique* 20, No. 2, pp 129-170.
- Rowe, P. W., 1962. The Stress-dilatancy for Static Equilibrium of an Assembly of Particles in Contact. *Proceedings of Royal Society, London. Serial A*, Vol. 269, pp 500-527.
- Rowe, P. W., 1969. The Relationship Between The Shear Strength of Sands in Triaxial Compression, Plane Strain and Direct Shear. *Geotechnique* 19, No. 1, pp 75-86.
- Scott, J. D. and Kosar, K. M., 1984. Geotechnical Properties of Athabasca Oil Sands. *Proceeding of WRI-DOE Tar Sand Symposium*, June 26-29, Vail, Colorado.
- Setarri, A., Kry, P. R. and Yee, C. T., 1988. Coupling of Fluid Flow and Soil Behavior to Model Injection into Unconsolidated Oil Sands. *Annual Technical Meeting, Petroleum Society of CIM*. Paper No. 88-39-72.
- Skempton, A. W., 1954. The Pore Pressure Coefficients A and B. *Geotechnique* 4, No. 4, pp 143-145.
- Skempton, A. W. and Bishop, A. W., 1950. Measurement of Shear Strength of Soils. Discussion by A. W. Bishop. *Geotechnique* 2, No. 2, pp 113-115.
- Swokowski, E. W., 1975. *Calculus With Analytical Geometry*. Prindle, Weber and Schmidt, Incorporated, 20 Newbury Street, Boston, Massachusetts 02116.
- Varizi, H., 1989. A New Constitutive Stress Strain Model for Describing the Geomechanical Behavior of Oil Sands. *Proceeding of The 40th Annual Technical Meeting of The Petroleum Society of CIM*, May 28 - 31, Banff. Paper No. 89-40-67, Vol. 2, pp. 67-1 to 67-16.
- Vesic, A. S. and Clough, G. W., 1968. Behavior of Granular Materials Under High Stresses. *Journal of the Soil Mechanics and Foundations Division, Proceedings of American Society of Civil Engineers*, Vol. 94, SM3, pp 661-688.
- Vigrass, L. W., 1977. Trapping of Oil Intre-Mannville (Lower Cretaceous) Disconformity in Lloyminster, Alberta and Saskatchewan, *American Petroleum Geologists Bulletin*, 61, pp 1010-1028.

- Visser, K. Dankers, P. and Leckie, D., 1985. Mineralogy and Geology of the Clearwater Reservoir; Sands in the Wolf Lake Area, Cold Lake, Alberta. Third UNITAR Conference On Heavy Crude and Tar Sands. June 22-31, Long Beach, CA, USA, pp 119-133.
- Wan, R., Chan, D. H. and Kosar, K. M., 1989, A Constitutive Model for the Effective Stress-strain Behavior of Oil Sands. The 40th Annual Technical Meeting of The Petroleum Society of CIM, May 28 - 31, Banff. Paper No. 89-40-66, Vol. 2, pp.66-1 to 66-13.
- Wightman, D. M. and Berezniuk, T., 1991. Resource Characterization and Depositional Modelling of the Clearwater Formation, Cold Lake Oil Sands Area, East Central Alberta. Canadian heavy Oil Association Reservoir handbook. pp 267-282.
- Wong, R. C. K., Barr, W. E. and Kry, P. R., 1993. Stress-strain Response of Cold Lake Oil Sands. Canadian Geotechnical Journal, Vol. 30, pp 220-235.
- Yin, J.-H., Saadat, F. and Graham, J., 1990. Constitutive Modelling of a Compacted Sand-bentonite Mixture Using Three-modulus Hypoelasticity. Canadian Geotechnical Journal, Vol. 27, No. 3, pp 365-372.

Appendix A

Sample Calculations

A.1 Determination of Specimen Dimensions After Isotropic Consolidation

Assume a specimen with length L , diameter D and volume V deforms homogeneously in cyclic isotropic consolidation. The deformation is, therefore, proportional to the length and diameter of the specimen in axial direction and radial direction respectively. Let the volume change caused by the consolidation be ΔV_c , and the reduction in length be ΔL . The length and diameter of the specimen after consolidation will be

$$L_c = L - \Delta L \quad (A.1.1)$$

$$D_c = D - \frac{D}{L} \Delta L \quad (A.1.2)$$

Where L_c and D_c are the length and diameter of the specimen after consolidation. The volume of the specimen after consolidation, V_c is

$$\begin{aligned} V_c &= V - \Delta V_c \\ &= \left(\frac{D_c}{2}\right)^2 \pi L_c = \left(\frac{D - \frac{D}{L} \Delta L}{2}\right)^2 \pi (L - \Delta L) \end{aligned} \quad (A.1.3)$$

Equation (A.1.3) can be rewritten

$$\Delta V_c - \frac{3}{4} \pi D^2 + \frac{3}{4} \pi \frac{D^2}{L} \Delta L^2 - \frac{\pi}{4} \left(\frac{D}{L}\right)^2 \Delta L^3 = 0 \quad (A.1.4)$$

The high order item with ΔL^3 that does not have a significant influence on the final result can be eliminated. Therefore,

$$\Delta v - \frac{3}{4} \pi D^2 + \frac{3}{4} \pi \frac{D^2}{L} \Delta L^2 = 0 \quad (\text{A.1.5})$$

Solving this equation, ΔL can be obtained. Going back to the equations (A.1.1) and (A.1.2), the dimensions of the specimen after the consolidation can be calculated. This dimension is used to determine the physical condition prior to shearing.

A.2 Calculation of Physical Parameters

Example: Test CU6

Before consolidation

Specimen information:

Length L(mm)	Diameter D(mm)	Weight W(gms)	Volume V(cm ³)	Bulk Density $\rho_{\text{lab}}(\text{g/cm}^3)$
50.3	39.0	112.41	60.09	1.87

Extraction results (by mass):

Water (%)	Bitumen (%)	Solids (%)
11.8	7.15	81.05

In situ volume (eq. 4.2.1):

$$V_i = \frac{M_w}{G_w} + \frac{M_b}{G_b} + \frac{M_s}{G_s} = 55.71 \text{ cm}^3$$

$$M_w = 112.41 \times 11.8\% = 13.26 \text{ g}$$

$$M_b = 112.41 \times 7.15\% = 8.04 \text{ g}$$

$$M_s = 112.41 \times 81.05\% = 91.11 \text{ g}$$

$$G_w = 1.00$$

$$G_b = 1.03$$

$$G_s = 2.63$$

The expansion of the specimen in the laboratory compared with in situ:

$$\Delta V = V - V_i = 60.09 - 57.71 = 4.38 \text{ cm}^3$$

In situ density:

$$\rho_{in} = \frac{W}{V_i} = 2.02 \text{ g/cm}^3$$

In situ porosity:

$$n_{in} = \frac{\frac{M_w}{G_w} + \frac{M_b}{G_b}}{V_i} = 0.3782$$

These calculations of in situ properties assume that no free gas exists in the pores. Well bore geophysical logs, for the wells the cores are from, generally show no free gas except immediately below thick shale strata.

Lab porosity:

$$n = \frac{\frac{M_w}{G_w} + \frac{M_b}{G_b} + \Delta V}{V} = 0.4235$$

Water saturation:

$$S_r = \frac{\frac{M_w}{G_w}}{\frac{M_w}{G_w} + \Delta V} = 0.8279$$

Lab dry density:

$$\gamma_d = \frac{\rho}{1+w} = 1.52 \text{ g/cm}^3$$

Index of disturbance:

$$I_d = \frac{n - n_{in}}{n} = 11.98\%$$

After consolidation

Volume change and volume:

$$\Delta V_c = 3.82 \text{ cm}^3 \quad V_c = 56.27 \text{ cm}^3$$

Bulk density:

$$\rho_c = \frac{W + \Delta V \gamma_w - \Delta V_c \gamma_w}{V_c} = 2.01 \text{ g/cm}^3$$

Porosity:

$$n_c = \frac{\frac{M_w}{G_w} + \frac{M_b}{G_b} + \Delta V - \Delta V_c}{V_c} = 0.3844$$

Index of disturbance:

$$I_{dc} = 1.6\%$$

Dry density:

$$\gamma_{dc} = 1.62 \text{ g/cm}^3$$

A.3 Calculation of the Parameters in a CIU Test

Pore pressure parameter A

Pore pressure parameter A is calculated using the formula derived by Bishop and Henkel (1953).

$$\Delta u = B[\Delta \sigma_3 + A(\Delta \sigma_1 - \Delta \sigma_3)] \quad (\text{A.3.1})$$

Δu is the change in pore pressure; A and B are the pore pressure parameters; $\Delta \sigma_1$ and $\Delta \sigma_3$ are the change in major and minor principal stresses. In triaxial compression, the confining pressure is kept constant, that is, $\Delta \sigma_3 = 0$. Before shear starts, $\sigma_{1o} = \sigma_{3o}$, so that $\Delta \sigma_1 = \sigma_1 - \sigma_3$. For the CIU specimens B was approximately 1.

$$A = \frac{\Delta u}{\sigma_1 - \sigma_3} \quad (\text{A.3.2})$$

The parameter A is not a constant throughout the test. It changes with the vertical stress mobilized by axial strain. A_f is denoted as the parameter A at shear failure, which is shown in Table 6.2.1 for each individual test .

Stress path

Stress paths are usually plotted in both $s' - t$ and $p' - q$ coordinates. s' and t are defined as

$$t = \frac{\sigma_1 - \sigma_3}{2} \quad (A.3.3)$$

$$s' = \frac{\sigma_1' + \sigma_3'}{2} \quad (A.3.4)$$

Since undrained compression causes the change in pore pressure, s' is a function of pore pressure in shear.

$$\begin{aligned} s' &= \frac{\sigma_1' + \sigma_3'}{2} = \frac{\sigma_1 + \sigma_3 - 2u}{2} = \frac{\sigma_1 - \sigma_3}{2} + \sigma_3 - (\Delta u + u_0) \\ &= t + \sigma_{30}' - \Delta u \end{aligned} \quad (A.3.5)$$

Where u_0 is the initial pore pressure (back pressure in consolidation before the undrained compression), Δu is the change in pore pressure (positive in contraction and negative in dilation), and σ_{30}' is the initial effective confining pressure in shear.

Similarly, p' and q are defined as follows

$$q = \sigma_1 - \sigma_3 \quad (A.3.6)$$

$$p' = \frac{\sigma_1' + 2\sigma_3'}{3} = \frac{\sigma_1 + 2\sigma_3 - 2u}{3} = \frac{\sigma_1 - \sigma_3}{3} + \sigma_3 - (\Delta u + u_0)$$

$$= \frac{q}{3} + \sigma_{30}' - \Delta u \quad (A.3.7)$$

A.4 Determination of Effective Confining Stress in a J_1 Constant Test

The J_1 constant test is conducted after isotropic cyclic consolidation.

The vertical effective stress is

$$\sigma_1' = \frac{P - a\sigma_3}{A} + \sigma_3' \quad (A.4.1)$$

where P - vertical load (MN)

a - cross section area of piston ($5.067 \times 10^{-4} \text{ m}^2$)

A - cross section area of specimen (m^2)

σ_3 - cell pressure (MPa)

Before shear starts, $\sigma_1' = \sigma_3'_0$, $P = P_0 = a\sigma_{30}$

When shear starts, $P = P_0 + \Delta P$

Therefore,

$$\begin{aligned} \sigma_1' &= \frac{P_0 + \Delta P - a\sigma_3}{A} + \sigma_3' = \frac{a\sigma_{30} + \Delta P - a\sigma_3}{A} + \sigma_3' \\ &= \frac{a(\sigma_{30}' - \sigma_3') + \Delta P}{A} + \sigma_3' \end{aligned} \quad (A.4.2)$$

$$J_1 = \frac{\sigma_1' + 2\sigma_3'}{3} \quad (A.4.3)$$

From Eq. (A.4.2) and (A.4.3)

$$\sigma_3' = \frac{J_1 - \frac{a\sigma_{30}' + \Delta P}{3A}}{1 - \frac{a}{3A}} \quad (A.4.4)$$

The effective confining stress is determined by Eq. (A.4.4).

A.5 Pore Pressure Injection Test Procedure

1. Stress Ratio

A pore pressure injection test (CAI) is conducted under an anisotropic stress condition which can be established referring to the drained test results.

A total of five tests were conducted under different stress conditions. The stress path for a CAI test is shown in Fig 4.4.1. After the isotropic cyclic consolidation, an effective confining pressure, $\sigma_3'i = 8$ MPa, is imposed on the specimen, and then the vertical stress is increased to a certain level to start anisotropic consolidation. Referring to the CID failure envelope, choosing t in an increment of 0.5 MPa, the initial stress conditions for the anisotropic consolidation and anticipated failure stress conditions in the pore pressure injection are calculated and listed in the following table.

The Initial And Anticipated Failure Stress Conditions In CAI Tests

No.	$\sigma_3'i$ MPa	t MPa	$\sigma_1'-\sigma_3'$ MPa	$\sigma_1'i$ MPa	$s'i$ MPa	$(\sigma_1'/\sigma_3')_i$	$s'f$ MPa	$(\sigma_1'/\sigma_3')_f$
CI1	8.0	0.5	1	9	8.5	1.13	0.6	11.0
CI2	8.0	1.0	2	10	9.0	1.25	1.31	7.5
CI3	8.0	1.5	3	11	9.5	1.38	2.09	6.1
CI4	8.0	2.0	4	12	10.0	1.50	2.96	5.2
CI5	8.0	2.5	5	13	10.5	1.63	3.99	4.4

The magnitude of a pore pressure increment used in a test is chosen based on the initial stress ratio with which the pore pressure injection test starts. It decreases with the increase in the initial stress ratio because the larger the stress ratio, the closer the initial stress condition is to the failure line.

2. Vertical Loading

Since an anisotropic stress condition is required for a pore pressure injection test, a strain controlled loading frame used in the CID and the CIU tests is no longer suitable. A bellofram shown in Fig. 4.1.5 is employed. This bellofram has a capacity of about 20000 N in force when connected to the air pressure supply in the laboratory. About 18 MPa vertical stress can be imposed on a specimen of 38 mm in diameter. This stress is

enough to create the anisotropic stress conditions required in the pore pressure injection tests.

3. Pore Pressure Injection

Pore pressure is increased through a back pressure line after the anisotropic consolidation is completed. The general procedures are as follows.

- 1). Complete an isotropic consolidation test as usual;
- 2). Set a required vertical stress and complete the anisotropic consolidation;
- 3). Increase the back pressure step by step until failure occurs, measure the volume change and vertical strain from each pore pressure increment.

The volume change in the pore pressure injection test is measured with a volume change measuring device connected to the back pressure line. This measuring method is better than measuring the volume change from the cell pressure port because the reference volume is small. The volume change is determined when water flows into the specimen rather than determined by squeezing water out of the cell due to specimen volume increase.

Increasing back pressure in a pore pressure injection test causes an expansion of the volume change measuring device. To obtain an accurate volume change measurement, the expansion is eliminated by calibration. To do this, one can simply close the back pressure valve to the triaxial cell, and then increase the back pressure gradually and record the " volume change " resulting from the apparatus expansion.

A.6 Correction To A Stress-Strain Curve

When a cell pressure is applied to a specimen, the piston of the cell is subjected to an uplift pressure which is recorded by a load cell transducer sitting on the top of the piston. This load can be the initial reading for the vertical loading system. As shear starts, the piston travels down, and the friction of the piston in the cell bushing is mobilized gradually. The real load acting on the specimen can be determined by subtracting the

initial reading and the piston friction from the total load recorded by the load cell transducer. The piston friction is not a constant, it changes with cell pressure. Calibration shows that the friction approximately has a linear relation with the cell pressure. Making use of this calibration, the recorded load can be corrected to the real load imposed on the specimen.

In some cases, the vertical strain measured in a test also needs correction. Without correction, the stress strain curve usually looks like Fig A.1. There is a linear portion on the curve between point a and b. It can be seen that the strain before point a is large and the mobilized stress is relatively small. The reason is that, at the beginning of shear, the piston is not sitting on the loading cap properly, as shown in Fig A.2. In this type of triaxial cell, the piston is not attached to the cap. During cyclic isotropic consolidation, the cell pressure may push the piston upward. Therefore, the contact between the piston and the cap is poor. As well, a vertical displacement caused by consolidation of the specimen also enlarges the gap between the piston and the cap. As a result, the load is not fully mobilized until the piston has a solid contact with the cap. To correct the error, the line ba on the stress-strain curve in Fig A.1 is extended to point c on the strain axis. Point c is taken to be the origin of the stress-strain curve.

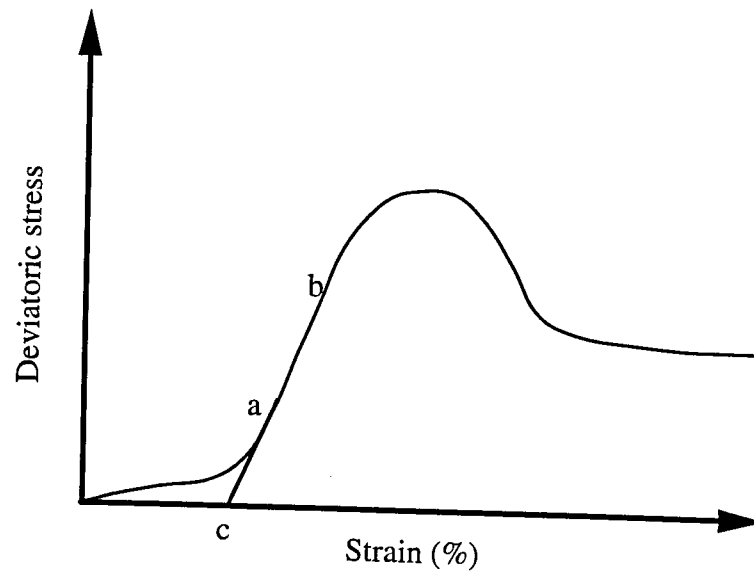


Fig A.1 Stress-strain Relationship in a Triaxial Test

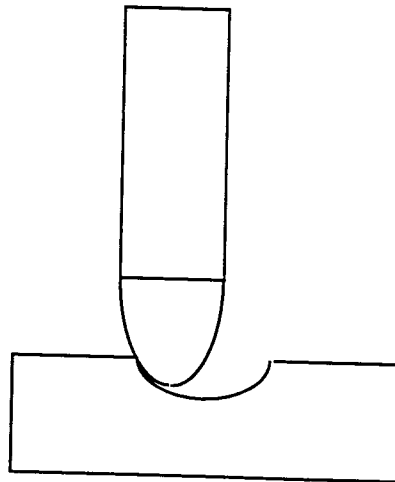


Fig A.2 Possible Piston Position in Triaxial Test

Appendix B

Calibrations

B.1 The Calibration Coefficients For Pressure Transducers And Load Cell

Type	No.	Coefficient	Unit
PT	SN 67462	280.19	kPa/mv
	SN 129606	1307.82	kPa/mv
	SN 33495	1399.14	kPa/v
	SN 12179	2377.447	kPa/v
	CELESCO	211.97	kPa/mv
	388073	467.894	kPa/mv
	45723	141.396	kPa/mv
LC	87C55	1.1772	KN/mv
	SN 398876	45.2125	kgf/mv
BVMD		32.1157	cm ³ /v
		0.644	cm ³ /MPa

PT - Pressure Transducer

LC - Load Cell Transducer

BVMD - Bellow Volume Change Measuring Device

B.2 Friction Of Triaxial Cell Piston

Piston friction is not a constant. It changes with the strain rate and cell pressure. Since the strain rate used in strain controlled tests is usually 0.013 mm/min, the piston friction is only a function of cell pressure. The relationship between cell pressure and piston friction at a strain rate of 0.013 mm/min is shown in Fig B.1. It gives a coefficient of 2.44 N/MPa.

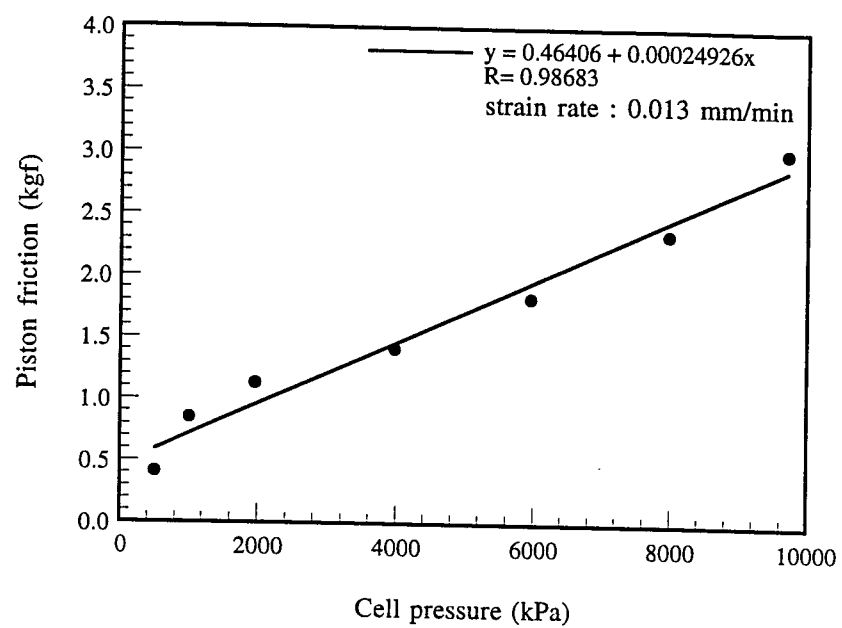


Fig B.1 Piston Friction Calibration

Appendix C
Plots of Isotropic Cyclic Consolidation Results
and Grain Size Analyses

Figures C.1 to C.21: Isotropic Cyclic Consolidation Results

Figures C.22 to C.48: Grain Size Analyses

Figure C.49: Failure Modes in Triaxial Tests

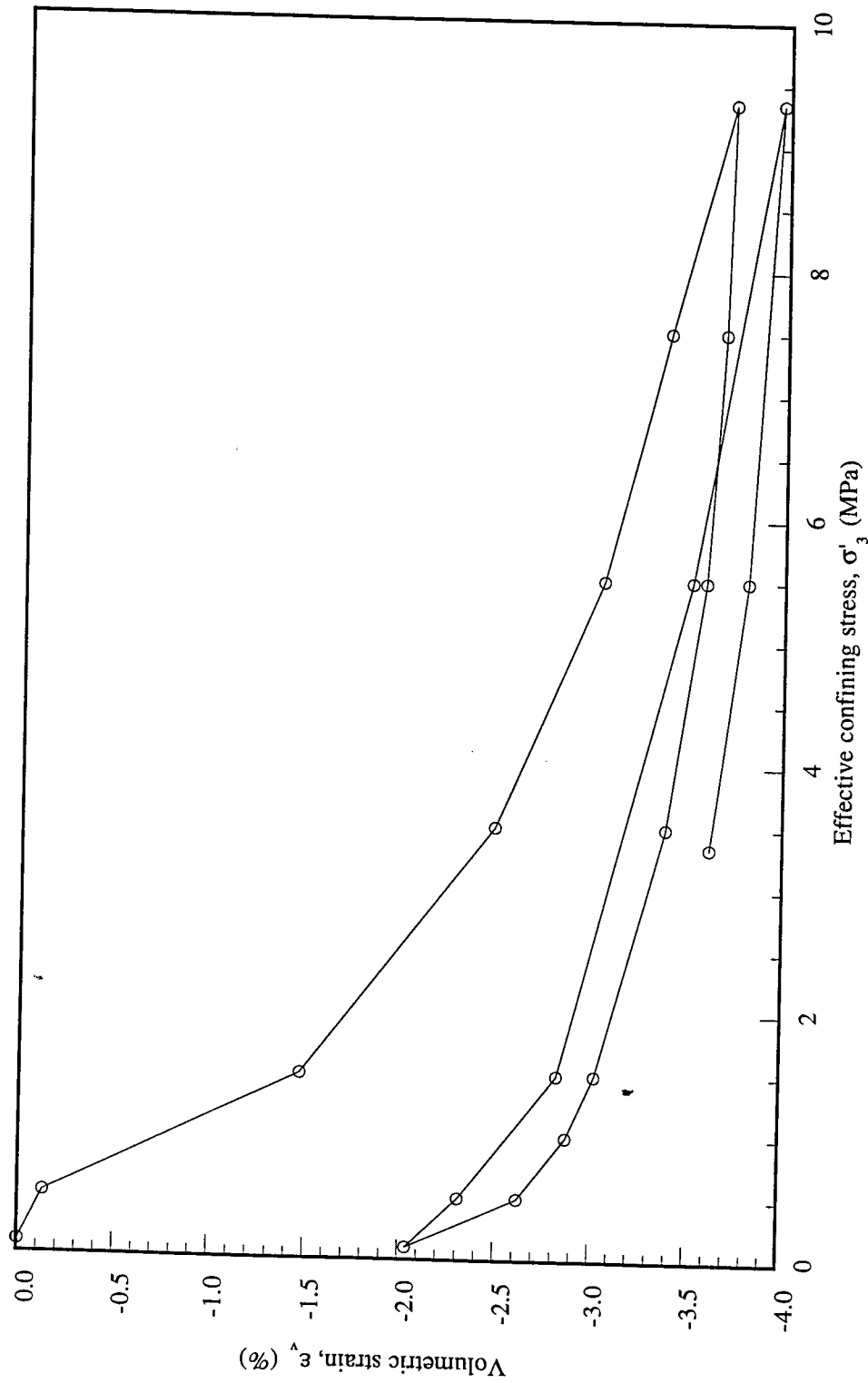


Fig C.1 Test CD3: Isotropic Cyclic Consolidation

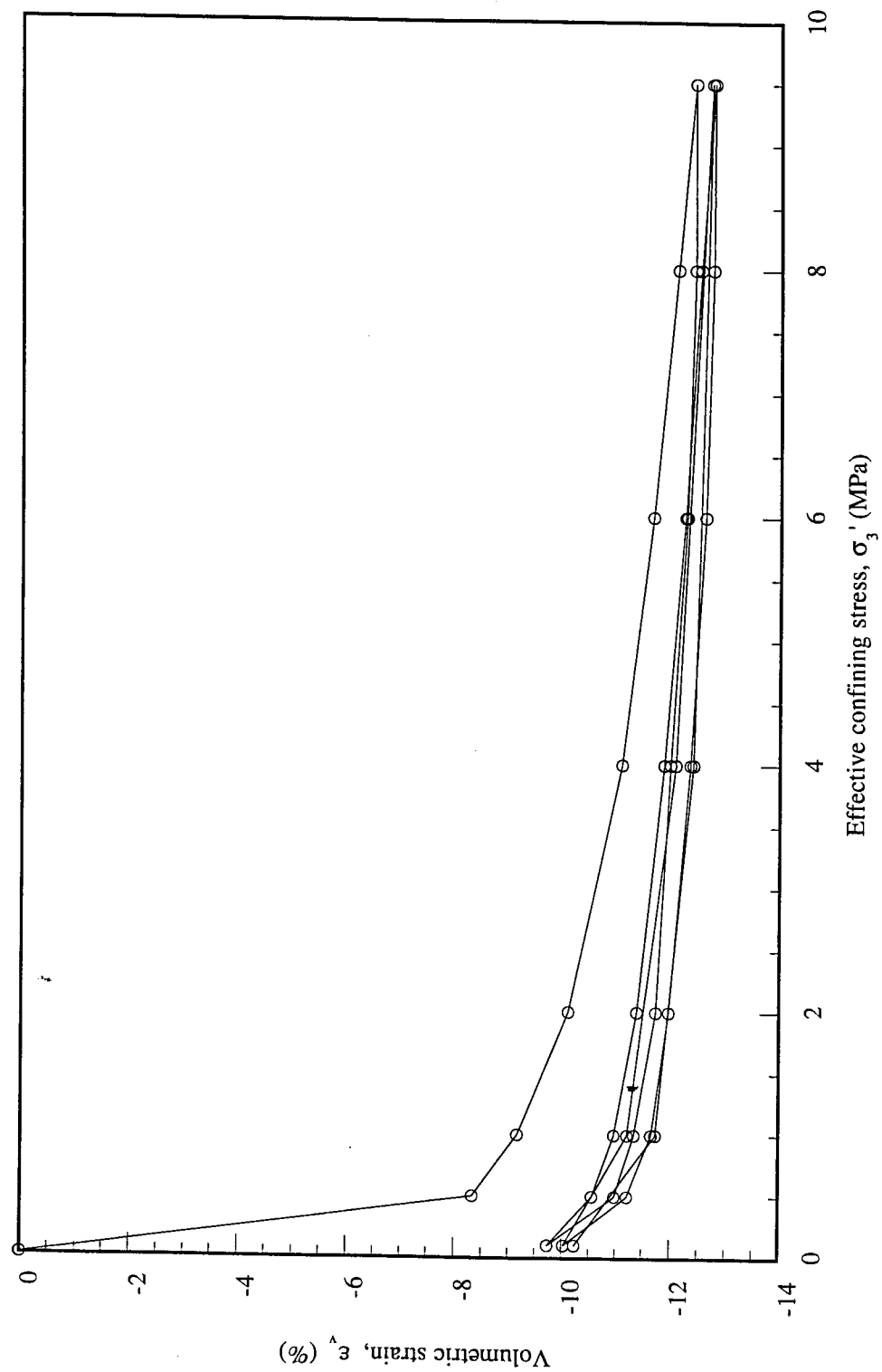


Fig C.2 Test CD4: Isotropic Cyclic Consolidation

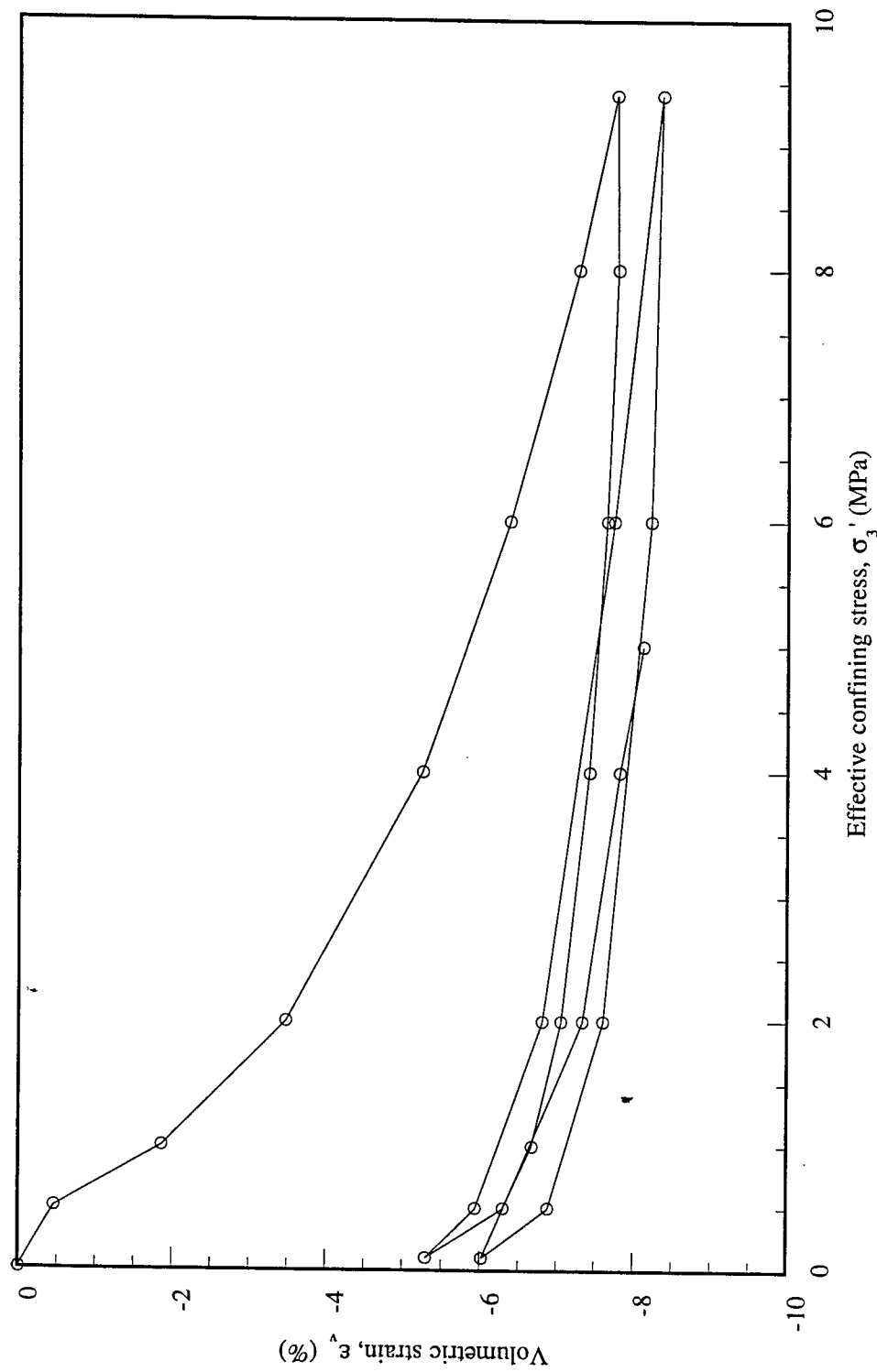


Fig C.3 Test CD5: Isotropic Cyclic Consolidation

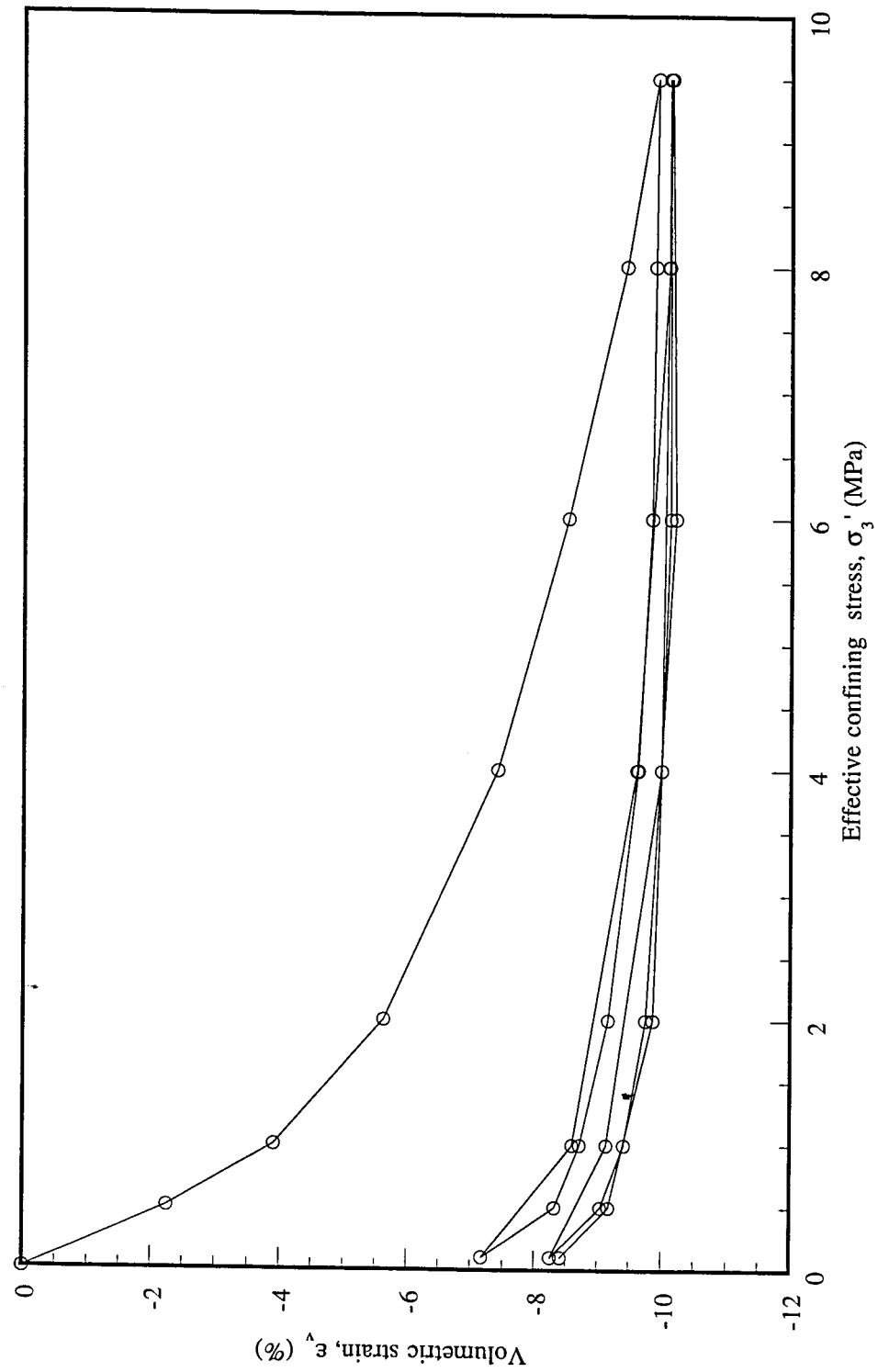


Fig C.4 Test CD6: Isotropic Cyclic Consolidation

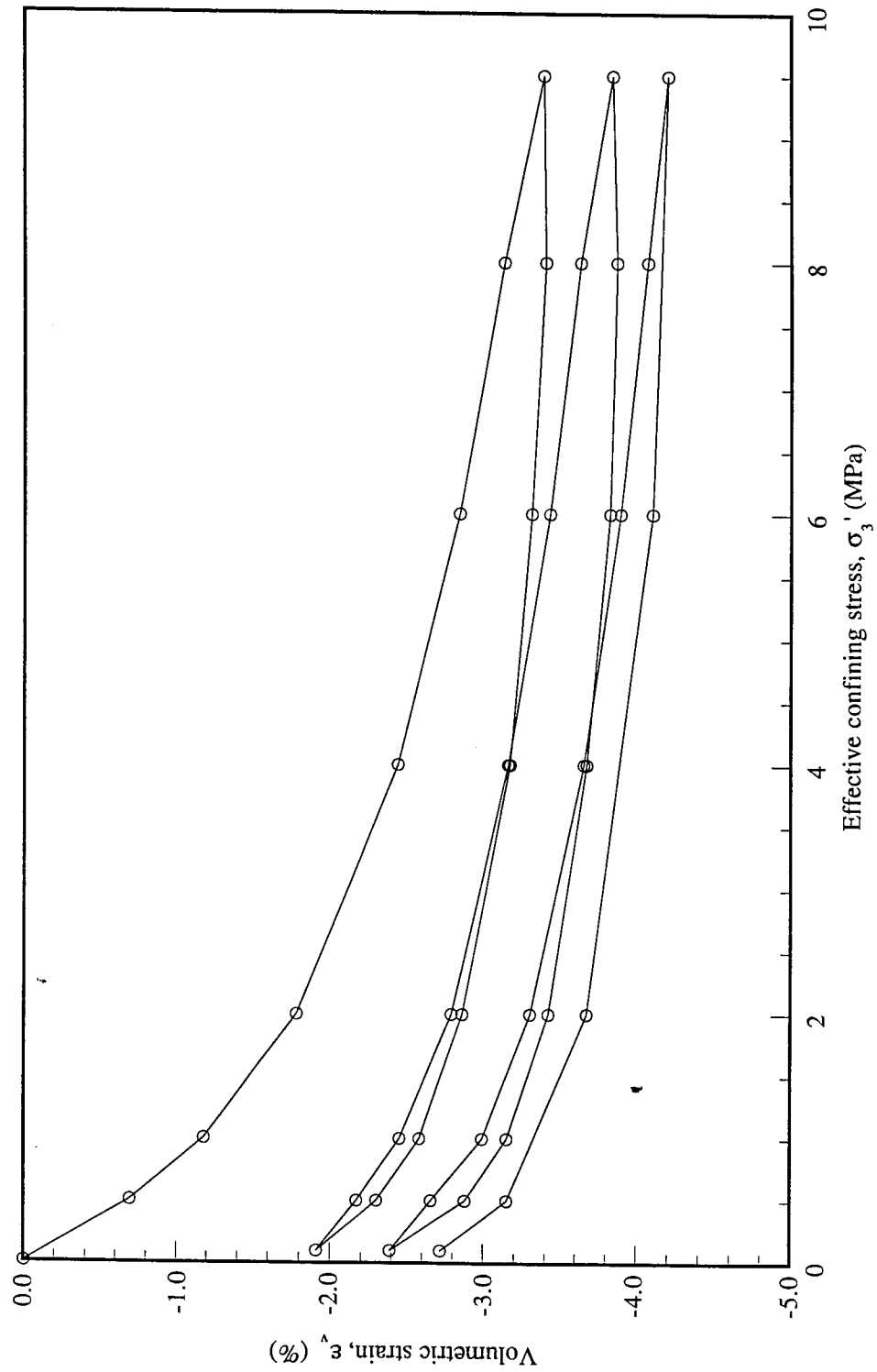


Fig C.5 Test CU1: Isotropic Cyclic Consolidation

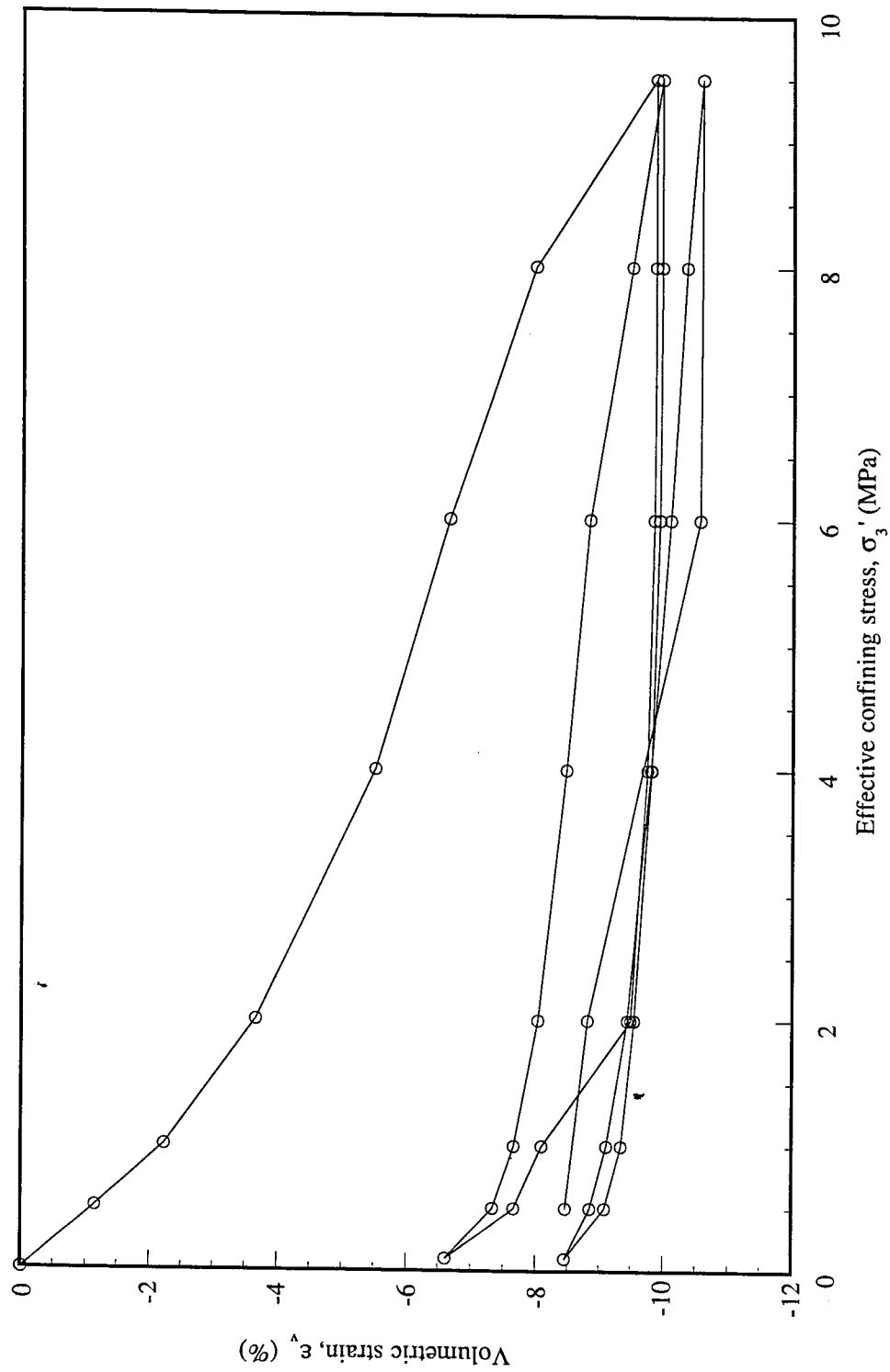


Fig C.6 Test CU3: Isotropic Cyclic Consolidation

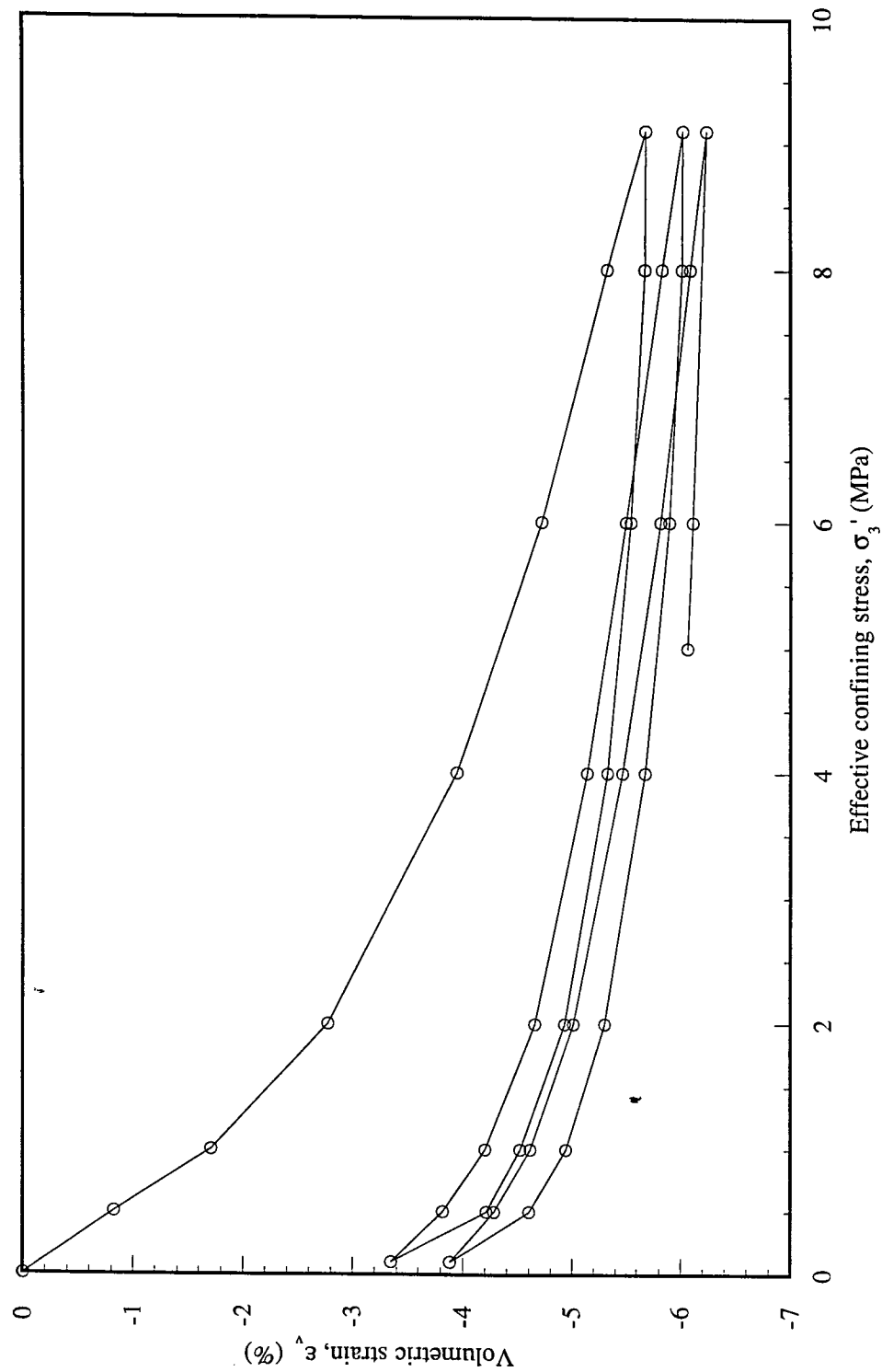


Fig C.7 Test CU4: Isotropic Cyclic Consolidation

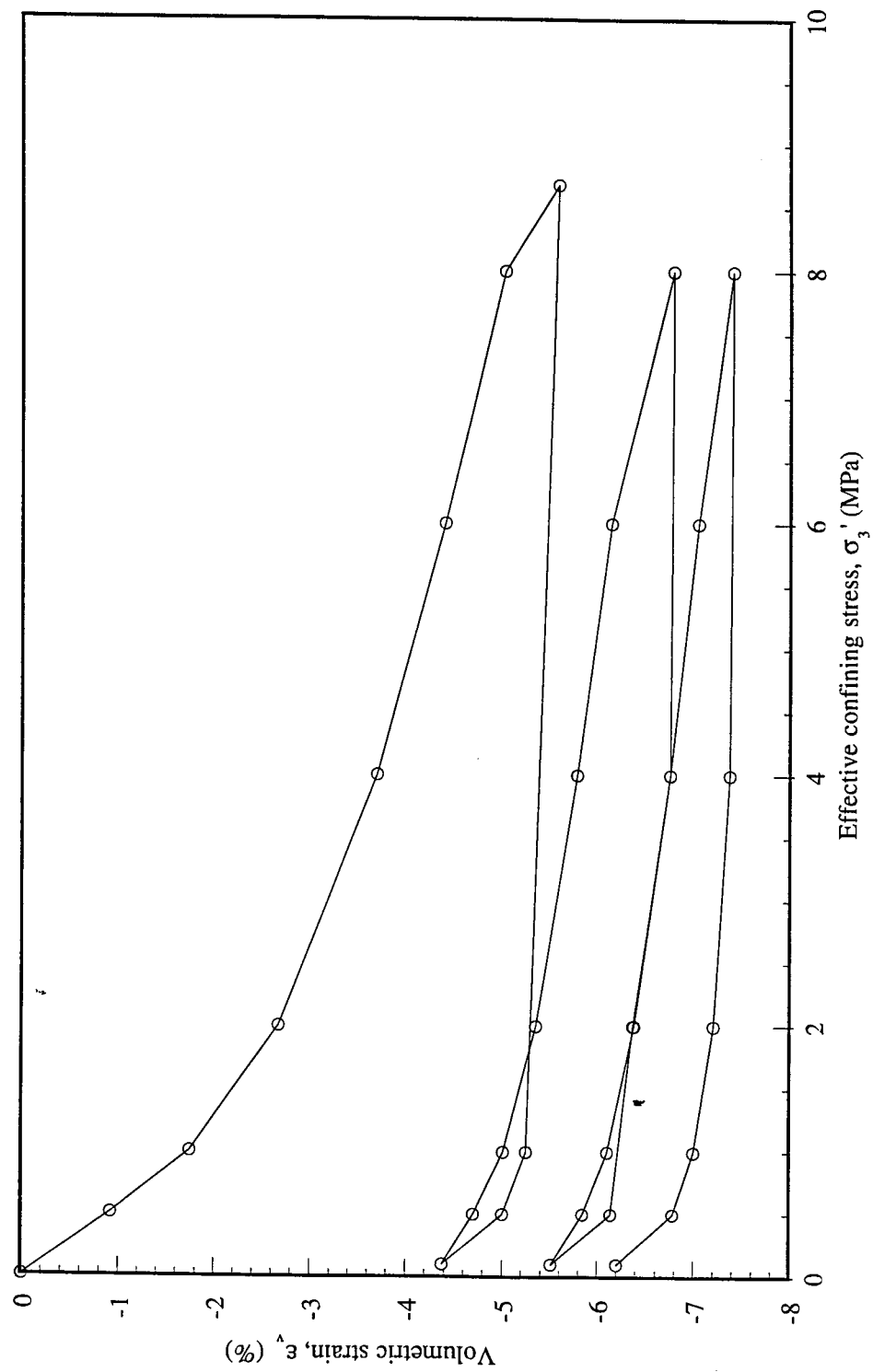


Fig C.8 Test CU5: Isotropic Cyclic Consolidation

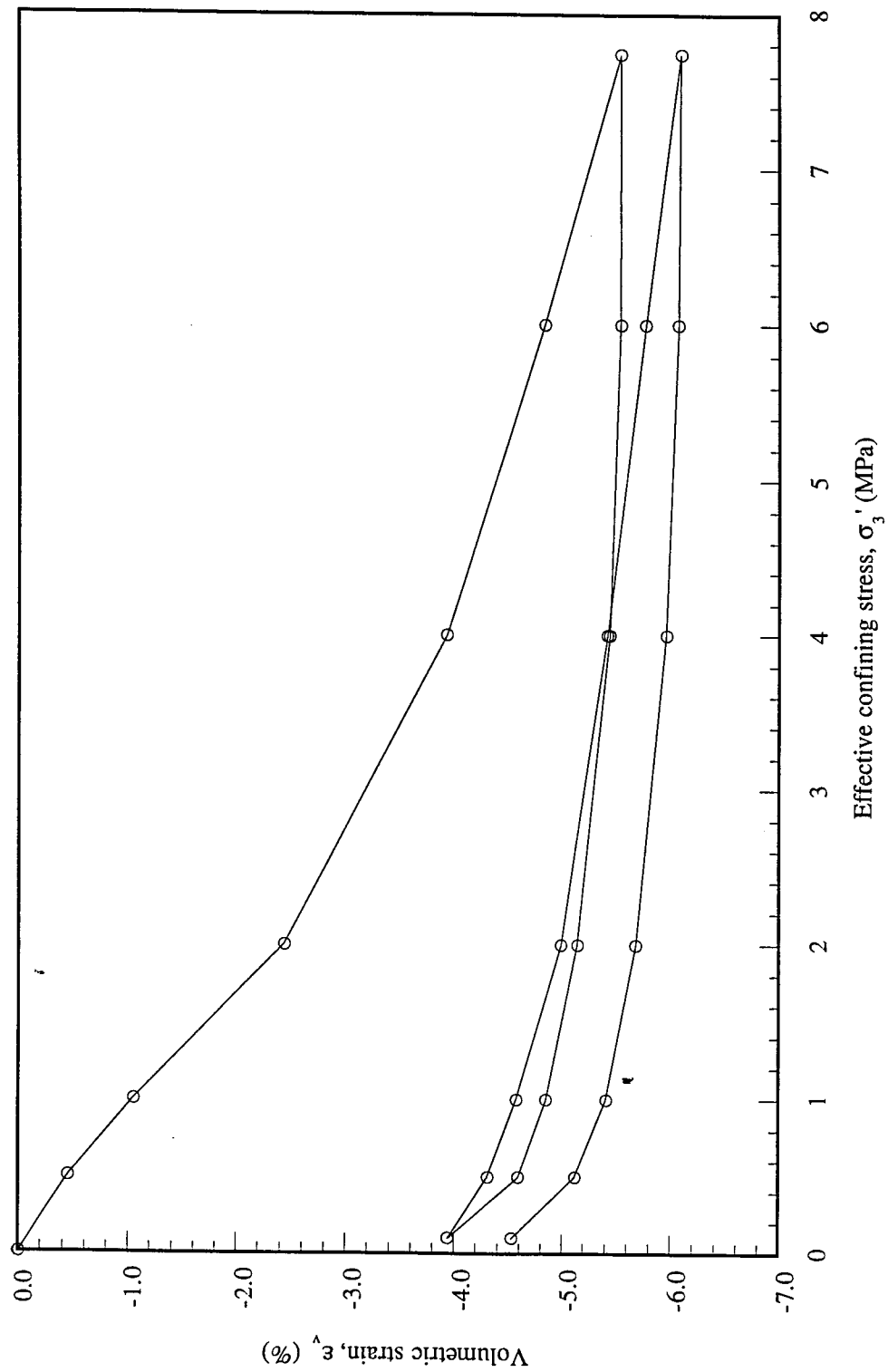


Fig C.9 Test CU8: Isotropic Cyclic Consolidation

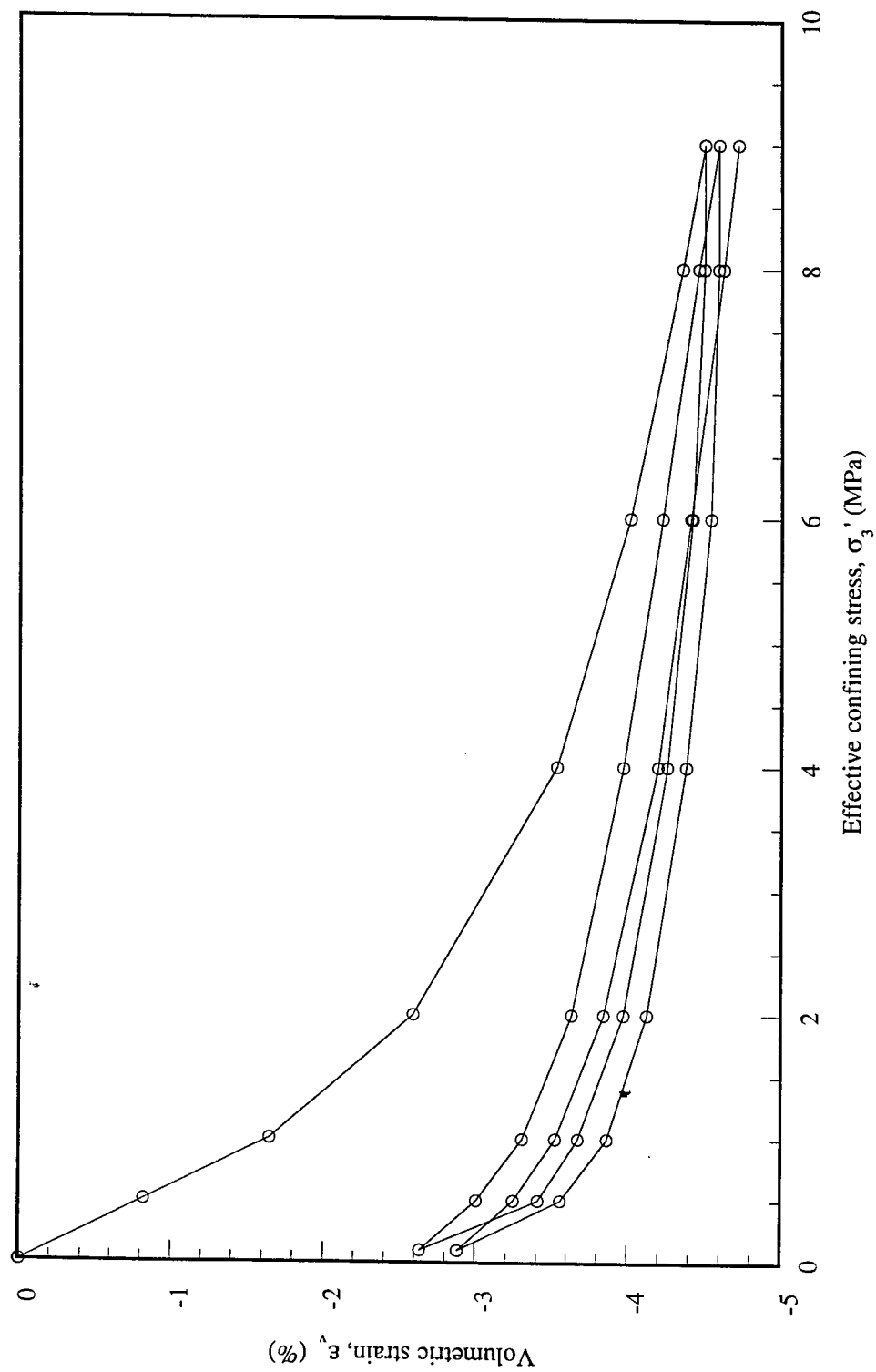


Fig C.10 Test CP1: Isotropic Cyclic Consolidation

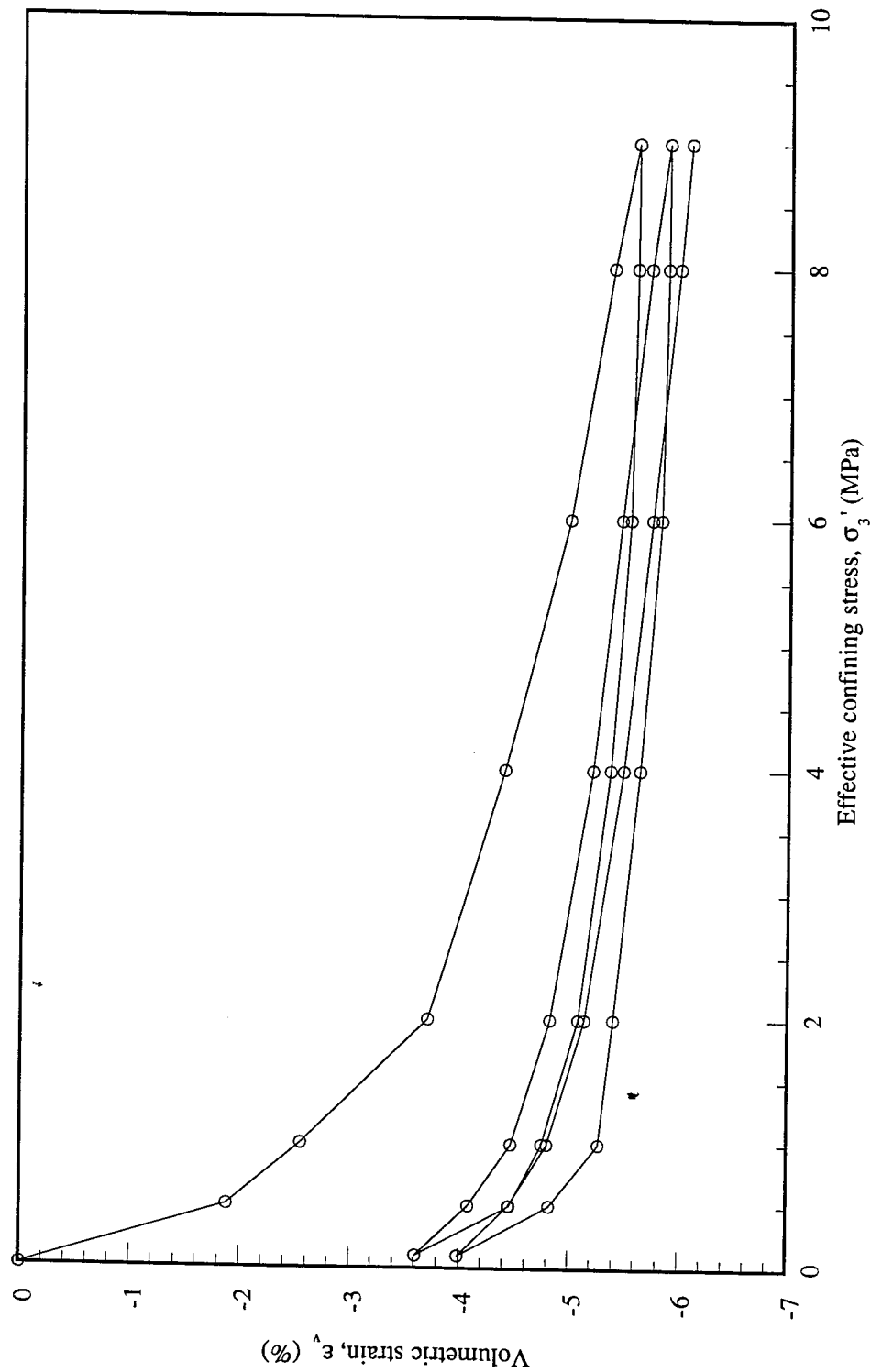


Fig C.11 Test CP2: Isotropic Cyclic Consolidation

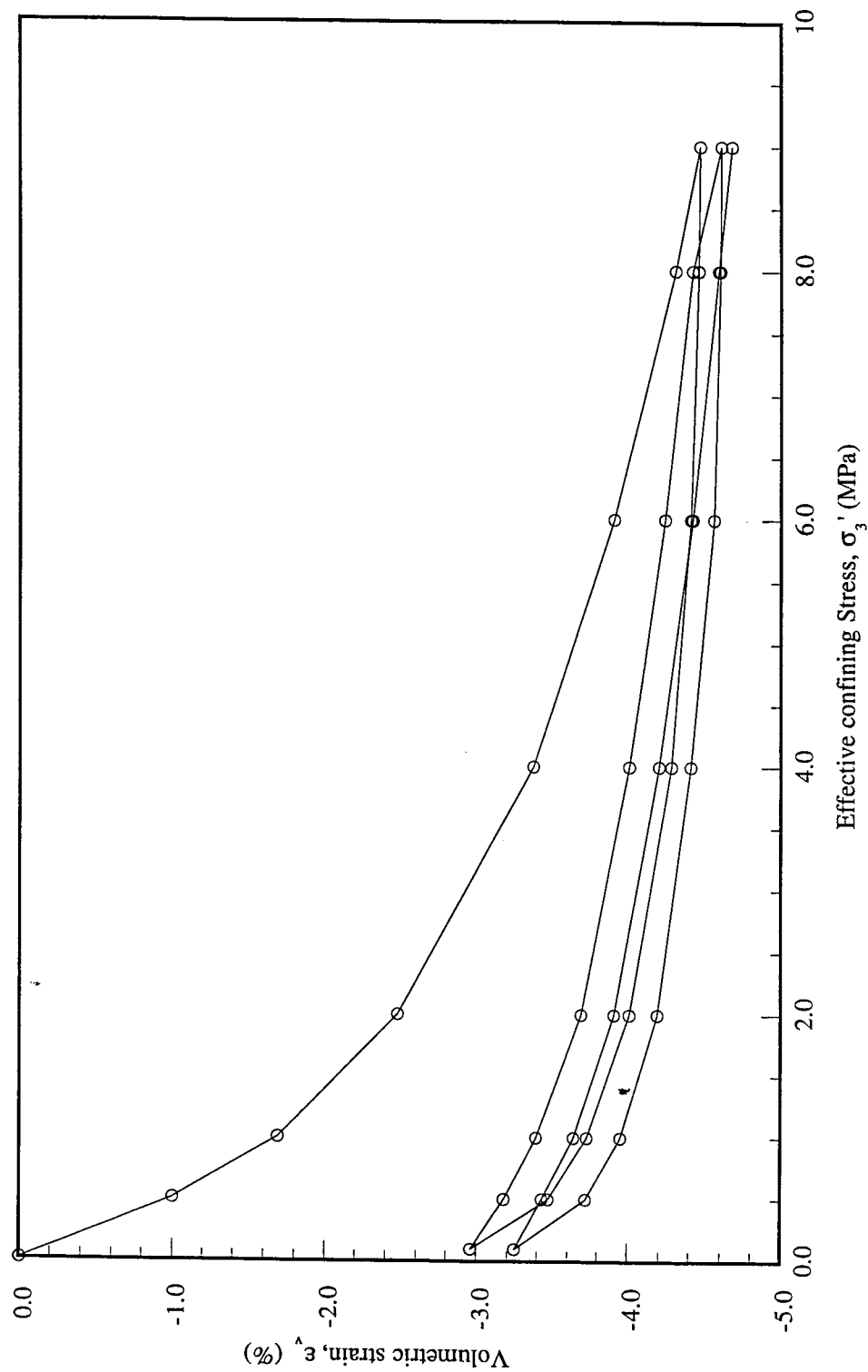


Fig C.12 Test CP3: Isotropic Cyclic Consolidation

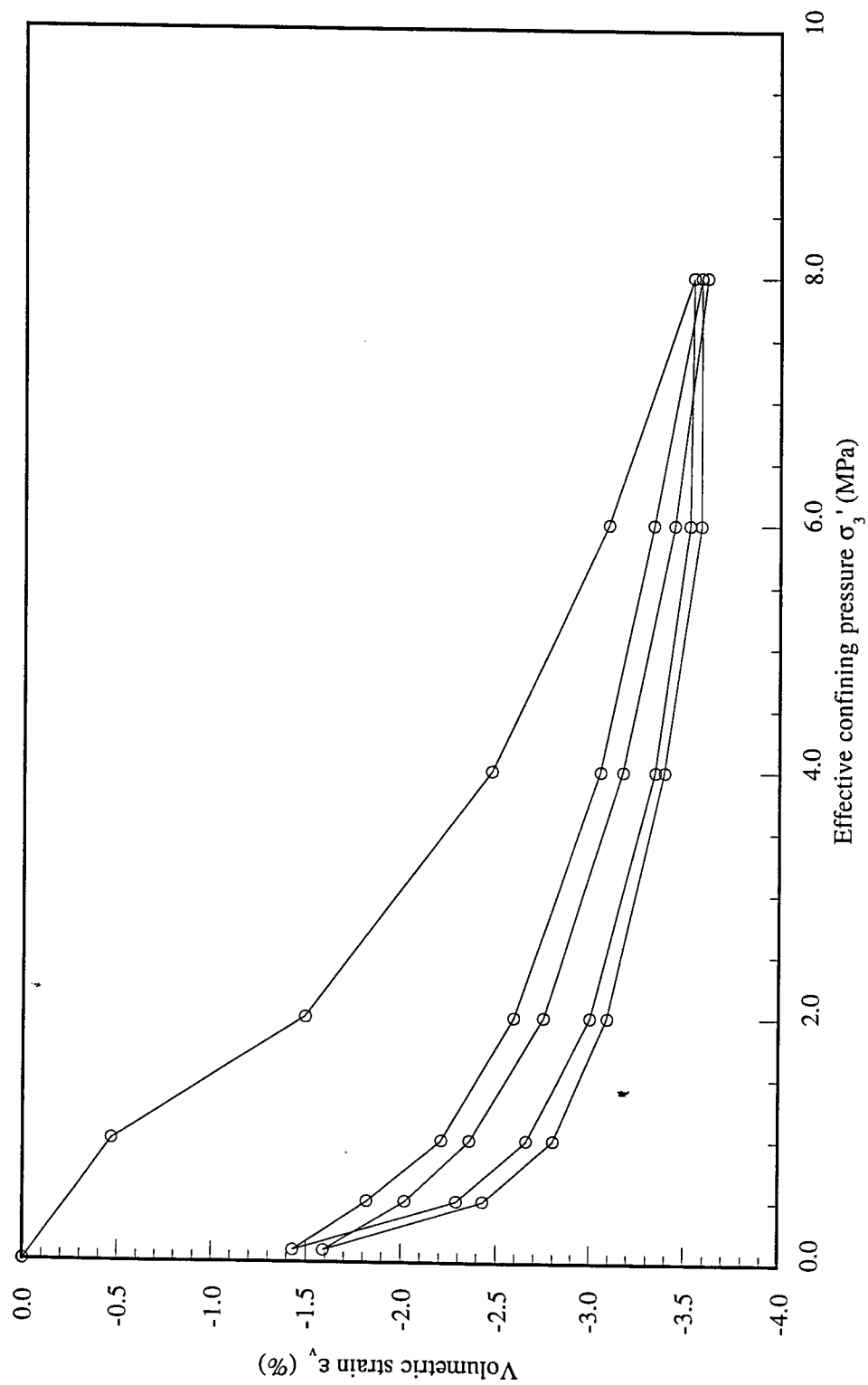


Fig C.13 Test CP4: Isotropic Cyclic Consolidation

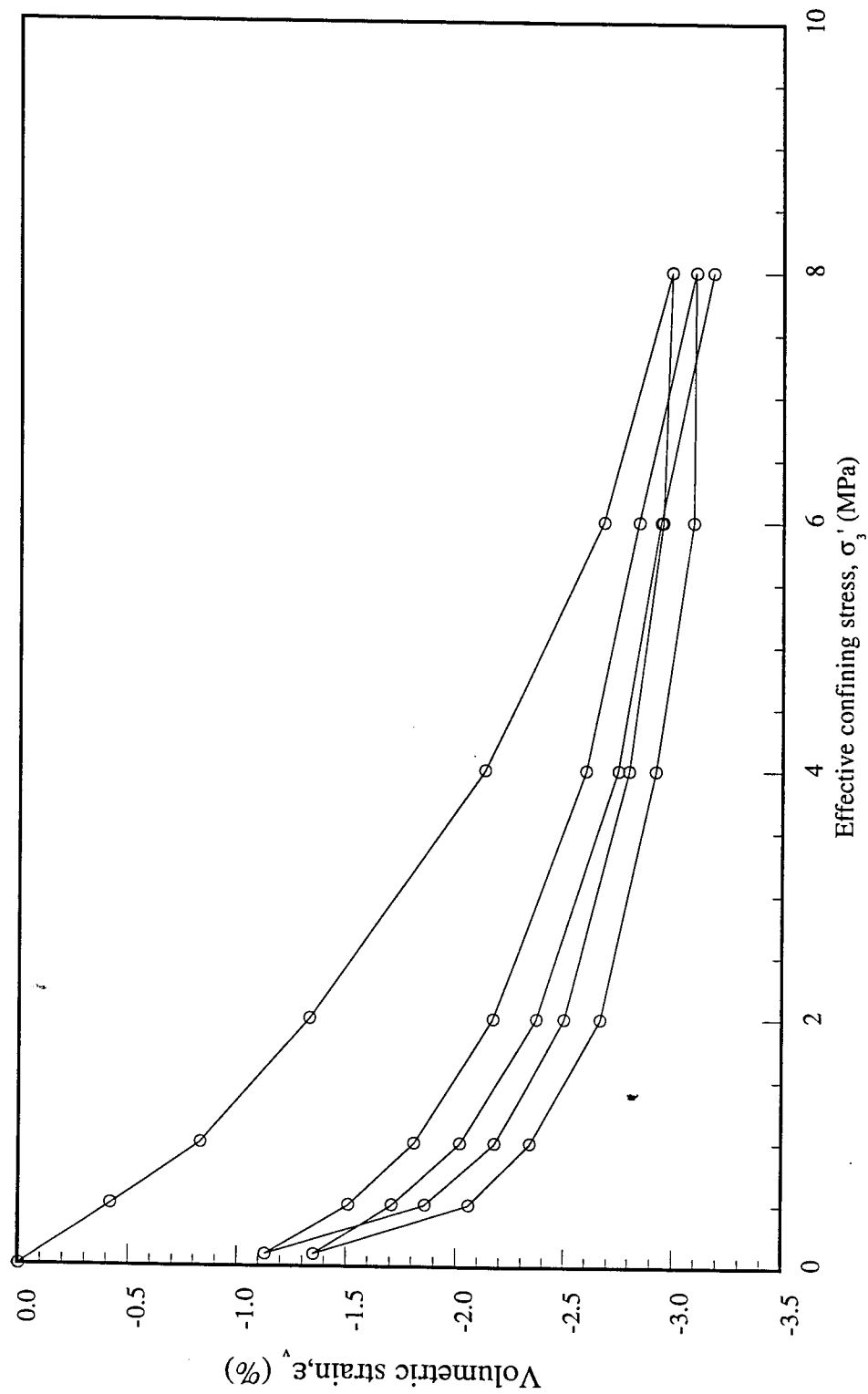


Fig C.14 Test CP5: Isotropic Cyclic Consolidation

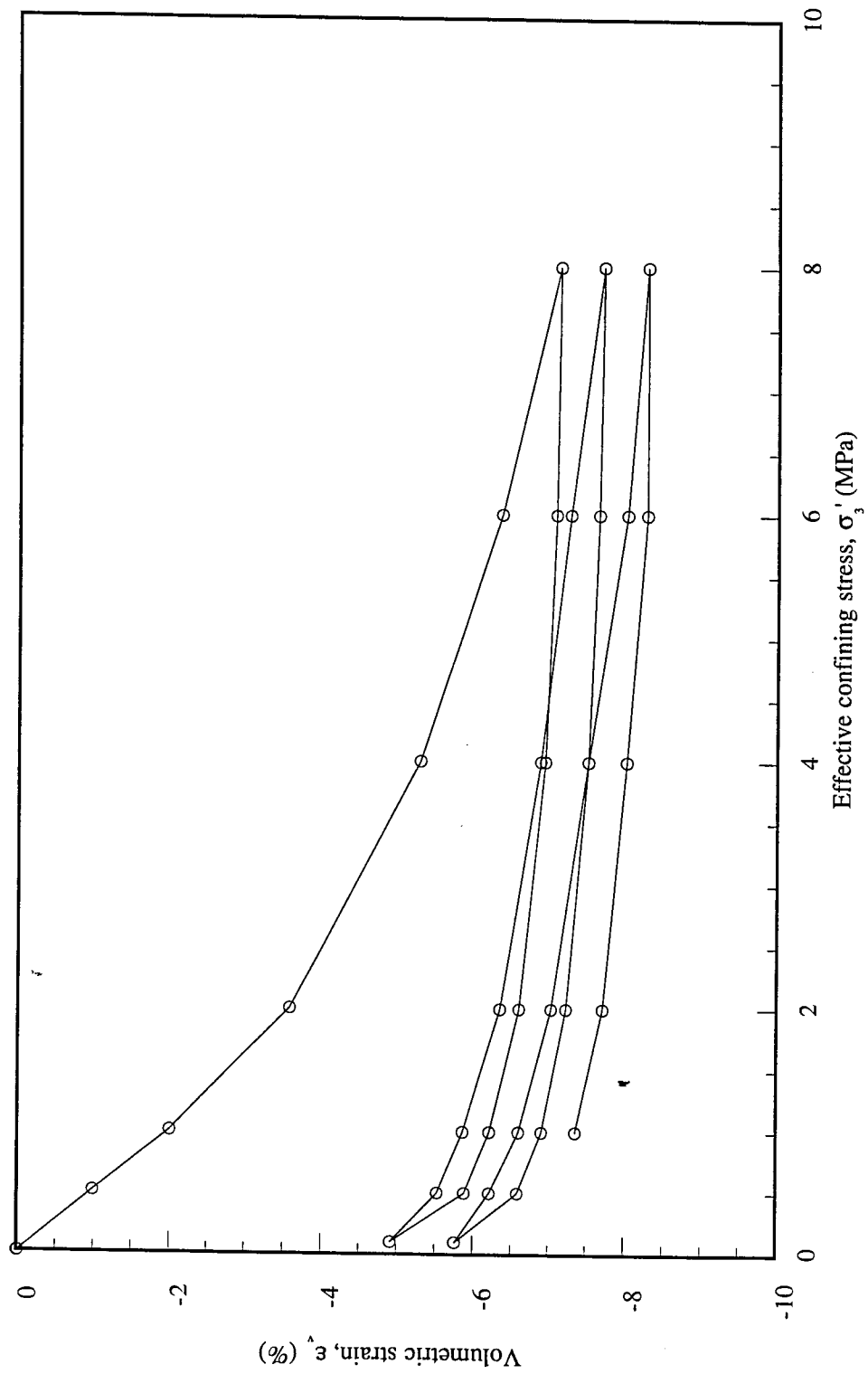


Fig C.15 Test CP6: Isotropic Cyclic Consolidation

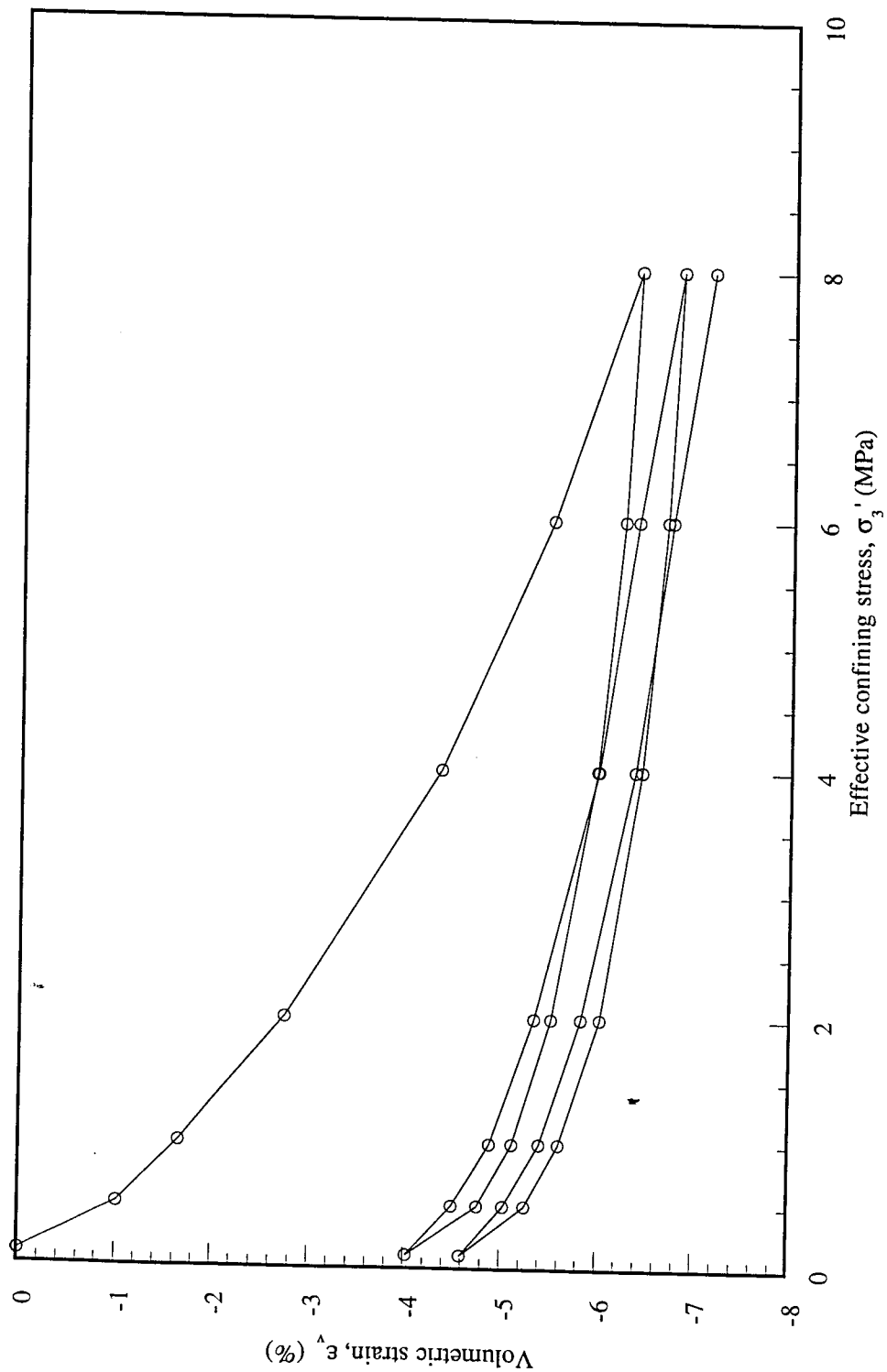


Fig C.17 Test CH1: Isotropic Cyclic Consolidation

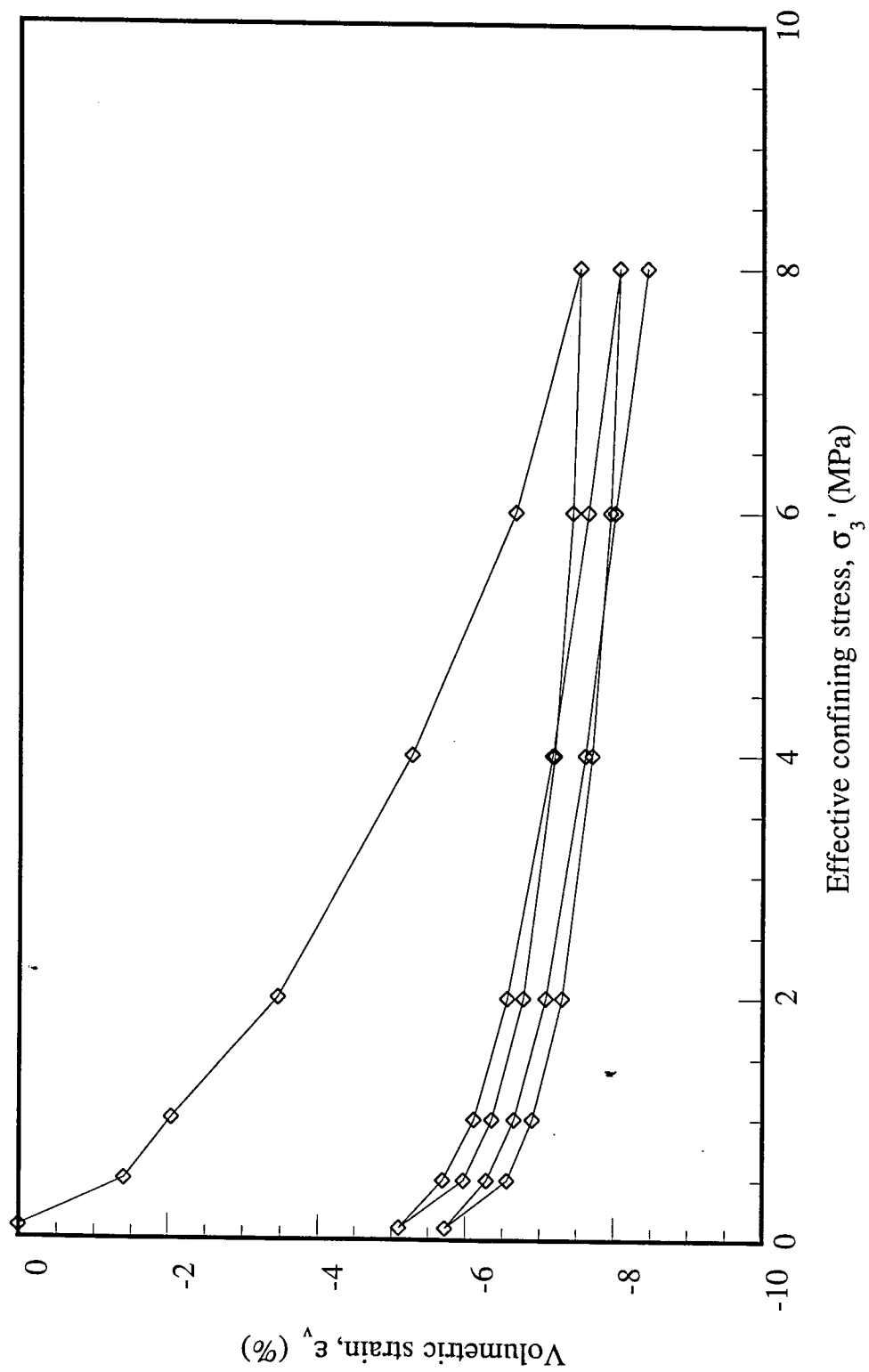


Fig C.18 Test CI2: Isotropic Cyclic Consolidation

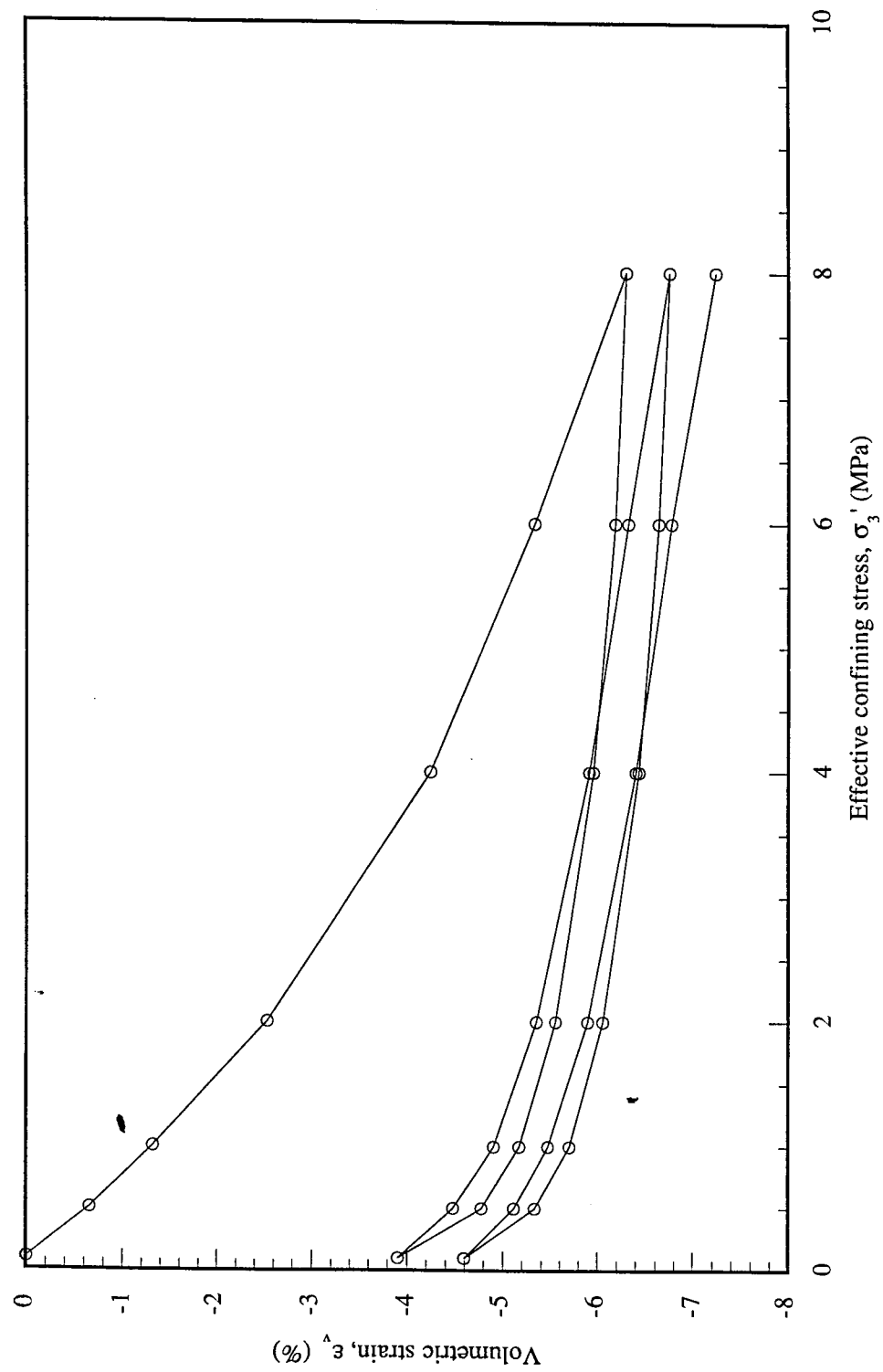


Fig C.19 Test CI3: Isotropic Cyclic Consolidation

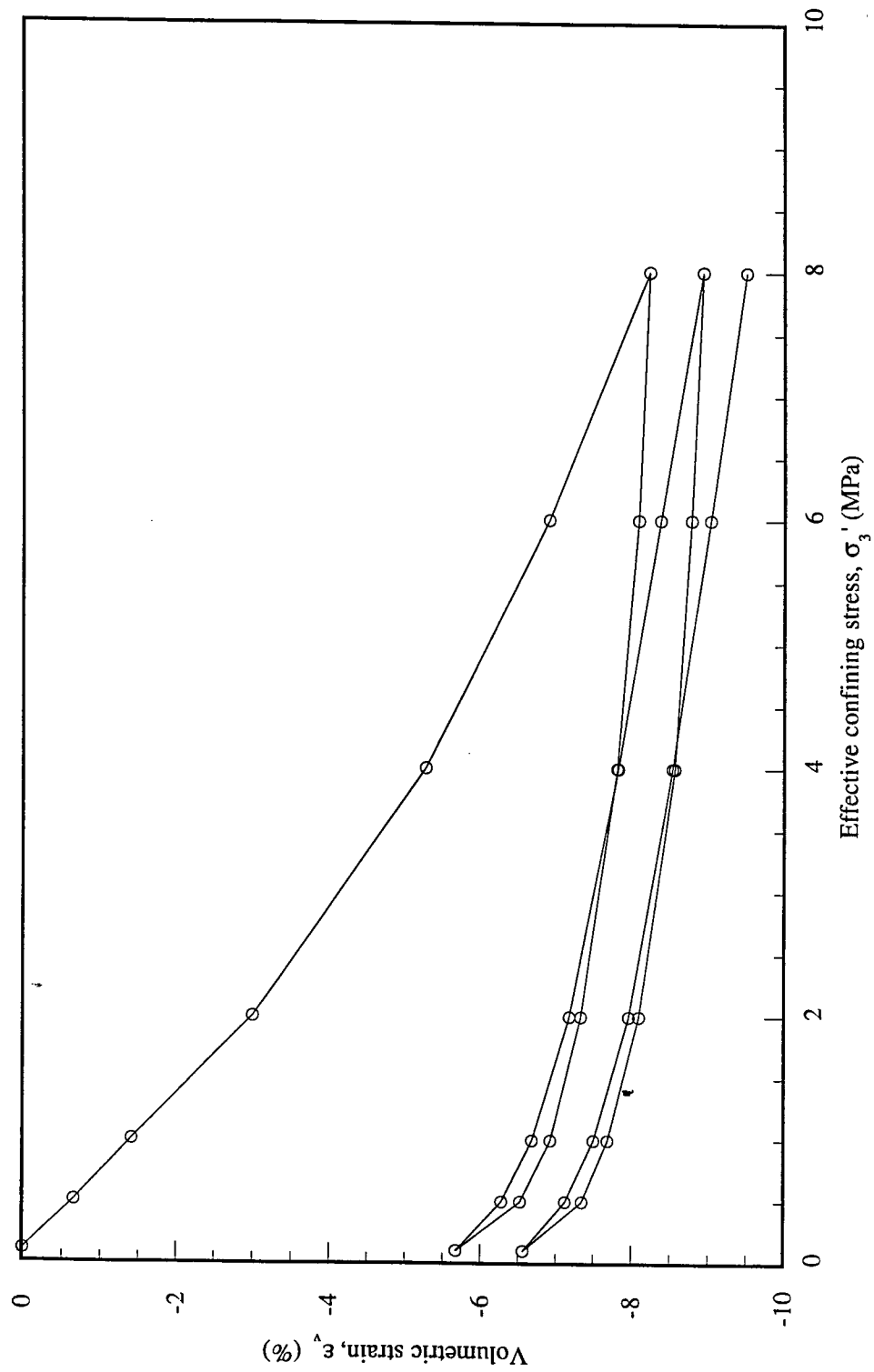


Fig C.20 Test CI4B: Isotropic Cyclic Consolidation

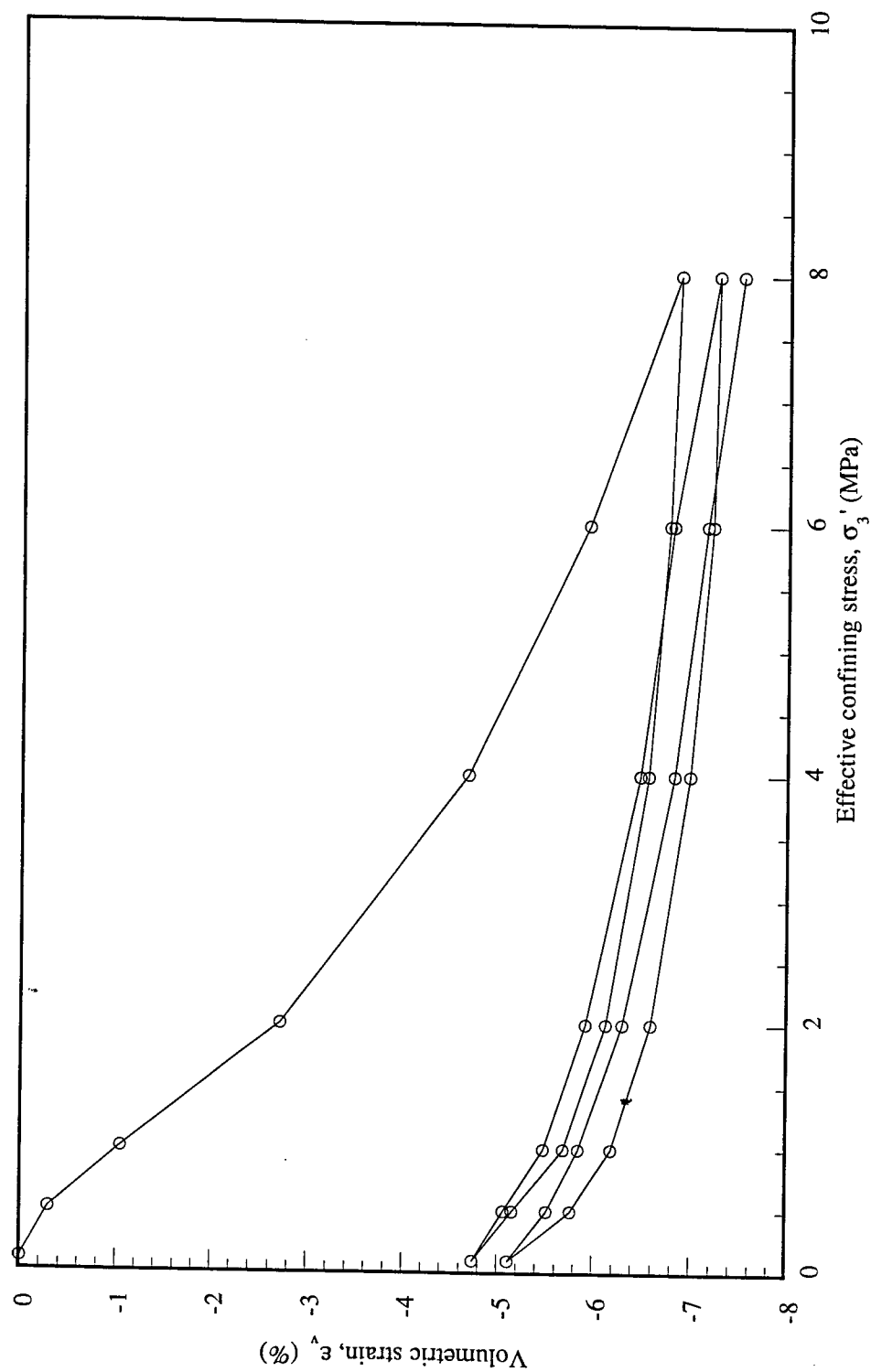


Fig C.21 Test CI5: Isotropic Cyclic Consolidation

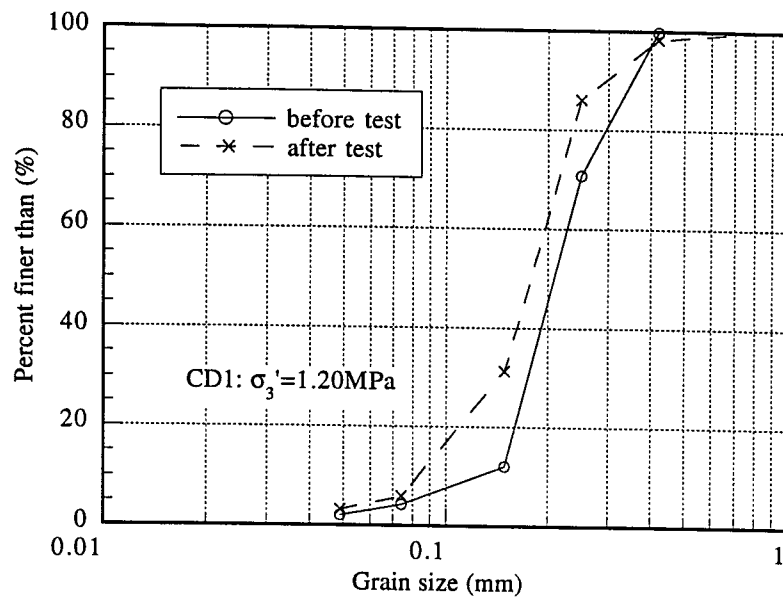


Fig C.22 Test CD1: Grain Size Analysis

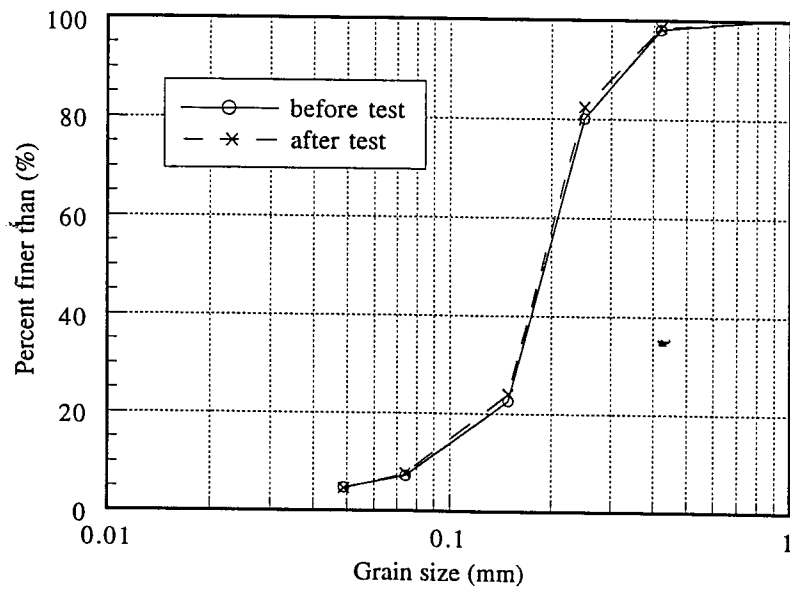


Fig C.23 Test CD2: Grain size analysis

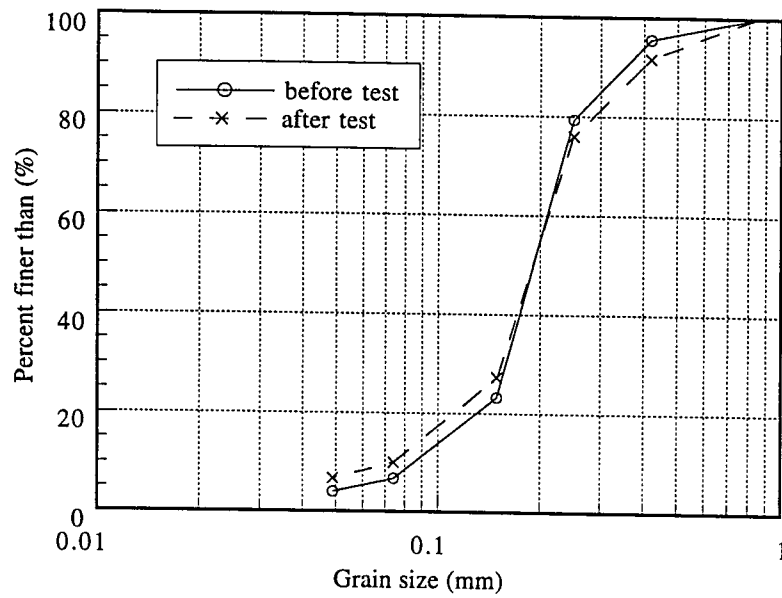


Fig C.24 Test CD3: Grain Size Analysis

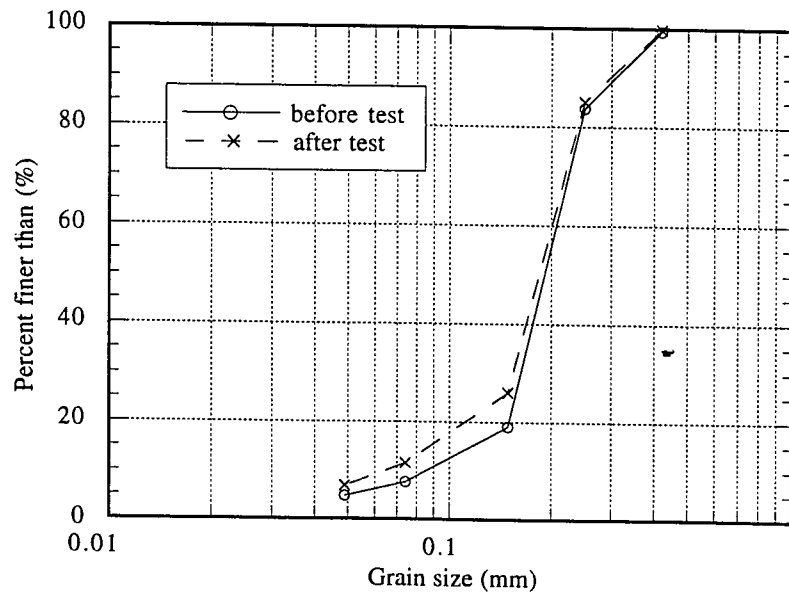


Fig C.25 Test CD5: Grain Size Analysis

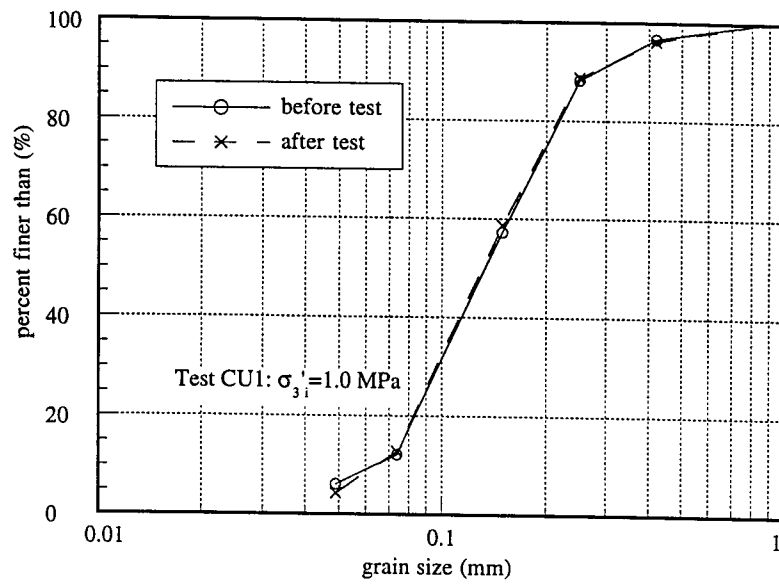


Fig C.26 Test CU1: Grain Size Analysis

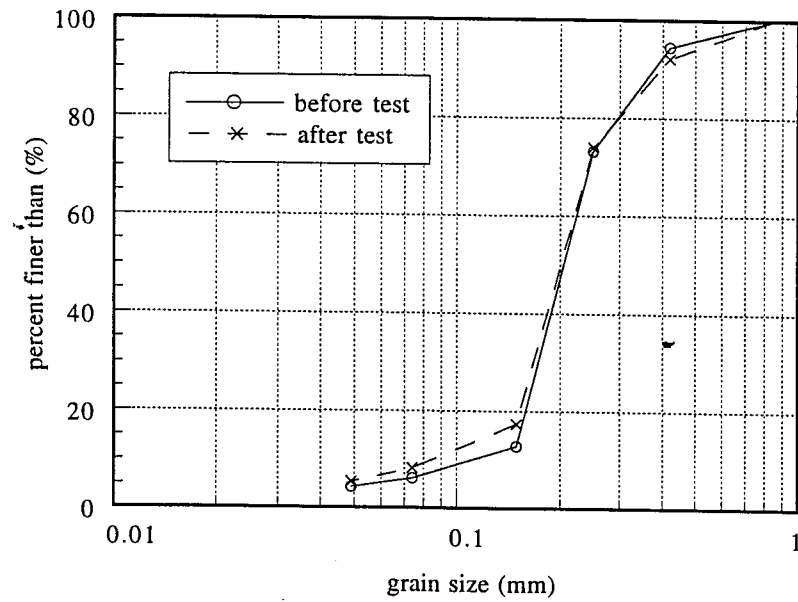


Fig C.27 Test CU2: Grain Size Analysis

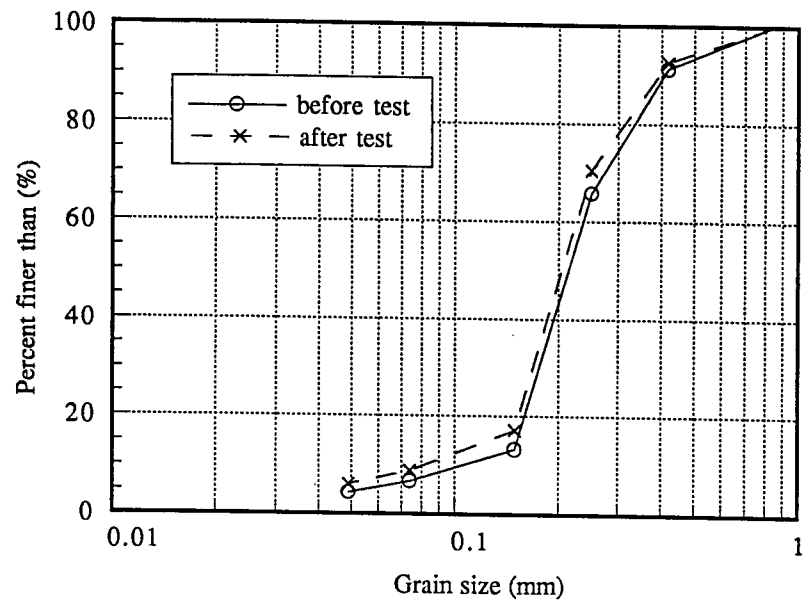


Fig C.28 Test CU3: Grain Size Analysis

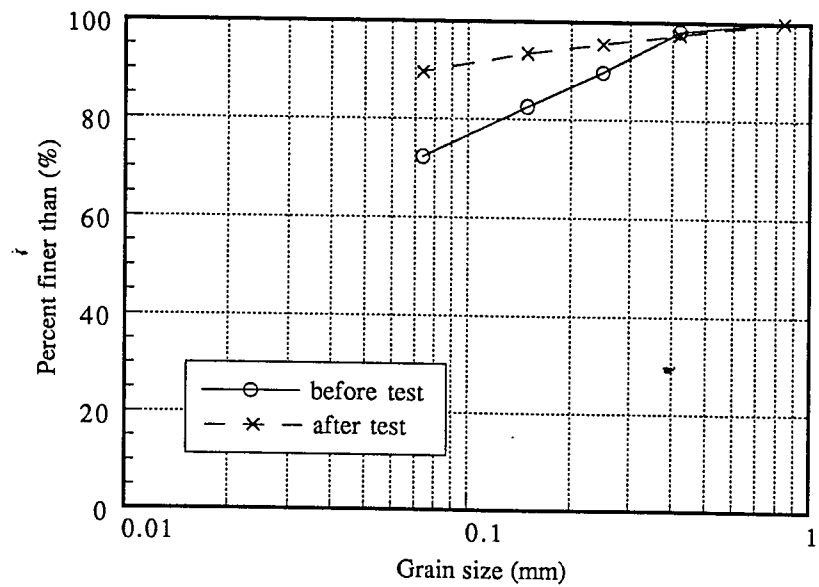


Fig C.29 Test CU4: Grain Size Analysis

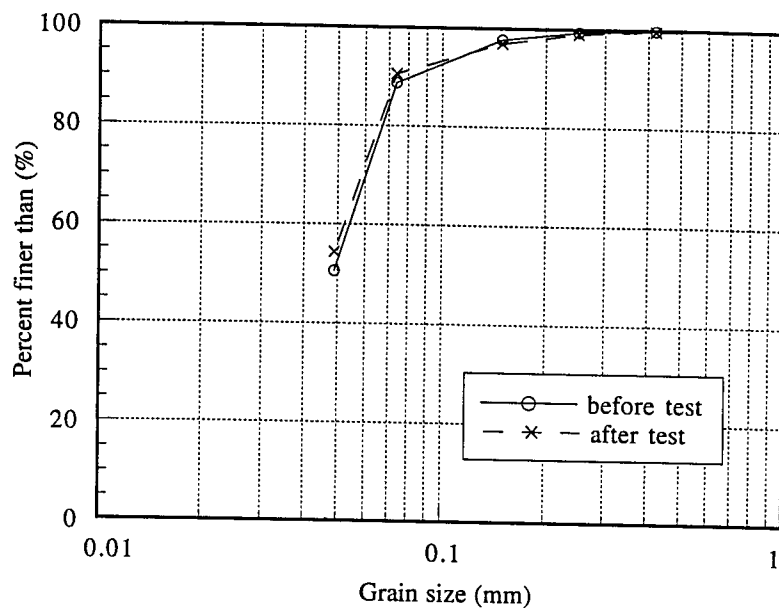


Fig C.30 Test CU5: Grain Size Analysis

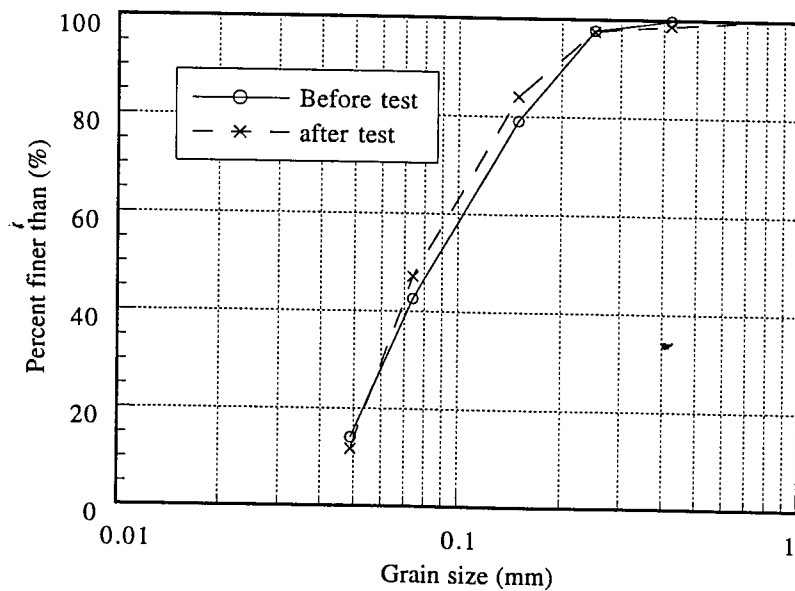


Fig C.31 Test CU6: Grain Size Analysis

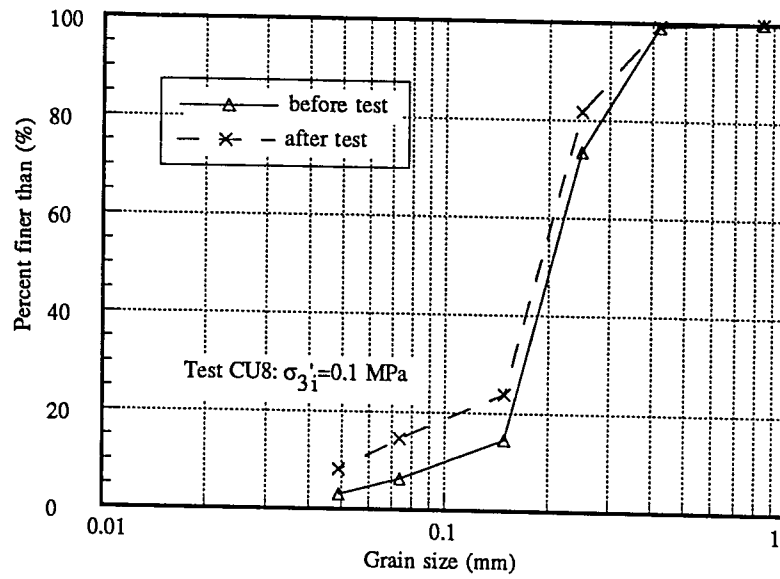


Fig C.32 Test CU8: Grain Size Analysis

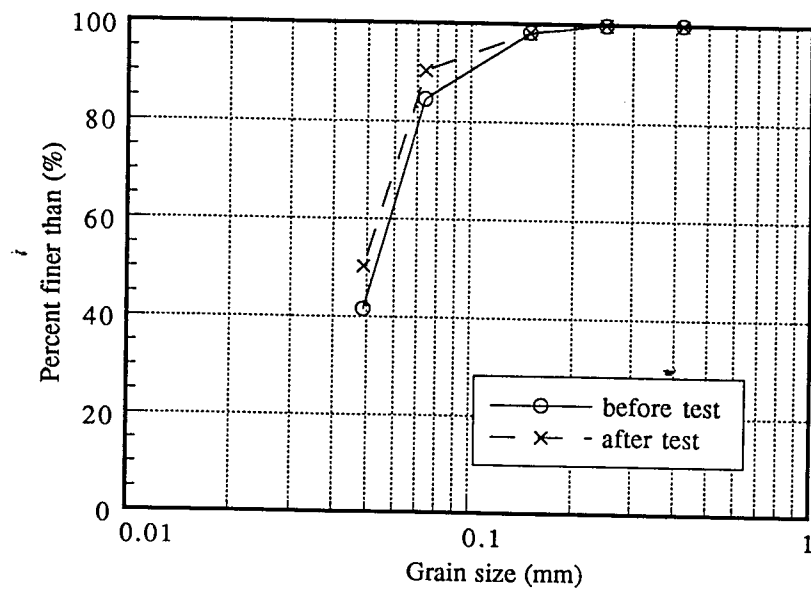


Fig C.33 Test CP1: Grain Size Analysis

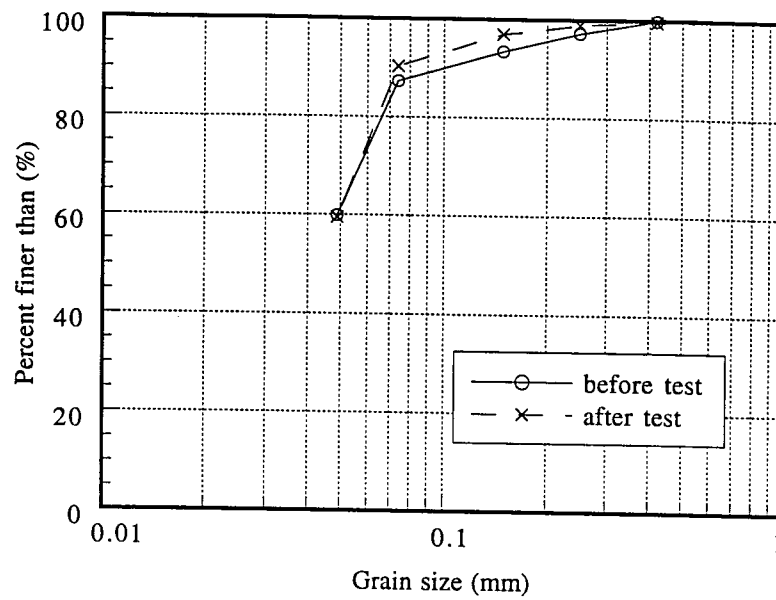


Fig C.34 Test CP2: Grain Size Analysis

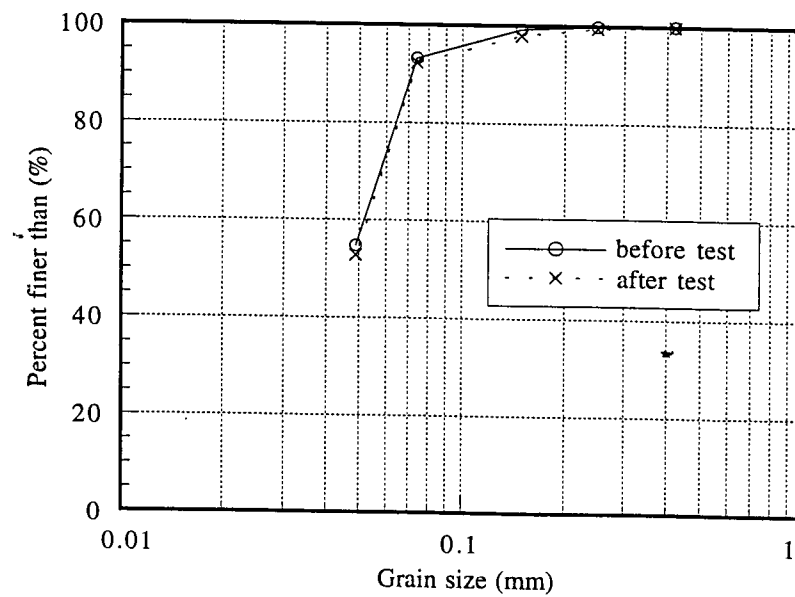


Fig C.35 Test CP3: Grain Size Analysis

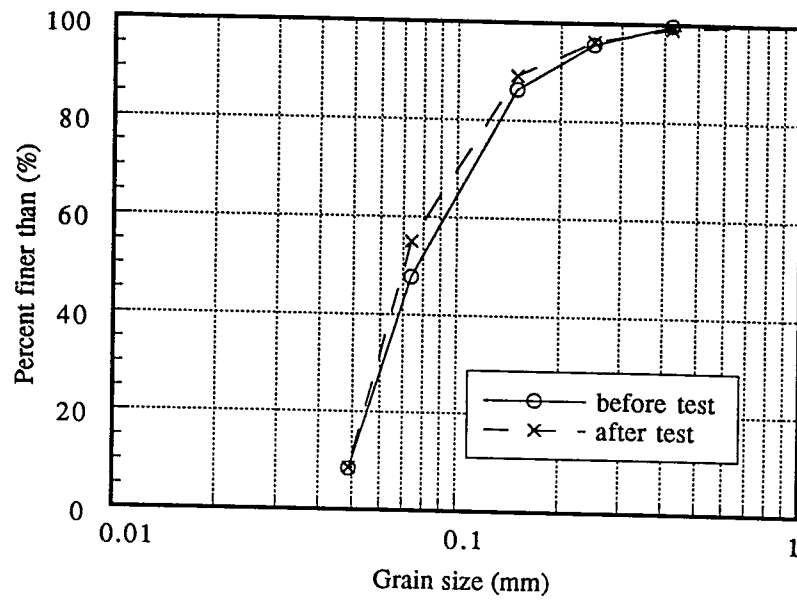


Fig C.36 Test CP4: Grain Size Analysis

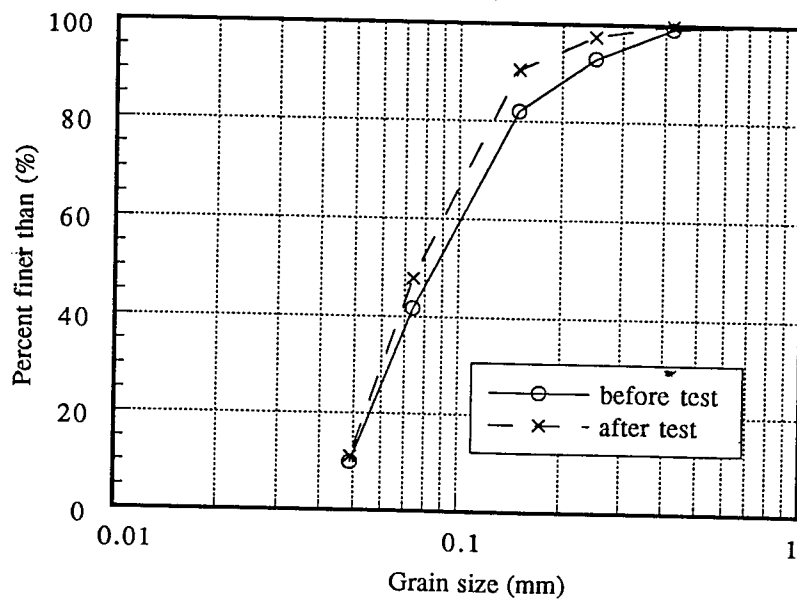


Fig C.37 Test CP5: Grain Size Analysis

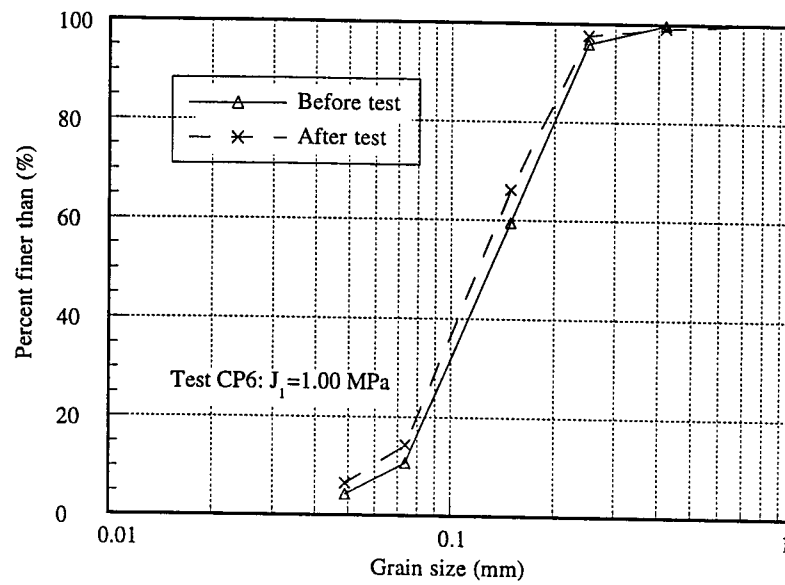


Fig C.38 Test CP6: Grain Size Analysis

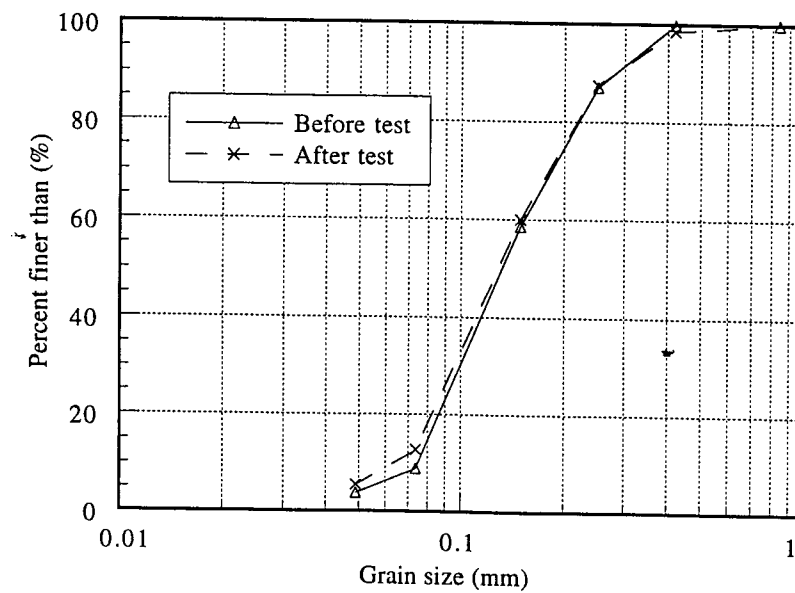


Fig C.39 Test CP7: Grain Size Analysis

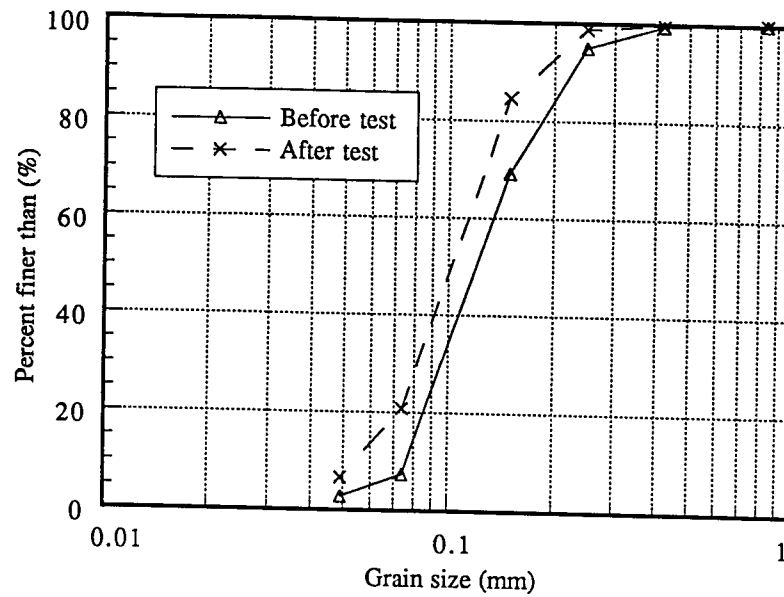


Fig C.40 Test CP8: Grain Size Analysis

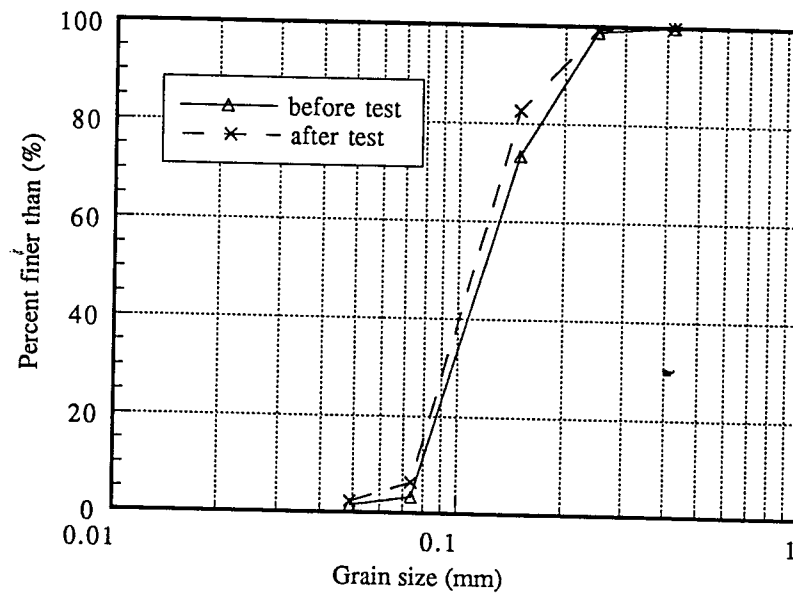


Fig C.41 Test CII: Grain Size Analysis

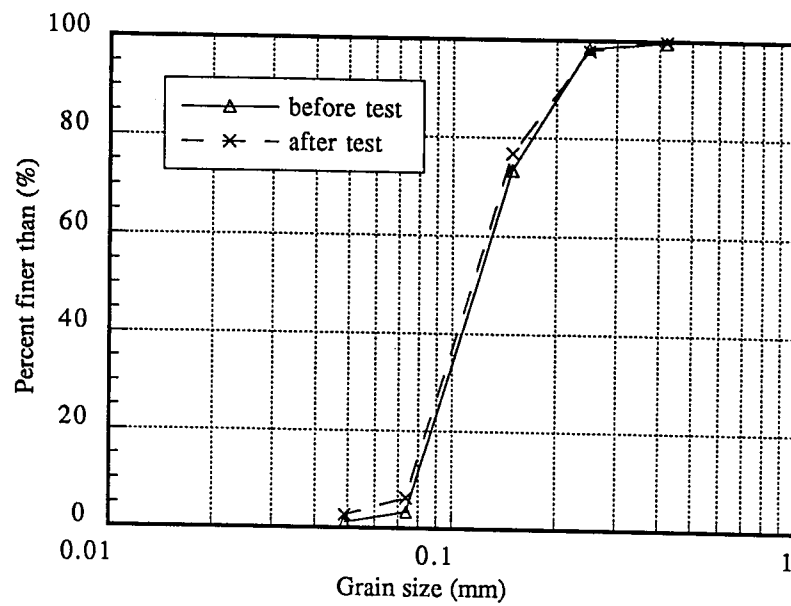


Fig C.42 Test CI2: Grain size analysis

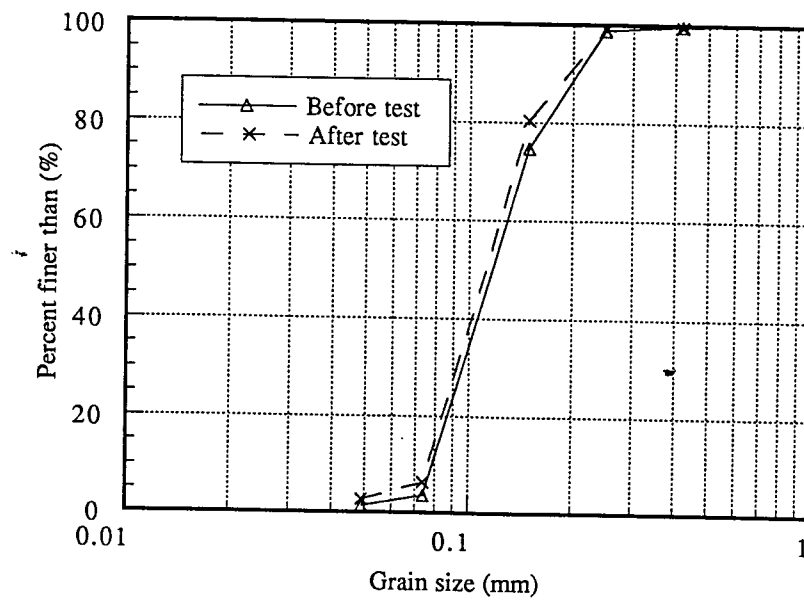


Fig C.43 Test CI3 : Grain Size Analysis

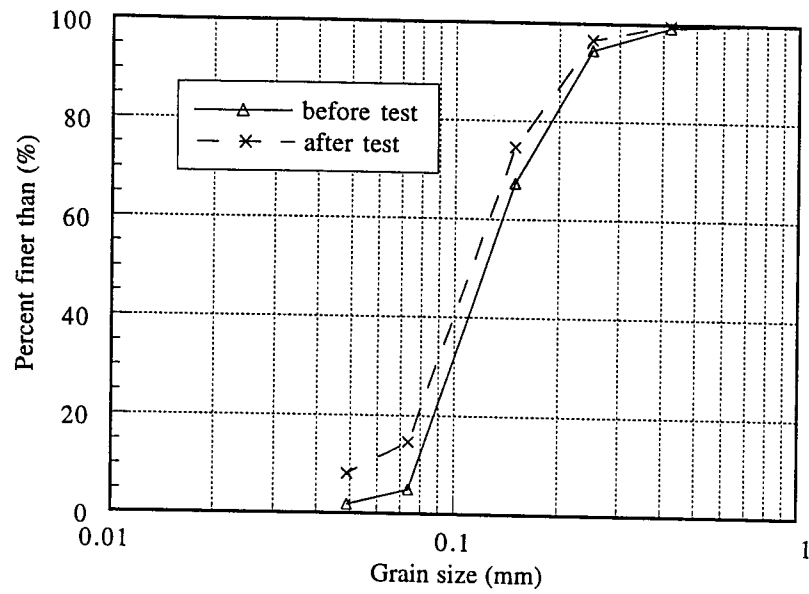


Fig C.44 Test CI4: Grain Size Analysis

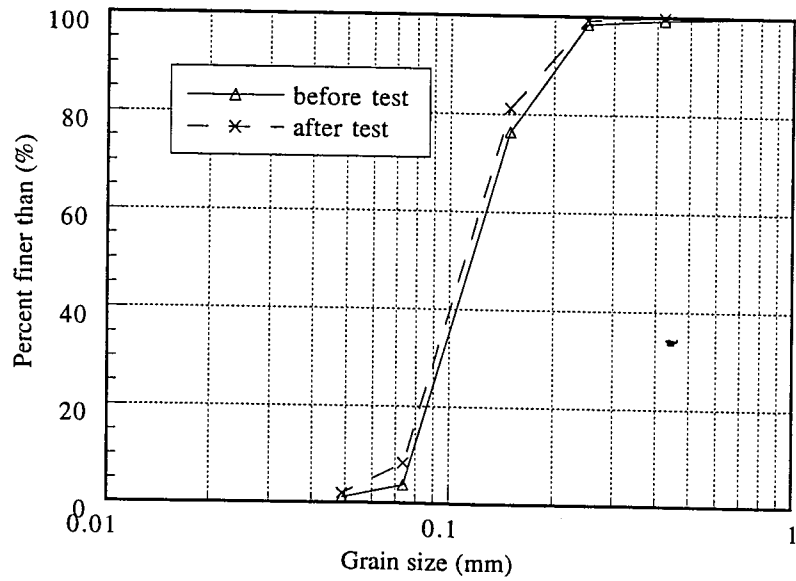


Fig C.45 Test CI4A: Grain Size Analysis

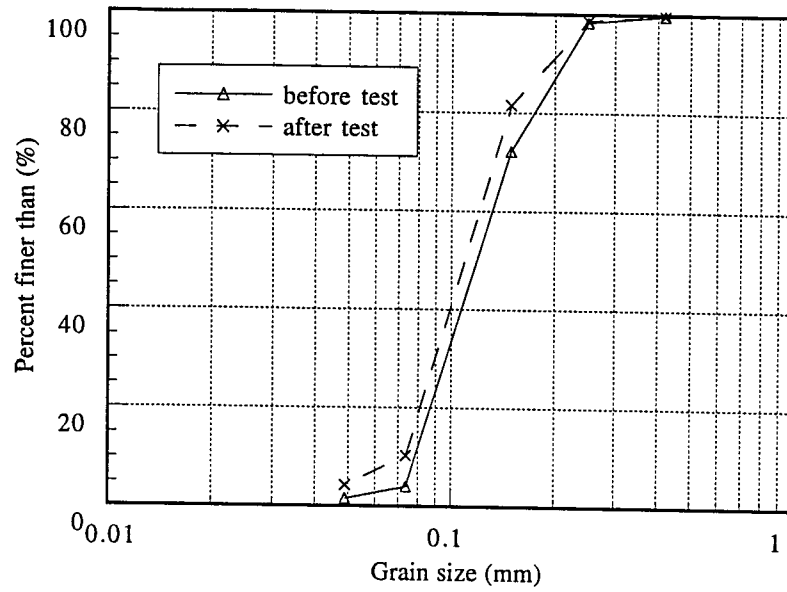


Fig C.46 Test CI4B: Grain Size Analysis

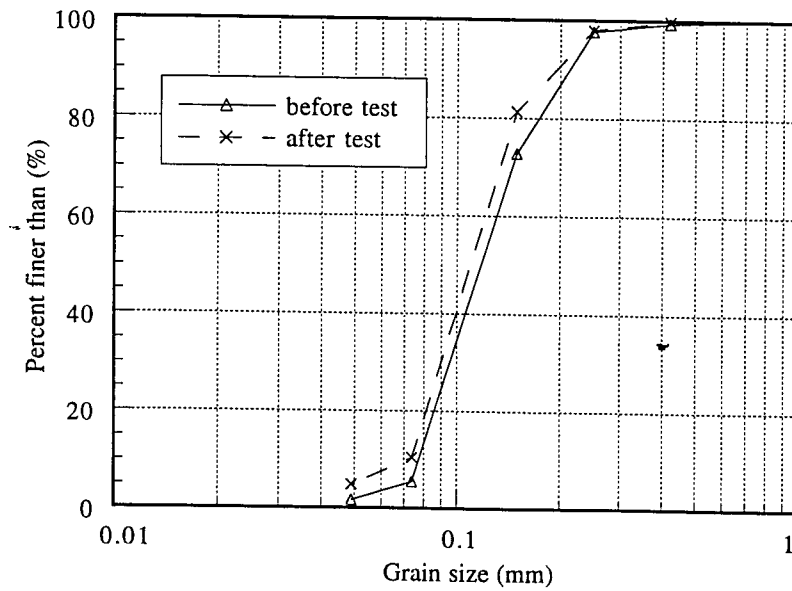


Fig C.47 Test CI5: Grain Size Analysis

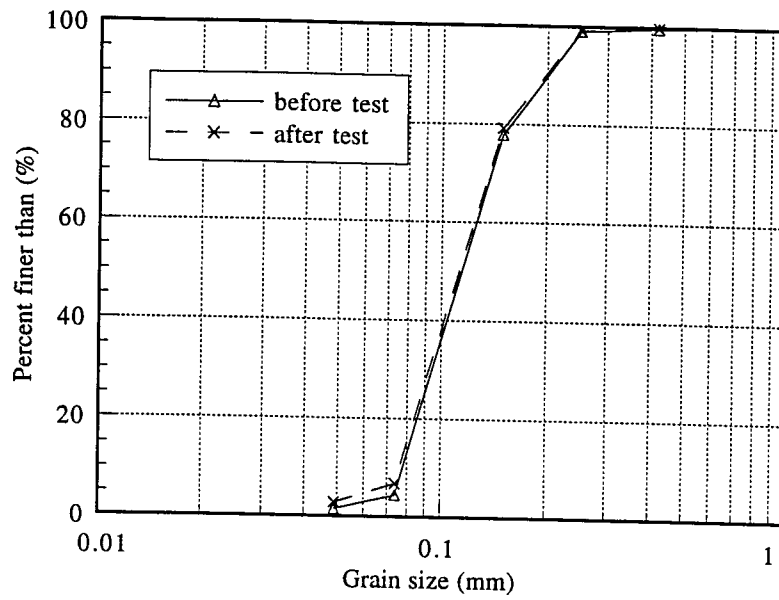
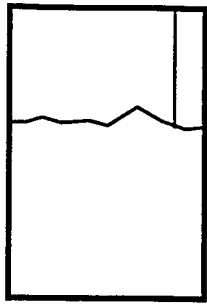
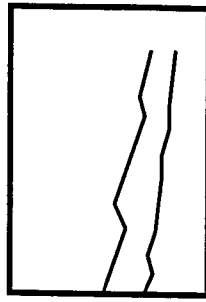


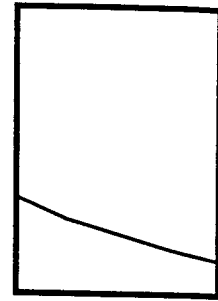
Fig C.48 Test CI5A : Grain Size Analysis



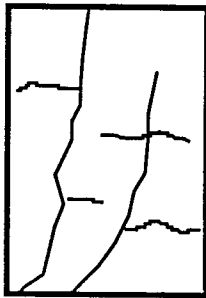
Test CD1



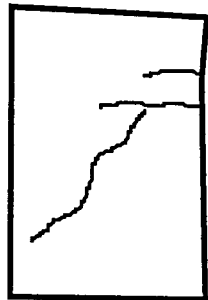
Test CD2



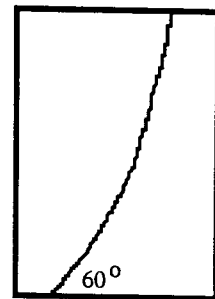
Test CD3



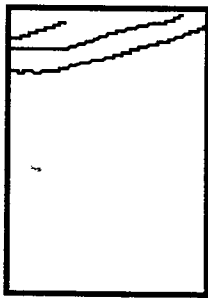
Test CD4



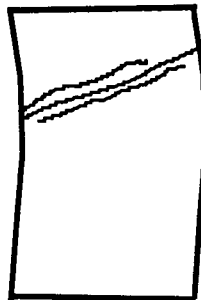
Test CD5



Test CD6



Test CU1

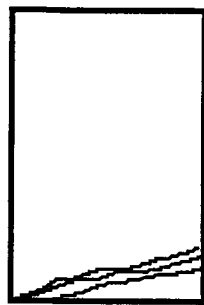


Test CU2



Test CU3

Fig C.49 Failure Modes in Triaxial Tests (1)



Test CU4



Test CU5



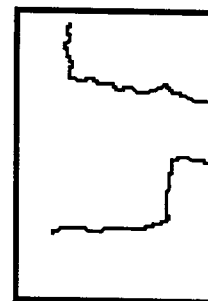
Test CU6



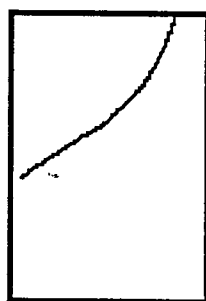
Test CU8



Test CP1



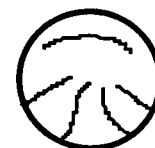
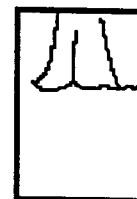
Test CP2



Tes CP3

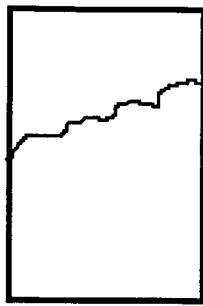


Test CP4

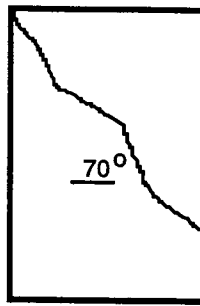


Test CP5

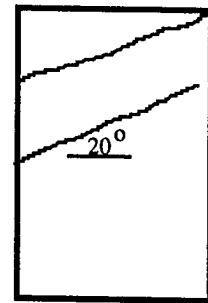
Fig C.49 Failure Modes in Triaxial Tests (2)



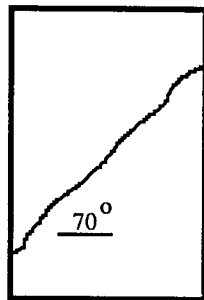
Test CP6



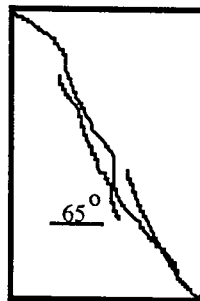
Test CP7



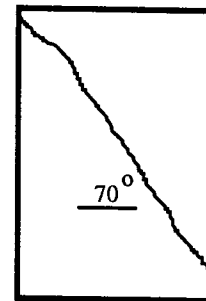
Test CP8



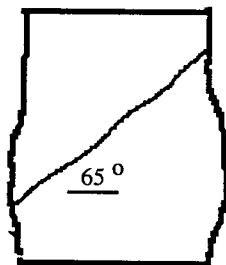
Test CI1



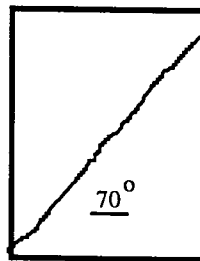
Test CI2



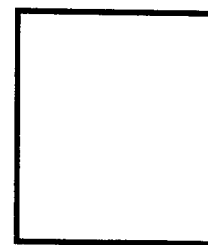
Test CI3



Test CI4



Test CI4B



Test CI5A

Fig C.49 Failure Modes in Triaxial Tests (3)